Surface Formation and Degradation of Cathode Active Materials during Synthesis and Battery Operation

Oberflächenentstehung und Degradation
von Kathodenaktivmaterialien
während Synthese und Batteriebetrieb

dem Fachbereich Biologie und Chemie der
Justus-Liebig-Universität Gießen

vorgelegte Dissertation zur Erlangung
des akademischen Grades
Doktor der Naturwissenschaften
-Dr. rer. nat.-

Sören Lukas Dreyer

21.05.2024

Dekan / Dean	Prof. Dr. Thomas Wilke
1. Gutachter / 1st reviewer	Prof. Dr. Jürgen Janek (Justus-Liebig-Universität Gießen)
2. Gutachter / 2nd reviewer	Prof. Dr. Philipp Adelhelm (Humboldt-Universität zu Berlin)
Eingereicht / submitted	20.02.2024
Disputation / disputation	21.05.2024

Eidesstattliche Erklärung

Die vorliegende Arbeit wurde im Zeitraum vom 01.09.2020 bis 19.02.2024 am Battery and Electrochemistry Laboratory (BELLA) des Instituts für Nanotechnologie am Karlsruher Institut für Technologie unter Betreuung von Prof. Dr. Jürgen Janek angefertigt.

Ich erkläre:

Ich habe die vorgelegte Dissertation selbstständig und ohne unerlaubte fremde Hilfe und nur mit den Hilfen angefertigt, die ich in der Dissertation angegeben habe. Alle Textstellen, die wörtlich oder sinngemäß aus veröffentlichten Schriften entnommen sind, und alle Angaben, die auf mündlichen Auskünften beruhen, sind als solche kenntlich gemacht. Ich stimme einer eventuellen Überprüfung meiner Dissertation durch eine Antiplagiat-Software zu. Bei den von mir durchgeführten und in der Dissertation erwähnten Untersuchungen habe ich die Grundsätze guter wissenschaftlicher Praxis, wie sie in der „Satzung der Justus-Liebig-Universität Gießen zur Sicherung guter wissenschaftlicher Praxis“ niedergelegt sind, eingehalten.

Gießen, 20.02.2024

_____

Sören Lukas Dreyer

Abstract

Lithium-ion batteries (LIBs) offer both a relatively high energy and high power density, and thus see widespread application and continuous research and development efforts, especially to increase their energy density further and to decrease their cost. Sodium-ion batteries (SIBs) are considered, both in research and industry, as a complementary battery technology to LIBs, with on the one hand lower energy densities, yet on the other hand with lower costs, due to the ubiquity of sodium in contrast to the relative scarcity of lithium. In both LIBs and SIBs, the cathode active material (CAM) makes up the largest part each of battery weight and cost. Consequently, understanding and improving CAMs is of utmost importance to further develop battery technology.

This work focusses on the CAM surface from various perspectives, with *in situ* gas evolution studies as an additional bridging element, as various reactions on and of the CAM surface can be understood from the gasses they evolve. First, a review of *in situ* gas evolution studies on battery materials is presented, focusing on novel materials and cell concepts. The gas evolution of SIBs in contrast to LIBs is identified as a research gap.

The first original research work in this thesis then considers the formation of CAM surfaces in dependence of the process route of CAM preparation. Specifically, it is shown that Zr^{4+}, when introduced into $LiNiO_2$ (LNO) as a dopant, is enriched on the primary particle grain boundaries, acting as a grain growth inhibitor. The doping process route determines the initial Zr^{4+} distribution, and thus the extent of the grain growth inhibition, yielding LNO primary particles of different specific surface areas. This in turn determines both electrochemical performance and gas evolution of the CAM.

In a second work, the exposure of new surfaces due to crack formation during battery cycling is studied *operando* via Acoustic Emission (AE) for a series of SIB CAMs with increasing configurational entropy. It is shown that AE allows to distinguish between less degradative intergranular cracking, i.e. deagglomeration of particles, and more degradative intragranular cracking, while not being sensitive to gas evolution.

Lastly, the gas evolution of Prussian white (PW), a SIB CAM, especially the evolution of $(CN)_2$ and HCN from its hexacyanoferrate structure, is studied in detail, after a previous study finding first evidence for $(CN)_2$ evolution, indicating a new surface degradation mechanism for PW CAMs. It is found that the CAM water content determines the evolution of H_2, which is the most prominently evolved gas. Yet, the conductive salt anion in the electrolyte determines CO_2 and $(CN)_2$ evolution between $NaPF_6$- and $NaClO_4$-based electrolytes. The oxidative properties of $NaClO_4$ are identified as the cause for increased $(CN)_2$ evolution in its presence at the CAM surface, and a plausible reaction mechanism is presented in light of the available literature.

Keywords: Cathode Active Material, Surface Formation, Surface Degradation, Gas Evolution, Acoustic Emission

Zusammenfassung

Die Lithium-Ionen-Batterie (LIB) bietet sowohl eine relativ hohe Energiedichte als auch Leistungsdichte. Sie erfährt daher weitverbreitete Anwendung und kontinuierliche Forschungs- und Entwicklungsbemühungen, insbesondere um die Energiedichte weiter zu steigern und die Kosten zu senken. In Forschung und Industrie wird die Natrium-Ionen-Batterie (SIB) als eine komplementäre Technologie zur Lithium-Ionen-Batterie erwogen, mit der auf der einen Seite zwar geringere Energiedichten erzielt werden, dies auf der anderen Seite aber auch mit geringeren Kosten verbunden ist, da Natrium im Vergleich zu Lithium allgegenwärtig ist. Das Kathodenaktivmaterial (CAM) trägt in beiden Fällen den größten Anteil sowohl zum Gewicht als auch zu den Kosten der Batterie teil. Für die Weiterentwicklung von Batterietechnologien sind das Verständnis und die Verbesserung des Kathodenaktivmaterials daher von zentraler Bedeutung.

In dieser Dissertation wird die Oberfläche von Kathodenaktivmaterialien aus verschiedenen Perspektiven betrachtet, wobei *in situ* Studien der Gasentwicklung ein weiteres verbindendes Element darstellen, da verschiedene Reaktionen auf und mit der Oberfläche anhand der dabei entwickelten Gase untersucht werden können. Zuerst wird eine Übersichtsarbeit zu diesen *in situ* Gasentwicklungsstudien an Batteriematerialien vorgestellt, deren Fokus auf neuen Materialien und Zellkonzepten liegt. Hierin wird die Gasentwicklung in Natrium-Ionen-Batterien im Vergleich zu Lithium-Ionen-Batterien als Forschungslücke identifiziert.

Die erste eigenständige Forschungsarbeit in dieser Dissertation behandelt die Ausbildung der CAM-Oberfläche in Abhängigkeit von der gewählten Syntheseroute. Es wird gezeigt, dass Zr^{4+}, welches $LiNiO_2$ (LNO) zur Dotierung zugegeben wird, sich an den Korngrenzen der Primärpartikel anreichert und das Partikelwachstum hemmt. Die gewählte Dotierprozessroute bestimmt die anfängliche Zr^{4+}-Verteilung und damit auch das Ausmaß der Partikelwachstumshemmung, was schlussendlich zu Primärpartikeln unterschiedlicher spezifischer Oberfläche führt. Von dieser Oberfläche wiederum hängen die elektrochemischen Eigenschaften und die Gasentwicklung des Kathodenaktivmaterials maßgeblich ab.

In der zweiten Veröffentlichung wird die Entstehung neuer Partikeloberflächen durch Ausbildung von Rissen während des Ladens und Entladens für eine Reihe von SIB-Kathodenaktivmaterialien mit zunehmender Konfigurationsentropie durch Messungen der akustischen Emission (AE) *operando* verfolgt. Es wird gezeigt, dass diese Methode eine Unterscheidung von wenig degradativer Rissbildung zwischen Primärpartikeln und stärker degradativer Rissbildung innerhalb eines Partikels ermöglicht, während die parallele Gasentwicklung nicht detektiert wird.

In einem letzten Beitrag wird die Gasentwicklung, insbesondere von $(CN)_2$ und HCN, des SIB-Kathodenaktivmaterials Preußisch Weiß detailliert untersucht, nachdem eine vorhergehende Studie erste Hinweise auf die $(CN)_2$-Entwicklung als neuen Oberflächendegradationsmechanismus gegeben hatte. Der Wassergehalt bestimmt maßgeblich die Entwicklung von H_2, welches das am meisten gebildete Gas ist. In einem Vergleich von Elektrolyten auf Basis von $NaPF_6$ und $NaClO_4$ ist es allerdings das Anion

des Leitsalzes, welches die Entwicklung von CO_2 und $(CN)_2$ bestimmt. Die oxidativen Eigenschaften von $NaClO_4$ werden als ursächlich für die verstärkte $(CN)_2$-Entwicklung in seiner Gegenwart an der CAM-Oberfläche identifiziert und ein unter Betrachtung der verfügbaren Literatur plausibler Reaktionsmechanismus wird vorgestellt.

Schlüsselwörter: Kathodenaktivmaterial, Oberflächenbildung, Oberflächendegradation, Gasentwicklung, Akustische Emission

List of Abbreviations

AE	Acoustic emission
BELLA	Battery and electrochemistry laboratory
BEV	Battery electric vehicle
BMS	Battery management system
CAM	Cathode active material
CEI	Cathode electrolyte interphase
DEMS	Differential electrochemical mass spectrometry
DRX	Disordered rock-salt transition metal oxide
EC	Ethylene carbonate
EPR	Electron paramagnetic resonance
FEC	Fluoroethylene carbonate
GC-MS	Gas chromatography-mass spectrometry
HC	Hard carbon
ICP-OES	Inductively coupled plasma-optical emission spectroscopy
LA-ICP-MS	Laser ablation-inductively coupled plasma-mass spectrometry
LCO	Lithium cobalt oxide, $LiCoO_2$
LFP	Lithium iron phosphate, $LiFePO_4$
LIB	Lithium-ion battery
LNO	Lithium nickel oxide, $LiNiO_2$
NCA	Lithium nickel cobalt aluminum oxide, $LiNi_xCo_yAl_zO_2$
NCM	Lithium nickel cobalt manganese oxide, $LiNi_xCo_yMn_zO_2$
NMR	Nuclear magnetic resonance
NTC	Negative temperature coefficient
NVPF	Sodium vanadium phosphate fluoride, $Na_3V_2(PO_4)_2F_3$
OCV	Open circuit voltage
OEMS	Online electrochemical mass spectrometry
PBA	Prussian blue analogue
pCAM	Precursor cathode active material, i.e. a (mixed) transition metal hydroxide
PDF	Pair distribution function
PVDF	Polyvinylidene difluoride
PW	Prussian white
RIXS	Resonant inelastic X-ray scattering
SEI	Solid electrolyte interphase
SIB	Sodium-ion battery
SOC	State of charge
SOH	State of health
SSB	Solid-state battery
STEM-EDS	Scanning transmission electron microscopy with energy-dispersive X-ray spectroscopy
TMS	Titration mass spectrometry
ToF	Time of flight
ToF-SIMS	Time of flight-secondary ion mass spectrometry
XAS	X-ray absorption spectroscopy
XPS	X-ray photoelectron spectroscopy

Table of Contents

1. Introduction

The first battery, a stack of alternating copper and zinc disks, was reported by Volta in 1800, and such a galvanic cell became later known as Volta pile.[1] In the early days of electrochemistry, it played an important role as a source of direct current and relatively high voltages. With galvanic cells as a current source for electrolysis, Davy discovered sodium, potassium, magnesium, calcium, strontium, barium and boron, and clarified the nature of chlorine soon after.[2-6] It was his assistant Faraday, who, again with the help of early batteries, later described the laws of electrolysis, studied the nature of electromagnetism and also popularized electrochemical terminology, such as anode, cathode and electrolyte.[7,8] Their and many others' discoveries ushered in the era of electrification. Various practical batteries, such as the Daniell cell,[9] were subsequently invented to electrochemically store and supply electric energy on demand. Battery technology saw further improvements when portable and rechargeable batteries, i.e. secondary cells, were developed, such as the lead-acid battery in 1860, for which a multi-billion dollar industry has developed up to today.[10]

During the 20th century, many other cell chemistries were developed, and cells manufactured in various forms and sizes according to application needs. For households and end customers, the most common battery chemistries were based on aqueous alkaline electrolytes, such as Ni-Cd, Zn-MnO_2 and later Ni-metal hydride cells.[11] Concurrently, the electrochemical groundwork for the non-aqueous lithium-ion battery (LIB), which will be discussed in more detail in chapter 1.1., was laid, and the LIB saw commercialization in the early 1990s,[12] just as the rise of portable consumer electronics and the "wireless revolution"[13] increased the global demand for batteries.[11] With the spread of smartphones and associated wearable technology like smart watches and wireless headphones, this increasing need for small, lightweight cells continues until today.[11,14] Even more importantly, LIBs today are at the heart of the global transition from internal combustion engine vehicles to battery electric vehicles (BEV), which reshapes industries and value chains worldwide, as the battery constitutes more than 25% of a BEV's value and the global BEV battery demand is forecasted to be between 1.9 and 4.3 TWh by 2030, with the LIB supply chain at that time reaching 400 billion US$ annual revenue.[15-18] At the same time, the electrical grid continues to transition from electricity production at centralized fossil fuel power plants to decentralized production from renewable energy sources, whose availability is more volatile.[19,20] Therefore, grid energy storage also contributes to rising battery demand.

Except for some designs based on cells originally developed for handheld electronics, such as the 18650 cylindrical cell format,[12] BEVs and grid storage commonly require larger cells, be they cylindrical, prismatic or in pouch format.[21,22] Both for large BEV batteries, as well as in miniature consumer electronics, batteries are required to be as small and lightweight as possible while still supplying the necessary electrical power and energy for their application. The battery's power and energy density are therefore key parameters, defined as the ratio between available power (in W) or energy (in Wh) and battery weight (gravimetric) or volume (volumetric), respectively. Of all widely available battery chemistries, it is the LIB that can offer both the highest power and energy densities, as shown in **Figure 1a**.[23-25] As of 2021, i.e. after more than a decade of intensive BEV cell development efforts, energy densities even above 250 Wh kg^{-1} and 700 Wh g^{-1}, respectively, have been realized on the cell level.[15,26]

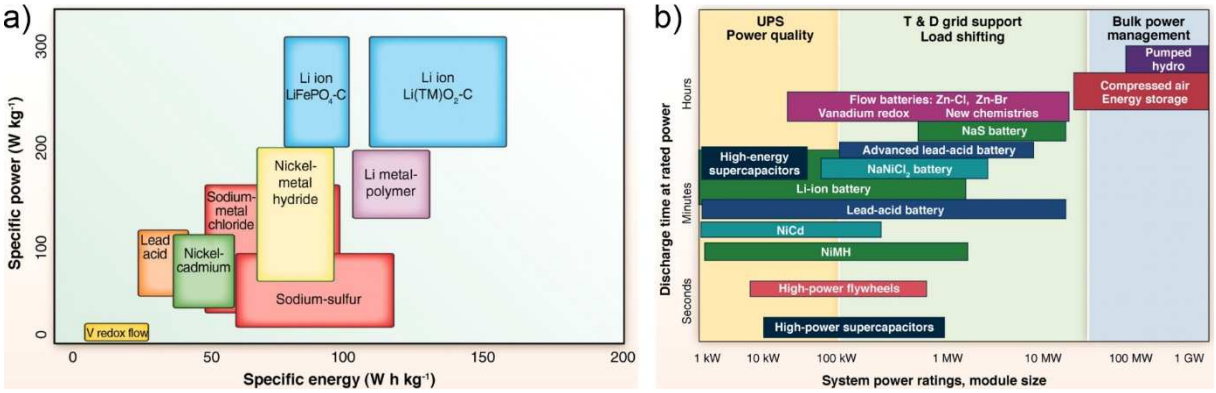

Figure 1: a) Power and energy densities realized by various battery chemistries. b) Batteries and complementary technologies in electrical grid applications. Adapted with permission from ref. [25]. Copyright © 2011 AAAS.

One specific battery chemistry or design can, however, not fulfill all application scenarios at the same time, and a trade-off between power and energy density is commonly observed.[24,26] Another key factor to consider, especially for cheap BEVs and in grid storage, where space and weight constraints are less severe, is the cost of batteries. While cost per cell is often increased with increasing energy density, the cost per unit of stored energy can also decrease, as less cells in total are required.[27,28] Battery chemistry and design selection further depend on the expected required cycle and calendric life time, safety considerations, the typical discharge time and the required power output, while highly specialized applications, such as batteries for spacecrafts[29] or biomedical implants,[30] may also come with further individual requirements. Especially for the scales of grid energy storage and grid stabilization, batteries are also not the only possible storage technology, with alternatives ranging from capacitators to

pump-storage hydroelectricity also being available, as shown in **Figure 1b**.[25] Other electrochemical solutions, most importantly hydrogen fuel cell/electrolyzer combinations and redox-flow cells, have been developed for on-demand electricity generation and storage, also in mobility contexts.[31,32]

While the LIB today is the most prominent battery technology, especially so for BEVs, various other cell chemistries and design concepts are being researched and developed for different use cases, mostly with the aim of realizing higher energy and power densities or lower costs or a combination thereof in comparison to LIBs. These include lithium-sulfur,[33] sodium-sulfur,[34] metal-air,[35] sodium-ion (SIB),[36] potassium-ion[37] and solid-state batteries (SSB).[38] Especially SIBs, mainly offering reduced raw material costs for the price of reduced energy density, are considered as a near-future complementary technology to LIBs,[36,39] since their conceptual similarity allows for the production of cells on existing LIB production lines and in existing format standards.[40] SIB technology and materials, also in contrast to LIB materials, are discussed in more detail in chapter 1.

1.1. Lithium-Ion Batteries

Against the backdrop of the oil crises, principal works that shaped the development of LIBs were carried out in the 1970s, when Whittingham first reported on the reversible electrochemical intercalation of Li^+ ions into the layered structure of TiS_2.[41] Combined with a Li-metal anode and non-aqueous electrolyte, this way about 2.5 V open circuit voltage (OCV) were realized. Soon after, Goodenough and coworkers proposed layered oxides, such as lithium cobalt oxide (LCO, $LiCoO_2$) and lithium nickel oxide (LNO, $LiNiO_2$) as an alternative class of intercalation hosts and cathode active materials (CAMs), obtaining more than 4 V OCV against Li-metal anodes.[42,43] The use of Li-metal anodes, however, impeded early commercialization efforts (MoLi Energy, with MoS_2 CAM) due to safety concerns over fire hazards.[12,14] Parallel to the development of intercalation CAMs, however, Besenhard and Armand had reported intercalation of Li^+ ions also into graphite.[44,45] Yoshino and coworkers developed carbonaceous anodes for LIBs,[46] and graphite itself became a viable anode material when it was discovered that exfoliation of graphite, as it was observed with previous electrolyte mixtures, can be suppressed by the use of ethylene carbonate (EC) as electrolyte solvent, since its decomposition forms a stable solid-electrolyte interphase (SEI) on graphite that prevents further degradation.[47,48] The term “rocking-chair” battery was coined for a cell based on two intercalation materials as anode and cathode, respectively, as the Li^+ ions “rock” from one host material to another during operation.[49] Such a cell is depicted in **Figure 2**, commonly referred to as full cell, in contrast to Li-metal half-cells. A separator is required to prevent electrical contact, i.e. short circuits, between the electrodes. Equations 1 and 2 describe the (de)intercalation in cathode and anode, respectively, and equation 3 summarizes the overall reaction, wherein $x = 0$ describes a fully discharged cell, and $x = 1$ a cell charged to its theoretical limit, and x expressed in percent is often also referred to as state of charge (SOC):

$$\mathrm{LiTMO_2} \rightleftharpoons \mathrm{Li_{1-x}TMO_2} + \mathrm{x\,Li^+} + \mathrm{x\,e^-} \quad (\mathrm{TM = Ni, Co}) \tag{1}$$

$$\mathrm{C_6} + \mathrm{x\,Li^+} + \mathrm{x\,e^-} \rightleftharpoons \mathrm{Li_xC_6} \tag{2}$$

$$\mathrm{LiTMO_2} + \mathrm{C_6} \rightleftharpoons \mathrm{Li_{1-x}TMO_2} + \mathrm{Li_xC_6} \tag{3}$$

For their contributions to the development of the LIB, Whittingham, Goodenough and Yoshino were awarded the Nobel Prize in 2019. This does, however, not mark the end of LIB development, and a summary of current development trends and challenges, with a focus on CAM, is given in the following.

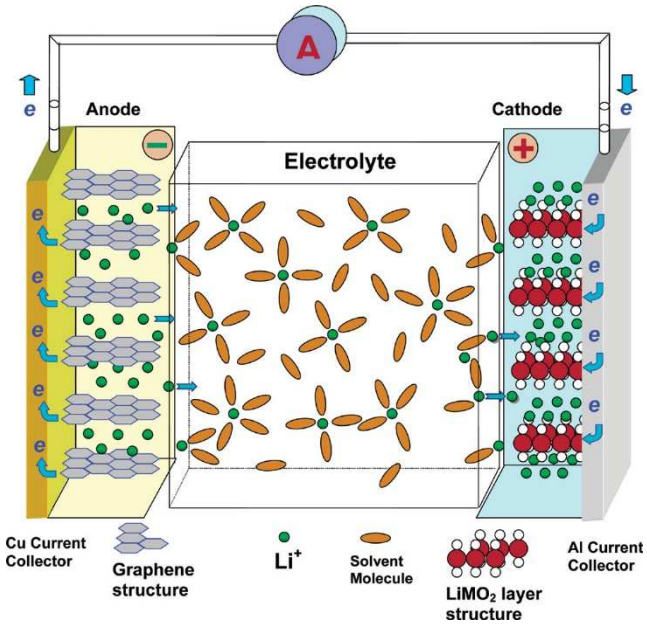

Figure 2: LIB with intercalation electrode materials graphite and layered transition metal oxide, respectively. Reprinted with permission from ref. [50]. Copyright © 2004 American Chemical Society.

The energy stored in a battery depends both on the potential difference between the active materials and on their capacity. Each material's potential is in many cases further depending on the SOC. Individual active materials are therefore commonly described by their counter-electrode independent specific capacity (in mAh g^{-1}) on the one hand, and the curve of potential (versus a reference, in LIBs typically vs. Li^+/Li) against SOC during (dis)charge on the other hand. While a high potential vs. Li^+/Li is favorable for the energy density in the case of CAM, for anode materials consequently a low potential is required. Due to limitations of the potential windows and material stability, active materials also cannot be (de)lithiated to their theoretical ($x = 1$) specific capacity, but only to a lower, practical specific capacity.

While graphite is the far most common anode material in LIBs due to its favorable handleability, availability, low potential (0.25 to 0.05 V vs. Li^+/Li) and stability due to beneficial SEI formation, with 372 mAh g^{-1}, it's theoretical specific capacity is only about 10% of the specific capacity of Li-metal itself (3861 mAh g^{-1}).[51] This is easily explained by the weight contribution of carbon atoms, as in fully lithiated state, see equations 1.2 and 1.3, for each intercalated lithium atom, six carbon atoms are present. Briefly, the intercalation of lithium between the graphene layers that make up graphite occurs in distinct stages, i.e. every third interlayer lithiated in LiC_{18}, every second in LiC_{12} and each in LiC_6, that are visible as steps in the potential.[52,53] This intercalation goes hand in hand with lattice expansion that changes the volume of graphite particles

(~13%).[54] The SEI, which builds up mostly during the first cycles (formation), by the reduction under gas evolution of either EC, or SEI-forming additives, such as vinylene carbonate or fluoroethylene carbonate (FEC), has to accommodate these volume changes or additional SEI is formed under consumption of electrolyte and lithium inventory.[55] Silicon is currently widely considered as a possible future anode material, as it alloys with lithium, providing 10-11 times more specific capacity, yet at the price of 300-400% volume change during (de)lithiation, leading to severe cracking and SEI growth challenges.[51,56] To mitigate these side reactions, various solutions, like Si/C composites, core-shell particles, etc. exist.[51,56] In any full cell, the overall available Li inventory is limited to the Li initially present in the active material and in the electrolyte in the form of a conductive Li salt, such as $LiPF_6$ or $LiClO_4$. Therefore, anode and cathode capacities have to be matched in order to utilize a maximum amount of Li, with their ratio referred to as n/p ratio.[57] Commonly, anodes are slightly oversized to avoid plating of Li metal on the anode surface, which leads to the growth of dendrites that can pierce separators and to the loss of Li inventory, when the lithium itself is isolated by SEI incapsulation.[58] It is these very side reactions that also complicate the use of Li-metal anodes.[59]

Various cathode material families, such as polyanionic compounds, spinel oxides, layered oxides and Li-rich oxides, are available for LIBs, differing significantly in key properties, such as specific capacity, rate capability (i.e. the dependence of charge and discharge capacities on the current), cost, cycle life, average potential and safety.[60-63] Polyanionic lithium iron phosphate (LFP, $LiFePO_4$), on the hand, offers a long cycle life, high thermal safety and moderate cost due to inexpensive base materials, on the other hand, with a theoretical specific capacity of 170 mAh g^{-1}, stemming from Fe^{3+}/Fe^{2+} redox, and an average potential of 3.4 V vs. Li^+/Li, no high energy densities can be obtained.[64,65] The potential can be increased by substitution of Fe^{2+} by Mn^{2+} (up to 4.1 V vs. Li^+/Li for $LiMnPO_4$), yielding lithium manganese iron phosphate (LMFP, $LiMn_yFe_{1-y}PO_4$), yet all of these olivines suffer from low electronic and ionic conductivity, limiting their rate capability and requiring carbon coating and particle milling in order to be used as CAM.[64,65]

$LiNi_{0.5}Mn_{1.5}O_4$, as a prominent example of spinel oxides, has a far higher ionic conductivity and thus rate capability than LFP and comes with similarly moderate costs and high thermal stability. Yet, it has a theoretical specific capacity from Ni^{4+}/Ni^{2+} redox of only 147 mAh g^{-1}, even lower than LFP, which is compensated for by the very high

operating potential of 4.7 V vs. Li^+/Li, posing challenges due to degradation by electrolyte oxidation but resulting in higher energy densities than LFP cells.[60,62,66]

The first reported layered oxide CAM LCO offers 274 mAh g^{-1} theoretical specific capacity based on Co^{4+}/Co^{3+} redox and a higher average potential than LFP, yet only about half of that specific capacity is practically available due to structural instability upon further delithiation.[42,43] While the isostructural LNO was considered as an alternative to LCO due to the high cost and limited availability of Co, it was found to be more difficult to synthesize while also suffering from structural stability issues.[67]

LCO found application in portable batteries, but it was soon found that more balanced properties and lower material costs could be realized by combining Ni, Co and either Mn or Al in the transition-metal layer, resulting in the nickel cobalt manganese oxide (NCM, $LiNi_xCo_yMn_zO_2$, $x + y + z = 1$) and nickel cobalt aluminum oxide (NCA, $LiNi_xCo_yAl_zO_2$, $x + y + z = 1$) families of cathode materials.[68] Both Mn^{4+} and Al^{3+} are redox-inactive and do not contribute to the specific capacity of the CAMs directly, however, for every Mn^{4+} ion in the transition-metal layer, one Ni^{2+} ion instead of Ni^{3+} ion has to be present to maintain overall charge neutrality.[61,68] While the theoretical specific capacity does not change significantly, the composition of the NCM and NCA materials determines the practical specific capacity available in a voltage window of material and electrolyte stability. For a fixed upper cut-off voltage, a higher Ni content leads to a higher specific capacity, yet at the price of lower structural stability and thus faster degradation.[69,70] Compositions are often referred to by the fraction of each transition metal contained, e.g. NCM622 for $LiNi_{0.6}Co_{0.2}Mn_{0.2}O_2$ and NCM811 for $LiNi_{0.8}Co_{0.1}Mn_{0.1}O_2$. In recent years, Ni contents of >80% have been realized in commercial materials, offering more than 200 mAh g^{-1} of practical specific capacity, with 91-94% Ni content CAMs closing in on commercial maturity, and studies on these and the end member LNO reported capacities exceeding 240 mAh g^{-1} in the first cycle.[67,71,72]

The structure, synthesis, processing, side reactions and degradation mitigation of NCM materials, and the influence of NCM composition on this, will be discussed in detail below. However, a last type of CAM should be listed first. While in the materials discussed so far, all theoretical capacity can be explained (conventionally, as will be discussed in chapter 4.1.) by the redox reaction of transition metals to compensate Li^+ ion (de)intercalation, in so-called Li-rich CAM this is no longer the case, and some, or even

all, of the charge capacity is stemming from the oxidation of lattice oxygen in the so-called oxygen redox reaction. When replacing a part of the transition metals in the transition-metal layer of a layered oxide with Li^+, overall charge neutrality requires the remaining transition metals to be in higher valence states. After replacing a third of all transition metals with Li^+, all remaining metals are tetravalent, such as in $Li[Li_{1/3}Mn_{2/3}]O_2$ and $Li[Li_{1/3}Ni_{2/3}]O_2$, alternatively written as $Li_{1.33}Mn_{0.67}O_2$ and $Li_{1.33}Ni_{0.67}O_2$ or Li_2MnO_3 and Li_2NiO_3, respectively. Still, these materials can be electrochemically delithiated, obtaining large charge capacities, which stem exclusively from the oxidation of lattice oxygen to O_2 gas, as can be shown by differential electrochemical mass spectrometry (DEMS), a technique discussed in chapters 2, 4.1. and 4.4.[73,74] As this is, however, irreversible, discharge capacities are much lower, and continuous cycling of the thus oxygen-depleted structures is only possible at a fraction of the initial capacity. A higher reversibility and less O_2 loss are obtained either by using more covalently bonding 4d and 5d transition metals, such as Ru, Mo and Ir, or by reducing the lithium content of the transition-metal layer below 1/3, e.g. $Li_{1.2}TM_{0.8}O_2$ (TM = Ni, Mn, Co), so that some transition-metal redox contribution remains, and lattice oxygen is oxidized only to per- and superoxides instead of O_2 gas.[61,75,76] This way, such Li-rich, and often Mn-rich materials can offer high specific capacities, around 300 mAh g^{-1}, but suppression of gas evolution, voltage hysteresis and fast capacity fading remain challenging.[61,75-77]

Notably, Li-rich transition metal oxides no longer necessitate a layered structure for Li diffusion, as it can also occur in cation-disordered rock-salt oxides (DRX) through a percolating network of intermediate tetrahedral sites neighboring one or less transition metals.[78] DRX CAMs can provide reversible specific capacities above 300 mAh g^{-1}, and while DRX structures require redox-inactive d^0 species for stability (Ti^{4+}, Nb^{5+}, Mo^{6+}), a CAM based on Fe, Mn and Ti is appealing also in terms of cost.[79]

As of today, however, Li-rich materials still are in the development stage, and NCM/NCA layered oxides remain the CAMs of choice for high energy density cells. They crystallize in the *R–3m* space group, with alternating slabs of transition-metal-oxygen octahedra and interslabs of Li in octahedral sites, perpendicular to the *c*-axis.[60,67,80] Layering occurs due to the difference in ionic radii between Li^+ (0.76 Å) on the one hand and Ni^{3+} (low spin: 0.56 Å), Co^{3+} (low spin: 0.55 Å) and Mn^{4+} (0.53 Å) on the other hand, that leads to thicker interslabs and thinner slabs.[81] Especially for Ni-

rich materials, however, Ni^{2+}, with an ionic radius of 0.69 Å, is found in $Ni_{Li}^{\bullet}$ substitutional point defects in the Li layer.[67,80,81] This, commonly referred to as off-stoichiometry, reduces the available capacity and is almost[82] unavoidable due to synthesis conditions, and even well-prepared LNO shows around 2% $Ni_{Li}^{\bullet}$ defects, which can be determined via Rietveld refinement and is reflected in the *c*/*a* ratio.[67]

Typically, NCM materials are synthesized in two steps, first a (mixed) transition-metal hydroxide is precipitated from solutions of sulfates in the targeted stoichiometry.[83] This co-precipitated hydroxide precursor cathode active material (pCAM) is then calcined together with a lithium source, either $Li(OH)\cdot H_2O$ or Li_2CO_3, to yield the final NCM material. With increasing Ni content, the calcination temperature is lowered to reduce cation intermixing, and is commonly 700 °C for LNO, ruling out the use of Li_2CO_3, as it's melting point (725 °C) is too high.[67] A slight excess of Li source has to be used in order to compensate loss of Li at high temperatures and further avoid defect formation.[84,85]

Under typical conditions, both pCAM and CAM show a polycrystalline morphology of smaller primary particles agglomerated to larger secondary particles, wherein the precipitation of the pCAM controls the secondary particle size,[83] and temperature and Li excess during calcination determine the primary particle size.[84] This particle size, and the resulting specific surface area exposed to electrolyte, was recently shown to determine the electrochemical performance of LNO, where a lower first-cycle capacity loss was found for smaller primary particles.[86] The effect of dopant introduction into LNO on the particle size is discussed in chapter 4.2.

After calcination, remaining excess Li forms surface impurities in the form of LiOH and Li_2CO_3 upon exposure to ambient air.[87,88] These impurities not only negatively affect the electrochemical performance of the CAM and lead to gas evolution, but can already disrupt electrode manufacturing due to slurry gelling, as they react with the common polyvinylidene difluoride (PVDF) binder, which then may crosslink.[89] While the excess Li can be removed by washing of the CAM, contact to water or even prolonged contact to humid air during storage also results in extraction of Li from the layered structure by Li-proton exchange reaction, which over time forms a densified, resistive, Li-poor and oxygen-depleted surface layer and additional LiOH.[87,90-92] Especially Ni-rich NCM materials, in which the sensitivity towards ambient air is increased, therefore require both

processing in dry room atmosphere and optimized and careful washing and drying procedures.[88,89]

Electrochemically, CAM delithiation can occur either in a solid-solution (single-phase) reaction or in a two-phase reaction, i.e. during a phase transition. LFP for example commonly shows a pronounced two-phase delithiation behavior and the associated voltage plateau between a lithiated ($LiFePO_4$) and delithiated phase ($FePO_4$), meaning that a partially delithiated Li_xFePO_4 does not exist uniformly, but is rather represented as (x $LiFePO_4$ + (1–x) $FePO_4$), with distinct phase boundaries proceeding through LFP particles.[93-95] In layered oxides, the phase-transition behavior is more complicated, as changes in unit cells, symmetry, lithium/vacancy ordering or even transition-metal slab gliding lead to the existence of various different phases.[96] Pristine (x = 1) Li_xNiO_2 is present in a hexagonal phase (H1), which is first delithiated in a single-phase reaction to $x \approx 0.8$, when a monoclinic phase (M), in which lithium/vacancy ordering occurs, starts to form, and both H1 and M phase coexist briefly.[67,97] The phase transition is observed on the one hand as a voltage plateau in the charge curve (voltage vs. time or capacity) and a corresponding peak in the differential capacity (dq/dV vs. voltage), and on the other hand by X-ray diffraction (XRD), as the reduced symmetry of the M phase results in splitting of Bragg reflections.[98] At $x \approx 0.4$-0.5, a second hexagonal phase is formed (H2), soon after ($x \approx 0.25$) followed by a prolonged transition to a third hexagonal phase (H3), with this transition at a high potential (4.1-4.2 V vs. Li^+/Li) contributing significantly to the energy density of LNO, and the potential increase to 4.3 V vs. Li^+/Li after it also commonly ending the charge of LNO.[67,96,98] The H2 and H3 phase differ significantly in their c lattice parameter, as delithiation first results in increased transition-metal slab repulsion and distance, i.e. increased c compared to pristine LNO, in the H2 phase, while further delithiation leads to a collapse of the layered structure, with a significantly smaller c found in the H3 phase, resulting in an overall unit-cell volume change of around 9%.[67,98] Generally, NCM materials show a more significant change in c parameter and unit-cell volume with increasing Ni content, which is a key reason for their faster degradation, which will be discussed in the following.[67,70,99]

As expansion and contraction of the unit cell occurs primarily along the c-axis, the resulting volume change is anisotropic in nature and causes chemomechanical degradation in the form of intergranular fracture, as randomly oriented primary particles may expand against each other, leading to the appearance of cracks between them.[99-101] While these intergranular cracks follow the grain boundaries between primary particles,

intragranular cracks within primary particles are also formed at high voltages, with these cracks oriented parallel to the layers of the CAM, i.e. perpendicular to the *c*-axis.[102,103] Detection of intra- and intergranular cracks and the effect of both on CAM cycling performance is discussed in detail in chapter 4.3. Briefly, the exposure of additional CAM surface area to the electrolyte leads to degradative side reactions.

The most significant degradation reaction at the CAM surface is the loss of the layered structure due to its transformation into a densified rock-salt-type phase. In delithiated CAM, nickel is reduced to Ni^{2+} and displaced into the lithium layer, while lattice oxygen is oxidized to O_2 gas, and thus irreversibly lost, with the reaction occurring through a series of intermediate phases with increasing Ni to O ratio, ending in redox-inactive rock-salt-type NiO.[67,104,105] While the rock-salt NiO can take up Li, as also occurs during CAM synthesis, the lithium diffusion and electronic conduction in this surface layer is hindered, which is reflected in impedance increasing with the size of the rock-salt-type layer during cycle life.[106-109] At the same time, the lattice oxygen release may occur in the form of highly reactive singlet oxygen ($^1O_2$), which subsequently reacts with the electrolyte, causing the evolution of CO_2 and electrolyte degradation.[110,111] A possible formation mechanism is complex, however, as $^1O_2$ may not occur from a direct electrochemical step, but only as a result of a chemical reaction step.[112,113] In Li-rich CAM, oxygen release is commonly even more pronounced, as it is more readily oxidized, as will be discussed in a detailed review of gas evolution in LIBs and SIBs in chapter 4.1. The rock-salt-type phase formation requires highly charged (i.e. oxidized) CAM, and gas evolution studies detected the onset of O_2 evolution at an SOC of around 75-80% of the theoretical capacity in NCM materials, almost independent of their composition.[106,114,115] As the higher specific capacities obtained in Ni-rich materials, however, result from higher degrees of delithiation available at a given cut-off voltage, this results in an onset of gas evolution already at lower voltages for Ni-rich NCM materials.[106,114,115] Over prolonged cycling, NCM materials experience fatigue, i.e. a decrease in the maximum SOC achieved under constant conditions, due to the growth of the rock-salt-type layer. On the one hand, it reduces ionic and electronic conductivity, imposing kinetic limitations, on the other hand a lattice mismatch between rock-salt-type and layered phase causes interfacial lattice strain at higher SOC due to the collapse of the *c*-axis.[109,116] As the rock-salt-type phase also grows around intragranular nanopores, this strain further causes intragranular cracks.[117]

The thickness of the rock-salt-type layer further depends on the electrolyte employed, with especially EC leading to a thicker layer, indicating that the degradation reaction involves an interaction between electrolyte and CAM surface.[118,119]

Another example for electrolyte-influenced degradation of CAM is the dissolution of transition-metal ions due to acidic species, especially HF as a product of $LiPF_6$ hydrolysis, in the electrolyte.[120-123] Similar to the formation of the SEI at the anode side, electrode-electrolyte interactions and reactivity lead to the formation of a related cathode-electrolyte interphase (CEI), composed of various electrolyte and cathode decomposition species, such as polycarbonates, lithium and transition-metal fluorides, carbonates, oxides and fluorophosphates, which can be identified by surface-sensitive analytical techniques, such as time of flight-secondary ion mass spectrometry (ToF-SIMS) or X-ray photoelectron spectroscopy (XPS).[118,123-126] The gas evolution of CEI formation is discussed in chapter 4.1., while in chapter 4.4., a new type of CEI formation reaction between hexacyanoferrate-based SIB CAMs and conductive salts in the electrolyte is proposed. **Figure 3** summarizes the degradation mechanisms discussed herein.

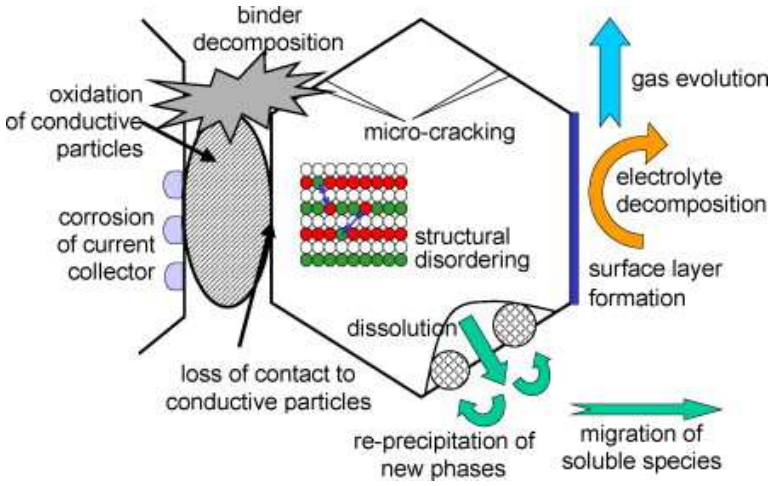

Figure 3: Schematic overview of degradation mechanisms of layered oxide CAMs. Reproduced with permission from ref. [123]. Copyright © 2005 Elsevier B.V..

Various stabilization approaches have been developed in order to alleviate CAM degradation reactions, the most common being doping, coating and morphology modifications.[127,128] Metal dopants, depending on their ionic radius, may be introduced either on the Li site, where they act as pillaring ions that prevent the collapse of the layered structure and the associated unit-cell volume change and crack formation, or on the transition-metal site, where they affect the Ni oxidation state and oxygen bond strength,

preventing the formation of the rock-salt-type phase or reduce the amount of Ni^{2+} on the Li site.[67,128,129] In many cases, however, dopants also affect the surface composition and particle size and orientation of the CAM, as they may enrich or segregate at grain boundaries, and as will be shown in chapter 4.2., even the choice of a process route of dopant introduction can alter the outcome of the doping process. In a similar fashion, coatings that are applied to the CAM surface may prevent side reactions with the electrolyte, e.g. by scavenging HF or suppressing O_2 evolution and the associated growth of the rock-salt-type layer, but depending on the coating treatment, diffusion of coating elements into the CAM may lead to surface doping.[88,129] The industrial co-precipitation process further allows the synthesis of core-shell and gradient CAM particles with a Ni-rich core and a less reactive shell.[130] Typical morphology modifications beyond a variation of primary and secondary particle size include radially oriented, elongated primary particles, in which the anisotropic volume change is alleviated, as the particles are no longer randomly oriented, and lithium diffusion is faster, as the Li interslabs are also radially oriented.[131-133] A further reduction of intergranular cracking and increase in CAM tap density is possible by the preparation of single-crystalline instead of polycrystalline CAM, as larger, deagglomerated particles are not in contact with each other. Since crack-formation is suppressed, however, lithium diffusion paths are longer in these materials, and their size thus can limit the rate capability, while intragranular cracking may still occur.[128,134,135] Yet, no longer bound by the co-precipitation process, single crystals can be prepared in various particle shapes and faceting, e.g. by molten-salt synthesis, in order to optimize lithium diffusion and surface stability.[131,134-137]

One shortcoming of LIBs can hardly be remediated and is amplified by the increase in demand for BEVs: Lithium is scarce and expensive, and the raw materials, especially Co for NCM, come not only with high prices, but also high supply chain strain and risks, as their primary production is concentrated in a limited number of countries and comes with concerns regarding human rights.[138-140] While the use of LFP instead of NCM can reduce cell costs, it still contains Li, and even P is considered a critical raw material due to its geographic concentration and increasing demand for it in the production of fertilizers.[141,142] Recycling of used batteries can reduce the dependency on primary, i.e. extractive, production. However, it has to be economically feasible and will come into effect only after a large number of batteries have been not only produced, but also reached the end of their lifespan, often including also a second-life application, e.g. in

grid energy storage.[138,143-145] Entirely Li-free SIBs, on the other hand, can serve as a complementary technology based on cheap and abundant Na and can be produced even with the same equipment as LIBs due to their conceptual similarity, yet with reduced energy density.[39,40] The SIB technology is introduced in more detail in the following chapter.

1.2. Sodium-Ion Batteries

SIBs are conceptually very similar to LIBs, as the rocking-chair working principle remains the same, and only the intercalated ion changes from Li^+ to Na^+. As discussed in the previous paragraph, rising Li cost and supply chain issues can be mitigated by the use of SIBs, especially with Co-free CAM.[146] However, there are some differences worth discussing at this point. Firstly, the Na^+ ion itself is significantly larger (1.02 Å ionic radius) than the Li^+ ion, which affects its layering, intercalation and solvation properties.[81,82,147] While half-cell potentials of Li^+/Li (–3.05 V vs. NHE) and Na^+/Na (–2.71 V vs. NHE) are commonly used to explain differences in LIB and SIB cell voltage, these values are based on water, and include the effect of solvation of the ions, introducing a solvent, i.e. electrolyte dependency, while a shift of redox potentials and full-cell voltage is rather due to a difference in the Gibbs free energy change of the intercalation reaction.[147-149]

Different reactivities of Li and Na both ease and complicate cell design. While Li alloys with Al, and thus Cu current collectors are required for the LIB anodes, Na does not, allowing cheaper Al current collectors to be used, which further means that SIBs can be discharged to 0 V or even short circuited, whereas in LIBs the Cu current collector would dissolve.[146,150] This 0 V discharge is useful e.g. for the safe transport of SIBs, but SEI degradation may still occur.[151] On the downside, the SEI formation and stability, as well as the anode material selection, are more challenging in SIBs. In contrast to Li, Na does not form a binary intercalation structure with graphite, and while an intercalation is possible in the form of solvent co-intercalation in glyme electrolytes, the resulting specific capacity of ~100 mAh g^{-1} is rather low.[152] Non-graphitizing hard carbon (HC) is commonly used as an alternative anode material, offering specific capacities above 300 mAh g^{-1}, however, HC suffers from low initial Coulomb efficiency, i.e. high irreversibility of the first sodiation process.[153] This is in large parts due to SEI formation, as the highly porous HC has a large specific surface area.[154] Synthesis, structure and sodium-storage mechanism in HC are rather complex, as in contrast to the well-stacked graphene layers of graphite, HC consists of discrete graphenic sheets that, while locally oriented in a turbostratic manner, appear bent and curved, with no long-range ordering or preferred orientation.[154,155] The resulting presence of nanopores allows reversible sodium storage by adsorption, while remaining functional groups can bind Na^+ permanently.[154-156] Similar to Si anodes for LIBs, various alloying anode materials, such as Sn, P and Sb, exist for SIBs, but also suffer from volume

changes and interfacial instability, leaving HC as the anode material of choice in ongoing commercialization projects.[156-158] The CAMs utilized in these projects, however, are very different, as will be discussed in the following.

While the LFP equivalent $NaFePO_4$ exists, it shows rather limited performance due to sluggish kinetics and a significant volume change during desodiation. More promising properties are found for vanadium-based polyanionic compounds, such as $Na_3V_2(PO_4)_3$ and $Na_3V_2(PO_4)_2F_3$ (NVPF), which allow deintercalation of two Na^+ equivalents and deliver 100-120 mAh g^{-1} specific capacity.[158-160] NVPF further provides a high cell voltage, with two plateaus at 3.7 V and 4.2 V vs. Na^+/Na, respectively, and a high rate capability, i.e. power density, thus NVPF/HC-based high power cells have been commercialized by SAS Tiamat.[158,161] Like LFP and phosphates in general, the materials suffer from rather low electronic conductivity, with the high-voltage plateau in NVPF also resulting in electrolyte decomposition and vanadium dissolution.[159,161]

For SIBs, two main families of Na_xTMO_2 layered oxides have to be distinguished, which are referred to as P2- and O3-type in the notation of Delmas, where P and O describe prismatic and octahedral coordination of sodium by the surrounding oxygen, while 2 and 3 refer to the number of repeating units in the oxygen stacking (AB BA vs. AB CA BC).[36,159,162,163] P2-type SIB CAM allows for faster sodium diffusion compared to O3-type CAM due to a larger interslab size and directly neighboring prismatic sites, which in turn results in higher rate capability and power density.[36,162,163] The main disadvantage of the often Mn-rich P2-type materials, such as $Na_xNi_{1/3}Mn_{2/3}O_2$ or $Na_xNi_{1/4}Mn_{3/4}O_2$, is that they are generally obtained in Na-deficient form (x < ~0.7 in Na_xTMO_2) in the synthesis, while further sodium intercalation is possible electrochemically.[164-167] The deficiency leads to a reduced first charge capacity, and while in half-cells, i.e. against a Na-metal anode, additional sodium is available for a full sodiation of the CAM, the Na inventory of full cells is limited. As irreversible Na loss on HC anodes during formation also occurs, such full cells therefore require presodiation, for which various solutions exist, such as preformation of HC in half-cells before dis- and reassembly into full cells, direct contact of HC with Na metal, sacrificial Na-salt additives or the utilization of residual Na residues after CAM synthesis.[153,168,159] The specific capacity obtainable from P2-type CAM further strongly depends on the applied voltage window; at high degrees of desodiation, it tends to suffer from chemomechanical degradation due to significant volume variation and slab gliding associated with the main phase transition from P2 to O2, as well as from surface densification and

oxygen loss, analogous to the formation of the rock-salt-type layer in NCM.[164-167,170,171] In contrast, sodiation beyond the initial Na content occurs under reduction of Mn^{4+} to Jahn-Teller active Mn^{3+}, which results in a distorted P'2 unit cell and mechanical stress, while Mn^{3+} may further disproportionate to Mn^{2+} and Mn^{4+}, with Mn^{2+} dissolving into the electrolyte.[164,166,167,171] Chapter 4.3. discusses the degradation analysis of a series of P2-type SIB CAMs via the *operando* detection and distinction of inter- and intragranular cracks.

There is no clear dependency between P2- or O3-type structure and either specific capacity or average voltage, as both depend on the transition-metal combination employed, for which a wider variety is possible in SIBs compared to LIBs, since e.g. Mn, Fe and Ti also form layered oxides with Na.[36,160,162] Still, layered oxides of the O3-type (to which also the layered oxides for LIBs belong), such as $NaNiO_2$ or $NaNi_{0.5}Mn_{0.5}O_2$, are obtained in a fully sodiated state and thus do not require presodiation to realize maximal capacity. On the downside, the diffusion of the large Na^+ ions is slower in O3- than in P2-type CAMs, as it occurs not directly from octahedral to octahedral site, but through a tetrahedral interstitial site.[36,162,163] O3-type CAMs tend to show a complex phase behavior, especially for single transition-metal oxides, and chemomechanical degradation resulting from it, while multimetal oxides can show a more solid-solution-like behavior.[147,159,162] At this point, it should be noted that hybrid P2/O3 CAM also exists, and that air and moisture sensitivity, as well as the degradation due to surface densification, represent a common challenge for both CAM types.[159] Interestingly, both CAM types can show oxygen redox activity and also the associated increase in irreversible O_2 loss, even without oversodiation, as the transition-metal layer can contain a variety of redox-inactive transition metals as well as lithium, owing to the larger ionic radius of Na^+.[172] The challenges of layered oxide SIB CAMs are often outweighed by a combination of the capacities available from these materials, the low cost of key transition metals, like Fe and Mn, and the possibility of production on LIB production equipment, so that various cell manufacturers, such as CATL, Faradion and HiNa, have developed SIBs based on layered oxides.[156-158]

Even though Mn and Fe are cheap and abundant, thus reducing cost and supply chain risks, the layered oxides still require an energy-intensive and costly high-temperature calcination.[173-175] A third family of SIB CAMs, also Fe and Mn based, are the so-called Prussian blue analogue (PBA) and Prussian white (PW) materials, which do not require any calcination, as they can be precipitated from aqueous solutions. Named after the

blue pigment $Fe_4[Fe(CN)_6]_3$, PBAs can be described generally by the formula $A_xM_A[M_B(CN)_6]_{1-y}\square_y \cdot zH_2O$, wherein A is an alkali metal, x ($0 < x < 2$) the alkali metal content of the phase in question, M_A and M_B transition metals, most common Fe or sometimes Mn, □ a $M_B(CN)_6$ vacancy and y ($0 < y < 1$) its concentration, while z describes the number of lattice water molecules per formula unit.[174-176] The octahedrally coordinated metal sites are bridged by the cyanide anions, with M_A being coordinated by N and M_B by C, resulting in a three-dimensional open framework, which can accommodate various cations, such as Li^+, Na^+ and K^+, and allows for fast ion diffusion.[177] In contrast to layered oxides, in these materials, higher specific capacities are obtained from the larger Na^+ and K^+ ions.[176,178] Sodium-rich structures, in which both M_A and M_B are divalent, are often referred to as PW, since such a reduction of the namesake pigment also results in a white product. An ideal Fe-based PW $Na_2Fe[Fe(CN)_6]$ would have a theoretical specific capacity of 172 mAh g^{-1}. Yet, the CAM is typically obtained with a Na deficit and vacancies, resulting in available capacities around 150 mAh g^{-1}.[159,179-181] As synthesized $Na_2Mn[Mn(CN)_6]$, on the other hand, can be further sodiated electrochemically to $Na_3Mn[Mn(CN)_6]$, with the C-coordinated Mn reduced to Mn^{1+}, providing a specific capacity above 200 mAh g^{-1}, yet requiring presodiation upon use in full cells, as discussed previously.[178] While these gravimetric capacities are similar to those available in layered oxides, the density of PBA/PW materials is only about half, resulting in a lower volumetric energy density.[175,177]

The preparation of PBA/PW CAM is commonly performed via precipitation of the CAM upon addition of a transition-metal nitrate or chloride solution to a solution of sodium hexacyanoferrate, or by addition of both solutions to a third, as simplified in equation 4.

$$TMCl_2 + Na_4[Fe(CN)_6] \longrightarrow Na_2TM[Fe(CN)_6] \downarrow + 2\,NaCl \qquad (4)$$

However, this precipitation occurs rapidly, leading to the formation of small particles that show a low Na and high vacancy content.[159,176] To optimize the CAM properties, additional Na^+ ions can be added to the solutions, e.g. in the form of NaCl, while complexation agents, such as sodium citrate, slow nucleation and crystal growth, resulting in less vacancies and larger particles.[159,174,182]

If both metal sites are to be filled by the same transition metal, a precipitation can be carried out directly by adding a solution of the transition metal to a solution of NaCN,

as shown in equation 5,[178] or by acid decomposition of sodium hexacyanoferrate, as shown in equation 6.[179-181,183]

$$2\ \mathrm{Mn(NO_3)_2} + 6\ \mathrm{NaCN} \longrightarrow \mathrm{Na_2Mn[Mn(CN)_6]} \downarrow + 4\ \mathrm{NaNO_3} \quad (5)$$

$$2\ \mathrm{Na_4[Fe(CN)_6]} + 6\ \mathrm{HCl} \longrightarrow \mathrm{Na_2Fe[Fe(CN)_6]} \downarrow + 6\ \mathrm{HCN} + 6\ \mathrm{NaCl} \quad (6)$$

In both cases, one of the toxic cyanides NaCN or HCN are present, posing a safety challenge, as will be discussed in chapter 4.4. However, the industrial production of any hexacyanometallate precursor will eventually be based on HCN, a commodity chemical available via the Andrussow process.[184]

While the acid decomposition reaction, which can also be carried out by complexating acids, e.g. ascorbic acid, and in NaCl-rich solutions, already leads to controlled crystal growth and low vacancy contents, air contact leads to the oxidation of Fe^{2+} to Fe^{3+}, which results in a reduced sodium content for overall charge neutrality, so that PW synthesis further needs to be carried out under inert gas.[179-181,183] Lastly or alternatively, the partially oxidized, Na-deficient PW may be reacted with a reducing agent, such as NaI or $NaBH_4$ in a follow-up reaction to maximize the Na content.[181,183]

Due to the aqueous synthesis and eventually, also aqueous electrode processing, all PBA/PW materials contain significant amounts of water after precipitation, found in the form of adsorbed water, lattice water and coordinated water (in place of vacancies), with the difficulty of removal increasing in this order.[159,185] While PBA/PW CAMs also find application in aqueous SIBs,[177,182] for use in nonaqueous cells, a removal of as much water as possible is necessary for best performance, safety and cycling stability, as residual water affects the sodium diffusion and reacts with the electrolyte, leading to significant gas evolution, which is reported in more detail in chapter 4.4.[186,187] Drying is commonly performed under vacuum or inert gas at elevated temperatures for a prolonged time, and while PBA or PW CAMs crystallize in different lattice systems depending on their composition, a phase transition during drying, as shown in **Figure 4**, is commonly observed, such as from monoclinic to rhombohedral symmetry in the case of Na-rich PW $Na_xFe[Fe(CN)_6]$.[160,174,185,187,188] However, the water removal and phase transition are reversible upon even short exposure of the CAM to moisture, with extended exposure also to O_2 resulting in the extraction of Na to form NaOH, oxidation of Fe^{2+} to Fe^{3+} and formation of surface impurities in the form of $Fe(OH)_3$ and

$Na_4[Fe(CN)_6]$, yielding a passivating layer that prevents further degradation, yet at the price of higher surface resistance.[188]

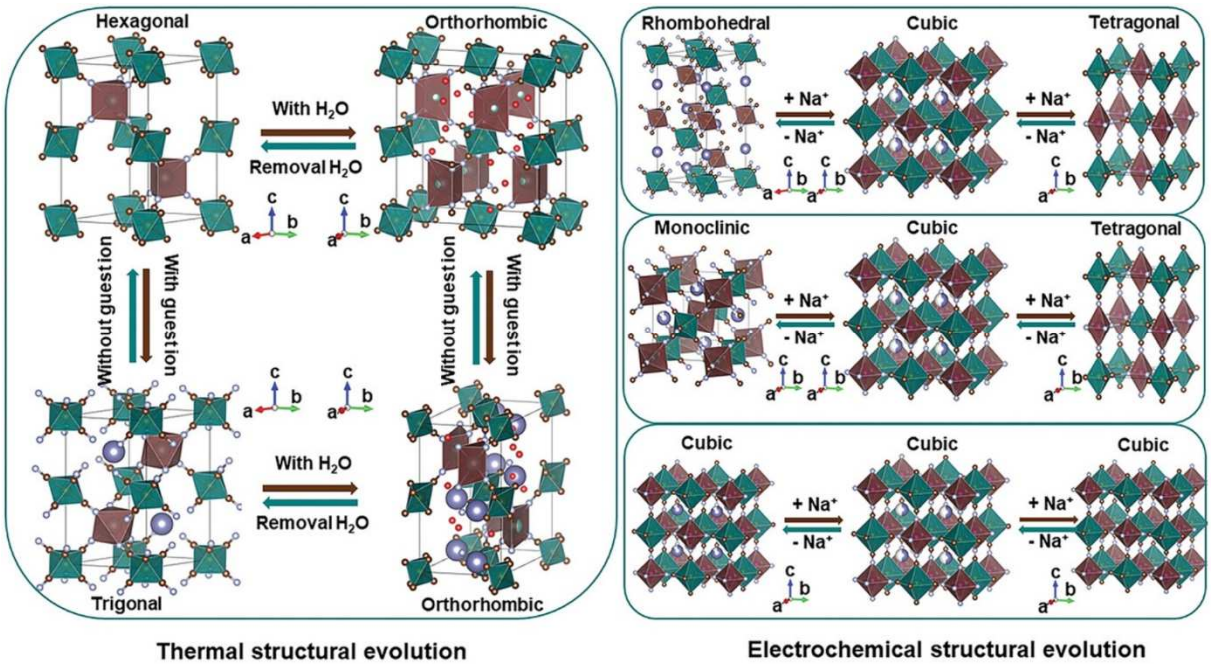

Figure 4: Phase transitions observed in PBA/PW materials upon removal of water and (de)sodiation. Reprinted with permission from ref. [174]. Copyright © 2022 John Wiley & Sons.

During cycling of PBA/PW CAMs, phase transitions and the associated unit-cell volume change and distortion, as shown in **Figure 4**, are commonly, yet not always,[189] observed, amplified by the Jahn-Teller distortion of various ions, such as Mn^{3+}.[159,174,177,184] A dried, Na-rich PW $Na_xFe[Fe(CN)_6]$, for example, undergoes a transition from the initial rhombohedral phase to a cubic phase during a first voltage plateau around 3.0-3.1 V vs. Na^+/Na, which is associated with oxidation of the N-coordinated, high-spin Fe^{2+} on the M_A site, while the C-coordinated low-spin Fe^{2+} on the M_B site is oxidized in a following plateau around 3.3-3.4 V vs. Na^+/Na.[181] The aforementioned $Na_3Mn[Mn(CN)_6]$ consequently shows an additional third plateau associated with the C-coordinated Mn^{2+}/Mn^{1+} redox.[178]

Due to the advantages of PBA/PW CAMs in terms of raw material cost and supply as well as sustainability, various industrial manufacturers have started the production of cells based on these materials, most recently Northvolt AB, supplied with PW CAM from Altris AB,[190] CATL, the now defunct Novasis Energies and Natron Energy, the latter producing an aqueous electrolyte cell with an Fe-based PBA cathode and a Mn-based PBA anode.[156,157,174] Surprising in the face of such commercial investments,

however, and especially in contrast to layered oxides, publicly available knowledge on CEI formation and composition, gas evolution, electrolyte and thermal stability of PBA/PW CAMs is rather sparse. While fully sodiated, i.e. discharged PBA/PW has indeed a higher thermal stability than layered oxides, and especially shows no O_2 evolution during thermal runaway, Li *et al.* demonstrated that charged PBA CAM during thermal decomposition exhibits a far stronger exothermic heat flow and higher weight loss, associated with the evolution of the toxic gasses HCN and cyanogen [$(CN)_2$].[191] In chapter 4.4., factors influencing the evolution also of these gasses and CEI formation during regular cycling and overcharge are discussed in detail. This study directly resulted from our prior finding of $(CN)_2$ evolution during cycling of high-entropy PBA and PW, as observed via DEMS.[189,192,193]

1.3. High-Entropy Materials

Work in this thesis is partially carried out on so-called high-entropy materials, or inspired by findings on such materials. Therefore, the high-entropy concept will be briefly introduced. Whereas doping refers to the addition of traces of other elements to a phase based on one or a few principal elements, such as the addition of Cr to Fe in the manufacture of stainless steel or the addition of Zr to LNO, as discussed in chapter 4.1., high-entropy materials consist of multiple elements in similar amounts, often with no discernible main element, in one phase.[194] One definition of high-entropy materials is therefore a content of at least five principal elements in atomic percentages between 5% and 35% each.[194] Another definition is based on a configurational entropy ΔS_{conf} higher than $1.5R$, with R being the universal gas constant, which can be calculated according to equation 7, where x_i is the mole fraction of element i.[194-196]

$$\Delta S_{conf} = -R \sum_{i=1}^{n} (x_i \ln x_i) \quad (7)$$

While first applied to alloys, the high-entropy concept has now spread to a variety of materials, including battery materials both for LIBs and SIBs.[194-197] While e.g. the high-entropy PBA $Na_xFe_{0.2}Mn_{0.2}Ni_{0.2}Cu_{0.2}Co_{0.2}[Fe(CN)_6]$ ($\Delta S_{conf} = 1.61R$) consists of an equal amount of each metal on the M_A site, the high-entropy P2-type layered oxide $Na_{0.67}(Mn_{0.45}Ni_{0.18}Co_{0.18}Ti_{0.1}Mg_{0.03}Al_{0.04}Fe_{0.02})O_2$ ($\Delta S_{conf} = 1.52R$) still requires an excess of Mn, both to support crystallization in the P2 structure and for redox-activity.[171,191] The vast compositional space of high-entropy material combinations requires a development hand in hand with high-throughput experimentation and computational materials science.[198] The high configurational entropy promotes the formation of a single-phase solid solution, and as the involved ions are all of slightly different size, a distorted lattice is obtained that may reduce defect formation and increase material hardness.[195] Lastly, the various possible synergetic interactions between the elements contained in a high-entropy material are summarized as the so-called “cocktail effect”, resulting in overall properties that exceed those expected from the sum of its components.[195] Taken together, these effects can improve battery material performance, e.g. by suppressing phase transitions, crack formation and gas evolution, while increasing reversibility and ion diffusion.[171,191] In chapter 4.3., it will be demonstrated that the aforementioned high-entropy P2-type SIB CAM shows less degradation via intragranular crack formation, as the P2-O2 phase transition is suppressed in favor of a solid-solution (de)sodiation.[170]

1.4. Motivation and Research Objectives

In this thesis, the surface of CAMs for both LIBs and SIBs is studied from various perspectives, with the aim of gaining a deeper understanding on the role of these surfaces throughout the CAMs lifecycle, from synthesis over CEI formation to degradation. Especially, interplays between surface and bulk properties are discussed. First, the role of different dopant introduction processes on LNO surface composition, and thus particle growth during synthesis, is considered. Then, the formation and exposure of fresh surfaces due to cracking are studied, investigating the role of bulk composition and phase-transition behavior on an exemplary series of P2-type SIB CAMs. Lastly, the surface degradation and CEI formation of PW materials is investigated, as the vastly different composition and structure of these materials, when compared to layered oxides, allows for other, lesser understood reactions to occur.

To this end, two less common *in situ* methods are applied and further developed, namely DEMS and Acoustic Emission (AE), which are each introduced in the following chapters. As the gas evolution of NCM materials in LIBs has been studied in detail in recent years, for DEMS, a literature review is carried out first to summarize not only the findings of these studies, but also of applications towards new materials and cell concepts, with the aim of consolidating available knowledge, identifying current research gaps and predicting the future development of DEMS as a method. Further work is then performed according to the identified research gap of SIB gas evolution, especially from PBA/PW materials, while DEMS measurements also serve as a bridging element between the works in this thesis.

In the field of battery materials, AE, which has previously been implemented at BELLA, is mostly used to characterize an individual material, e.g. towards its cracking behavior. A further aim of this study is to develop AE as a method so that not only characterization, but also comparison and evaluation of related materials can be performed, for which the complex data obtained from AE require further analysis.

The purpose behind the works forming this thesis is therefore threefold: (i) To provide a scientific and mechanistic understanding of the observed surface formations and reactions. (ii) To develop methods that allow a comparative *in situ* study of such reactions. (iii) To yield findings that support optimization of CAM composition and synthesis, as well as provide evaluation criteria for commercial applications of the CAMs studied, including the previously unreported $(CN)_2$ evolution from PW materials.

2. *In Situ* Gas Analysis

Mass spectrometry as an analytical technique able to separate ions by their mass to charge ratio (*m*/*z* ratio) has seen rapid development in the century since its invention, at first providing experimental evidence for the existence of isotopes, and today being an integral part of various analytical applications, such as gas chromatography-mass spectrometry (GC-MS).[199,200] A very notable exception to the otherwise analytical nature of its application is the calutron, essentially a preparative mass spectrometer developed for the enrichment of ^{235}U within the Manhattan project, today being used for the separation of stable isotope precursors to radioactive isotopes used in medical imaging and treatment.[201] It is therefore not surprising that mass spectrometry also found application in combination with electrochemistry, first to identify volatile reaction products on a porous electrode, and soon after *in situ* via a membrane inlet, keeping the aqueous electrolyte out of the mass spectrometer.[202,203] This application is commonly referred to as DEMS, with differential referring to the measurement of evolution rates instead of total evolved amounts. For an overview of DEMS instrumentation and application in general electrochemistry, the reader is referred to the literature.[204] Battery-related DEMS studies started in 1986 with the investigation of LIB electrolyte oxidation on Pt electrodes by Eggert and Heitbaum, and Imhof and Novák reported the first battery-specific DEMS setup for the study of electrolyte reduction on graphite and oxidation on CAMs in 1998.[205-207] Membranes, however, suffered from penetration by nonaqueos electrolytes, and instead, partially inspired by similar *in situ* gas evolution studies carried out on metal-air batteries, headspace sampling techniques were developed. Open headspace setups utilize the constant flow of an inert carrier gas to extract evolved gasses, while a semi-closed headspace, as developed by McCloskey *et al.* is only intermittently purged by carrier gas and sampled.[208] The measurement of a closed headspace through a crimped capillary, as developed in Gasteiger's group, resulting in total gas amounts instead of gas evolution rates, is commonly referred to as online electrochemical mass spectrometry (OEMS).[209] A more detailed account of the history and development of *in situ* gas evolution studies on batteries is given later in chapter 4.1., which further presents a review of state-of-the-art DEMS/OEMS instrumentation, applications and results in the study of battery materials. In the following, the DEMS setup used in the work forming this thesis and the principles of mass spectrometry relevant for technical discussions in chapter 4.4. are summarized.

BELLA's DEMS setup, established by Berkes *et al.*, is based on an open headspace design, using a constant flow (2.5 mL min^{-1}) of He as a carrier gas flowing through a customized cell housing, and then, in a variation of previous designs, through a cold trap before entering the mass spectrometer.[210,211] Electrolyte carried out of the cell due to its vapor pressure is condensed in this cold trap to prevent it from causing background noise in the spectrometer. To offset the loss of electrolyte in the cell, a bubbler can be used to saturate the carrier gas with electrolyte, however, for faster changes of the various electrolytes used without the need for electrolyte purging, this was not done for the work herein. Similarly, the cold trap temperature setting was varied in dependence of electrolytes and species of interest, as is discussed in chapter 4.4. A calibration curve was obtained by passing a series of calibration gas dilutions with known concentrations for species of interest through the cell. The mass spectrometer (OmniStar GSD 320, Pfeiffer Vacuum GmbH) is evacuated first by a membrane roughing pump and finally by a turbomolecular pump. It utilizes electron ionization of the analyte, followed by a quadrupole mass filter and a secondary electron multiplier (SEM) to amplify the resulting ion current.[212] This measurement principle and the components involved, as shown in **Figure 5**, are discussed in the following.

By passing a heating current trough an Y_2O_3-coated Ir filament, a smaller current of electrons is emitted, accelerated towards an anode cage (at electron energies typically around 70 eV) and colliding with analyte molecules on the way. An impact with a gas molecule ideally leads to ionization of the molecule by removal of a further electron, however, other interactions, such as fragmentation, excitation or electron capture, may also occur, mostly depending on electron energy.[199,200,212] The resulting cations are accelerated in an electric field and the resulting beam focused via ion optics, leading to an ion current, with the strength of the current depending on the emission current, pressure and ionization cross section of the present analyte molecules. The cations then enter the quadrupole mass filter, consisting of four long cylindrical rods arranged in a square parallel to each other and the ion beam. The rods opposite of each other are at the same potential, and in addition to a constant potential difference to the rod pairs, a high-frequency alternating potential is applied to them. The resulting electric field varies over time and within the plane perpendicular to the rods and incoming beam, forcing the ions on a helical path, which is only stable for a narrow range of m/z ratios that can be calculated from the Mathieu equations, while all other ions collide with the rods, losing their charge.[199,212] By increasing the applied potentials, keeping

the ratio between constant potential and alternating potential amplitude constant, the *m*/*z* ratio of passing ions is increased, and a stepwise or continuous scan over the *m*/*z* range of interest can be performed. After passing the mass filter, the remaining ion current can be measured in a Faraday cup via the current required to neutralize the charges of the ions that impacted the cup in a given timespan. To measure very small ion currents at high scan speeds, typically a SEM is used, which increases sensitivity and signal-to-noise ratio. Upon impact of ions on a layer of material with a low work function, the impact may cause the release of secondary electrons, which after acceleration in an electric field can cause the same emission of secondary electrons, leading to a cascading effect either between discrete dynodes or in a continuous SEM. The latter consists of a horn-shaped curved glass funnel coated with a high-resistance low work function material on the inside, to which a high voltage is applied that accelerates the secondary electrons, resulting in an avalanche of electrons and thus a detectable current at the end of the SEM.[199,200,212] In the DEMS application, ion currents are amplified by a factor of ~1000, with higher amplification possible, yet at the risk of saturation, as discussed in chapter 4.4. On the downside, the SEM ages due to contaminations and reactions of ions with the emission layer, requiring an adjustment of the high voltage applied to it, as will also be discussed in chapter 4.4.

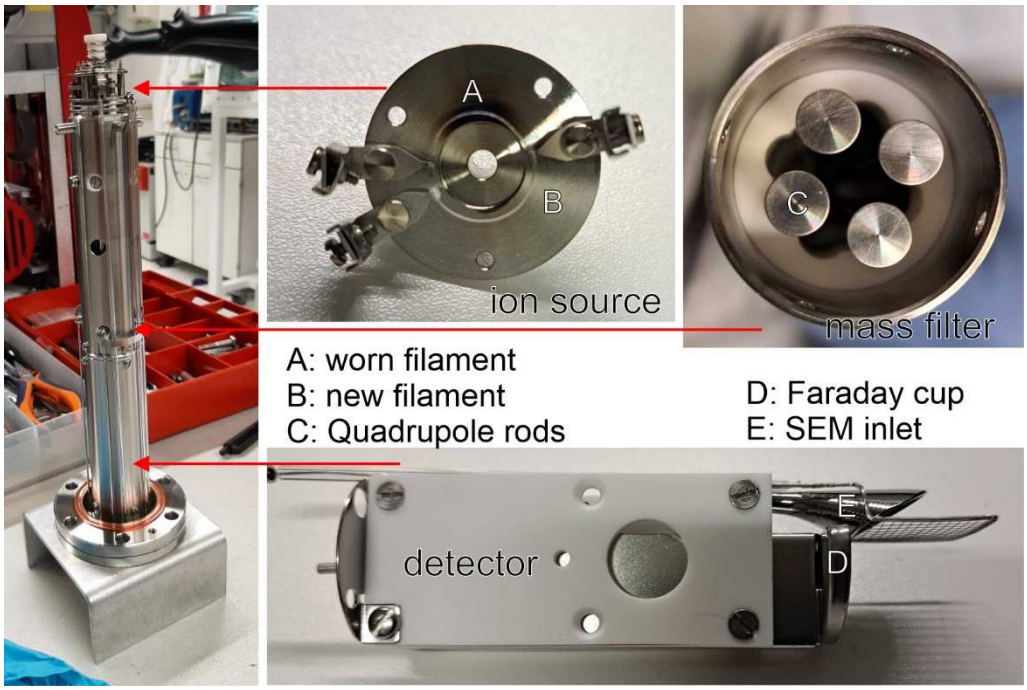

Figure 5: Analyzer unit of the mass spectrometer consisting of ion source, mass filter and detector.

3. Acoustic Emission

While many sophisticated methods have been developed for the *in situ* and *operando* investigation of batteries and battery materials, most of these still require specialized cells and extensive instrumentation, such as X-ray sources and detectors[213] or, as discussed previously, mass spectrometers, effectively limiting their application to laboratory environments. Therefore, these methods cannot be used to continuously monitor batteries, e.g. in terms of state of health (SOH) and early detection of undesirable conditions and faults, such as short circuits, overcharge and onsetting thermal runaway. Similarly, monitoring is also required already as a part of quality control after cell assembly, especially in the formation process, where deviations indicate faulty production, an issue plaguing battery manufacturing, with scrap rates of at best 5% and at worst up to 30% being reported.[214,215]

In field applications, this monitoring, with the aim of maximizing battery lifetime and minimizing safety risks, is performed by the battery management system (BMS) at a cell or even module level and commonly based on electrical parameters, i.e. voltage, current and resistance, combined with a simple temperature measurement, often by a negative temperature coefficient (NTC) thermistor.[216] This simple, cheap and lightweight NTC thermistor serves as a temperature sensor and is a widely applied example of sensing methods to monitor cell conditions, found even in small cell phone batteries, which come with a third terminal to connect the sensor to the phone. In contrast to extensive laboratory instrumentation, sensing methods do allow for continuous monitoring of batteries also in real-world application, as they only require one or more sensors in or near a cell, while signal processing is carried out in the BMS or computers nearby.[217,218] Substantial research efforts are therefore directed towards the development and improvement of sensors and sensing methods for application in battery manufacturing and monitoring, often summarized under the term non-destructive testing.[219-221] Fiber optic sensors within the cell, utilizing fiber Bragg grating, have been shown to be able to measure various properties, such as strain, internal temperature and pressure.[221-224] With some modifications, even electrolyte properties, such as refractive index and turbidity, as well as electrolyte infrared spectra (infrared fiber evanescent wave spectroscopy), can be monitored.[225,226] Yet, apart from strain and temperature measurements on the cell exterior, the optical fibers need to be placed inside of the cell and connected to an external light source and interferometer, as light waves otherwise cannot leave the cell. This requires either an inclusion of the fragile fibers

already in manufacturing or an opening and resealing of the cells at a later stage, which makes these methods invasive. Acoustic waves, however, may transmit through the cell housing, making acoustic sensing not only non-destructive, but also non-invasive. Acoustic sensing can be carried out both in active and passive manner. In active sensing, an ultrasound transducer generates acoustic waves, which pass through the cell and are detected either in transmission or reflection. Information is gained from variations in signal amplitude, scattering and time of flight (ToF), as different materials result in different wave velocities and acoustic impedance, which are further affected by physical changes to the material.[227,228] This way, changes in the SOC are reflected in the ToF, while e.g. gas bubbles strongly reduce signal intensities.[229] In multilayer cells, a general ToF increase can indicate cell swelling, while ultrasonic testing even provides layer-specific resolution, as reflection in each layer results in a different ToF, with repeated reflection creating an echo-chamber effect, however.[230,231] Ultrasonic monitoring finds commercial application in quality control of cell wetting and formation, and various other applications have been reviewed in the literature.[227,228,232,233] Active sensing requires the use of an ultrasound transducer as a source of acoustic waves, while passive acoustic sensing detects acoustic waves emitted by the battery itself, thus requiring only a detector. This passive, non-destructive and non-invasive measurement is called Acoustic Emission (AE), and its fundamentals will be presented below, while its application to P2-type SIB CAM forms chapter 4.3. of this thesis.

Typical and commercial applications of AE involve monitoring of structural integrity by detection of crack formation, from tensile strength testing of welded joints[234] over laminates, such as wind turbine blades,[235,236] to rock, steel and concrete structures in civil engineering.[237,238] In a further abstraction, not only crack formation itself, but the processes leading to it, from machine wear[236,239] over termite feeding on wood[240] to corrosion,[241] can be studied, including the study of power systems, such as solar cells, fuel cells and batteries.[227,236] Such studies are, however, complicated by the non-trivial attribution of AE signals to their likely source of origin.

Mechanical disturbances, such as from local structural rearrangement by plastic deformation or cracking, releasing strain energy, can propagate through elastic solid media in various forms of elastic waves, also called acoustic waves, in addition to the sometimes audible sonic waves propagating through the air.[238,242,243] In contrast to gases, solids possess not only volume, but also shear elasticity, which complicates the phys-

ics behind waveforms, propagation, scattering and reflection enough to become scientific branches of their own in the form of acoustics and seismology. For this reason, AE as a method of non-destructive testing of complex systems relies less on a fundamental theoretical model, which yields analytical equations, and more on empirical and numerical approaches.[238,244] By means of a transducer at the sample surface, commonly a piezoelectric sensor that converts the elastic deformation into a voltage signal, acoustic waves and therefore the processes from which they originate can be recorded.[238,243] The recording and analysis process is shown in **Figure 6**.

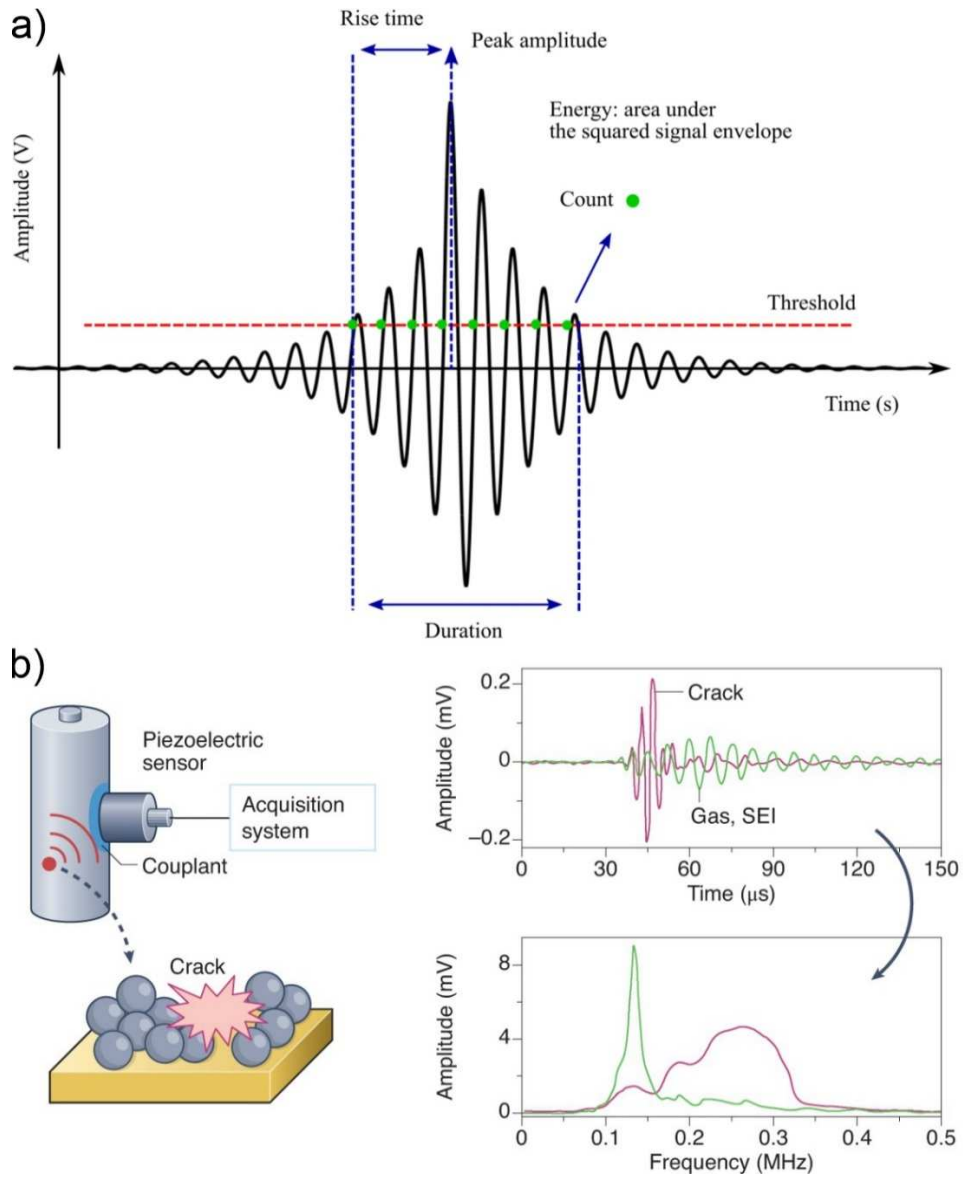

Figure 6: a) Schematic acoustic wave associated with one hit and the respective hit properties, adapted with permission from ref. [245]. Copyright © 2017 IOP Publishing Ltd. b) Schematic acquisition and different waveforms in time and frequency domain, respectively, adapted with permission from ref. [221]. Copyright © 2022 Springer Nature.

If the signal obtained from a single acoustic wave, as shown in **Figure 6a**, passes a deflection threshold for at least a given number of times (counts), it is registered as a so-called hit, which is further characterized by a set of parameters characteristic of the waveform detected.[245] These include, but are not limited to, the number of counts, the duration between first and last count, the amplitude, energy (area under squared signal envelope), rise time (time between first crossing of the threshold until maximum amplitude and, obtained after Fourier transformation, the frequency distribution and especially peak frequency.[227,235,238,242] The frequencies monitored depend on the sensor, and typical bandwidths for piezoelectric sensors are between 50 kHz to 1 MHz, far above the human audible spectrum.[227,236]

While in a few applications the mere detection of hits or the rate by which hits are observed can indicate and measure a process of interest, it is often found that only hits of certain waveform, i.e. of certain characteristic parameter combinations, are correlated with the process of interest, and that multiple acoustically active processes occur simultaneously. The identification and interpretation of hit patterns typically involves not only filtering out background noise, but also data handling and analysis methods ranging from manual classification over principal component analysis to machine learning and neural networks, or even complete physical and mathematical models.[235,236,241,242,245,246] The result of such an analysis is a correlation that allows to determine or even predict a certain state or process in the object investigated by the AE detected. In a battery context, cell venting or explosion are examples of processes that can be detected by the mere presence of acoustic signals, while e.g. determining cell SOC or (non-zero) SOH from AE activity, and the associated waveform parameters result in complex correlation matrices.[247-250] In such correlative studies, a black box model is assumed for the battery, i.e. the exact cause of AE activity is not determined. Only in a further step of analysis can certain AE hits be associated with a causal mechanism of their origin. In the AE characterization of various battery materials, it was found that gas evolution, film growth, such as SEI or CEI formation, and crack formation are detected via AE and can further be distinguished by hit classification, as the peak frequency increases and rise time decreases in the order gas evolution, film growth and crack formation.[227,251-53] This is schematically shown in **Figure 6b**. Applying AE to LNO, Schweidler *et al.* classified AE hits into three groups of increasing peak frequency, finding that hits below 300 kHz of peak frequency are mostly limited to the

first charge, where they occur consistently, while hits of a third group with peak frequencies above 400 kHz also occurred in the following cycles, and mostly concurrently with the H2-H3 phase transition, indicating that the latter are the result of particle fracture, while the former result from CEI formation.[251] In chapter 4.3., AE application and hit classification in the context of battery materials is discussed further, while it is shown that for a series of P2-type SIB CAMs, even intragranular and intergranular cracking can be distinguished via AE, utilizing the setup developed by Schweidler *et al*.[170,251]

Briefly, in this setup coin cells are cycled with the electrode of interest at the bottom of the cell, and the cell bottom is slightly pressed against the AE sensor, with silicon grease acting as acoustic couplant. The recorded signal is preamplified by a preamplifier and then processed via a dedicated acquisition card, which converts the continuous sensor signal, once it exceeds the threshold, into hit-based datasets, as defined by acquisition parameters, such as sampling rate, and a lockout time to avoid recording reflected waves. The signal processing is described in more detail in the available literature.[238,242,243,251] Via proprietary software (all Mistras Group, Inc.), further filters (number of counts, high pass etc.) can be applied and the data exported. While a calibration of the sensor itself is possible by breaking a pencil lead,[238,244] the overall sensitivity of the setup depends mostly on the coin-cell assembly and connection of the cell with the sensor, so that commonly different absolute amounts of hits are recorded in repeat measurements, requiring normalization, as further discussed in chapter 4.3.

4. Results and Discussion

In the works constituting this thesis, various CAMs both for LIBs and SIBs are prepared and analyzed, with a focus on the formation and reactivity of their respective surfaces. As previously introduced, the formation of gaseous products at and from the CAM surface is commonly observed. However, a detailed *in situ* study of the gas evolution, e.g. via DEMS, requires specific, often self-developed instrumentation and techniques, and is thus restricted to only a limited number of research groups, including BELLA. Chapter 4.1. contains a review of instrumentation, applications and possibilities of such *in situ* gas evolution studies, as DEMS measurements are applied to all materials in the following studies, serving as a connecting element in this thesis. This spans from the formation and purity of Zr-doped LNO primary particle surfaces in dependence of the dopant introduction process route, as presented in chapter 4.2., over crack formation leading to exposure of new P2-type SIB CAM surfaces to the electrolyte and its study by AE, as presented in chapter 4.3., and the degradation of PW CAM surface in contact with various electrolytes, as presented in chapter 4.4.

4.1. Review: In situ analysis of gas evolution in liquid- and solid-electrolyte-based batteries with current and next-generation cathode materials

At the beginning of this PhD project the DEMS setup was taken over from predecessors at BELLA,[210,211,254,255] and the gas evolution mechanisms of NCM materials in combination with organic carbonate electrolytes in LIBs were reasonably well understood (with the exception of the prevalent decomposition mechanism of surface carbonates, see below). For this reason, a literature review was conducted to summarize this understanding and identify research gaps and novel applications for *in situ* gas evolution studies. While existing reviews focused on either instrumentation[256] or the evolved gasses themselves,[257] this review focusses on the methodology and application of *in situ* gas evolution studies to novel materials and cell concepts on the one hand, and to the isotope-labelling assisted elucidation of complex reaction mechanisms on the other hand.

It was found that even though the gassing of NCM in LIBs was mostly understood, with the emergence of new cell concepts, chemistries and materials, especially cathode materials exhibiting partially irreversible oxygen redox, electrolyte additives and materials for SIBs, a second spring for gas evolution studies was likely to occur. At the same time, the main limitation for *in situ* gas evolution studies was the need to establish customized setups and their correct and reliable operation. The gas evolution of SIB CAMs was identified as least investigated and chosen to be a focus of BELLA's DEMS study activities next to the unique application of DEMS to SSBs.

Indeed, since the conception of the review, various new works on *in situ* gas evolution studies have been published. This includes further review articles with slightly other focus aspects, such as the role of gas evolution in safety and thermal stability,[258-260] the development of DEMS for various cell concepts,[261,262] electrolyte decomposition mechanisms,[263] correct calibration,[264] further mass spectrometry-based techniques in battery research, such as GC-MS and ToF-SIMS,[124,125] and review articles highlighting DEMS/OEMS as a relevant characterization method, e.g. on CAM morphology,[135] CEI formation[126] or oxygen redox.[75,76] Furthermore, various works have reported the development of novel setups and methods for gas evolution studies, featuring new cell designs,[265-268] measurements in large format multi-layer cells,[269,270] measurements at elevated temperature and during thermal runaway,[247,248,271] setups

including multiple other analytical methods in parallel,[247,248,267] measurements on capacitators,[272] setups with increased gas sensitivity,[273-276] setups with increased time resolution,[276,277] and a combination of DEMS data with a computational chemical reaction network.[278] Similarly, new concepts have also been demonstrated for pressure measurements in commercial cells.[279,280] At BELLA, the DEMS setup was, in one case, also modified to investigate the stability of surface-modified graphite felt electrodes for vanadium redox-flow batteries.[281]

Since the publication of the review, DEMS and OEMS continue to be used in the context of investigations on conventional NCM chemistries, such as electrochemical stability window determination,[106] effects of CAM doping,[282,283] $Ni_{Li}^{\bullet}$ defects,[284,285] single-crystalline morphology and surface reactivity,[286-288] SEI formation,[289,290] Si anodes,[291] effects of electrolyte additives[292,293] and the benefits of localized high-concentration or saturated electrolytes over conventional electrolyte compositions.[294-296] On the issue of Li_2CO_3, Li *et al.* and Zheng *et al.* have reported a beneficial use of Li_2CO_3 as a cathode additive in full cells, providing additional Li inventory, arguing that evolved CO_2 is dissolved in the electrolyte and has a further beneficial effect on SEI formation.[297,298] However, Cai *et al.* stressed that Li_2CO_3 impurities on NCM lead to a thicker rock-salt-type layer and more electrolyte degradation.[299] Regarding the degradation mechanism, Song *et al.* demonstrated that the chemical decomposition of Li_2CO_3 depends on the $LiPF_6$ concentration in EC-based electrolytes. EC either coordinates to the PF_6 anion or is present as “free” EC, which the authors argue undergoes dehydrogenation faster and at lower potentials, providing the acid proton necessary for chemical decomposition of the carbonate.[300] On the other hand, Cao *et al.* performed an extensive study on the decomposition mechanism, utilizing isotope labelling and combining DEMS and GC-MS for a distinction of CO_2 and CO. They find that when using LiTFSI in tetraglyme as electrolyte, only electrochemical decomposition of Li_2CO_3 occurs even in the presence of water, while only upon use of $LiPF_6$, both in an EC-based electrolyte and in tetraglyme, chemical decomposition occurs.[301] A similar investigation of the unexpected role of conductive salt and electrolyte solvent on DEMS results is presented in this thesis in chapter 4.4.

The review also includes titration mass spectrometry (TMS) in combination with isotope labelling as a quantitative *ex situ* investigation method for the presence of carbonates on the CAM surface and the oxidation state of both transition metals and ox-

ygen. Since the writing of the review, TMS continues to find application in CAM analysis,[302-304] but most recent development has focused on the anode side, which was overlooked in the review. In earlier works, Schmitz *et al.* showed via mass spectrometry that the hydrolysis of a Li-metal SEI yielded acetylene, indicating the presence of lithium carbide in the SEI,[305] while Fang *et al.* showed that inactive (insulated) Li in a Li-metal anode can be quantified from the H_2 evolution after addition of water, ruling out a contribution of LiH in the SEI by a titration with D_2O.[306] McShane *et al.* performed TMS on graphite anodes after fast charging, quantifying not only inactive Li, but also SEI components.[307] After publication of the review, various TMS setups and studies ranging from graphite to Li-metal to Li-free anodes have been reported, often utilizing isotope labelling, that allow to quantify the SEI composition and correlate it with initial Coulomb efficiency, i.e. optimize the SEI formation process.[308-313]

As predicted, DEMS/OEMS continues to find application in the study of Li-rich materials with oxygen redox contribution, where the suppression of irreversible anion oxidation to O_2 is a key challenge. This includes both layered oxides, where on the one hand the tuning of cation and anion redox contributions,[314] on the other hand the effect of coatings and dopings on gas evolution can be assessed,[315,316] but also DRX CAMs. Crafton *et al.* used DEMS and TMS to study the effect of increased fluorine content on oxygen redox and gas evolution in oxyfluoride DRX materials, also using the TMSPa additive to track F^- dissolution via DEMS.[304] Huang *et al.* expanded their TMS method of tracking Ni and O redox contributions, as already featured in the review[317] into a two-step process, also able to track Mn oxidation states via the oxidation of oxalic acid to CO_2.[303] Yin *et al.* ruled out reversible oxygen redox in $Li_4Mn_2O_5$ via DEMS,[318] and Zhou *et al.* reported on increased lattice oxygen stability achieved in the high-entropy $Li_{1.25}Ni_{0.1}Co_{0.1}Fe_{0.1}Cr_{0.1}Ti_{0.2}Nb_{0.15}O_{1.8}F_{0.2}$ DRX material compared to the lower entropy counterpart, $Li_{1.25}Ni_{0.4}Nb_{0.35}O_{1.8}F_{0.2}$.[319]

The study of oxygen redox not only via DEMS/OEMS, but also via the complementary method, resonant inelastic X-ray scattering (RIXS), has been discussed in the review, including the observation of vibrational peaks corresponding to the 1.2 Å bond length of trapped molecular O_2 via high-resolution RIXS in oxygen redox active SIB CAM by House *et al.*[320] They have reported the formation of trapped O_2 also for various Li-rich CAMs, and after writing of the review, further applied neutron pair distribution function (PDF) analysis, again observing the 1.2 Å bond length associated with molecular O_2 in charged CAM.[321,322] Recently, they reported that in stored, charged electrodes the

magnetic moment, as well as the O_2 RIXS and nuclear magnetic resonance (NMR) spectroscopy features increase over time, concluding that delocalized electron holes on O^{2-} become increasingly localized in the form of molecular O_2 trapped in clustered vacancies formed by in-plane transition-metal migration.[323] The underlying RIXS feature has been observed also by Li *et al.*,[324] and Wu *et al.* observed molecular O_2 via electron paramagnetic resonance (EPR) spectroscopy while deriving a Nb-surface doping strategy to suppress O_2 loss from P2-SIB CAM.[325] However, the contribution of oxygen redox to the capacity of even conventional NCM materials, in which no O_2 trapping should happen, due to the lack of transition-metal layer vacancies, has also received increased attention. Menon *et al.* observed the same molecular O_2 feature in high-resolution RIXS of W-doped LNO that House *et al.* had associated to trapped molecular O_2 in Li-rich oxides.[326] Thus, Menon *et al.* argue that the feature may not be attributed to molecular O_2 after all, and the understanding of transition-metal and oxygen redox contributions needs to be reconsidered. In this regard, Genreith-Schriever *et al.* reported that it is oxygen oxidation that provides most capacity in LNO, based on calculations and simulations, in good agreement with experimental X-ray absorption spectroscopy (XAS) data, also finding the 1.2 Å bond length in a molecular dynamics simulation of trace water-based O-O dimerization and explaining the formation of singlet oxygen from a peroxide intermediate.[113]

In the field of SIBs, subsequent gas evolution studies continued to focus on layered oxides and the effects of composition and coatings on the associated oxygen loss.[327,328] For a P2-type CAM, Shao *et al.* reported that a combined Li_2ZrO_3 coating and Li^+/Zr^{4+}-doping reduced the gas evolution during cycling.[329] Also in LNO, the coating or doping process affects the distribution of Zr^{4+} between coating (Li_2ZrO_3 phase) and true doping, as is discussed in chapter 4.2.[330] Ding *et al.* reported that in O3-type $Na_{0.95}Li_{0.07}Cu_{0.11}Ni_{0.11}Fe_{0.3}Mn_{0.41}O_{1.97}F_{0.03}$, increased configurational entropy, i.e. including partial replacement of O by F, increased transition-metal redox and reduced gas evolution due to irreversible oxygen oxidation.[331]

Pfeiffer *et al.* observed a bimodal CO_2 evolution profile of a P2-type CAM, with one peak of gas evolution rate observed at the onset of the P2-O2 phase transition, and another at the upper cut-off voltage, which they explained by the formation of cracks and the associated exposure of additional CAM surface area.[164] The *in situ* detection of crack formation and gas evolution of P2-type CAMs with varying configurational entropy via AE is further discussed in chapter 3.3.[170,171]

Lee *et al.* found that crack formation in P2-type CAM can occur already during storage by exposure to moisture and CO_2, which extract Na from the structure to form NaOH, $NaHCO_3$ and Na_2CO_3 surface impurities, leading to decomposition of the CAM under O_2 evolution, as demonstrated by mass spectrometry.[332] Zhang *et al.* used acetic acid washing to remove such surface impurities, as they lead to slurry gelling, and via DEMS interestingly observed that not only the gas evolution from surface impurities is reduced, but that also the thus formed sodium acetate during the first charge undergoes a Kolbe reaction,[333] leading to evolution of not only CO_2, but also ethane.[168]

Geisler *et al.* developed a three-electrode DEMS setup aimed towards SIBs, comparing diglyme- and propylene carbonate-based electrolytes, and identified dimethyl ether as a degradation product of diglyme.[268] Furthermore, Geisler also confirmed the evolution of $(CN)_2$ from PW CAM, as was observed at BELLA.[189,192,193,266] Ge *et al.*, on the other hand, did not detect $(CN)_2$ from PW CAM when investigating the role of PW water content on gas evolution, likely due to insuficcient instrumentation.[334] In chapter 4.4., both the role of PW water content on gas evolution and limitations of $(CN)_2$ detection are discussed in detail.

The review was initiated and designed by Dr. Torsten Brezesinski and the author of this thesis. Literature collection and review, as well as the writing of the original manuscript was done by the author. Dr. Torsten Brezesinski and the author prepared the figures. Dr. Aleksandr Kondrakov, Prof. Dr. Jürgen Janek and Dr. Torsten Brezesinski supervised the work. The manuscript was edited by all authors.

Reprinted from S. L. Dreyer, A. Kondrakov, J. Janek, T. Brezesinski, *J. Mater. Res.* **2022**, *37*, 3146–3168, DOI 10.1557/s43578-022-00586-2

Journal of MATERIALS RESEARCH

Invited Feature Paper-Review
DOI:10.1557/s43578-022-00586-2

MULTISCALE CHARACTERIZATION AND ANALYSIS FOR UNDERSTANDING ENERGY STORAGE MECHANISMS IN RECHARGEABLE BATTERIES

In situ analysis of gas evolution in liquid- and solid-electrolyte-based batteries with current and next-generation cathode materials

Sören L. Dreyer[1], Aleksandr Kondrakov[1,2], Jürgen Janek[1,3,a)], Torsten Brezesinski[1,a)]

[1] Battery and Electrochemistry Laboratory (BELLA), Institute of Nanotechnology, Karlsruhe Institute of Technology (KIT), Hermann-von-Helmholtz-Platz 1, 76344 Eggenstein-Leopoldshafen, Germany
[2] BASF SE, Carl-Bosch-Str. 38, 67056 Ludwigshafen, Germany
[3] Institute of Physical Chemistry & Center for Materials Research (ZfM/LaMa), Justus-Liebig-University Giessen, Heinrich-Buff-Ring 17, 35392 Giessen, Germany
[a)] Address all correspondence to these authors. e-mails: juergen.janek@kit.edu; torsten.brezesinski@kit.edu

Received: 6 February 2022; accepted: 28 April 2022; published online: 23 May 2022

The operation of combined mass spectrometry and electrochemistry setups has recently become a powerful approach for the in situ analysis of gas evolution in batteries. It allows for real-time insights and mechanistic understanding into different processes, including battery formation, operation, degradation, and behavior under stress conditions. Important information is gained on the safety and stability window as well as on the effect of protecting strategies, such as surface coatings, dopings, and electrolyte additives. This review primarily aims at summarizing recent findings on the gassing behavior in different kinds of liquid- and solid-electrolyte-based batteries, with emphasis placed on novel cathode-active materials and isotope labeling experiments, to highlight the relevance of in situ gas analysis for elucidation of reaction mechanisms. Various instrumental and experimental approaches are presented to encourage and inspire both novices and experienced scientists in the field.

Introduction

As the increasing societal and commercial demand for large-scale energy storage and electric vehicles continues to promote innovations in battery research, new or improved materials and concepts are in the focus of scientific interest. Main motives for these innovations are improvements in one or more of energy density, longevity, safety, sustainability, and ultimately costs.

For current generation lithium-ion batteries (LIBs) with graphite as anode material, the focus is on the tradeoff between larger energy density and lower costs by increased Ni content in the layered transition metal oxide cathode-active material (CAM) and reduced cycle life resulting from the change in composition and reactivity. While incremental improvements, mostly from suppressing degradation mechanisms, such as particle fracture (exposing additional [reactive] surface area to the electrolyte) or phase transitions/transformations, are made to these CAMs, their Ni content approaches 100%, thus limiting the possibilities for further energy density increases at the positive electrode side [1, 2].

For improvements beyond, Li-rich CAMs, both layered and with rock-salt-type structures, are currently being discussed. These materials gain additional capacity by involving lattice oxygen in the redox, but the often limited reversibility of this reaction remains a challenge [3–5].

A relatively large increase in energy density at the anode side can be achieved by substitution of the graphite as standard electrode material by Li metal. However, because of dendrite formation, cells with Li metal anodes are prone to failure. The solid-state battery (SSB) promises to solve this problem by replacing the liquid electrolyte with a solid electrolyte (SE), which also reduces the cell's flammability [6]. For this reason, bulk SSBs are receiving increasing interest lately. Nevertheless, cell manufacturing and especially the development of the key component, an SE with favorable mechanical properties as well as high (electro)chemical stability and Li-ion conductivity, still require additional research in order to achieve SSBs with competitive energy and power densities [7].

Journal of MATERIALS RESEARCH

Invited Feature Paper-Review

Meanwhile, the much higher abundance of sodium compared to lithium makes sodium-ion batteries (SIB) a suitable candidate in the field of post-LIB technologies. While the CAMs introduced so far can rarely match their lithium equivalents in terms of specific capacity, the lower costs and environmental impact make SIBs promising for large-scale energy storage [8, 9].

For all battery materials and concepts mentioned so far, key to their continuous development and improvement is a thorough understanding of (side) reaction mechanisms at play during formation, operation, and degradation. In situ techniques allow for the characterization of materials within the relevant environment of a battery cell, while *operando* techniques go one step further and enable real-time monitoring during cycling operation (i.e., within a dynamic, operating system). Thus, it comes as no surprise that various review papers on in situ characterization studies are available in the literature [10–13]. However, most in situ or *operando* methods applied to battery materials, such as (electron) microscopy, spectroscopy and X-ray-based techniques, are restricted in their working principle to condensed matter or even crystalline phases only [13, 14].

As for the materials and concepts discussed above, reactions that include gas evolution are relevant to their evaluation, such as the surface (im)purity, structural (in)stability, interface formation, and electrolyte degradation. The in situ gas analysis is therefore a useful addition to routine electrochemical experiments and other analytical techniques for better understanding of reaction mechanisms. To this end, mass spectrometry (MS) is typically performed simultaneously with battery operation. While existing reviews focus mostly on instrumentation [15] and standard materials [16], in this work, an overview of recent developments in the field of in situ instrumentation and gas evolution studies is given, with emphasis placed on novel CAMs (with layered and rock-salt or related lattice structures) and cell concepts.

In situ gas evolution measurements

Instrumentation

The combination of electrochemical testing and MS allows for a variety of experiments, with in situ measurements usually referred to as differential electrochemical mass spectrometry (DEMS) [17, 18]. In the battery context, pioneering work has been reported by Imhof et al. as early as 1998, studying the solid-electrolyte interphase (SEI) formation on graphite by using a porous electrode and a hydrophobic membrane separating the cell from applied vacuum to selectively extract evolved gases from the working electrode [19]. The development history of in situ MS in the battery field has been described in more detail by Schiele et al. [15] and Lundström et al. [20]. As the hydrophobic membrane can be passed by organic solvents, especially those of low boiling point, a stream of carrier gas can be used instead to extract the evolving gasses from the cell's headspace [21]. The use of carrier gas comes at the price of stressing the cell by electrolyte depletion, because the electrolyte solvents are carried out of the cell, albeit at a slower rate, and also detected by the mass spectrometer. Berkes et al. implemented both a bubbler to saturate the carrier gas with electrolyte solvents before entering the cell and a cold trap near the outlet of the cell to remove them from the carrier gas again [22]. While reducing noise and allowing for longer battery operation time, the introduction of carrier gas and cold trap affects the achievable time resolution. For this reason, Jusys et al. chose to keep working with a fluoropolymer membrane in their recent setup [23].

An alternative to carrier gas or membranes is the use of closed or semi-closed headspaces. In a semi-closed headspace, as introduced by McCloskey et al. [24], He et al. [25] and recently by Lundström et al. [20], see Fig. 1(a), the evolved gasses are purged at set time intervals, again sacrificing time resolution, but gaining an environment that closer resembles a standard battery, as well as a potentially higher detectability of trace gasses, as these have time to accumulate and are not constantly diluted in the carrier gas. An additional benefit of this approach compared to the continuous measurement of gas evolution is the possibility of monitoring the gassing of multiple cells with just one spectrometer by purging them subsequently. The choice of purging interval has to be reasonable compared to the timeframe of battery cycling, but with cells often cycled at a 0.1C rate, sampling every 10 min already generates 60 data points for a single charge or discharge cycle. The reader should keep in mind that even when "continuously monitoring," a standard quadrupole mass spectrometer may only measure a single m/z ratio at a time, thus also affecting the possible time resolution, especially during broadband monitoring (e.g., all m/z from 1 to 100 are

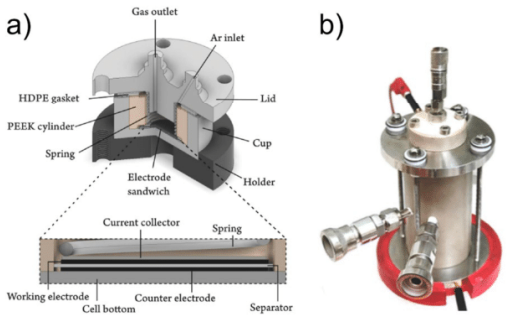

Figure 1: (a) Measurement cell used by Lundström et al. Adapted with permission from [20]. (b) Setup to analyze gassing of commercial 18650 cells. Adapted with permission from [30].

Journal of MATERIALS RESEARCH

Invited Feature Paper-Review

measured). Because of the discrete nature of the sampling times and the accumulation of gasses in the headspace, the gas analysis from a semi-closed headspace is typically referred to as online electrochemical mass spectrometry (OEMS) instead.

The closed headspace approach developed in the group of Gasteiger is also referred to as OEMS. In this case, a small capillary leak connects the headspace of the cell continuously and directly to the mass spectrometer, with only very small gas flow necessary, thereby eliminating the need for carrier gas, membranes, purge valves, and cold traps [26, 27]. Notably, as the headspace is not purged, the gas composition is measured and has to be differentiated to obtain gas evolution rates. As the headspace gas is not refilled, the pressure within the cell is decreasing over time, limiting the maximum measurement time. For this setup, a two-compartment solution via Li-ion conducting glass ceramic has been used to selectively measure the gas evolution at one electrode only [27].

We note that many of the experimental setups discussed herein are derived from setups for the study of metal–air batteries by in situ MS. Because of conceptual differences and the contrasting role of gas presence, this article excludes metal–air battery studies.

A further simplified OEMS design has been reported by Hahn et al., using an X-shaped Swagelok-type cell, yet with challenges in response time and quantification, and result dependency on the exact capillary position [28]. Recently, Geng et al. established OEMS measurements on pouch cells via the closed headspace principle [29] and Mattinen et al. even demonstrated an OEMS setup that is capable of monitoring the gassing of commercial 18650 cells, see Fig. 1(b) [30].

Irrespective of the chosen design approach, quantification of the gases evolved is achieved by flushing the cell with a calibration gas of known composition (e.g., in ppm for each gas of interest) after the measurement. If doing so in steps of different dilution with carrier gas, a calibration curve (e.g., ion current to ppm of gas) can be obtained. Using either the flow rate (open headspace) or cell volume (closed headspace), a conversion of concentration to evolution rate or amount of gas is possible. A detailed description for the calibration of a semi-closed headspace system is provided elsewhere [20].

Gas chromatography (GC) can also be applied to batteries in situ [31]. In this case, it is even possible to replace the mass spectrometer by a simpler detector, such as thermal conductivity [32] or barrier ionization discharge detectors [33]. However, it should be noted that the possible sampling rate is strongly decreased due to the chromatographic retention times of the gaseous species, so that measurements have to be performed very slowly or only at certain potentials [32, 33]. Horsthemke et al. used in situ GC–MS to examine the consumption of vinylene carbonate (VC) and the formation of electrolyte aging products, including their identification [34]. Because electrolyte and aging products are not gaseous and their detection relies on the extraction procedure and heating ramps applied during GC, such studies are outside the scope of this article. The same holds true for works limited to a specific gas or ion, such as the detection of evolved oxygen via reduction at a rotating ring disk electrode, as described by Yin et al. [35].

Readers keen on establishing own DEMS or OEMS setups are encouraged to take a look at the available literature, as well as to consider their own needs and interests, as the setups should be tailored to the system(s) of interest. This kind of tailoring is highlighted when comparing the OEMS setups of Mattinen et al. [30] and Lundström et al. [20], which, while published recently and almost at the same time, are fundamentally different in almost any aspect. Commercial turnkey DEMS solutions are available, but are in most cases not optimized for battery research. Some criteria to consider are the intended operation time and (dis)charge rate of the cell; the size and loading of electrodes; the use of standard (calendered) electrode tape versus the need to specifically coat membranes, separators, or mesh [15]; the ability to measure multiple cells at the same time; the expected amount of evolved gasses; the ability to do measurements in pouch cells, Swagelok-type cells, or in a customized cell setup; the ability to switch between electrode materials and electrolytes; the volume of electrolyte required; restrictions of electrolyte by vapor pressure or melting point, and the need for a cold trap.

State-of-the-art LIBs

For an introduction into and the history of gas evolution in batteries, the reader is referred to the existing literature [15, 16]. In this article, more recent findings relevant to the fundamental mechanistic understanding of gas evolving (side) reactions and Ni-rich CAMs will be reviewed.

Cathode gassing

For $LiNi_xCo_yMn_zO_2$ (NCM) materials, CO_2 is the main component of gasses released at the cathode side. Additionally, a concurrent evolution of CO is usually observed. Apart from surface carbonate impurities, which will be discussed separately in the next section, the CAM itself does not contain carbon, leaving conductive carbon black, polymer binder, and electrolyte as possible sources. Because O_2 evolution from the CAM is often also detected, albeit at a lower level, the conclusion of oxidation of one of the aforementioned components is only logical. However, it should be noted that the organic carbonate electrolytes, such as the widely used ethylene carbonate (EC), can also release CO_2 upon hydroxide-catalyzed hydrolysis.

The exact nature of the electrolyte oxidation reaction, with different onset potentials reported earlier, as well as of the O_2 release, has been clarified by Jung et al. and Streich et al. They

Journal of MATERIALS RESEARCH

Invited Feature Paper-Review

demonstrated that for NCM811 (80% Ni), NCM622 (60% Ni), and NCM111 (33% Ni), the onset of gas evolution varies, being at a lower potential with increasing Ni content (when the state of charge (SOC) reaches ≥ 80%) [36, 37]. From this observation, Jung et al. were able to assign the SOC-dependent CO_2 evolution below 4.7 V vs. Li^+/Li to the chemical oxidation of EC by O_2 released from the NCM lattice. Above 4.7 V, also electrochemical oxidation was apparent, as demonstrated with an electrode containing no CAM. In a follow-up study, they further showed that the onset potential is not dependent on temperature, but only on SOC, which at a given potential only changes slightly with increasing temperature [38]. They also observed an increase in gas evolution at elevated temperature and, using ^{13}C-labeled electrolyte, identified (and quantified) electrolyte hydrolysis and impurity oxidation as the reasons for gas evolution prior to the O_2 release from the NCM.

As lattice oxygen is released, the layered oxide surface undergoes a reconstruction toward a redox-inactive rock-salt-like phase. The thickness of this layer can be calculated from the observed gas evolution (O_2 and CO_2 from chemical electrolyte oxidation) and the CAM's specific surface area [37]. However, as Oswald et al. recently demonstrated in a comparison of polycrystalline and single-crystalline NCM CAMs, the increase in specific surface area due to particle fracture upon delithiation (charge) has to be taken into account [39]. In a follow-up study, they examined the role of particle morphology, i.e., primary particle size, finding both a lower total gas release, with no O_2 but only CO_2 evolution, for single-crystalline material [40].

Metzger et al. investigated the electrochemical oxidation of carbon black and EC containing different supporting lithium salts at various temperatures by using ^{13}C-labeled carbon electrodes and common ^{12}C-electrolyte in order to distinguish the reaction products ($^{13}CO_2$ and $^{12}CO_2$) in OEMS [41]. They observed that the conductive carbon is oxidized in the presence of $LiClO_4$, but not in the presence of $LiPF_6$, lithium bis(trifluoromethanesulfonyl)imide (LiTFSI) or $LiBF_4$, whereas EC oxidation took place in the presence of $LiPF_6$, thus concluding that $LiBF_4$ is best suited for use at high potentials.

A major discovery in the field of battery gas evolution was the in situ observation of singlet oxygen ($^1O_2$) generation by both NCM and Li-rich CAMs, which will be discussed separately, by Wandt et al. [42]. In previous works, it has already been speculated that the released oxygen is highly reactive, because the electrolyte is not oxidized when handled in air. Using the 633 nm photon emission of $^1O_2$ dimers upon return to ground state, Wandt et al. developed an *operando* photomultiplier setup that is capable of detecting the released photons, revealing the presence of $^1O_2$ above ~ 80% SOC and correlation with the gas evolution from OEMS. This work has major implications, as it suggests that not stability against electrochemical oxidation, but instead against $^1O_2$ is the foremost requirement for electrolytes when CAMs are operated at high SOC. Freiberg et al. also demonstrated the reaction of EC or dimethyl carbonate (DMC) with $^1O_2$ using rose bengal dye to excite oxygen dissolved into the electrolyte upon irradiation while also monitoring the gas evolution [43]. In EC, they observed the formation of CO_2 (but no CO) and consumption of O_2, while in DMC no signal above a background experiment without dissolved oxygen was detected, highlighting the stability of DMC against $^1O_2$. A reaction mechanism has been proposed from density functional theory (DFT) calculations, including (in the first step) the dehydrogenation of EC with the formation of VC and H_2O_2. The presence of H_2O_2 has been confirmed colorimetrically via the $[Ti(O_2)]^{2+}$ complex and its subsequent oxidation probed using OEMS, revealing the evolution of O_2 at 4.4 V vs. Li^+/Li, leaving H_2O and acid protons behind. The formation of H_2O and acid protons has multiple detrimental effects, such as the hydrolysis of $LiPF_6$, producing HF and leading to transition metal leaching from the CAM [44].

The effect of increased Ni content in NCM CAMs on gas evolution has been studied by considering the endmember $LiNiO_2$ (LNO). de Biasi et al. used DEMS to show that some (mostly minor) O_2 evolution (and thus also CO_2 evolution) already occurs in the H2 region (x(Li) ≈ 0.3), with the gassing being reduced during the H2–H3 phase transformation before a large increase in rate of gas evolution is observed (SOC > 80%). Surprisingly, they also detected O_2 evolution in the H2 region during discharge [45]. A mechanistic insight on oxygen evolution has been given by Li et al. They combined DEMS with synchrotron X-ray absorption spectroscopy (XAS) and resonant inelastic X-ray scattering (RIXS) and showed that during charge, starting from 4.3 V vs. Li^+/Li, O_2 evolution is observed, with the Ni ions at and near the surface decreasing in oxidation state again. This result indicates the presence of oxidized oxygen, for which a RIXS feature remains present until discharge to 3.8 V [46]. Figure 2(a) shows the corresponding RIXS and DEMS results. The oxidation of oxygen anions to form molecular O_2 thus goes in hand with the reduction of Ni^{4+}. In a follow-up study, Li et al. demonstrated that doping with Al^{3+} leads to increased oxygen redox and O_2 evolution, as the local concentration of redox-active cations is reduced [47].

Papp et al. compared the gas evolution of $LiCoO_2$ (LCO) and LNO upon charging to 5 V vs. Li^+/Li, focusing on the electrochemical electrolyte oxidation. They revealed that while LNO releases one order of magnitude more CO_2 in the initial cycle, it shows much less gas evolution in the following cycles [48]. The authors inferred that LNO has a higher electrocatalytic activity for electrolyte degradation, but at the same time forms a passivation layer faster. A distinction between chemical and electrochemical oxidation was possible through the use of ^{18}O-enriched CAM.

Journal of MATERIALS RESEARCH

Invited Feature Paper-Review

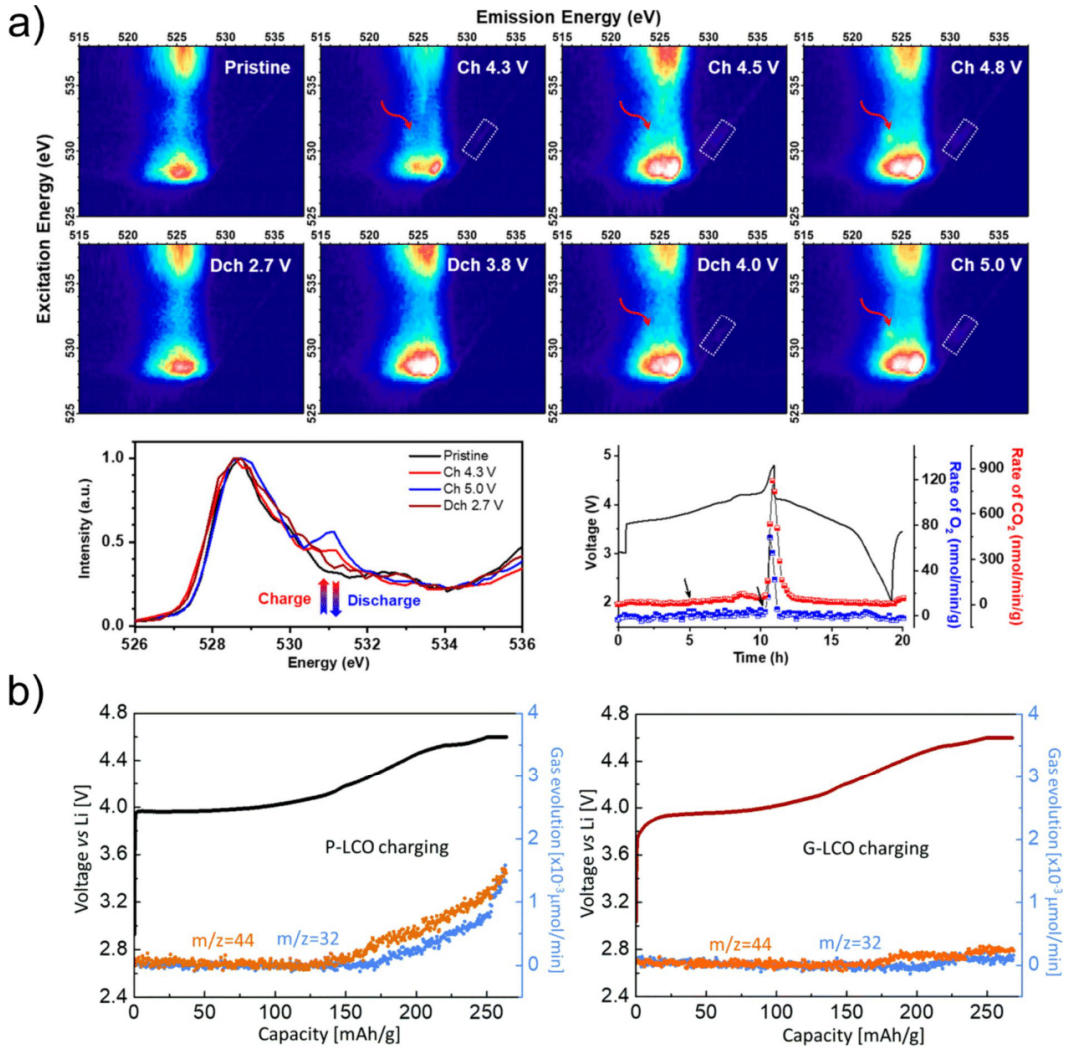

Figure 2: (a) Demonstration of oxygen redox in LNO via RIXS and DEMS. Adapted with permission from [46]. (b) Effect of a solid shell around the LCO core on the LCO gassing. P-LCO and G-LCO refer to pristine and gradient LCO, respectively. Adapted with permission from [54] .

Surface modification is a well-established concept to mitigate CAM degradation, and it is not surprising that also the gas evolution can be affected by cathode electrolyte interphase (CEI)-forming additives [49, 50] or coatings [51–53]. For example, Zhu et al. demonstrated that by enclosing LCO in a shell of $LiMn_{0.75}Ni_{0.25}O_2$, the oxygen redox can be utilized with no apparent O_2 evolution, yielding a specific charge capacity of more than 250 mAh/g at 4.6 V vs. Li^+/Li, see Fig. 2(b) [54]. Comparing the gassing behavior of coated and uncoated CAMs requires attention to the amount of surface impurities, as they will affect the gas evolution, especially in the case of carbonates, as discussed in the following.

The role of carbonates, peroxides, and surface treatments

Impurities are regularly found on the surface not only of NCM but of LIB CAMs in general, with Li_2CO_3 and LiOH being the most common. They are formed from excess reagents during synthesis and exposure to ambient air and moisture, thus being more or less unavoidable. Li_2CO_3 decomposes under release

Journal of MATERIALS RESEARCH

Invited Feature Paper-Review

of CO_2 and therefore is of great importance in gassing studies. In situ gas analysis setups can be modified to determine the amount of carbonates present by measuring the CO_2 evolution upon addition of acid to the CAM, and the contribution of carbonate decomposition to the total CO_2 evolution, which is significant in the initial cycle, can be quantified by isotope labeling [55, 56]. CO_2 is released both by chemical decomposition in acidic environment (Eq. 1) or by electrochemical oxidation at potentials above 3.8 V vs. Li^+/Li (Eq. 2).

$$Li_2CO_3 + 2H^+ \rightarrow 2Li^+ + H_2O + CO_2 \quad (1)$$

$$2Li_2CO_3 \rightarrow 4Li^+ + 4e^- + 2CO_2 + O_2 \quad (2)$$

While the rate of Li_2CO_3 decomposition has been found to increase with electrode potential and the reaction is known from metal–oxygen (air) batteries, no O_2 evolution is usually detected. Using carbon/Li_2CO_3 electrodes, Mahne et al. demonstrated that the electrochemical oxidation leads to the formation of $^1O_2$, similar to the release of lattice oxygen from NCM CAMs, which is typically not detected, as it reacts quickly with the electrolyte [57]. The authors achieved this in an experiment using 9,10-dimethylantracene as chemical probe in the electrolyte to trap the $^1O_2$ and then detect the reaction product, and in another experiment by detecting O_2 evolution after adding a quencher to the electrolyte. However, the slow and incomplete decomposition of carbonate species in SSB cells, i.e., in the absence of liquid electrolyte, raises the question of the rate at which the electrochemical decomposition occurs [58, 59].

Freiberg et al. have shown via OEMS that a carbon/$Li_2{}^{13}CO_3$ electrode releases the amount of $^{13}CO_2$ equal to complete carbonate decomposition even when separated from the working electrode by a non-conducting polyester layer, making direct electrochemical oxidation impossible [60]. The source of acid protons necessary for the chemical decomposition of carbonates has been determined to be the oxidation of alcoholic impurities, which already occurs at 3.5 V vs. Li^+/Li and helps explain the often observed early onset of carbonate decomposition. The presence of protons has a catalytic effect, as H_2O formed by the carbonate decomposition hydrolyzes $LiPF_6$, leading to the generation of additional HF and POF_3. In contrast, Kaufman et al. observed no $^{13}CO_2$ evolution when performing an experiment similar to that of Freiberg et al., in which they used a $Li_2{}^{13}CO_3$-containing separator instead of a disconnected carbon/$Li_2{}^{13}CO_3$ interlayer [61]. Figure 3(a) and (b) shows the results from both groups. Overall, the individual contributions of the chemical and electrochemical pathways to carbonate decomposition remain disputed.

Performing acid titration either on charged or discharged cathodes, Renfrew et al. found that charged cathodes have a larger carbonate content than the pristine ones and the content is only reduced below that of pristine cathodes upon discharge. This result indicates that the degradation of organic carbonates leads to the formation of a surface layer containing carbonate-type side products during charge, which are desorbed with discharge [55]. In the same study, the authors also observed O_2 evolution in acid titration experiments using charged cathodes, which they explained by the formation of a peroxo-like surface layer, notably prior to the onset of lattice oxygen evolution. Upon acid titration, peroxides release oxygen according to (Eq. 3).

$$2Li_2O_2 + 4H^+ \rightarrow 2H_2O + O_2 + 4Li^+ \quad (3)$$

From a follow-up study, indicating that the thickness of the peroxo-like layer is not dependent on the electrolyte but the SOC [62], the authors suggested that organic carbonates are deposited onto the cathode, where they can react with lattice oxygen, explaining the origin of CO_2 containing isotope-labeled lattice oxygen before the actual release of O_2 from the lattice. The observation of electrolyte fragments attached to diatomic oxygen during acid titration, including both ^{16}O from the lattice and ^{18}O from $Li_2C^{18}O_3$ by Kaufman et al. indicates a complex interplay of the carbonate species and the lattice reactivity [61]. Taking the peroxo-like surface layer and carbonate decomposition together, Houchins et al. proposed a mechanism for $^1O_2$ generation based on superoxide formation and disproportionation [63].

Removal of surface carbonates via washing of the CAM appears obvious. However, while indeed reducing their amount, the overall effect on gas release is complex. Depending on the exposure time to H_2O and the applied drying procedure, the surface reactivity of the CAM varies, as discussed by Pritzl et al. [64] and Renfrew et al. [65]. Not only are washing steps directly decreasing the peroxo-like character, but also removing lithium from the CAM, thereby negatively affecting the capacity and forming a Li-deficient surface layer. Upon heating (drying), the latter may decompose to a rock-salt or spinel-type phase with increased impedance. For this reason, washing procedures have to be developed with care.

For Li-rich CAMs, similar surface treatments have been shown to suppress O_2 evolution by the formation of a passivating surface film [66, 67]. For example, carbonates [68, 69] or ternary lithium metal oxide shells [70, 71] have been deliberately prepared to later be washed off, eventually showing lower gas evolution.

Anode/electrolyte gassing

The gassing behavior of electrolytes and anodes is interwoven, as the SEI formation is the most relevant process in terms of gas evolution. The SEI is a complex surface layer, with its formation and composition depending on many factors. Herein, only in situ studies on the SEI formation are reviewed.

Journal of MATERIALS RESEARCH

Invited Feature Paper-Review

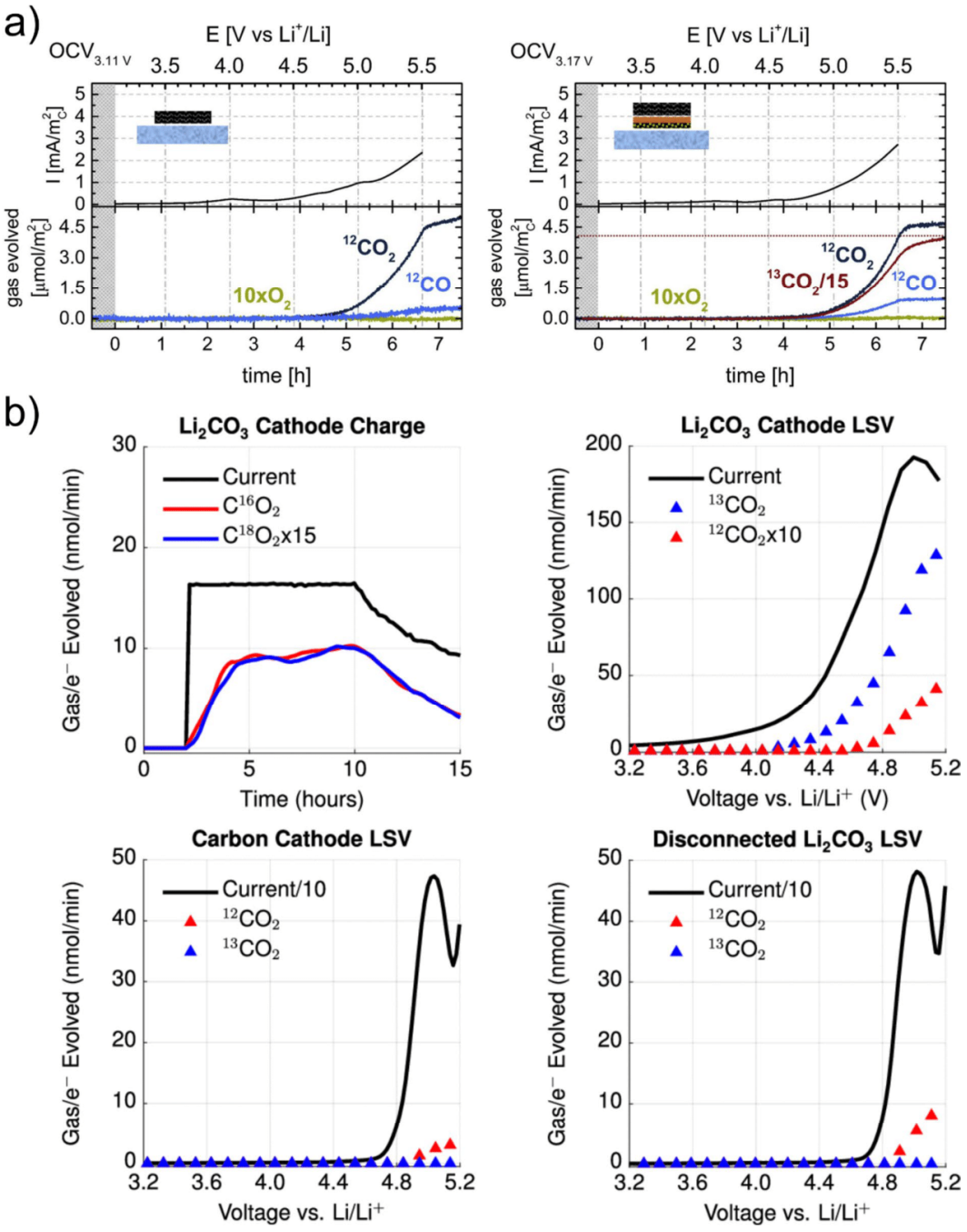

Figure 3: Conflicting ^{13}C-labeling experiments on electrically isolated $Li_2{}^{13}CO_3$ providing (a) supporting and (b) disputing evidence for chemical decomposition in a battery environment. Adapted with permissions from [60, 61].

Journal of MATERIALS RESEARCH

Invited Feature Paper-Review

Trace H_2O and acid-derived protons are reduced to evolve H_2 while leaving OH^- ions and other anions behind. These ions lead to the hydrolysis of cyclic organic carbonates, such as EC or propylene carbonate (PC), resulting in the evolution of CO_2 and generation of alkoxide anions, which in turn can react with the electrolyte solvent to produce glycol species [72]. The main gas evolution at the anode side is the electrolyte reduction, which below ~ 0.9 V vs. Li^+/Li leads to the formation of lithium ethylene dicarbonate (LEDC) as an SEI component and C_2H_4 in the case of EC and lithium propylene dicarbonate and C_3H_6 in the case of PC [73]. Note that for the detection of C_2H_4, the (fragment) signal at $m/z = 26$ is suited best, because both N_2 and CO are also detected at $m/z = 28$.

The role of H_2O impurities present in the battery cell has been discussed by Bernhard et al. [74] and Kitz et al. [75], observing increased rates of H_2 and CO_2 evolution with increasing H_2O level. With the closed headspace OEMS used by Bernhard et al., the subsequent consumption of CO_2 has been seen. This consumption can be explained by the formation of Li_2CO_3 in a reaction of CO_2 with OH^- ions. Indeed, by combining OEMS with electrochemical quartz crystal microbalance (EQCM), Kitz et al. found that the addition of trace H_2O leads to a thicker and more rigid SEI with increased Li_2CO_3 content. Using additionally surface-enhanced Raman spectroscopy, Mozhzhukhina et al. observed a carbonate band appearing at 1.8 V vs. Li^+/Li, while LiF was found to deposit onto the electrode after the onset of H_2 evolution [76]. The latter stems from HF, which results from the hydrolysis of $LiPF_6$, as discussed previously.

Combining OEMS and EQCM, Melin et al. were also able to show that both EC and PC do form an SEI with accompanying gassing upon reduction. However, the gas evolution rate and mass deposition were much higher in the case of PC, forming a thicker layer that re-dissolves when current is no longer applied, thus explaining the lack of stable SEI formation in PC [73]. Figure 4 summarizes the discussed anode gas evolution processes and SEI formation in EC- and PC-based LIB electrolytes.

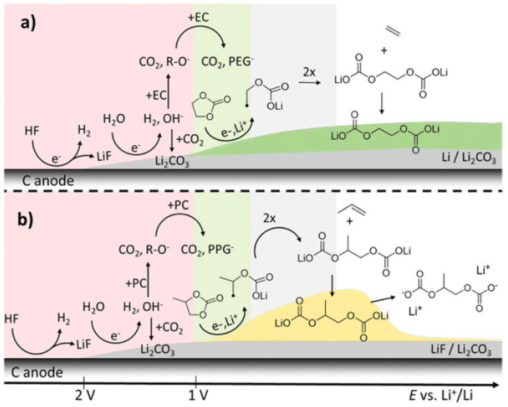

Figure 4: Gas evolution and SEI formation in (a) EC and (b) PC electrolytes. Reproduced with permission from [73].

The common electrolyte additives VC and fluoroethylene carbonate (FEC) have been investigated by Schwenke et al. [77] and Kitz et al. [78] regarding their effect on gas evolution during SEI formation and the resulting SEI properties. Both groups observed the evolution of CO_2 upon reduction, as opposed to the evolution of C_2H_4 for EC-containing electrolyte. Because the additives are decomposed at higher potentials (1.3–1.1 V for VC and 1.45–0.95 V for FEC) [78] than EC, they mitigate the subsequent electrolyte reduction by passivating the anode, resulting in a thinner SEI (note that the evolved CO_2 can lead to the formation of Li_2CO_3). While FEC also leads to the formation of LiF in the SEI, VC is capable of suppressing it. Based on these observations, Schwenke et al. demonstrated that a CO_2 atmosphere in the cell can lead to the formation of a carbonate-containing SEI even for EC-free electrolytes. Specifically, they used OEMS to track the consumption of $^{13}CO_2$ during cycling. Alternatively, Solchenbach et al. introduced lithium oxalate as an electrolyte additive, which is oxidized to CO_2 in the first charge cycle, and demonstrated the effect on the SEI formation while using OEMS to verify a 1 e^-/CO_2 conversion [79].

Solchenbach et al. also studied the effect that cathode transition metal leaching has on the SEI by adding either $Ni(TFSI)_2$ or $Mn(TFSI)_2$ to the electrolyte and monitoring the C_2H_4 signal. They observed a larger evolution in the case of Ni and a larger and continuous evolution over multiple cycles in the case of Mn [80]. However, by preforming the SEI, the additional gassing could be strongly suppressed. By switching to DMC, which does not release C_2H_4, after preforming the anode and then still detecting C_2H_4 evolution in the presence of Mn, the authors were able to conclude that Mn^0 species can catalytically reduce LEDC to Li_2CO_3 and C_2H_4, leading to a carbonate-rich SEI.

Regarding beneficial additives, Tezel et al. showed reduced CO_2 and H_2 evolution during SEI formation by tris(hexafluoroisopropyl)borate [81]. A systematic study of phosphate additives has been presented by Zhao et al. They found via DEMS that the unsaturated compounds, especially the alkyne-containing ones, greatly suppress gas evolution both at the cathode and anode, with thinner and more uniform CEI and SEI, respectively [49].

Although the reactivity of $LiPF_6$, especially toward acid protons and hydrolysis, has already been mentioned earlier, some more observations shall be summarized here. As demonstrated by Solchenbach et al. and Guéguen et al., protic (electrolyte) oxidation products can already trigger decomposition, resulting in the formation of PF_5, which is detected as POF_3 owing to high reactivity with moisture [82, 83]. Bolli et al. demonstrated that tris(trimethylsilyl)phosphate (TMSPa) not only serves as

Journal of MATERIALS RESEARCH

Invited Feature Paper-Review

chemical scavenger for HF and LiF, but that the product of this reaction, Me_3SiF, can be detected by OEMS ($m/z = 77$) and therefore is suited as an *operando* probe for fluoride formation in batteries [84]. They were able to study the formation of LiF from FEC and the proton release by electrolyte oxidation at the cathode side and subsequent $LiPF_6$ decomposition. They also demonstrated the presence of HF in a cell free of fluorinated compounds except for polyvinylidene fluoride (PVDF), proving that the binder is indeed dehydrofluorinated under operating conditions. Guéguen et al. added the similar component tris(trimethylsilyl)phosphite (TMSPi) in a follow-up study comparing TMSPa and TMSPi, demonstrating that both additives mainly work as acid scavengers [85]. Protons and protic side products lead to H_2 evolution at the anode due to electrochemical cross-talk, which Metzger et al. revealed by employing a sealed diffusion barrier between cathode and anode [86].

Other anode materials for LIBs, such as Li_3VO_4 [87], $TiNb_2O_7$ [88], Si in carbon shells [89], and NbO_2/carbon nanohybrids [90], to name a few, have also been investigated regarding their gassing behavior, typically to examine the stability of the SEI formed on these electrodes.

Lithium-rich cathode-active materials

A good introduction to the history and development of Li-rich CAMs can be found in the literature [4]. The same holds true for the recent progress and future perspectives [3]. Herein, we aim to discuss the role of gas evolution measurements in the characterization and design of these materials.

Layered cathodes

Substituting lithium for transition metals in the respective layer requires compensation for the lower charge of lithium ions compared to the transition metal ions. For this reason, the valence state of the remaining metals is increased, limiting the amount of lithium replacement to 1/3 of the atoms in the transition metal layer, where then all remaining ions are in oxidation state 4+. The resultant structure can be written as $Li[Li_{1/3}M_{2/3}]O_2$ (M = Ni, Mn) or $Li_{1.33}M_{0.67}O_2$ to express the similarity to NCM CAMs, or it can be summarized as Li_2MO_3. Intriguingly, lithium can be electrochemically de-intercalated from these materials, resulting in large specific charge capacities, even though all of the transition metals are in the highest (expected) valence state and cannot be oxidized further for charge compensation. This opens the possibility of anionic redox, i.e., the at best reversible oxidation of oxygen anions to either peroxide or even superoxide species or to molecular oxygen. Rana et al. have shown via DEMS that for Li_2MnO_3 almost all charge current can be attributed to oxidation of lattice oxygen to O_2 ($4\,e^-/O_2$ process) and reversible oxygen redox is negligible, as no corresponding RIXS feature was detected and MS titration experiments revealed minor amounts of peroxides (equivalent to 10 mAh/g) [91]. Because the O_2 released from the lattice is $^1O_2$ [42], CO_2 evolution due to electrolyte oxidation also needs to be considered. Depending on the experimental procedures, either of these two gas species might be predominantly observed, as discussed by Guerrini et al., who also demonstrated that oxygen oxidation/loss is the main contributor to the charge capacity of Li_2MnO_3 [92]. For Li_2NiO_3, Bianchini et al. have shown via DEMS that almost all charge capacity of the CAM is due to O_2 evolution, leaving a rock-salt-type structure behind, which after 100 cycles still delivered about 100 mAh/g [93].

While detailed gas analysis indicates that reversible anion redox cannot be utilized in Li_2MnO_3, a reduced lithium content leads to materials of the form $Li[M_{1-x}Li_{x/3}Mn_{2x/3}]O_2$ (M = Co, Ni, Mn), which can also be written as $xLi_2MnO_3{\cdot}(1-x)LiMO_2$, representing a layered NCM-type CAM with nanoscale domains of Li_2MnO_3 [94]. For $Li_{1.2}Ni_{0.2}Mn_{0.6}O_2$, Armstrong et al. demonstrated already in 2006 that the charge plateau at 4.5 V vs. Li^+/Li is associated with O_2 evolution [95]. For the same material and also for $Li_{1.2}Ni_{0.13}Co_{0.13}Mn_{0.54}O_2$, Luo et al. examined the anion redox in detail, observing only CO_2 evolution at the 4.5 V plateau, with additional O_2 evolution at higher potentials [96, 97]. By enriching the lattice oxygen with ^{18}O, the authors were able to show that the CO_2 (containing $C^{16/18}O_2$) in fact contains lattice oxygen, see Fig. 5(a). These CAMs revealed a stable cycling behavior from the second cycle onward, achieving specific discharge capacities of about 270 mAh/g. Using RIXS, the authors demonstrated the presence of oxidized oxygen in the charged cathodes. At the same time, the electrodes did not show Raman bands representing peroxide species, with the authors concluding that localized electron holes are formed on oxygen

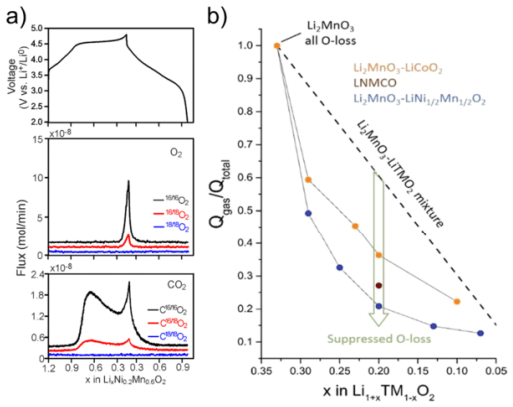

Figure 5: (a) Evidence of lattice oxygen loss from the $Li_{1.2}Ni_{0.2}Mn_{0.6}O_2$ cathode at 4.5 V vs. Li^+/Li during the first cycle. Reproduced with permission from [96]. (b) Substituting Ni and/or Co for Mn decreases the fraction of charge capacity stemming from oxygen loss. Reproduced with permission from [106].

Journal of MATERIALS RESEARCH

Invited Feature Paper-Review

ions coordinated by Mn^{4+} and Li^+. Based on the gas evolution in DEMS, they calculated an oxygen redox contribution of 0.5 e^-/formula unit (~ 157 mAh/g) and of only 0.05 e^-/formula unit (~ 16 mAh/g) by O_2 evolution for $Li_{1.2}Ni_{0.13}Co_{0.13}Mn_{0.54}O_2$.

Bulk transformation of the Li_2MnO_3 domains toward electrochemically active $LiMnO_2$ under lithium extraction and O_2 evolution, referred to as "activation," is often used to explain the behavior of Li-rich CAMs in the first charge cycle. However, the amount of O_2 detected in the aforementioned studies and by Strehle et al. for $Li_{1.17}[Ni_{0.22}Co_{0.12}Mn_{0.66}]_{0.83}O_2$ [98] is far too low to sustain the assumption of a bulk transformation. Instead, Strehle et al. calculated the thickness of a spinel surface layer based on the quantified gas evolution in OEMS, reaching 2–3 nm, in good agreement with transmission electron microscopy (TEM) observations. Teufl et al. analyzed the gas evolution of $xLi_2MnO_3 \cdot (1-x)LiMO_2$ compositions with varying x. They found significant increases in oxygen evolution and spinel surface layer thickness with increasing x, starting to also observe bulk spinel formation at $x = 0.5$ [99]. The authors emphasize that for a fair comparison between the different CAMs and also with the corresponding NCM ($x = 0$), the gas evolution has to be normalized to the specific surface area, which was ~ 10 times larger for the Li-rich materials. In contrast to the spinel surface layer formation, Yin et al. reported about a bulk phase transformation by adding a constant voltage charge at 4.8 V vs. Li^+/Li for $Li_{1.2}Ni_{0.13}Mn_{0.54}Co_{0.13}O_2$, upon which they observed strong O_2 evolution and were able to detect the new bulk phase via in situ X-ray diffraction (XRD) [100].

The at least partially unavoidable gas evolution of Li-rich CAMs is a main challenge for commercial application. Recently, Schreiner et al. disclosed the production of multilayer pouch cells using $Li_{1.14}[Ni_{0.26}Co_{0.14}Mn_{0.60}]_{0.86}O_2$ on a pilot scale production line [101]. Via OEMS, they found that a formation step at 45 °C instead of 25 °C allows to concentrate most gas evolution into the initial cycle.

Multiple structural modifications and protection strategies have been reported to suppress the gas evolution of Li-rich CAMs. Cao et al. demonstrated that the preparation via chemical ion exchange from the Na-containing precursor results in less O_2 loss compared to the preparation via electrochemical ion exchange [102]. Following a similar approach, Cao et al. obtained both a Li-deficient (in the lithium layer) and Li-rich (in the transition metal layer) CAM $Li_{0.8}[Li_{0.2}Mn_{0.8}]O_2$, for which they quantified the irreversible O_2 loss via DEMS and observed an increasing peroxide character during charge [103].

The role of Ni and Co bulk doping in stabilizing Li-rich and Mn-rich CAMs has been examined by multiple groups. Shen et al. gradually replaced Ni by Co, starting from $Li_{1.13}Ni_{0.275}Mn_{0.58}O_2$. With increasing Co content, they observed a strong increase in O_2 evolution via OEMS (also leading to increased spinel layer formation), which was barely detectable against the background signal in the Co-free material [104]. However, it should be noted that at the same time, the CO_2 evolution rates decreased and the authors did not provide a comparative quantification of the total gas amounts released, thus leaving the contribution of chemical electrolyte oxidation unattributed. A similar observation of reduced gas evolution and spinel formation has been made by Huang et al. for Mn-rich NCM CAMs [105]. Boivin et al. compared the irreversible charge capacities resulting from gas evolution after doping Li_2MnO_3 with Ni and/or Co and observed reduced gassing for both dopants, yet with Ni having a more pronounced effect, see Fig. 5(b) [106]. The authors showed that unlike Co, Ni doping leads to a Ni-rich, Li-poor rock-salt-type shell, mitigating surface degradation due to gas evolution. Zhang et al. found that Zr doping of $Li_{1.21}Ni_{0.28}Mn_{0.51}O_2$ leads to the formation of Li_2ZrO_3 slabs in the structure, affecting the oxygen redox by reducing the formation of O_2 versus electron holes localized on the oxygen anions [107]. Shin et al. performed a computational screening of dopants regarding their effectiveness in increasing oxygen retention, confirming experimentally that 2% Ta-doped $Li_{1.3}Nb_{0.3}Mn_{0.4}O_2$ shows surface enrichment effects and a substantially reduced O_2 evolution [108]. Increased surface carbonate content, as confirmed by acid titration experiments, explained the larger CO_2 evolution for the doped CAM, again highlighting the importance of surface carbonates for correct interpretation of in situ gas analysis results.

Wang et al. reported that the lattice oxygen release from $Li_{1.2}Ni_{0.27}Mn_{0.53}O_2$ was reduced by anion doping with chlorine ($Li_{1.2}Ni_{0.27}Mn_{0.53}O_{1.976}Cl_{0.024}$), finding both lower O_2 and CO_2 evolution [109]. As early as 2008, Zheng et al. demonstrated via DEMS that by coating $Li_{1.2}Ni_{0.2}Mn_{0.6}O_2$ with AlF_3, the ratio between the released gasses changes, with mostly O_2 evolving from coated CAM and CO_2 from pristine CAM [110]. A decade before the experimental detection of $^1O_2$, the authors already proposed that the oxygen may become less reactive while passing through the coating. Li et al. presented a three-in-one strategy, consisting of a Na_2SiO_3 coating with concurrent Na and Si doping, for which they showed reduced O_2 evolution via DEMS. However, they did not report the CO_2 evolution profiles, thus hindering a quantitative comparison (including chemical oxidation of electrolyte) [111]. With a similar Na_5AlO_4 coating, Maiti et al. achieved suppressed gas evolution for Li-rich NCM up to 4.65 V vs. Li^+/Li. A strong increase in O_2 release was observed at higher potentials and explained by the decomposition of the coating, resulting in Na_2O_2 formation among others [112]. Gim et al. further reported the lack of O_2 detection by coating of Li-rich CAM (40 nm thickness) using $CoPO_4$ nanoparticles, albeit not discussing CO_2 evolution [32]. Organometallic reagents like those used in atomic layer deposition (ALD) have been found by Evenstein et al. and Rosy et al. to alter the free surface of Li-rich CAMs by forming a layer of reduced transition metal oxide and

Journal of MATERIALS RESEARCH

Invited Feature Paper-Review

metal species from the reagent, a process they refer to as atomic surface reduction [113, 114]. For both diethylzinc- and trimethylaluminum-treated Li-rich NCM, they observed reduced O_2 and CO_2 evolution rates. Sun et al. studied a thin lithium polyacrylate coating, for which reduced CO_2 evolution, yet no change in O_2 evolution, was observed at high potentials, thus indicating a beneficial effect mostly against electrochemical electrolyte oxidation, supported by the finding of reduced CO_2 and POF_3 evolution with glassy carbon electrodes [115].

With the inherent O_2 release of Li-rich CAMs during the first charge cycle and the high working potential of these materials, the stability of electrolytes against oxidation is of great importance. By comparing the CO_2 evolution for EC and FEC both on carbon black and NCM622 electrodes, Teufl et al. demonstrated that both electrolytes show a similar stability against electrochemical oxidation, while EC is more readily chemically oxidized by lattice oxygen [116]. Consequently, when using preactivated CAM, the performance in EC is greatly improved.

Wu et al. were able to demonstrate that with the ionic liquid electrolyte N-butyl-N-methylpyrrolidinium bis(fluorosulfonyl) imide a stable CEI is formed on $Li_{1.2}Ni_{0.2}Mn_{0.6}O_2$, leading to reduced gas evolution and rock-salt-type phase formation [117]. Han et al. investigated the working mechanism of lithium fluoromalonato(difluoro)borate as electrolyte additive, also observing the formation of a stable CEI. Using DEMS, they showed that after the initial decarboxylation of the additive, reduced O_2 evolution is achieved [118].

Li-rich layered oxides are not necessarily based on Mn. Xu et al. found that the replacement of 3d Mn by 4d Ru in $Li_{1.2}Ni_{0.2}M_{0.6}O_2$ (M = Mn, Ru) leads to lower irreversible charge capacity and the absence of severe evolution of both O_2 and CO_2, even after increasing the potential to 5 V vs. Li^+/Li [119]. A RIXS feature indicating anion redox was only present for $Li_{1.2}Ni_{0.2}Mn_{0.6}O_2$, while in situ XAS revealed reversible cation redox of Ru in $Li_{1.2}Ni_{0.2}Ru_{0.6}O_2$. Yu et al. probed the oxygen redox of Li_2RuO_3, demonstrating O–O coupling through extensive synchrotron characterizations, and used DEMS to quantify the oxygen loss during the first charge. The observed reduction of Ru at high potentials cannot be explained by oxygen loss alone, thus anion redox must be present [120]. In a follow-up study, Yu et al. examined the effect that Ru substitution in Li_2RuO_3 (by Ti, Cr, Mn, Fe, Ru, Sn, Ir, and Pt) has on the reversibility of oxygen redox, which they quantified from integration of dq/dV and DEMS curves, see Fig. 6 [121]. The irreversibility increased with the ionic character of the substituents, an observation explained by increased distortion of the M–O octahedra, enabling easier O–O dimer formation. Ning et al. demonstrated that O–O dimerization is suppressed in intralayer-disordered Li_2RuO_3, which they prepared via ion exchange from Na_2RuO_3 [122]. In contrast to common Li_2RuO_3, where cations in the intralayer show the so-called honeycomb arrangement, no O_2 and less CO_2 were detected for the disordered material.

McCalla et al. synthesized the model compounds Li_4FeTeO_6 (specifically $Li_{4.27}Fe_{0.57}TeO_6$) and Li_4FeSbO_6 for the detailed study of anion redox and O_2 release [123, 124]. For the former, they found via DEMS that nearly all charge capacity is reflected in O_2 evolution. For the latter, Fe oxidation and O oxidation upon charge (4.2 V plateau) have been observed, with incomplete reduction of the oxygenated species during discharge. However, when the material was charged beyond the plateau,

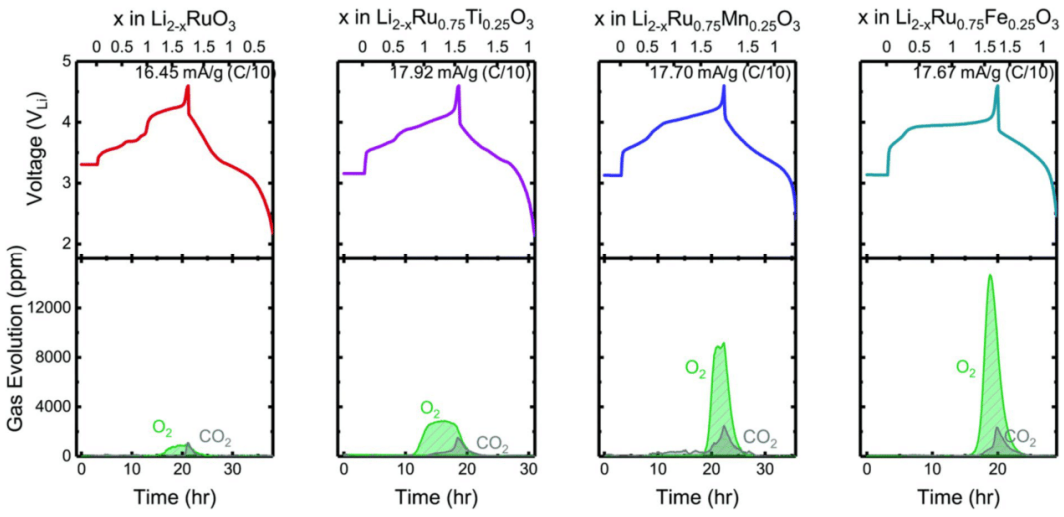

Figure 6: The effect of transition metal substitution on gas evolution of $Li_2Ru_{0.75}M_{0.25}O_3$ (M = Ru, Ti, Mn, Fe). Adapted with permission from [121].

Journal of MATERIALS RESEARCH

Invited Feature Paper-Review

strong CO_2 and O_2 evolution occurred. At 5 V, Fe was found to be reduced again, accompanied by O_2 evolution. Ting et al. confirmed the existence of such a reductive couple (Fe and oxygenated species), with oxygen redox also for the Ni-containing equivalents Li_4NiTeO_6 and $Li_{1.15}Ni_{0.47}Sb_{0.38}O_2$, yet limited to the surface of the materials [125]. While observing O_2 evolution via OEMS, the outgassing was much smaller for the latter materials than the Fe-containing ones.

Jaquet et al. studied the anion redox and gas evolution of layered CAMs of composition $Li_3Ru_yIr_{1-y}O_4$ and reported reduced gassing for the Ir-free Li_3RuO_4. For Li_3RuO_4, they found a new degradation mechanism, namely, the dissolution of RuO_4/RuO_4^-, oxidizing the electrolyte and forming CO_2 and solid RuO_x [126]. The presence of Ir can suppress the dissolution. However, in this case, increased gas evolution has been detected.

Li_3RuO_4 has a rock-salt structure and can either possess Li-only layers alternating with Li/Ru layers or show a random arrangement of Li and Ru, with the former structure being referred to as ordered and the latter as disordered rock-salt (DRX). Li et al. reported similar gas evolution in the initial charge cycle for both polymorphs [127]. In a recent study, Li et al. demonstrated that $Li_{1.2}Ni_{0.4}Ru_{0.4}O_2$ can be prepared with intergrown layered and DRX phases, exhibiting anion redox with minimal O_2 evolution, thus combining the benefits of both layered and DRX materials [128].

Disordered rock-salt cathodes

While the formation of a rock-salt-type surface layer in NCM CAMs is detrimental, in DRX materials, the percolation of the so-called 0-TM diffusion channels, in which the tetrahedrally coordinated (activated) lithium site is not neighbored by a transition metal ion, can lead to high and SOC-independent Li mobility, as demonstrated by Lee et al. [129]. A main benefit of cation disorder is the much lower and isotropic volume change of the CAM upon battery operation. For a detailed review of mechanisms, possibilities and constraints of DRX materials, the reader is again referred to the literature [5]. DRX materials require a certain amount of Li excess to enable 0-TM percolation, and like layered Li-rich CAMs therefore show limited capacity by transition metal redox. They rely on anion redox to achieve high specific capacities, with the risk of showing substantial O_2 evolution. As an example, Cambaz et al. observed via DEMS that O_2 evolution only occurs in the Li-rich DRX $Li_{1.2}Ni_{1/3}Ti_{1/3}W_{2/15}O_2$, but not in stoichiometric $LiNi_{0.5}Ti_{0.5}O_2$ [130]. No longer constrained by the requirements of a layered structure, the partial replacement of oxygen by fluorine has been shown to suppress the evolution of O_2, while the lower valence of fluoride ions allows for an increase in the redox-active transition metal content, as demonstrated by Lee et al. in a comparison of $Li_{1.15}Ni_{0.375}Ti_{0.375}Mo_{0.1}O_2$ and $Li_{1.15}Ni_{0.45}Ti_{0.3}Mo_{0.1}O_{1.85}F_{0.15}$ [131]. Not only Ni, but also both Mn redox couples (Mn^{2+}/Mn^{4+} and Mn^{3+}/Mn^{4+}) can be utilized in DRX cathodes, where again fluorination reduced the O_2 evolution [132–135]. Combining DEMS and the titration of peroxide-like species and carbonates, Crafton et al. examined the effect of fluorination by comparing $Li_{1.2}Mn_{0.6}Nb_{0.2}O_2$ (LMNO) and $Li_{1.2}Mn_{0.625}Nb_{0.175}O_{1.95}F_{0.05}$ (LMNOF) [136]. They found reduced and delayed O_2 evolution, see Fig. 7(a), and were able to show that the contribution of anion redox as a whole is reduced by fluorination, as the fraction of redox-active cations with lower initial oxidation number is increased. Using TMSPa as a probe (evolution of gaseous Me_3SiF), the authors also showed that fluorinated cathodes suffer from fluoride dissolution near the end of charge over multiple cycles. Sathish et al. demonstrated that soaking the same CAM in electrolyte leads to the removal of Li and F, thereby increasing the material's capacity retention and suppressing O_2 evolution, similar to the already discussed acid washing steps [137].

Huang et al. recently showed that DEMS and related acid titration methods in combination with ^{18}O enrichment can be used to deconvolute the redox processes in $Li_{1.15}Ni_{0.45}Ti_{0.3}Mo_{0.1}O_{1.85}F_{0.15}$. During acid titration, oxidized

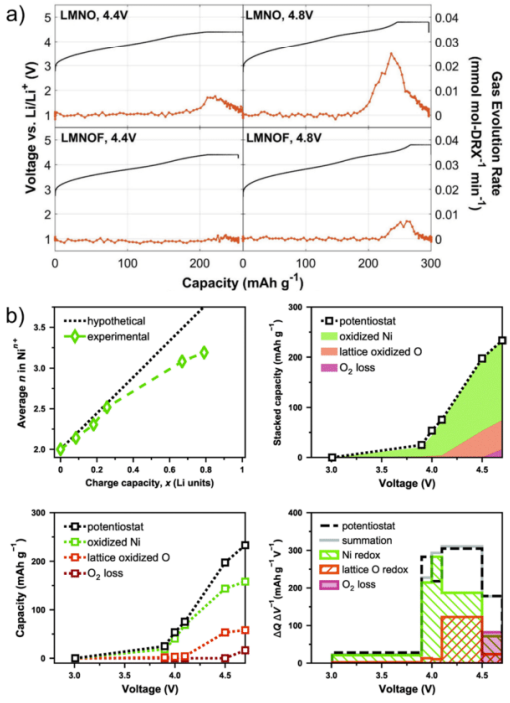

Figure 7: (a) Reduced oxygen evolution upon fluorination of LMNO. Adapted with permission from [136]. (b) Electrochemical contributions determined by combining isotope labeling, DEMS and acid titration measurements. Adapted with permission from [138].

Journal of MATERIALS RESEARCH

Invited Feature Paper-Review

lattice oxygen (the contribution of anion redox) is released as (^{18}O-enriched) O_2 according to Eq. (3), while at the same time the CAM is dissolved and both Ni^{3+} and Ni^{4+} (the contribution of cation redox) oxidize H_2O, leading to O_2 evolution without isotope enrichment. This way, the relative contributions can be calculated from the observed isotope ratio, see Fig. 7(b) [138]. Consequences of a large reliance on anion redox have been demonstrated by Kan et al. for single-crystalline $Li_{1.3}Nb_{0.3}Mn_{0.4}O_2$, where the authors reported not only gas evolution, but also volume changes leading to particle fracture [139].

The choice of the redox-active transition metal and its effect on the anion redox and electrochemical properties have been analyzed by Jaquet et al. by comparing $Li_{1.3}Ni_{0.27}Ta_{0.43}O_2$ and $Li_{1.3}Mn_{0.4}Ta_{0.3}O_2$ [140]. They found that the Ni-containing CAM exhibits a large voltage hysteresis and increased gas evolution coinciding with partial Ni reduction, which the authors both attributed to a smaller charge-transfer band gap (supported by DFT calculations).

To stabilize DRX structures, redox-inactive (in the given voltage range) d^0 metal ions, such as Ti^{4+} and Nb^{5+}, are often required [141]. While being redox-inactive, they still affect the anion redox, as demonstrated for $Li_{1.3}M_{0.3}Mn_{0.4}O_2$ (M = Nb, Ti) by Chen et al. [142]. For Nb, the authors found increased O_2 evolution and a larger capacity contribution of anion redox in the initial cycles, while Ti stabilized oxidized oxygen species, thereby increasing the reversibility of anion redox and leading to a lower O_2 evolution and reduced CAM degradation. By comparing RIXS data of cycled electrodes, the authors also demonstrated that anion redox features decrease stronger for Nb than Ti. Yue et al. found that the introduction of Mo into $Li_{1.15}Ni_{0.35}Ti_{0.5}O_{1.85}F_{0.15}$ (yielding $Li_{1.15}Ni_{0.45}Ti_{0.3}Mo_{0.1}O_{1.85}F_{0.15}$) results in a lower voltage hysteresis after migration of Mo into the tetrahedral sites, yet with increased O_2 evolution [143]. Cambaz et al. observed via DEMS and X-ray photoelectron spectroscopy (XPS) that concurrent with O_2 evolution from $Li_{1.2}Ni_{1/3}Ti_{1/3}Mo_{2/15}O_2$, partial reduction of Mo^{6+} to Mo^{4+} is occurring at the particle surface, indicating a reductive couple and formation of a densified surface layer [144].

Finally, the introduction of configurational entropy (high-entropy concept) into DRX materials and their gas evolution behavior have been reported by Breitung et al. and Lun et al. [145, 146]. Lun et al. found improved energy density and better rate capability for high-entropy $Li_{1.3}Co_{0.1}Cr_{0.1}Mn_{0.2}Nb_{0.2}Ti_{0.1}O_{1.7}F_{0.3}$ compared to low-entropy $Li_{1.3}Mn_{0.4}Ti_{0.3}O_{1.7}F_{0.3}$. However, the former material showed stronger CO_2 evolution, which the authors attributed to increased interfacial side reactions with the electrolyte.

In summary, in situ gas analysis has proven indispensable in the study of Li-rich CAMs both with layered and DRX structures, as it can provide quantitative information on the irreversibility and extent of anion redox, a key feature of these electrode materials.

Solid-state batteries

On the one hand, the gas analysis of SSBs is simplified by the lack of continuous liquid electrolyte degradation and accompanied electrolyte fragment detection. On the other hand, the assembly of a test cell is complicated by the fact that most SSBs are cycled under external pressure to assure proper contacting and conductivity. Bartsch et al. first reported about DEMS measurements on SSBs with Li_3PS_4 as SE in 2018, utilizing pellets of NCM622 CAM, SE separator and In anode, as well as a rather robust cell housing [58]. They attributed the H_2 evolution to the initial reduction of trace H_2O, while both CO_2 and O_2 were detected clearly in the charge cycle. The only possible source for CO_2 in this configuration were residual carbonates, as proven by ^{13}C-labeling experiments. The authors observed minor amounts of CO_2 compared to the overall carbonate content, presumably due to the lack of acid protons. O_2 evolved from the NCM lattice at high SOC and from the electrochemical carbonate decomposition, as discussed previously. Oxidation of the SE by the reactive oxygen has been observed, leading to traces of SO_2 being detected. In later studies, the same group examined the effect of Li_2CO_3, Li_2CO_3/$LiNbO_3$ (with Li_3PS_4 as SE) [147], Li_2CO_3/Li_2ZrO_3 (with argyrodite Li_6PS_5Cl as SE) [148], and more complex nanoparticle coatings [149] on NCM CAMs on the gas evolution, observing that a Li_2CO_3 coating alone leads to increased CO_2 release as expected, but in a dual coating, the CO_2 evolution is greatly reduced and minor or no SO_2 is detected. From this observation, DEMS allowed for the conclusion of a uniform (hybrid) coating structure, as opposed to areas in which only the carbonate is present. Li_2ZrO_3 prevented the formation of SO_2, even when the coated CAM was annealed in air (note that in this case the carbonate content and CO_2 evolution were larger than for the uncoated material). Extending the scope of CAMs to LNO, CO_2 has only been detected in the initial cycle, while the release of lattice O_2 continued at high potentials during the second cycle [150]. In all aforementioned studies, H_2 and CO_2 have been detected at the onset of charge (first cycle). In a liquid cell, such gassing behavior would be attributed to organic carbonates reacting at the anode side, which does not apply to SSBs. Because the H_2 evolution is explained by the reduction of trace H_2O in the cell, the authors assume a correlation between H_2 and CO_2 evolution.

Major challenges of SSBs are the variation in performance and lack of scalability for pellet-stack cells. Tape-cast electrodes can alleviate these issues while requiring the development of slurry recipes and the use of polymer binders. Teo et al. studied the binder choice for SSB cathodes containing NCM622 CAM, Li_3PS_4 SE, conductive carbon, and one of three binders using

Journal of MATERIALS RESEARCH

Invited Feature Paper-Review

a design of experiments (DOE)-guided approach [151]. The binders tested were polyisobutene (OPN), poly(styrene-co-butadiene) rubber (SBR) and hydrogenated nitrile butadiene rubber (hNBR) having different functional groups on the polymer chain. Using DEMS, the influence of the binder choice has been investigated, initially revealing a distinct double peak in CO_2 evolution, not observed in previous SSB studies, indicating that in addition to carbonate gassing also binder oxidation occurs. OPN-based cathodes showing the best performance overall revealed the most pronounced gas evolution (O_2, CO_2, and SO_2), which seems counterintuitive, but was explained by the higher SOC achieved with this binder. Using $LiNbO_3$-coated NCM622 instead, a comparison of OPN- and SBR-based cathodes at similar SOC was possible, see Fig. 8(a). In this case, a

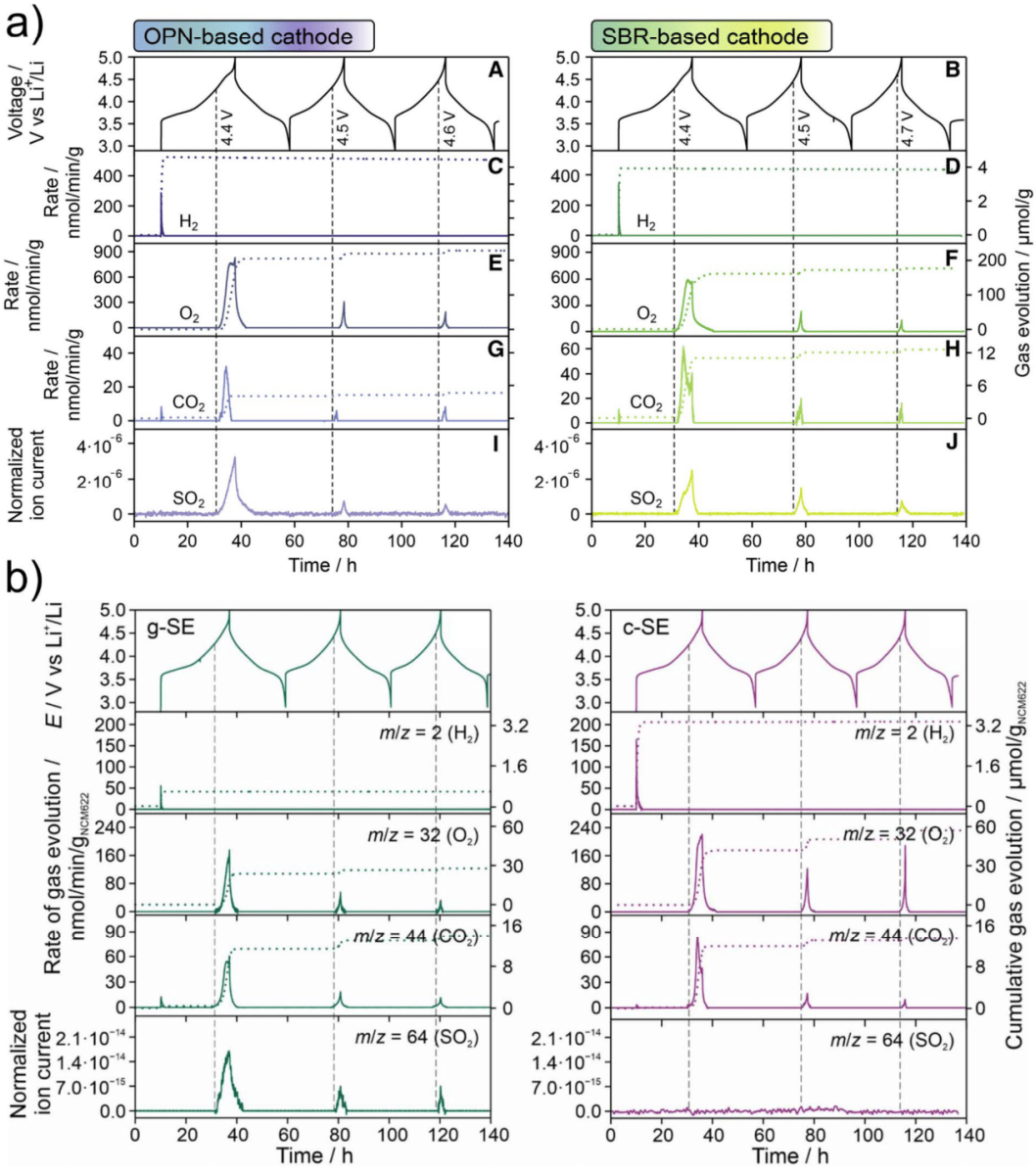

Figure 8: Gas evolution comparisons between (a) OPN and SBR polymer binders for tape-cast SSB electrodes and (b) glassy and crystalline SEs. Adapted with permissions from [151, 154].

Journal of MATERIALS RESEARCH

Invited Feature Paper-Review

larger O_2 evolution was found for OPN, but a more distinct double peak and cumulative amount of CO_2 for SBR, demonstrating that SBR is more readily oxidized than OPN.

For an SSB, the properties of the SE have a profound effect on the cell characteristics. For this reason, the influence of SEs on the gas evolution has been studied by various groups. In an OEMS comparison of a solid polymer electrolyte (SPE) based on trimethylene carbonate units with liquid organic carbonates containing LiTFSI as supporting salt, Sångeland et al. noted that during reduction, the SPE releases CO_2, while the liquid electrolyte releases C_2H_4 [152]. The formation of CO_2 has been explained by the presence of trace H_2O, forming H_2 and OH^- ions upon reduction, the latter leading to hydrolysis with subsequent decarboxylation of the electrolyte. At the cathode side, both electrolytes degrade under evolution of CO_2 and H_2 (formed at the anode from protic degradation species) and, interestingly, SO_2 originating from the decomposition of TFSI upon radical attack, due to the weak N–S bond.

Strauss et al. reported a quantitative comparison of the gas evolution of ^{13}C-carbonate-labeled NCM622 CAM in combination with two SEs (Li_3PS_4 and Li_6PS_5Cl) and a liquid electrolyte (LP57), noting minor differences in the cumulative amounts of O_2 and CO_2 (virtually only $^{13}CO_2$) between the SEs. However, SO_2 evolution has been observed when using Li_3PS_4 [153]. Because SO_2 was absent for Li_6PS_5Cl, a higher stability of this electrolyte against reactive oxygen and/or formation of only solid degradation products was suggested. In comparison, in liquid electrolyte cells, much larger CO_2 evolution, with more $^{12}CO_2$ from electrolyte oxidation than $^{13}CO_2$, and lower O_2 evolution have been detected, indicating almost complete consumption of the released reactive oxygen. By acid titration after cycling, it was shown that in the SSB cathodes, a larger fraction of $Li_2{}^{13}CO_2$ remained, presumably due to the lack of acid protons and the known issue of inactive (isolated) CAM in SSBs. To ensure comparability of the gas evolution, a similar SOC was targeted by restricting the specific charge capacity of the liquid electrolyte cells to 240 mAh/g, resulting in a lower upper cutoff potential.

Teo et al. compared the crystalline SE Li_6PS_5Cl with the glassy SE $1.5Li_2S$-$0.5P_2S_5$-LiI via DEMS among others (in slurry-cast cathodes with $LiNbO_3$-coated NCM622). They observed relatively more O_2, but no SO_2 evolution in the former and less O_2, but also SO_2 evolution in the latter, see Fig. 8(b) [154]. This finding is well explainable by the consumption of oxygen for the formation of SO_2 and supported by the observation of oxygenated sulfur and phosphorus species via XPS and time-of-flight secondary ion mass spectrometry (ToF–SIMS). However, although more SE degradation has been observed, the electrochemical performance of SSB cells using the glassy SE was better, indicating that a stable and ion-conducting layer of degradation products with good contact to the CAM particles forms and the increased SO_2 evolution is a side effect of tight contact between CAM and SE.

The decomposition of SE, in this case based on polyethylene oxide (PEO), has also been studied by Nie et al. [155]. They found that while PEO itself only starts to decompose via dehydrogenation and formation of protonated TFSI (HTFSI) at 4.5 V vs. Li^+/Li, in the presence of LCO, this reaction can occur at potentials as low as 4.2 V vs. Li^+/Li, due to undercoordinated surface oxygen of LCO, a problem solved via coating the cathode with $Li_{1.4}Al_{0.4}Ti_{1.6}(PO_4)_3$. Seidl et al. identified methanol and 2-methoxyethanol as degradation products of HTFSI formation, but observed limited capability for the determination of onset voltages due to low sampling rate [156]. Li et al. prepared a sandwich composite polymer SE, consisting of reduction-resistant PEO and oxidation-resistant polyacrylonitrile with a PVDF layer in between, each containing $Li_{3x}La_{2/3-x}TiO_3$ fibers. Using DEMS, they showed that while the individual layers alone degrade under gas generation in an NCM811|SE|Li cell, no gas evolution is detected for the sandwich composite [157]. However, the authors reported only the evolution rates of C_2H_2, C_2H_4, C_2H_6, and H_2 and did not include CO_2.

Lastly, the gassing behavior of garnet SEs has also been investigated. Delluva et al. demonstrated that $Li_7La_3Zr_2O_{12}$ (LLZO) will release CO_2 and O_2 at potentials above 3.8 V vs. Li^+/Li, as expected for the electrochemical oxidation of Li_2CO_3 impurities, not only in an $LiMn_2O_4$|LLZO|Li cell, but also in an Au|LLZO|Li cell, ruling out CAM contributions to the gas evolution [158]. The authors concluded that at the cathode|SE interface, Li_2CO_3 impurities of the SE are oxidized, with the resulting gas release leading to delamination, thus highlighting the need for fast and carbonate-free processing of LLZO. For the related $Li_{6.4}La_3Zr_{1.4}Ta_{0.6}O_{12}$, Yang et al. have shown that by coating the garnet SE with a thin layer of LCO, surface contamination is suppressed and stability against Li_2CO_3 formation in air is achieved [159].

In summary, the (out)gassing tendency of CAMs is similar for liquid- and solid-electrolyte-based cells. However, because many follow-up reactions are occurring at the interface to the electrolyte, SSBs have unique features that allow for an advanced characterization of SE and said interface.

Sodium-ion batteries

Driven by the scarcity of lithium and relative abundance of sodium, many efforts are made to introduce SIBs as a cheaper and more sustainable or complementary alternative to LIBs [160], mostly in the field of stationary energy storage [9]. Among the existing CAMs, layered oxides of either P2 or O3 structure, differing in the coordination and amount of Na per formula unit, show the largest resemblance to LIB cathodes. Apart from that, polyanionic cathodes, foremost $Na_3V_2(PO_4)_2F_3$

Journal of MATERIALS RESEARCH

Invited Feature Paper-Review

(NVPF) and Prussian blue analogs (PBAs), also hold promise for application in SIBs [8]. Herein, the outgassing of all three material families is reviewed as well the application of gas evolution measurements to study the SEI formation on different anode materials.

A systematic OEMS study of SIBs has been presented recently by Zhang et al., including screening of common electrolyte solvents (EC, DMC, PC) and a comparison of the CAMs NVPF (polyanionic and showing biphasic behavior), $NaNi_{0.45}Zn_{0.05}Mn_{0.4}Ti_{0.1}O_2$ (NNZMTO, layered and showing purely cation redox and solid-solution behavior), and $NaLi_{1/3}Mn_{2/3}O_2$ (NLMO, involving anion redox) [161]. Versus Na metal anodes, they observed recurring strong H_2 evolution at higher potentials with NNZMTO and NVPF cathodes and explained this by the reduction of protic electrolyte degradation products at the anode. A direct comparison of gas evolution rates may be misleading, as the two cathodes were charged to different potentials. Using hard carbon as negative electrode, the H_2 evolution was reduced, probably due to better passivation of the anode. Instead, C_2H_4 was observed as a result of SEI formation. NNZMTO also released CO_2 at high potentials, yet only during the first cycle, thus suggesting surface carbonates as the cause. For NLMO, significant O_2 release at high potentials in the initial cycle has been detected, with evolution of CO_2 also in the subsequent cycles, proving the partial irreversibility of anion redox. It is worth to point out that the authors attempted isotope labeling experiments, but ran into purity issues with the labeled solvents, highlighting another challenge that comes with such experiments.

Starting with P2 cathodes, Maitra et al. demonstrated that $Na_{2/3}Mg_{0.28}Mn_{0.72}O_2$ (NMMO) not only shows oxygen redox without alkali ions in the transition metal layer, but also that no O_2 loss occurs during charge, with the only gas evolution contributions coming from surface carbonates and electrolyte decomposition [162]. In a follow-up study, House et al. compared NMMO with the Li-containing $Na_{0.78}Li_{0.25}Mn_{0.75}O_2$ (NLMO) and found that both materials do not show O_2 loss at 4.5 V vs. Na^+/Na. Utilizing ^{18}O-labeled CAMs under CV charge at 5.0 V, a cell with NMMO only released $C^{16}O_2$ stemming from electrolyte decomposition, while a cell with NLMO also released $^{18}O_2$ as well as $C^{16}O^{18}O$ and $C^{18}O_2$, clearly indicating the irreversible oxygen loss and chemical oxidation of electrolyte, see Fig. 9(a) [163]. However, shortly after, the same group demonstrated via high-resolution RIXS that molecular oxygen formed both in NMMO and NLMO at 4.5 V, but has no way of escaping the solid phase and is reduced again during discharge. Note that a slight change in stoichiometry of NLMO to $Na_{0.6}Li_{0.2}Mn_{0.8}O_2$ led to a ribbon structure instead of a honeycomb structure, thereby preventing the formation of O_2 [164, 165]. This observation emphasizes the rare case that even with good signal-to-noise ratio and low detection limit, the lack of gas detection is necessary but not sufficient to exclude the underlying reaction mechanism.

Zhao et al. observed O_2 evolution during charge to 4.5 V vs. Na^+/Na for NLMO of again slightly different stoichiometry ($Na_{0.66}Li_{0.22}Mn_{0.78}O_2$) and found that partial bulk substitution of O by F, yielding NLMOF ($Na_{0.65}Li_{0.22}Mn_{0.78}O_{1.99}F_{0.01}$), suppresses this O_2 release [166].

Kulka et al. used OEMS to rule out O_2 evolution as a reason for capacity loss in $Na_{0.6}MnO_2$, albeit only at potentials up to 4.0 V vs. Na^+/Na [167]. It is in the nature of the P2 phase that as-synthesized materials are Na-deficient, and a higher degree of sodium intercalation is only achieved during operation. While not a problem in half-cells with near infinite Na supply, the capacity of full cells is thus reduced. Adding sacrificial sodium salts that decompose in the initial cycle to the cathode composite can alleviate this issue. Marelli et al. demonstrated that the addition of sodium rhodizonate ($Na_2C_6O_6$) increases the full cell performance of $Na_{0.67}Mn_{0.5}Fe_{0.5}O_2$ and used OEMS to verify the decomposition to CO_2 (the onset of oxidation was as low as 3.8 V vs. Na^+/Na) [168].

Only recently, CAMs with O3-type structure have been characterized via in situ gas analysis. Wang et al. used OEMS to quantify the first cycle O_2 loss due to anion redox for $NaLi_{1/3}Mn_{2/3}O_2$. From that, they calculated the composition of the charged cathode to be $Na_{0.09}Li_{1/3}Mn_{2/3}O_{1.86}$ while demonstrating the presence of peroxo-like species within the structure via hard XPS (HAXPES) and RIXS [169]. Two other studies have shown that both in $NaMn_{1/3}Fe_{1/3}Ni_{1/3}O_2$ [170] (charged up to 4.6 V vs. Na^+/Na) and in $NaNi_{2/3}Ru_{1/3}O_2$ [171] (charged up to 4.1 V vs. Na^+/Na) no O_2 evolution occurs, although the formation of peroxo-like species has been observed via X-ray absorption near edge spectroscopy (XANES) and XPS.

The DEMS investigation of the high-entropy PBA $Na_x(Fe_{0.2}Mn_{0.2}Ni_{0.2}Cu_{0.2}Co_{0.2})[Fe(CN)_6]_{1-y}$ for SIBs revealed that next to H_2 and CO_2 as expected gasses from crystal water, surface carbonates and electrolyte decomposition, ethanedinitrile [$(CN)_2$, cyanogen] evolves at high potentials, see Fig. 9(b) [172]. Overall, it has been shown clearly that the oxidative dimerization of anions is not limited to oxide CAMs.

In their extended study [161], Zhang et al. observed continuous gassing of linear carbonates in contact with Na metal, suggesting their inability to form a stable SEI. On hard carbon as the standard anode material, more and diffuse gas evolution has been observed for linear carbonates, compared to sharp gas evolution peaks with cyclic carbonates, indicating again a better SEI formation with the latter. H_2 evolution, due to cross-talk via the formation of soluble protic species, is also observed in the SIB systems. Equivalent findings to those in LIBs have been made when discussing the role of electrolyte additives. Both VC and FEC lead to suppressed C_2H_4 evolution, but increased CO_2

Journal of MATERIALS RESEARCH

Invited Feature Paper-Review

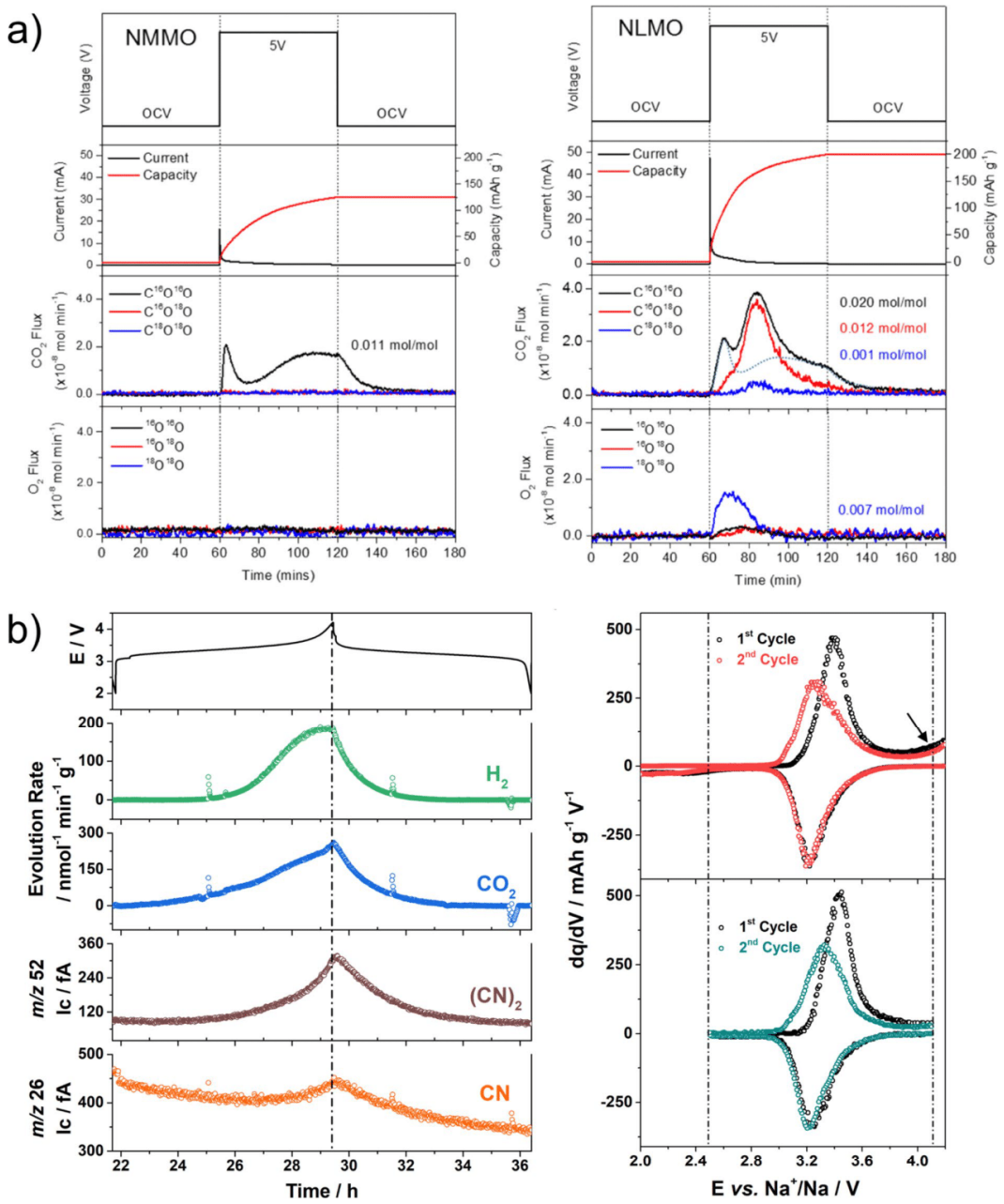

Figure 9: (a) Loss of lattice oxygen in NLMO, but not in NMMO, demonstrated via isotope labeling. Adapted with permission from [163]. (b) Formation of $(CN)_2$ in PBA cathodes indicating that anion oxidation is not limited to lattice oxygen. Adapted with permission from [172].

evolution during SEI formation, while TMSPi reacts with $NaPF_6$ resulting in constant POF_3 release. Sodium difluoro(oxalate) borate was able to suppress most of the gas evolution during SEI formation and cycling.

While graphite cannot reversibly intercalate large amounts of sodium when using standard electrolyte solvents and therefore hard carbon is applied as anode material instead, the use of ether-based electrolytes allows for the highly reversible co-intercalation of solvated sodium [173]. This raises questions

Journal of MATERIALS RESEARCH

Invited Feature Paper-Review

about the nature of the SEI involved. Goktas et al. used OEMS to probe the SEI formation on graphite in diglyme containing 1 M $NaPF_6$ as electrolyte, with the surprising finding that no SEI formation is observed via TEM, and yet gas evolution is restricted to the first cycle only [174]. The gas evolution is explained by the not recurring reaction of graphite surface groups, forming soluble reaction products (rather than an SEI). Hence, graphite in diglyme has been reported as the first SEI-free anode. In a following study, again utilizing OEMS, the authors showed that this observation depends on the conductive salt used. While diglyme containing NaOTf and $NaPF_6$ releases the least gas and forms no SEI on graphite, the use of sodium bis(fluorosulfonyl) imide (NaFSI) or NaTFSI leads to significant gas evolution, SEI formation, and capacity fading, as these salts have been found not to be stable against the anode [175].

Tin (Sn) is an alternative anode candidate in SIBs. However, the low initial Coulombic efficiency and poor cycle life are challenging. Both effects have been shown via DEMS to be caused by excessive gas evolution and poor SEI formation, due to electrolyte decomposition at the relatively higher electrode potential of tin than hard carbon. As found by Liu et al., lowering the potential by mechanically pre-alloying Sn and Na leads to the formation of a stable SEI with less concurrent gas evolution and a drastically improved Coulombic efficiency [176]. Qin et al. demonstrated that the use of glyme electrolytes leads to largely suppressed gas evolution and a more stable, inorganic SEI [177].

In summary, the (out)gassing of SIB electrode materials often shows analogies to their respective LIB counterparts, yet the broader chemistry range considered for application leads to a larger variety of possible reaction mechanisms and evolving gasses.

Challenges and future perspectives

As the search for solutions to improve or replace today's LIB technologies continues, novel and creative ideas are presented and for these, the in situ gas analysis plays an important role in understanding stability, redox activity, and degradation—mostly related to side reactions occurring at electrode interfaces. Thus, it comes as no surprise that more and more research groups develop their own, customized capabilities for in situ gas evolution measurements. After first being applied to understand reaction mechanisms in LIBs in detail, a second spring for gas analysis investigations is now imminent as part of the characterization and evaluation of new battery materials and concepts.

Gas evolution studies on various novel cell chemistries will certainly increase in the near future. First DEMS experiments on potassium-ion batteries have already been reported, showing that the K_xCrO_2 cathode does not undergo O_2 loss during potassium extraction at high potentials, while the evolved CO_2 could be attributed to electrolyte (EC/DEC) decomposition (after proving the absence of carbonates via acid titration) [178]. Similarly, DEMS has been used to probe F_xReO_3 as a host material for fluoride ions, demonstrating that it does not release oxygen upon fluorination and oxidative current is in fact due to operation of the cathode rather than electrolyte decomposition [179]. Beneficial O_2 evolution in the first charge cycle has been reported for the zinc-ion battery cathode material $Ca_2Mn_3O_8$ by Wang et al., allowing for the controlled introduction of performance-enhancing vacancies [180].

In situ gas evolution measurements can, after a comparatively low initial investment [181], be performed on a daily basis in a regular laboratory. However, establishing an experimental setup tailored to the needs not only of today's, but also tomorrow's research remains a challenging task (because of many choices and necessary work in design, manufacture, and assembly of custom-built parts). Apart from that, correct operation, data acquisition, and assignment, also of unusual gassing phenomena or m/z signals, require mental and resource commitment, even more so when involving isotope labeling experiments. It is to hope that academic cooperation and exchange are fostered by the DEMS/OEMS community, working on making gas evolution measurements available to a broader range of researchers.

While the study of gas evolution has been shown to allow for insights into many reaction mechanisms, some conclusions can be drawn too fast, especially when comparing materials, due to the complex interplay of SOC/potential, composition, and surface impurities. Moreover, even mechanisms that seem established in the community, such as the $^1O_2$ evolution during battery operation, can be challenged based on the possibility of side reactions and theoretical considerations [182].

Conclusions

In this review article, recent developments in the field of in situ gas analysis of batteries have been discussed, spanning from instrumentation and state-of-the-art LIBs over Li-rich cathode materials and SIBs to SSBs, emphasizing the versatility of the method and its role in the evaluation of current and next-generation electrode materials. The unique gas detection and quantification capabilities of DEMS/OEMS allow elucidating formation, operation and degradation mechanisms in batteries that cannot be assessed by other in situ techniques. Isotope enrichment has been shown to be a powerful and versatile tool, with which multiple processes evolving the same gas species can be distinguished from one another. Still, reaction mechanisms can be more complex than they initially seem, highlighted by the development in understanding the decomposition of surface carbonate impurities among others. At the same time, the combination of gas analysis with complementary techniques, such as EQCM in the study of SEI formation or RIXS in the

Journal of MATERIALS RESEARCH

Invited Feature Paper-Review

study of anion redox, can help to provide detailed insights into complex phenomena and becomes more relevant as DEMS/OEMS matures.

The increasing number of research groups performing in situ gas evolution measurements demonstrates the method's appeal, and we hope that this article will inspire and encourage readers to include gas analysis in their future work.

Acknowledgments

This work was supported by BASF SE. We thank J. H. Teo for insightful discussion.

Funding

Open Access funding enabled and organized by Projekt DEAL.

Data availability

Data sharing not applicable to this article as no datasets were generated or analyzed during the current study.

Declarations

Conflict of interest The authors declare no conflict of interest.

Open Access

References

1. M. Bianchini, M. Roca-Ayats, P. Hartmann, T. Brezesinski, J. Janek, Angew. Chem. Int. Ed. **58**, 10434–10458 (2019)
2. H.J. Noh, S. Youn, C.S. Yoon, Y.K. Sun, J. Power Sources **233**, 121–130 (2013)
3. X. Ji, Q. Xia, Y. Xu, H. Feng, P. Wang, Q. Tan, J. Power Sources **487**, 229362 (2021)
4. P. Rozier, J.M. Tarascon, J. Electrochem. Soc. **162**, A2490–A2499 (2015)
5. R.J. Clément, Z. Lun, G. Ceder, Energy Environ. Sci. **13**, 345–373 (2020)
6. J. Janek, W.G. Zeier, Nat. Energy **1**, 16141 (2016)
7. C. Li, Z. Wang, Z. He, Y. Li, J. Mao, K. Dai, C. Yan, J. Zheng, Sustain. Mater. Technol. **29**, e00297 (2021)
8. N. Tapia-Ruiz, A.R. Armstrong, H. Alptekin, M.A. Amores, H. Au, J. Barker, R. Boston, W.R. Brant, J.M. Brittain, Y. Chen, M. Chhowalla, Y.S. Choi, S.I.R. Costa, M.C. Ribadeneyra, S.A.M. Dickson, E.I. Eweka, J.D. Forero-Saboya, C.P. Grey, Z. Li, S.F.L. Mertens, R. Mogensen, L. Monconduit, D.M.C. Ould, R.G. Palgrave, P. Poizot, A. Ponrouch, S. Renault, E.M. Reynolds, A. Rudola, R. Sayers, D.O. Scanlon, S. Sen, V.R. Seymour, B. Silv, G.S. Stone, C.I. Thomas, M.M. Titirici, J. Tong, T.J. Wood, D.S. Wright, R. Younesi, J. Phys. Energy **3**, 031503 (2021)
9. K. Chayambuka, G. Mulder, D.L. Danilov, P.H.L. Notten, Adv. Energy Mater. **8**, 1800079 (2018)
10. F. Strauss, D. Kitsche, Y. Ma, J.H. Teo, D. Goonetilleke, J. Janek, M. Bianchini, T. Brezesinski, Adv. Energy Sustain. Res. **2**, 2100004 (2021)
11. Z. Shadike, E. Zhao, Y.N. Zhou, X. Yu, Y. Yang, E. Hu, S. Bak, L. Gu, X.Q. Yang, Adv. Energy Mater. **8**, 1702588 (2018)
12. D. Liu, Z. Shadike, R. Lin, K. Qian, H. Li, K. Li, S. Wang, Q. Yu, M. Liu, S. Ganapathy, X. Qin, Q.H. Yang, M. Wagemaker, F. Kang, X.Q. Yang, B. Li, Adv. Mater. **31**, 1806620 (2019)
13. D. Goonetilleke, J.H. Stansby, N. Sharma, Curr. Opin. Electrochem. **15**, 18–26 (2019)
14. S. Lou, Z. Yu, Q. Liu, H. Wang, M. Chen, J. Wang, Chem **6**, 2199–2218 (2020)
15. A. Schiele, H. Sommer, T. Brezesinski, J. Janek, B.B. Berkes, *Differential Electrochemical Mass Spectrometry in Lithium Battery Research* (Elsevier, Amsterdam, 2018)
16. B. Rowden, N. Garcia-Araez, Energy Rep. **6**, 10–18 (2020)
17. T. Herl, F.M. Matysik, ChemElectroChem **7**, 2498–2512 (2020)
18. H. Baltruschat, J. Am. Soc. Mass Spectrom. **15**, 1693–1706 (2004)
19. R. Imhof, P. Novák, J. Electrochem. Soc. **145**, 1081–1087 (1998)
20. R. Lundström, E.J. Berg, J. Power Sources **485**, 229347 (2021)
21. P. Novák, D. Goers, L. Hardwick, M. Holzapfel, W. Scheifele, J. Ufheil, A. Würsig, J. Power Sources **146**, 15–20 (2005)
22. B.B. Berkes, A. Jozwiuk, H. Sommer, T. Brezesinski, J. Janek, Electrochem. Commun. **60**, 64–69 (2015)
23. Z. Jusys, M. Binder, J. Schnaidt, R.J. Behm, Electrochim. Acta **314**, 188–201 (2019)
24. B.D. McCloskey, D.S. Bethune, R.M. Shelby, G. Girishkumar, A.C. Luntz, J. Phys. Chem. Lett. **2**, 1161–1166 (2011)
25. M. He, L. Boulet-Roblin, P. Borel, C. Tessier, P. Novák, C. Villevieille, E.J. Berg, J. Electrochem. Soc. **163**, A83–A89 (2016)
26. N. Tsiouvaras, S. Meini, I. Buchberger, H.A. Gasteiger, J. Electrochem. Soc. **160**, A471–A477 (2013)

Journal of MATERIALS RESEARCH

Invited Feature Paper-Review

27. M. Metzger, C. Marino, J. Sicklinger, D. Haering, H.A. Gasteiger, J. Electrochem. Soc. **162**, A1123–A1134 (2015)
28. H. Hahn, R. Wagner, F. Schappacher, M. Winter, S. Nowak, J. Electroanal. Chem. **772**, 52–57 (2016)
29. L. Geng, D.L. Wood, S.A. Lewis, R.M. Connatser, M. Li, C.J. Jafta, I. Belharouak, J. Power Sources **466**, 228211 (2020)
30. U. Mattinen, M. Klett, G. Lindbergh, R. Wreland Lindström, J. Power Sources **477**, 228968 (2020)
31. K.N. Shitaw, S.C. Yang, S.K. Jiang, C.J. Huang, N.A. Sahalie, Y. Nikodimos, H.H. Weldeyohannes, C.H. Wang, S.H. Wu, W.N. Su, B.J. Hwang, Adv. Funct. Mater. **31**, 2006951 (2021)
32. J. Gim, J. Song, S. Kim, J. Jo, S. Kim, J. Yoon, D. Kim, S.G. Hong, J.H. Park, V. Mathew, J. Han, S.J. Song, J. Kim, Sci. Rep. **6**, 23394 (2016)
33. J.-P. Schmiegel, M. Leißing, F. Weddeling, F. Horsthemke, J. Reiter, Q. Fan, S. Nowak, M. Winter, T. Placke, J. Electrochem. Soc. **167**, 060516 (2020)
34. F. Horsthemke, M. Leißing, V. Winkler, A. Friesen, L. Ibing, M. Winter, S. Nowak, Electrochim. Acta **338**, 135894 (2020)
35. W. Yin, S. Mariyappan, A. Grimaud, J.M. Tarascon, J. Electrochem. Soc. **165**, A3326–A3333 (2018)
36. R. Jung, M. Metzger, F. Maglia, C. Stinner, H.A. Gasteiger, J. Phys. Chem. Lett. **8**, 4820–4825 (2017)
37. D. Streich, C. Erk, A. Guéguen, P. Müller, F.F. Chesneau, E.J. Berg, J. Phys. Chem. C **121**, 13481–13486 (2017)
38. R. Jung, P. Strobl, F. Maglia, C. Stinner, H.A. Gasteiger, J. Electrochem. Soc. **165**, A2869–A2879 (2018)
39. S. Oswald, D. Pritzl, M. Wetjen, H.A. Gasteiger, J. Electrochem. Soc. **168**, 120501 (2021)
40. S. Oswald, M. Bock, H. Gasteiger, J. Electrochem. Soc. (2022). https://doi.org/10.1149/1945-7111/ac5f7f
41. M. Metzger, P. Walke, S. Solchenbach, G. Salitra, D. Aurbach, H.A. Gasteiger, J. Electrochem. Soc. **167**, 160522 (2020)
42. J. Wandt, A.T.S. Freiberg, A. Ogrodnik, H.A. Gasteiger, Mater. Today **21**, 825–833 (2018)
43. A.T.S. Freiberg, M.K. Roos, J. Wandt, R. de Vivie-Riedle, H.A. Gasteiger, J. Phys. Chem. A **122**, 8828–8839 (2018)
44. N. Laszczynski, S. Solchenbach, H.A. Gasteiger, B.L. Lucht, J. Electrochem. Soc. **166**, A1853–A1859 (2019)
45. L. de Biasi, A. Schiele, M. Roca-Ayats, G. Garcia, T. Brezesinski, P. Hartmann, J. Janek, ChemSusChem **12**, 2240–2250 (2019)
46. N. Li, S. Sallis, J.K. Papp, J. Wei, B.D. McCloskey, W. Yang, W. Tong, ACS Energy Lett. **4**, 2836–2842 (2019)
47. N. Li, S. Sallis, J.K. Papp, B.D. McCloskey, W. Yang, W. Tong, Nano Energy **78**, 105365 (2020)
48. J.K. Papp, N. Li, L.A. Kaufman, A.J. Naylor, R. Younesi, W. Tong, B.D. McCloskey, Electrochim. Acta **368**, 137505 (2021)
49. H. Zhao, Y. Qian, S. Hu, G. Luo, C. Nie, P. Qiu, Y. Kang, H. Wang, Y. Chu, Q. Wang, J. Wang, H. Shao, K. Xu, Y. Deng, ACS Appl. Mater. Interfaces **13**, 29676–29690 (2021)
50. M.S. Milien, H. Beyer, W. Beichel, P. Klose, H.A. Gasteiger, B.L. Lucht, I. Krossing, J. Electrochem. Soc. **165**, A2569–A2576 (2018)
51. D. Weber, Đ. Tripković, K. Kretschmer, M. Bianchini, T. Brezesinski, Eur. J. Inorg. Chem. **2020**, 3117–3130 (2020)
52. S.L. Dreyer, K.R. Kretschmer, Đ. Tripković, A. Mazilkin, R. Chukwu, R. Azmi, P. Hartmann, M. Bianchini, T. Brezesinski, J. Janek, Adv. Mater. Interfaces **9**, 2101100 (2022)
53. L. Eisele, J. Skrotzki, M. Schneider, C. Bolli, C. Erk, T. Ludwig, A. Schaub, P. Novák, I. Krossing, J. Electrochem. Soc. **167**, 120505 (2020)
54. Z. Zhu, D. Yu, Z. Shi, R. Gao, X. Xiao, I. Waluyo, M. Ge, Y. Dong, W. Xue, G. Xu, W.K. Lee, A. Hunt, J. Li, Energy Environ. Sci. **13**, 1865–1878 (2020)
55. S.E. Renfrew, B.D. McCloskey, ACS Appl. Energy Mater. **2**, 3762–3772 (2019)
56. T. Hatsukade, A. Schiele, P. Hartmann, T. Brezesinski, J. Janek, ACS Appl. Mater. Interfaces **10**, 38892–38899 (2018)
57. N. Mahne, S.E. Renfrew, B.D. McCloskey, S.A. Freunberger, Angew. Chem. Int. Ed. **57**, 5529–5533 (2018)
58. T. Bartsch, F. Strauss, T. Hatsukade, A. Schiele, A.-Y. Kim, P. Hartmann, J. Janek, T. Brezesinski, ACS Energy Lett. **3**, 2539–2543 (2018)
59. F. Strauss, S. Payandeh, A. Kondrakov, T. Brezesinski, Mater. Futures **1**, 023501 (2022)
60. A.T.S. Freiberg, J. Sicklinger, S. Solchenbach, H.A. Gasteiger, Electrochim. Acta **346**, 136271 (2020)
61. L.A. Kaufman, B.D. McCloskey, Chem. Mater. **33**, 4170–4176 (2021)
62. S.E. Renfrew, B.D. McCloskey, J. Electrochem. Soc. **166**, A2762–A2768 (2019)
63. G. Houchins, V. Pande, V. Viswanathan, ACS Energy Lett. **5**, 1893–1899 (2020)
64. D. Pritzl, T. Teufl, A.T.S. Freiberg, B. Strehle, J. Sicklinger, H. Sommer, P. Hartmann, H.A. Gasteiger, J. Electrochem. Soc. **166**, A4056–A4066 (2019)
65. S.E. Renfrew, L.A. Kaufman, B.D. McCloskey, ACS Appl. Mater. Interfaces **11**, 34913–34921 (2019)
66. S. Ramakrishnan, B. Park, J. Wu, W. Yang, B.D. McCloskey, J. Am. Chem. Soc. **142**, 8522–8531 (2020)
67. S. Maiti, H. Sclar, Rosy, J. Grinblat, M. Talianker, L. Burstein, M. Noked, B. Markovsky, D. Aurbach, ACS Appl. Mater. Interfaces **12**, 32698–32711 (2020)
68. Q. Li, D. Ning, D. Zhou, K. An, D. Wong, L. Zhang, Z. Chen, G. Schuck, C. Schulz, Z. Xu, G. Schumacher, X. Liu, J. Mater. Chem. A **8**, 7733–7745 (2020)
69. B. Qiu, M. Zhang, L. Wu, J. Wang, Y. Xia, D. Qian, H. Liu, S. Hy, Y. Chen, K. An, Y. Zhu, Z. Liu, Y.S. Meng, Nat. Commun. **7**, 12108 (2016)
70. Q. Luo, Y. Xie, Z. Wu, Q. Xie, D. Yan, H. Zou, W. Yang, S. Chen, ACS Appl. Energy Mater. **4**, 4867–4878 (2021)

Journal of MATERIALS RESEARCH

Invited Feature Paper-Review

71. Z. Zhu, D. Yu, Y. Yang, C. Su, Y. Huang, Y. Dong, I. Waluyo, B. Wang, A. Hunt, X. Yao, J. Lee, W. Xue, J. Li, Nat. Energy **4**, 1049–1058 (2019)
72. M. Metzger, B. Strehle, S. Solchenbach, H.A. Gasteiger, J. Electrochem. Soc. **163**, A1219–A1225 (2016)
73. T. Melin, R. Lundström, E.J. Berg, Adv. Mater. Interfaces **9**, 2101258 (2022)
74. R. Bernhard, M. Metzger, H.A. Gasteiger, J. Electrochem. Soc. **162**, A1984–A1989 (2015)
75. P.G. Kitz, P. Novák, E.J. Berg, ACS Appl. Mater. Interfaces **12**, 15934–15942 (2020)
76. N. Mozhzhukhina, E. Flores, R. Lundström, V. Nyström, P.G. Kitz, K. Edström, E.J. Berg, J. Phys. Chem. Lett. **11**, 4119–4123 (2020)
77. K.U. Schwenke, S. Solchenbach, J. Demeaux, B.L. Lucht, H.A. Gasteiger, J. Electrochem. Soc. **166**, A2035–A2047 (2019)
78. P.G. Kitz, M.J. Lacey, P. Novák, E.J. Berg, J. Power Sources **477**, 228567 (2020)
79. S. Solchenbach, M. Wetjen, D. Pritzl, K.U. Schwenke, H.A. Gasteiger, J. Electrochem. Soc. **165**, A512–A524 (2018)
80. S. Solchenbach, G. Hong, A.T.S. Freiberg, R. Jung, H.A. Gasteiger, J. Electrochem. Soc. **165**, A3304–A3312 (2018)
81. A.O. Tezel, D.K. Streich, A. Guéguen, M. Hahlin, S. Sunde, K. Edström, P. Novák, A.M. Svensson, J. Electrochem. Soc. **167**, 130504 (2020)
82. S. Solchenbach, M. Metzger, M. Egawa, H. Beyer, H.A. Gasteiger, J. Electrochem. Soc. **165**, A3022–A3028 (2018)
83. A. Guéguen, D. Streich, M. He, M. Mendez, F.F. Chesneau, P. Novák, E.J. Berg, J. Electrochem. Soc. **163**, A1095–A1100 (2016)
84. C. Bolli, A. Guéguen, M.A. Mendez, E.J. Berg, Chem. Mater. **31**, 1258–1267 (2019)
85. A. Guéguen, C. Bolli, M.A. Mendez, E.J. Berg, ACS Appl. Energy Mater. **3**, 290–299 (2020)
86. M. Metzger, B. Strehle, S. Solchenbach, H.A. Gasteiger, J. Electrochem. Soc. **163**, A798–A809 (2016)
87. R. Asakura, C. Bolli, P. Novák, R. Robert, ChemElectroChem **7**, 2033–2041 (2020)
88. D. Parikh, L. Geng, H. Lyu, C.J. Jafta, H. Liu, H.M. Meyer, J. Chen, X.G. Sun, S. Dai, J. Li, ACS Appl. Mater. Interfaces **13**, 55145–55155 (2021)
89. A. Schiele, B. Breitung, A. Mazilkin, S. Schweidler, J. Janek, S. Gumbel, S. Fleischmann, E. Burakowska-Meise, H. Sommer, T. Brezesinski, ACS Omega **3**, 16706–16713 (2018)
90. Q. Ji, X. Gao, Q. Zhang, L. Jin, D. Wang, Y. Xia, S. Yin, S. Xia, N. Hohn, X. Zuo, X. Wang, S. Xie, Z. Xu, L. Ma, L. Chen, G.Z. Chen, J. Zhu, B. Hu, P. Müller-Buschbaum, P.G. Bruce, Y.J. Cheng, Adv. Funct. Mater. **29**, 1904961 (2019)
91. J. Rana, J.K. Papp, Z. Lebens-Higgins, M. Zuba, L.A. Kaufman, A. Goel, R. Schmuch, M. Winter, M.S. Whittingham, W. Yang, B.D. McCloskey, L.F.J. Piper, ACS Energy Lett. **5**, 634–641 (2020)
92. N. Guerrini, L. Jin, J.G. Lozano, K. Luo, A. Sobkowiak, K. Tsuruta, F. Massel, L.C. Duda, M.R. Roberts, P.G. Bruce, Chem. Mater. **32**, 3733–3740 (2020)
93. M. Bianchini, A. Schiele, S. Schweidler, S. Sicolo, F. Fauth, E. Suard, S. Indris, A. Mazilkin, P. Nagel, S. Schuppler, M. Merz, P. Hartmann, T. Brezesinski, J. Janek, Chem. Mater. **32**, 9211–9227 (2020)
94. M.M. Thackeray, S.H. Kang, C.S. Johnson, J.T. Vaughey, R. Benedek, S.A. Hackney, J. Mater. Chem. **17**, 3112–3125 (2007)
95. A.R. Armstrong, M. Holzapfel, P. Novák, C.S. Johnson, S.H. Kang, M.M. Thackeray, P.G. Bruce, J. Am. Chem. Soc. **128**, 8694–8698 (2006)
96. K. Luo, M.R. Roberts, N. Guerrini, N. Tapia-Ruiz, R. Hao, F. Massel, D.M. Pickup, S. Ramos, Y.S. Liu, J. Guo, A.V. Chadwick, L.C. Duda, P.G. Bruce, J. Am. Chem. Soc. **138**, 11211–11218 (2016)
97. K. Luo, M.R. Roberts, R. Hao, N. Guerrini, D.M. Pickup, Y.S. Liu, K. Edström, J. Guo, A.V. Chadwick, L.C. Duda, P.G. Bruce, Nat. Chem. **8**, 684–691 (2016)
98. B. Strehle, K. Kleiner, R. Jung, F. Chesneau, M. Mendez, H.A. Gasteiger, M. Piana, J. Electrochem. Soc. **164**, A400–A406 (2017)
99. T. Teufl, B. Strehle, P. Müller, H.A. Gasteiger, M.A. Mendez, J. Electrochem. Soc. **165**, A2718–A2731 (2018)
100. W. Yin, A. Grimaud, G. Rousse, A.M. Abakumov, A. Senyshyn, L. Zhang, S. Trabesinger, A. Iadecola, D. Foix, D. Giaume, J.M. Tarascon, Nat. Commun. **11**, 1252 (2020)
101. D. Schreiner, T. Zünd, F.J. Günter, L. Kraft, B. Stumper, F. Linsenmann, M. Schüßler, R. Wilhelm, A. Jossen, G. Reinhart, H.A. Gasteiger, J. Electrochem. Soc. **168**, 030507 (2021)
102. X. Cao, H. Li, Y. Qiao, M. Jia, P. He, J. Cabana, H. Zhou, Energy Storage Mater. **38**, 1–8 (2021)
103. X. Cao, H. Li, Y. Qiao, M. Jia, X. Li, J. Cabana, H. Zhou, Adv. Mater. **33**, 2004280 (2021)
104. S. Shen, Y. Hong, F. Zhu, Z. Cao, Y. Li, F. Ke, J. Fan, L. Zhou, L. Wu, P. Dai, M. Cai, L. Huang, Z. Zhou, J. Li, Q. Wu, S. Sun, ACS Appl. Mater. Interfaces **10**, 12666–12677 (2018)
105. W. Huang, C. Lin, M. Zhang, S. Li, Z. Chen, W. Zhao, C. Zhu, Q. Zhao, H. Chen, F. Pan, Adv. Energy Mater. **11**, 2102646 (2021)
106. E. Boivin, N. Guerrini, R.A. House, J.G. Lozano, L. Jin, G.J. Rees, J.W. Somerville, C. Kuss, M.R. Roberts, P.G. Bruce, Adv. Funct. Mater. **31**, 2003660 (2021)
107. J. Zhang, Q. Zhang, D. Wong, N. Zhang, G. Ren, L. Gu, C. Schulz, L. He, Y. Yu, X. Liu, Nat. Commun. **12**, 3071 (2021)
108. Y. Shin, W.H. Kan, M. Aykol, J.K. Papp, B.D. McCloskey, G. Chen, K.A. Persson, Nat. Commun. **9**, 4597 (2018)

Journal of MATERIALS RESEARCH

Invited Feature Paper-Review

109. T. Wang, C. Zhang, S. Li, X. Shen, L. Zhou, Q. Huang, C. Liang, Z. Wang, X. Wang, W. Wei, ACS Appl. Mater. Interfaces **13**, 12159–12168 (2021)
110. J.M. Zheng, Z.R. Zhang, X.B. Wu, Z.X. Dong, Z. Zhu, Y. Yang, J. Electrochem. Soc. **155**, A775–A782 (2008)
111. Q. Li, D. Ning, D. Zhou, K. An, G. Schuck, D. Wong, W. Kong, C. Schulz, G. Schumacher, X. Liu, Chem. Mater. **32**, 9404–9414 (2020)
112. S. Maiti, H. Sclar, R. Sharma, N. Vishkin, M. Fayena-Greenstein, J. Grinblat, M. Talianker, L. Burstein, N. Solomatin, O. Tiurin, Y. Ein-Eli, M. Noked, B. Markovsky, D. Aurbach, Adv. Funct. Mater. **31**, 2008083 (2021)
113. E. Evenstein, Rosy, S. Haber, H. Sclar, L. Houben, K. Leung, M. Leskes, M. Noked, Energy Storage Mater. **19**, 261–269 (2019)
114. Rosy, S. Taragin, E. Evenstein, S. Maletti, D. Mikhailova, M. Noked, ACS Appl. Mater. Interfaces **13**, 44470–44478 (2021)
115. B. Sun, M. El Kazzi, E. Müller, E.J. Berg, J. Mater. Chem. A **6**, 17778–17786 (2018)
116. T. Teufl, D. Pritzl, P. Krieg, B. Strehle, M.A. Mendez, H.A. Gasteiger, J. Electrochem. Soc. **167**, 110505 (2020)
117. F. Wu, G.T. Kim, T. Diemant, M. Kuenzel, A.R. Schür, X. Gao, B. Qin, D. Alwast, Z. Jusys, R.J. Behm, D. Geiger, U. Kaiser, S. Passerini, Adv. Energy Mater. **10**, 2001830 (2020)
118. J.G. Han, J.B. Lee, A. Cha, T.K. Lee, W. Cho, S. Chae, S.J. Kang, S.K. Kwak, J. Cho, S.Y. Hong, N.S. Choi, Energy Environ. Sci. **11**, 1552–1562 (2018)
119. J. Xu, M. Sun, R. Qiao, S.E. Renfrew, L. Ma, T. Wu, S. Hwang, D. Nordlund, D. Su, K. Amine, J. Lu, B.D. McCloskey, W. Yang, W. Tong, Nat. Commun. **9**, 947 (2018)
120. Y. Yu, P. Karayaylali, S.H. Nowak, L. Giordano, M. Gauthier, W. Hong, R. Kou, Q. Li, J. Vinson, T. Kroll, D. Sokaras, C.J. Sun, N. Charles, F. Maglia, R. Jung, Y. Shao-Horn, Chem. Mater. **31**, 7864–7876 (2019)
121. Y. Yu, P. Karayaylali, D. Sokaras, L. Giordano, R. Kou, C.J. Sun, F. Maglia, R. Jung, F.S. Gittleson, Y. Shao-Horn, Energy Environ. Sci. **14**, 2322–2334 (2021)
122. F. Ning, B. Li, J. Song, Y. Zuo, H. Shang, Z. Zhao, Z. Yu, W. Chu, K. Zhang, G. Feng, X. Wang, D. Xia, Nat. Commun. **11**, 4973 (2020)
123. E. McCalla, M.T. Sougrati, G. Rousse, E.J. Berg, A. Abakumov, N. Recham, K. Ramesha, M. Sathiya, R. Dominko, G. Van Tendeloo, P. Novák, J.M. Tarascon, J. Am. Chem. Soc. **137**, 4804–4814 (2015)
124. E. McCalla, A.S. Prakash, E. Berg, M. Saubanère, A.M. Abakumov, D. Foix, B. Klobes, M.-T. Sougrati, G. Rousse, F. Lepoivre, S. Mariyappan, M.-L. Doublet, D. Gonbeau, P. Novák, G. Van Tendeloo, R.P. Hermann, J.-M. Tarascon, J. Electrochem. Soc. **162**, A1341–A1351 (2015)
125. M. Ting, M. Burigana, L. Zhang, Y.Z. Finfrock, S. Trabesinger, A. Jonderian, E. McCalla, Chem. Mater. **32**, 849–857 (2020)
126. Q. Jacquet, A. Iadecola, M. Saubanère, L. Lemarquis, E.J. Berg, D. Alves Dalla Corte, G. Rousse, M.L. Doublet, J.M. Tarascon, Chem. Mater. **30**, 7682–7690 (2018)
127. H. Li, S. Ramakrishnan, J.W. Freeland, B.D. McCloskey, J. Cabana, J. Am. Chem. Soc. **142**, 8160–8173 (2020)
128. N. Li, M. Sun, W.H. Kan, Z. Zhuo, S. Hwang, S.E. Renfrew, M. Avdeev, A. Huq, B.D. McCloskey, D. Su, W. Yang, W. Tong, Nat. Commun. **12**, 2348 (2021)
129. J. Lee, A. Urban, X. Li, D. Su, G. Hautier, G. Ceder, Science **343**, 519–522 (2014)
130. M.A. Cambaz, A. Urban, S.A. Pervez, H. Geßwein, A. Schiele, A.A. Guda, A.L. Bugaev, A. Mazilkin, T. Diemant, R.J. Behm, T. Brezesinski, M. Fichtner, Chem. Mater. **32**, 3447–3461 (2020)
131. J. Lee, J.K. Papp, R.J. Clément, S. Sallis, D.H. Kwon, T. Shi, W. Yang, B.D. McCloskey, G. Ceder, Nat. Commun. **8**, 981 (2017)
132. J. Lee, D.A. Kitchaev, D.H. Kwon, C.W. Lee, J.K. Papp, Y.S. Liu, Z. Lun, R.J. Clément, T. Shi, B.D. McCloskey, J. Guo, M. Balasubramanian, G. Ceder, Nature **556**, 185–190 (2018)
133. Z. Lun, B. Ouyang, D.A. Kitchaev, R.J. Clément, J.K. Papp, M. Balasubramanian, Y. Tian, T. Lei, T. Shi, B.D. McCloskey, J. Lee, G. Ceder, Adv. Energy Mater. **9**, 1802959 (2019)
134. Y. Yue, N. Li, Y. Ha, M.J. Crafton, B.D. McCloskey, W. Yang, W. Tong, Adv. Funct. Mater. **31**, 2008696 (2021)
135. K. Zhou, S. Zheng, F. Ren, J. Wu, H. Liu, M. Luo, X. Liu, Y. Xiang, C. Zhang, W. Yang et al., Energy Storage Mater. **32**, 234–243 (2020)
136. M.J. Crafton, Y. Yue, T.Y. Huang, W. Tong, B.D. McCloskey, Adv. Energy Mater. **10**, 2001500 (2020)
137. R. Satish, L. Wichmann, M.J. Crafton, R. Giovine, L. Li, J. Ahn, Y. Yue, W. Tong, G. Chen, C. Wang, R.J. Clement, R. Kostecki, ChemElectroChem **8**, 3982–3991 (2021)
138. T.Y. Huang, M.J. Crafton, Y. Yue, W. Tong, B.D. McCloskey, Energy Environ. Sci. **14**, 1553–1562 (2021)
139. W.H. Kan, D. Chen, J.K. Papp, A.K. Shukla, A. Huq, C.M. Brown, B.D. McCloskey, G. Chen, Chem. Mater. **30**, 1655–1666 (2018)
140. Q. Jacquet, A. Iadecola, M. Saubanère, H. Li, E.J. Berg, G. Rousse, J. Cabana, M.L. Doublet, J.M. Tarascon, J. Am. Chem. Soc. **141**, 11452–11464 (2019)
141. D.A. Kitchaev, Z. Lun, W.D. Richards, H. Ji, R.J. Clément, M. Balasubramanian, D.H. Kwon, K. Dai, J.K. Papp, T. Lei, B.D. McCloskey, W. Yang, J. Lee, G. Ceder, Energy Environ. Sci. **11**, 2159–2171 (2018)
142. D. Chen, J. Wu, J.K. Papp, B.D. McCloskey, W. Yang, G. Chen, Small **16**, 2000656 (2020)
143. Y. Yue, Y. Ha, T.Y. Huang, N. Li, L. Li, Q. Li, J. Feng, C. Wang, B.D. McCloskey, W. Yang, W. Tong, ACS Nano **15**, 13360–13369 (2021)
144. M.A. Cambaz, B.P. Vinayan, H. Geßwein, A. Schiele, A. Sarapulova, T. Diemant, A. Mazilkin, T. Brezesinski, R.J. Behm, H. Ehrenberg, M. Fichtner, Chem. Mater. **31**, 4330–4340 (2019)
145. B. Breitung, Q. Wang, A. Schiele, Đ. Tripković, A. Sarkar, L. Velasco, D. Wang, S.S. Bhattacharya, H. Hahn, T. Brezesinski, Batter. Supercaps **3**, 361–369 (2020)

Journal of MATERIALS RESEARCH

Invited Feature Paper-Review

146. Z. Lun, B. Ouyang, D.H. Kwon, Y. Ha, E.E. Foley, T.Y. Huang, Z. Cai, H. Kim, M. Balasubramanian, Y. Sun, J. Huang, Y. Tian, H. Kim, B.D. McCloskey, W. Yang, R.J. Clément, H. Ji, G. Ceder, Nat. Mater. **20**, 214–221 (2021)
147. A.-Y. Kim, F. Strauss, T. Bartsch, J.H. Teo, T. Hatsukade, A. Mazilkin, J. Janek, P. Hartmann, T. Brezesinski, Chem. Mater. **31**, 9664–9672 (2019)
148. F. Strauss, J.H. Teo, J. Maibach, A.-Y. Kim, A. Mazilkin, J. Janek, T. Brezesinski, ACS Appl. Mater. Interfaces **12**, 57146–57154 (2020)
149. Y. Ma, J.H. Teo, F. Walther, Y. Ma, R. Zhang, A. Mazilkin, Y. Tang, D. Goonetilleke, J. Janek, M. Bianchini, T. Brezesinski, Adv. Funct. Mater. (2022). https://doi.org/10.1002/adfm.202111829
150. Y. Ma, J.H. Teo, D. Kitsche, T. Diemant, F. Strauss, Y. Ma, D. Goonetilleke, J. Janek, M. Bianchini, T. Brezesinski, ACS Energy Lett. **6**, 3020–3028 (2021)
151. J.H. Teo, F. Strauss, Đ. Tripković, S. Schweidler, Y. Ma, M. Bianchini, J. Janek, T. Brezesinski, Cell Rep. Phys. Sci. **2**, 100465 (2021)
152. C. Sångeland, B. Sun, D. Brandell, E.J. Berg, J. Mindemark, Batter. Supercaps **4**, 785–790 (2021)
153. F. Strauss, J.H. Teo, A. Schiele, T. Bartsch, T. Hatsukade, P. Hartmann, J. Janek, T. Brezesinski, ACS Appl. Mater. Interfaces **12**, 20462–20468 (2020)
154. J.H. Teo, F. Strauss, F. Walther, Y. Ma, S. Payandeh, T. Scherer, M. Bianchini, J. Janek, T. Brezesinski, Mater. Futures **1**, 015102 (2022)
155. K. Nie, X. Wang, J. Qiu, Y. Wang, Q. Yang, J. Xu, X. Yu, H. Li, X. Huang, L. Chen, ACS Energy Lett. **5**, 826–832 (2020)
156. L. Seidl, R. Grissa, L. Zhang, S. Trabesinger, C. Battaglia, Adv. Mater. Interfaces **9**, 2100704 (2022)
157. B. Li, Q. Su, C. Liu, Q. Wang, M. Zhang, S. Ding, G. Du, B. Xu, J. Power Sources **496**, 229835 (2021)
158. A.A. Delluva, J. Kulberg-Savercool, A. Holewinski, Adv. Funct. Mater. **31**, 2103716 (2021)
159. Y.N. Yang, Y.X. Li, Y.Q. Li, T. Zhang, Nat. Commun. **11**, 5519 (2020)
160. J.M. Tarascon, Joule **4**, 1616–1620 (2020)
161. L. Zhang, C. Tsolakidou, S. Mariyappan, J.M. Tarascon, S. Trabesinger, Energy Storage Mater. **42**, 12–21 (2021)
162. U. Maitra, R.A. House, J.W. Somerville, N. Tapia-Ruiz, J.G. Lozano, N. Guerrini, R. Hao, K. Luo, L. Jin, M.A. Pérez-Osorio, F. Massel, D.M. Pickup, S. Ramos, X. Lu, D.E. McNally, A.V. Chadwick, F. Giustino, T. Schmitt, L.C. Duda, M.R. Roberts, P.G. Bruce, Nat. Chem. **10**, 288–295 (2018)
163. R.A. House, U. Maitra, L. Jin, J.G. Lozano, J.W. Somerville, N.H. Rees, A.J. Naylor, L.C. Duda, F. Massel, A.V. Chadwick, S. Ramos, D.M. Pickup, D.E. McNally, X. Lu, T. Schmitt, M.R. Roberts, P.G. Bruce, Chem. Mater. **31**, 3293–3300 (2019)
164. R.A. House, U. Maitra, M.A. Pérez-Osorio, J.G. Lozano, L. Jin, J.W. Somerville, L.C. Duda, A. Nag, A. Walters, K.J. Zhou, M.R. Roberts, P.G. Bruce, Nature **577**, 502–508 (2020)
165. E. Boivin, R.A. House, M.A. Pérez-Osorio, J.J. Marie, U. Maitra, G.J. Rees, P.G. Bruce, Joule **5**, 1267–1280 (2021)
166. C. Zhao, Q. Yang, F. Geng, C. Li, N. Zhang, J. Ma, W. Tong, B. Hu, ACS Appl. Mater. Interfaces **13**, 360–369 (2021)
167. A. Kulka, C. Marino, K. Walczak, C. Borca, C. Bolli, P. Novák, C. Villevieille, J. Mater. Chem. A **8**, 6022–6033 (2020)
168. E. Marelli, C. Marino, C. Bolli, C. Villevieille, J. Power Sources **450**, 227617 (2020)
169. Q. Wang, S. Mariyappan, G. Rousse, A.V. Morozov, B. Porcheron, R. Dedryvère, J. Wu, W. Yang, L. Zhang, M. Chakir, M. Avdeev, M. Deschamps, Y.S. Yu, J. Cabana, M.L. Doublet, A.M. Abakumov, J.M. Tarascon, Nat. Mater. **20**, 353–361 (2021)
170. Y. Yu, D. Ning, Q. Li, A. Franz, L. Zheng, N. Zhang, G. Ren, G. Schumacher, X. Liu, Energy Storage Mater. **38**, 130–140 (2021)
171. N. Voronina, N. Yaqoob, H.J. Kim, K.S. Lee, H.D. Lim, H.G. Jung, O. Guillon, P. Kaghazchi, S.T. Myung, Adv. Energy Mater. **11**, 2100901 (2021)
172. Y. Ma, Y. Ma, S.L. Dreyer, Q. Wang, K. Wang, D. Goonetilleke, A. Omar, D. Mikhailova, H. Hahn, B. Breitung, T. Brezesinski, Adv. Mater. **33**, 2101342 (2021)
173. B. Jache, P. Adelhelm, Angew. Chem. Int. Ed. **53**, 10169–10173 (2014)
174. M. Goktas, C. Bolli, E.J. Berg, P. Novák, K. Pollok, F. Langenhorst, M.V. Roeder, O. Lenchuk, D. Mollenhauer, P. Adelhelm, Adv. Energy Mater. **8**, 1702724 (2018)
175. M. Goktas, C. Bolli, J. Buchheim, E.J. Berg, P. Novák, F. Bonilla, T. Rojo, S. Komaba, K. Kubota, P. Adelhelm, ACS Appl. Mater. Interfaces **11**, 32844–32855 (2019)
176. W. Liu, X. Chen, C. Zhang, H. Xu, X. Sun, Y. Zheng, Y. Yu, S. Li, Y. Huang, J. Li, ACS Appl. Mater. Interfaces **11**, 23207–23212 (2019)
177. B. Qin, A. Schiele, Z. Jusys, A. Mariani, T. Diemant, X. Liu, T. Brezesinski, R.J. Behm, A. Varzi, S. Passerini, ACS Appl. Mater. Interfaces **12**, 3697–3708 (2020)
178. H. Kim, D.H. Seo, A. Urban, J. Lee, D.H. Kwon, S.H. Bo, T. Shi, J.K. Papp, B.D. McCloskey, G. Ceder, Chem. Mater. **30**, 6532–6539 (2018)
179. N.H. Bashian, M. Zuba, A. Irshad, S.M. Becwar, J. Vinckeviciute, W. Rahim, K.J. Griffith, E.T. McClure, J.K. Papp, B.D. McCloskey, D.O. Scanlon, B.F. Chmelka, A. Van Der Ven, S.R. Narayan, L.F.J. Piper, B.C. Melot, Chem. Mater. **33**, 5757–5768 (2021)
180. L. Wang, Z. Cao, P. Zhuang, J. Li, H. Chu, Z. Ye, D. Xu, H. Zhang, J. Shen, M. Ye, ACS Appl. Mater. Interfaces **13**, 13338–13346 (2021)
181. N. Schlüter, P. Novák, D. Schröder, Adv. Energy Mater **12**, 2200708 (2022)
182. A. Schürmann, B. Luerßen, D. Mollenhauer, J. Janek, D. Schröder, Chem. Rev. **121**, 12445–12464 (2021)

4.2. The Effect of Doping Process Route on $LiNiO_2$ Cathode Material Properties

This study on the LNO CAM is a continuation of the works of Kurzhals *et al.* and Riewald *et al.*, who have by systematic variation of calcination conditions shown that the primary particle morphology, i.e. the (specific) surface area, determines the electrochemical properties, and especially the first-cycle capacity loss, which was previously mostly attributed to the cation intermixing.[84,86] It was shown that smaller primary particles lead to improved electrochemical properties, since due to particle cracking, the accessible surface area, tracked via the capacitance method developed by Oswald *et al.*,[335-337] increases during cycling. In many recent dopant comparisons for Ni-rich NCM, it was reported that the presence of boron or high-valence dopants leads to reduced primary particle size due to dopant segregation on the particle surface, which causes grain-growth inhibition.[338-343] However, different process routes of dopant introduction are described, and often very high dopant concentrations are chosen, to pronounce the difference between doped and undoped material.

In this study, three possible LNO-doping process routes were therefore compared, namely co-calcination (of pCAM and ZrO_2), pCAM impregnation (with ZrO_2 nanoparticles) and co-precipitation (of Zr^{4+} into the pCAM), using an industrially relevant, low concentration of Zr^{4+} (0.25 mol% relative to the total transition-metal content). Thus, supposedly equally doped LNO is obtained, yet it is indeed found that the primary particle size differs between the process routes, with only impregnation and co-precipitation leading to reduced primary particle size when compared to undoped material. An increased content of surface impurities (LiOH and esp. Li_2CO_3) was found in the LNO obtained from co-precipitation and traced back to carbon-containing impurities in the pCAM, likely from a Zr^{4+}-complexation agent, such as citric acid. If these impurities are removed by pre-heating the pCAM in O_2 atmosphere, the particle-size growth effect is reversed and separated small Zr^{4+}-rich grains are observed via scanning transmission electron microscopy with energy-dispersive X-ray spectroscopy (STEM-EDS), while all other materials showed an even distribution of Zr^{4+}, with however enrichment at grain boundaries, assumed to be Li_2ZrO_3. Laser ablation-inductively coupled plasma-mass spectrometry (LA-ICP-MS) was further employed as an innovative, quantitative and faster alternative to STEM-EDS in the evaluation of dopant distribution between secondary particles, finding that co-precipitation leads to the most even Zr^{4+} distribution. The electrochemical performance is best in LNO obtained from pCAM impregnation, as this gives the smallest primary particle size. In LNO obtained from co-precipitation,

even though primary particles are also small, and similar surface areas are expected based on capacitance measurements, the surface impurities lead to an increased amount of side reactions, as also found via DEMS, while for the other materials a correlation between particle size, i.e. specific surface area, and evolved CO_2 amount was found, as expected for gas-evolving reactions at the CAM surface.

The difference in particle size depending on the doping process route is due to the initial localization of the dopant, as grain-growth inhibition stems from dopant segregation at the primary particle surface. Via the impregnation route, dopant nanoparticles are already located there, while the other process routes require Zr^{4+} diffusion, either from within the primary particle (co-precipitation) or from the ZrO_2 precursor (co-calcination). Under these conditions, more initial grain growth, especially before reaching the final calcination temperature, at which Zr^{4+} is reasonably mobile, can occur. While there are other studies on low-concentration Zr^{4+} doping of Ni-rich NCM published concurrently (0.3 mol% co-precipitation,[344] 0.25-0.5 mol% co-calcination,[345,346] all no effect on grain size; 1 mol% impregnation, smaller grains[347]), this study remains the only one to discuss the role of the doping process route.

The study was initiated and designed by Dr. Philipp Kurzhals and the author of this thesis. Material synthesis, electrode preparation, electrochemical testing and electron microscopy were performed by Dr. Philipp Kurzhals and the author. Acid titration, inductively coupled plasma-optical emission spectroscopy (ICP-OES) and elemental analysis were carried out by the central analytical services of BASF SE after instruction by Dr. Philipp Kurzhals. Pouch-cell assembly and testing, as well as the DEMS investigation, were carried out by the author. Dr. Svenja B. Seiffert performed the LA-ICP-MS analysis. Dr. Philipp Müller performed the STEM-EDS investigation. Dr. Philipp Kurzhals and the author analyzed the data and created the figures. The original manuscript was written by the author. Dr. Aleksandr Kondrakov, Prof. Dr. Jürgen Janek and Dr. Torsten Brezesinski supervised the work. The manuscript was edited by all authors.

Reprinted from S. L. Dreyer, P. Kurzhals, S. B. Seiffert, P. Müller, A. Kondrakov, T. Brezesinski, J. Janek, *J. Electrochem. Soc.* **2023**, *170*, 060530, DOI 10.1149/1945-7111/acdd21

Journal of The Electrochemical Society, 2023 **170** 060530

The Effect of Doping Process Route on $LiNiO_2$ Cathode Material Properties

Sören L. Dreyer,[1] Philipp Kurzhals,[2] Svenja B. Seiffert,[2] Philipp Müller,[2] Aleksandr Kondrakov,[2] Torsten Brezesinski,[1,z] and Jürgen Janek[1,3]

[1]*Battery and Electrochemistry Laboratory (BELLA), Institute of Nanotechnology, Karlsruhe Institute of Technology (KIT), 76344 Eggenstein-Leopoldshafen, Germany*
[2]*BASF SE, 67056 Ludwigshafen, Germany*
[3]*Institute of Physical Chemistry & Center for Materials Research (ZfM/LaMa), Justus-Liebig-University Giessen, 35392 Giessen, Germany*

The pursuit of higher energy density in lithium-ion batteries has driven the increase of the nickel content in lithium nickel cobalt manganese oxide cathode active materials (CAMs), ultimately approaching $LiNiO_2$ (LNO). The downside of the high specific capacity of LNO is more severe degradation of the CAM during battery operation. A common approach to increase structural stability is the introduction of dopants. Various dopants are discussed and compared with each other when integrated into the CAM and tested against undoped materials in the literature, but little attention is given to the role of the process route of their introduction. In this work, we demonstrate with a series of nominally equally Zr-doped LNO samples that effects on various physico- and electrochemical properties are due not to the dopant itself, as one would assume in comparison to an undoped sample, but to the process route and the resulting particle morphology. Dopant, concentration and process routes (co-precipitation, impregnation and co-calcination) were chosen based on their significance for industrial application.
 [DOI: 10.1149/1945-7111/acdd21]

Manuscript submitted April 13, 2023; revised manuscript received May 25, 2023. Published June 20, 2023.

Supplementary material for this article is available online

The increasing demand for lithium-ion batteries with high energy density to power both portable electronics and electric vehicles is met with various research and development efforts to improve the performance from the materials side. As the cathode, and therein mostly the CAM, makes up the largest individual cost and weight contribution, many efforts focus on increasing its capacity.[1] Here, the $LiNi_xCo_yMn_zO_2$ (NCM) material family of layered oxides offers the highest capacities, which increase (for a fixed cut-off voltage) with the nickel content, exemplified by the endmember LNO showing a first-cycle specific discharge capacity above 245 mAh g^{-1}.[2–4] Polycrystalline NCM consists of smaller primary particles aggregated to larger secondary particles and, as some of the authors have recently demonstrated, the particle morphology is the main factor controlling the electrochemical properties.[5–7] Typically obtained from the calcination of $Ni(OH)_2$ and LiOH in the case of LNO or the respective transition-metal hydroxides in the case of NCM, the size of secondary particles depends mostly on the hydroxide precursor CAM (pCAM) particle size, which can be controlled in the precipitation process. At the same time, the size of the primary particles is controlled by the calcination temperature and lithium stoichiometry, the latter also affecting the fraction of Ni^{2+} on the Li-site, often referred to as off-stoichiometry.[5–7]

The main downside of establishing higher capacity (i.e. deeper delithiation) is the reduced structural stability, resulting in faster chemo-mechanical degradation on multiple length scales, i.e. capacity fading.[8,9] For Ni-rich NCM in general and LNO specifically, degradation during cycling is driven by two main phenomena. Firstly, structural rearrangement under loss of lattice oxygen forms a densified, rocksalt-type layer on the particle surface, which hinders lithium diffusion and renders nickel electrochemically inactive (increased share of Ni^{2+} up until approaching NiO stoichiometry).[4,10,11] Secondly, anisotropic unit-cell volume change, especially in the form of the decrease in *c* lattice parameter during the H2/H3 phase transition, leads to the formation of cracks and eventual pulverization of the secondary particles, also exposing additional (reactive) surface area.[3,4,12]

[z]E-mail: torsten.brezesinski@kit.edu

Several strategies have been developed to mitigate CAM degradation both at the particle surface and in the bulk, with coating, doping and morphology modification (i.e. single-crystalline materials) and combinations thereof being most prominent.[13–16] For Ni-rich NCM, various dopants and dopant combinations and their supposed function in performance improvement have been discussed and reviewed in the literature, ranging from elements as light as B to heavier elements like W.[3,4,17] Among the most common dopants are Mg, Al, Ti and Zr, while for LNO also Mn and Co could be considered as dopants.[4,13,15,16]

Depending on dopant and precursor, different process routes are followed to introduce the dopant. The most common are co-calcination of pCAM, lithium source and dopant particles on the one hand,[18–25] and co-precipitation of dopant ions into the pCAM during its preparation on the other hand.[26–39] The impregnation of pCAM with a dopant solution or a suspension of smaller dopant particles and subsequent solvent removal provides a third option, especially if co-calcination leads to insufficient mixing and/or phase separation.[40–51] Despite these and various other process routes being available,[13,15,52–56] comparisons between doped samples obtained from different routes are quite rare,[57,58] as usually comparisons are made with an undoped reference sample. The influence of the dopant on the CAM particle morphology is sometimes discussed in comparisons of doped and undoped samples.[17–19,26,30,41,47,49,50,52,57] Recently, Park et al. demonstrated that, in a series of co-precipitated $LiNi_{0.95}Co_{0.04}X_{0.01}O_2$ (X = one of Al, Ti, Ta, Sb, Nb, W, Mo), the primary particle size strongly depends on the chosen dopant, decreasing with dopant valence state. Furthermore, a linear trend between primary particle size of each doped CAM and capacity fading after 100 cycles was observed.[59] Sun et al. reported a similar finding for $LiNi_{0.90}Co_{0.09}X_{0.01}O_2$ (X = one of Mg, Al, Ti, Ta, Mo), also observing an increase in primary particle aspect ratio with increasing dopant valence.[20] A consideration of the role of the process route on CAM morphology is even rarer,[57] although the latter greatly affects the electrochemical performance.[5–7]

Zirconium has seen widespread use as a dopant for NCM materials and can be introduced into the structure by various routes, including co-calcination,[23–25] impregnation,[46,47,51] and co-precipitation.[26,30,31,39,57] Of note is the diffusion of Zr^{4+} at high temperatures, due to which

doping can also be achieved by heating Zr-coated CAM.[56,60] Vice versa, Zr^{4+} as a dopant is prone to enrich and phase separate at the surface of CAM particles, forming an additional Li_2ZrO_3 phase.[31,51,53,61,62] With this limited bulk solubility in mind, only some studies focused on industrially relevant dopant concentrations, i.e. below 1 mol%.[24,25,47,61,62] The atom position of Zr^{4+} in the structure is not fully understood, with literature reporting localization either in the lithium[63] or transition-metal layer,[23,43] or possibly both.[39,53,64]

Main effects and advantages attributed to the dopant include increased *c* lattice parameter, faster lithium diffusion, smoother H2/H3 phase transition, less volume change during delithiation, less crack formation and reduced surface-layer formation, ultimately resulting in longer cycle life, improved rate capability, reduced impedance and less polarization of the CAM.[23,24,31,47,56,60,62,65] At high state of charge (SOC), zirconium was shown to suppress charge transfer to oxygen, thereby reducing the loss of lattice oxygen and subsequent gas evolution.[46] In some studies, a difference in CAM particle size or morphology between doped and undoped material was observed and partially related to altered properties.[25,26,30,47,57]

In this article, we demonstrate on a series of 0.25 mol% Zr-doped LNO obtained from three different process routes, namely co-calcination, impregnation and co-precipitation, that not the dopant but the process route leads to a difference in physico- and electrochemical properties, especially considering primary particle morphology. The rather low dopant concentration is chosen due to its industrial relevance, i.e. the redox-active metal content remains high and the redox-inactive dopant concentration low for maximum energy density. Furthermore, a phase separation is avoided as much as possible, as the Zr^{4+} fraction is low enough to mostly remain in the bulk LNO.

Experimental

Doping and calcination.—Calcination of undoped LNO was performed as described in the literature[5] using a commercial $Ni(OH)_2$ precursor (d_{50} = 4 μm, Hunan Zoomwe Zhengyuan Advanced Material Trade Co., Ltd., China) and $LiOH{\cdot}H_2O$ (Albemarle Germany GmbH, Germany). In short, precursors were blended (1.02 mol eq. $LiOH{\cdot}H_2O$ per 1.0 mol eq. $Ni(OH)_2$) and calcined under O_2 flow (100 l h^{-1}, equal to about 10 furnace volume exchanges/h) in a box furnace (Linn High Term GmbH, Germany) at 400 °C for 4 h, then at 700 or 750 °C for 6 h, with intermediate heating ramps of 3 °C min^{-1}. Samples were cooled down to 120 °C and transferred to dry room atmosphere (21 °C, dew point < −40 °C) with minimal exposure to ambient air. The obtained powders were sieved (32 μm mesh) prior to further processing and characterization. Co-calcined Zr-doped LNO was obtained in the same way, but with the addition of ZrO_2 (Daiichi Kigenso Kagaku Kogyo Co., Ltd., Japan) to the blend (0.9975 mol eq. $Ni(OH)_2$, 0.0025 mol eq. ZrO_2, 1.02 eq. $LiOH{\cdot}H_2O$). To obtain Zr-impregnated pCAM, $Ni(OH)_2$ was dispersed in water (1:1 by weight), and a suspension of 20 wt% colloidal ZrO_2 nanoparticles (Nyacol Nano Technologies, Inc., USA) in water, stabilized with ammonia, was added dropwise under stirring. The solvent was removed at 120 °C in a vacuum overnight, and the obtained powder was heated to 500 °C for 3 h in the box furnace under O_2 flow, then transferred to the dry room and sieved as described above. To obtain LNO, the Zr-doped/coated NiO was blended with 1.02 mol eq. $LiOH{\cdot}H_2O$ and calcined as described above. Co-precipitated, 0.25 mol% Zr-doped pCAM (d_{50} = 4 μm) was obtained from Hunan Zoomwe Zhengyuan Advanced Material Trade Co., Ltd., China and calcined with 1.02 mol eq. $LiOH{\cdot}H_2O$ (per 0.9975 mol eq. $Ni(OH)_2$). In a variation, the doped pCAM was pre-dried similar to impregnated pCAM at 500 °C for 3 h before being blended with $LiOH{\cdot}H_2O$ and calcined as described above.

PXRD.—Synchrotron powder X-ray diffraction (PXRD) measurements were performed, in analogy to a previous work,[5] at the ALBA synchrotron BL04-MSPD beamline at a wavelength of λ = 0.62001 Å (calibrated using a Si NIST standard) using a Si 111 monochromator and a MYTHEN position sensitive detector in 2-theta angular range of 2°–82°. Samples were measured in flame-sealed borosilicate capillaries of 0.7 mm diameter and mounted on a spinning sample holder. Data were collected in Debye–Scherrer geometry for 27 different positions of the detector, with a data acquisition time of 30 s for each position. Rietveld refinement was performed using the FullProf software package, based on a hexagonal α-$NaFeO_2$ structure with *R*–3m space group. The instrumental broadening was determined by measuring a NAC ($Na_2Ca_3Al_2F_{14}$) standard in the same sample configuration. The model used for the fitting is based on Thompson-Cox-Hastings pseudo-Voigt convoluted with axial divergence asymmetry functions. Sample contribution to peak broadening was determined by the instrumental resolution function, so that a volume-averaged value of the crystallite size was obtained via the Scherrer equation. Refinement of the parameters of the structural model was done for consecutive iteration cycles until convergence was reached, and the quality of fit was checked by inspection of the R_{wp} (weighted profile factor with all non-excluded points), R_{Bragg} (Bragg *R*-factor) and χ^2 (reduced chi-square). In an initial LeBail fit, two asymmetry parameters were refined and held constant during subsequent Rietveld refinement. For all samples, in the final iteration, 12 parameters were refined: scale factor, zero shift, *a* and *c* lattice parameters, U, X, Y as parameters of the Gaussian (U) and Lorentzian (X, Y) contribution to the pseudo-Voigt function, fractional atomic coordinate of oxygen z_{ox}, occupancy of Ni^{2+} on the Li-site (assuming site remains fully occupied) and B_{iso} (isotropic displacement parameter) of O, Ni and Li.

Electron microscopy.—Scanning electron microscopy (SEM) was performed using an Ultra 55 (Carl Zeiss AG, Germany) microscope equipped with a thermal field-emission cathode and an Everhart-Thornley secondary electron detector at an operating voltage of 5 kV. Powder samples were fixed on conductive carbon cement (Plano GmbH, Germany) and a 6 nm Pt layer was added via sputter deposition (SCD 500 Sputter Coater, BalTec AG, Switzerland). Automated image segmentation was used to obtain the equivalent diameter of the primary particles from SEM images at 20 k magnification, as described previously.[6] At least 10 images per material were segmented.

Samples for transmission electron microscopy (TEM) were prepared by broad ion-beam milling using a Jeol (Jeol Ltd., Japan) Ar-ion slicer (EM-09100 IS) and/or focused ion beam milling using a Helios G4 machine (Thermo Fisher Scientific Inc., USA). The samples were imaged using a Tecnai Osiris (Thermo Fisher) operated at 200 kV and a Themis Z3.1 (Thermo Fisher) equipped with a probe-corrector operated at 300 kV both under high-angle annular dark-field scanning TEM (HAADF-STEM) conditions. Chemical composition maps were acquired by energy-dispersive X-ray spectroscopy (EDS) with integrated SuperX G1 and G2 detectors. Elemental maps were evaluated with the Esprit (version 2.1, Bruker, USA) and Velox 3 (Thermo Fisher) software.

Acid titration.—Residual LiOH and Li_2CO_3 in the LNO samples were determined by stirring a suspension of 2 g of CAM in 10 ml deionized water for 20 min under N_2 atmosphere in a glovebox and titrating the solution resulting after filtration through a syringe filter with 0.1 M HCl solution (Bernd Kraft GmbH, Germany). To this end, a Titrando 808 automatic titrator (Deutsche Metrohm GmbH & Co KG, Germany) and a glass pH electrode (Metrohm) were used. Two separate equivalent points were observed and used to distinguish between LiOH and Li_2CO_3, with hydroxide and carbonate ions being protonated first and the resulting bicarbonate being protonated again later.

ICP-OES.—0.3 g of CAM was digested in 5 M HCl under stirring and gentle heating. The solution was diluted with deionized water, and the concentrations of Ni, Li and Zr were measured with an

Agilent 5100 inductively coupled plasma-optical emission spectroscopy (ICP-OES) device (Agilent Technologies Inc., USA). For each sample, three individual measurements were performed.

LA-ICP-MS.—For single particle analysis using laser ablation-inductively coupled plasma-mass spectrometry (LA-ICP-MS), a 193 nm ArF excimer laser (NWR193 ablation system, Elemental Scientific Lasers, USA) equipped with a two-volume cell (Two Vol2 ablation cell, Elemental Scientific Lasers) was coupled to an ICP-MS (8900 ICP-MS Triple Quad, Agilent Technologies, USA). The samples were transported in a carrier gas flow (He, 850 ml min^{-1}) and introduced via a dual concentric injector (Elemental Scientific Lasers) to the ICP-MS. An additional gas flow (Ar, 1 l min^{-1}) was added and the sample transferred via a quartz injector pipe (2.5 mm inner diameter) into the plasma. The ICP-MS was equipped with a Pt sampler and skimmer. To reduce polyatomic interferences, it was operated in single quadrupole-kinetic energy discrimination mode adding He as collision gas. The RF coil was set to 1300 W, and the setup was tuned daily for maximum signal intensity and an oxide ratio (m/z:m/z = 232:248) below 0.8% with a NIST glass standard (NIST SRM 612). The samples were ablated with single spots and a laser pulse frequency of 100 Hz. A laser energy of 1.5 J cm^{-2} and 80 bursts ensured complete ablation of each particle. For each measurement, at least 200 particles were ablated. Additionally, the background of the carbon cement tab was tested. The ICP-MS was operated in time-resolved analysis mode, and for each element one isotope ($^{61}Ni^{+}$ and $^{90}Zr^{+}$) was detected with a dwell time of 100 μs. The short dwell time enabled the collection of >50 data points per particle, even for the smallest particles. Data evaluation was carried out using RStudio and a homemade script. Particle event integration was triggered by crossing a manually chosen peak trigger value and ended after a manually chosen timeframe (1 s). As nearly all background signals were 0 counts, the integrated particle events were not corrected.

Elemental analysis of carbon content.—In a single-use ceramic cup, 200 mg of pCAM was mixed with 500 mg of iron granulate, and the mixture was covered with 1.5 g of tungsten granulate. The sample was heated in a flow of pure O_2 in the induction furnace of the analyzer (Eltra CS 800, Eltra GmbH, Germany), and the released CO_2 was quantified via infrared spectroscopy.

Cathode preparation.—Electrodes for electrochemical characterization were prepared by mixing the CAM powders with Super C65 conductive carbon (Imerys Graphite & Carbon, Switzerland) and PVDF binder (Solef 5130, Solvay GmbH, Germany) in a 94:3:3 mass ratio. For this, a 7.5 wt% binder solution in N-methyl-2-pyrrolidone (NMP, BASF SE, Germany) was mixed with additional NMP and the conductive carbon for at least 24 min at 2000 rpm using an ARE 250 planetary mixer (Thinky Corporation, Japan). The CAM powder was added to the obtained slurry and mixed for additional 10 min. The solid fraction of the final slurries was 61 wt%. The slurries were cast onto 20 μm Al foil (Nippon Light Metal Co., Ltd., Japan) using a box-type coater (110 μm wet-film thickness, 6 cm width, Erichsen GmbH & Co. KG, Germany) and an automated coating table (5 mm s^{-1}, Coatmaster 510, Erichsen GmbH & Co. KG, Germany). The coated tapes were placed in a vacuum oven (VDL 23, Binder GmbH, Germany) and dried at 120 °C in a dynamic vacuum for 12 h. The cathode tapes were then compressed using a CA5 calendar (Sumet Systems GmbH, Germany) at a set line force of 30 N mm^{-1} and a roller speed of 0.5 m min^{-1}. The active material loading was 9 (±0.5) mg cm^{-2} and the electrode density was 3.0 (±0.2) g cm^{-3}.

Cell preparation.—For coin half-cells, circular electrodes with a diameter of 14 mm were punched out using a high-precision handheld punch (Nogamigiken Co., Ltd., Japan). After weighing, the electrodes were transferred to an Ar-filled glovebox for assembly of CR2032 coin cells (Hohsen Corp, Japan). To the cathode, a 17 mm diameter GF/D glass fiber separator (VWR International GmbH, Germany), a 15.8 mm diameter Li-metal anode (Shandong Gelon LIB Co., Ltd., China) and 95 μl LP57 electrolyte (1 M $LiPF_6$ in ethylene carbonate:ethyl methyl carbonate 3:7 by volume, BASF SE, Germany) were added, and the cells were sealed by crimping with an automated crimper (Hohsen Corp.). Single-layer pouch full cells were assembled in dry-room atmosphere from 40·20 mm^2 cathodes, 50·30 mm^2 microporous separators (Celgard 2500, Celgard, LLC, USA), 42·22 mm^2 graphite anodes (7 mg cm^{-2} loading) and 500 μl LP472 electrolyte (1 M $LiPF_6$ in ethylene carbonate:diethyl carbonate 3:7 by volume, with 2 vol% vinylene carbonate, BASF SE, Germany). The n/p ratio[66] was calculated based on the first-cycle specific capacity in half-cells (250 mAh g^{-1} for LNO, 330 mAh/g for graphite). With a graphite loading of 64 mg per anode and LNO loadings between 69 and 73 mg per cathode (8.6 to 9.1 mg cm^{-2}), n/p ratios of 1.16–1.22 were obtained.

Electrochemical testing.—Coin half-cells were cycled at 25 °C between 3.0 and 4.3 V vs Li^{+}/Li using a battery testing system (Series 4000, MACCOR, USA). Assuming 1 C as 200 mA g^{-1}, the applied current was equal to C/20 in the first two cycles and C/3 in the following cycles, with the exception of a rate test with one cycle each at C/3, C/10, 1 C and 2 C. Additional coin half-cells were cycled to determine the specific capacitance according to a recently presented method.[67] Cells were cycled between 2.5 and 4.3 V, while at the end of discharge an additional constant-voltage step was implemented (until the current was lower than C/250) to ensure the presence of blocking conditions. Then, an alternating current (C/50 amplitude, 100 mHz frequency, 20 periods duration) was modulated onto the discharge current. By fitting the current and voltage response to sine functions, the specific capacitance can be calculated from the phase shift, as demonstrated elsewhere.[67–69] Pouch full cells were cycled between 2.8 and 4.2 V at a rate of C/10 in the first two cycles and then at C/3 for 10 cycles. A rate test at C/3 charge and two cycles each at 0.5 C, 1 C, 2 C and 3 C discharge was implemented and subsequently repeated after every 100 cycles at C/3 rate.

DEMS.—For gas analysis via differential electrochemical mass spectrometry (DEMS), a custom-built cell containing a 30 mm diameter cathode with a 4 mm diameter hole in the center, a 40 mm diameter GF/D separator, a 32 mm diameter Li-metal anode and 800 μL LP57 electrolyte was cycled at 0.1 C rate between 3.0 and 4.3 V, while a constant 2.5 ml min^{-1} stream of He carrier gas (purity 6.0) was passed through the cell. The extracted gas mixture was analyzed with a mass spectrometer (GSD320, Pfeiffer Vacuum GmbH, Germany). For CO_2 quantification, a calibration was carried out using gas with 100 ppm CO_2 content. Further details can be found elsewhere.[70–72]

Results and Discussion

Precursors.—For the synthesis of undoped LNO and LNO doped via co-calcination and impregnation, a batch of spherical $Ni(OH)_2$ pCAM (d_{50} = 4 μm) with rod-like primary particles, as shown in Figs. S1a and S1b, was used. Figures S1c and S1d show the pCAM after impregnation with ZrO_2 nanoparticles and subsequent heating during which the $Ni(OH)_2$ is converted to NiO. In the following, this procedure is referred to as pre-drying ("predr." in figures), wherein full conversion was ensured by subsequent ICP-OES analysis revealing a composition of >77.5 wt% Ni, in contrast to ~64% for the initial $Ni(OH)_2$. The presence of fragmented pCAM particles is likely due to deagglomeration and sieving of the thus obtained NiO. Since also during LNO synthesis, the conversion of $Ni(OH)_2$ to NiO occurs already below 300 °C, prior to the onset of lithiation, no large change in reactivity is expected when employing NiO instead of $Ni(OH)_2$ as pCAM as long as particle morphology is conserved.[73,74] The Zr-containing, co-precipitated pCAM of equal size (d_{50} = 4 μm) is shown in Figs. S1e and S1f. It was surprisingly

found by elemental analysis that the co-precipitated pCAM contained more carbon than the regular pCAM, as detailed in Table S1. To reduce the carbon content, in one variation, the co-precipitated ("co-prec." in figures) pCAM was subjected to the same heating procedure in O_2 by which the impregnated pCAM was pre-dried, thereby oxidizing organic residues to CO_2 and converting $Ni(OH)_2$ to NiO. The resulting pCAM is shown in Figs. S1g and S1h. Probable sources of the residues are the use of organic complexing agents such as citric acid or lactic acid, the use of metal acetates as precursors in the precipitation reaction or base solution being exposed to atmospheric CO_2 before or during precipitation.[57,65,75,76]

The dopant distribution in the Zr-containing pCAMs was analyzed via STEM-EDS, as shown in Fig. S2. Impregnation resulted in the formation of a surface coating-like zirconium layer on the secondary particles, and there are no large agglomerates outside of the pCAM. Between secondary particles, Zr^{4+} seems evenly distributed, but the content within the particles is too close to the detection limit to be discussed quantitatively from EDS. Co-precipitated pCAM also shows Zr^{4+} to be evenly distributed between and within secondary particles, yet in the non-pre-dried pCAM particulate zirconium enrichment was observed in one case. No such enrichment was evident after pre-drying.

Composition and crystal structure.—Table I summarizes the composition of the 10 LNO samples discussed in this work according to ICP-OES and acid titration. As expected, a high content of Li_2CO_3 was found in the co-precipitated sample after calcination. Li_2CO_3 and LiOH are common impurities formed by residual lithium upon contact with CO_2 and H_2O in air.[77,78] The excess carbonate, however, was formed during calcination by the decomposition of organic residues in the pCAM (in the presence of lithium), since it is not observed for the other LNO samples, which were handled in the same way and the carbon source was already present in the pCAM. A fifth set of LNO was thus prepared from the pre-dried, co-precipitated pCAM.

PXRD patterns (see Figs. S3 and S4) of each sample confirm the LNO structure and additionally show the presence of aforementioned Li_2CO_3 impurities (see Figs. S5 and S6) for the co-precipitated samples. Rietveld refinement was performed to determine the unit-cell volume, apparent crystallite size and off-stoichiometry, with the results shown in Table II. As expected, a clear trend is observed between calcination temperature and crystallite size for all samples, as reported previously.[5,6] A slight increase in off-stoichiometry is also observed with increasing calcination temperature, except for the LNO obtained from co-precipitated pCAM. The higher off-stoichiometry in these materials is explained by the formation of Li-containing impurities. While Zr-doping is reported to increase the c lattice parameter and therefore the unit-cell volume,[26,43,46,53,60,65] the effect is likely overshadowed in this study due to the low chosen concentration and the also present effect of off-stoichiometry. At the same time, the low concentration of Zr^{4+} did not allow for inclusion of its position and occupancy in the refinement, which might explain the slightly lower quality of fit when compared to LNO from a previous report characterized under the same measurement conditions.[5]

Particle morphology.—SEM images of the different LNO particles calcined at 700 °C are shown in Fig. 1a. It is evident that the shape and size of primary particles are highly dependent on the chosen process route, while the secondary particle morphology and size were hardly affected. The primary particle size distribution determined by automated image segmentation[6] is shown in Fig. 1b and is in good agreement with the crystallite size obtained from PXRD.

No discernible difference in primary particle size is observed between undoped and co-calcined material, while LNO obtained from impregnated and non-pre-dried, co-precipitated pCAM is composed of smaller primary particles, with a large share of <200 nm particles. On the other hand, the pre-dried, co-precipitated pCAM resulted in larger primary particles compared to all other samples. It has previously been reported that Zr^{4+} doping is associated with reduced primary particle size,[47] as are other dopants, mostly of higher valence state.[20,49,50,59] The observed restriction of grain growth can be explained by a dopant-induced change in surface energy, including segregation of dopant along grain boundaries.[17,59] This is not limited to battery materials, but can be applied to the sintering of ceramics in general.[79,80]

Since in this work all LNO samples are doped by nominally equal amounts of Zr^{4+}, the difference in primary particle size must be connected to the process route by which zirconium was provided. During the synthesis, first the incorporation of lithium into the rocksalt structure of NiO and later the formation of LNO occur already at lower temperatures such as the herein applied hold at 400 °C, or during ramp up to the final calcination temperature, which is then held mostly to allow for layer formation, i.e. reduction of the amount of Ni^{2+} on the Li-site, and particle growth.[73,74] Assuming the role of Zr^{4+} as grain growth-reducing dopant and considering Fig. S2, a possible explanation for the difference in particle size is the initial distribution of Zr^{4+}. In case of impregnation, zirconium is already present at the grain boundaries, while in co-precipitated material, it has to diffuse from the bulk to the grain boundaries, and in case of co-calcination, from the ZrO_2 precursor to the CAM particles. In studies using the conversion of a ZrO_2 coating to achieve doping, diffusion of Zr^{4+} into the bulk was only observed at temperatures around 700 °C.[56,60]

For the non-pre-dried, co-precipitated material, the carbon-based impurity likely aided in Zr^{4+} diffusion or was an active segregant itself. Figure S7 shows the obtained particles and their size distribution for a final calcination temperature of 750 °C. Again, the crystallite size from PXRD refinement is in good agreement with the average primary particle size determined from image segmentation.[6] At higher temperature, faster Zr^{4+} diffusion and particle growth as well as change in Zr^{4+} solubility[64] alleviated the effect of dopant, with only the carbon-contaminated, co-precipitated pCAM yielding smaller primary particles.

Table I. ICP-OES and acid titration results.

LNO sample	Calcination temperature ϑ/ °C	Zr/(Ni+Zr)/mol%	Li_2CO_3/wt%	LiOH/wt%
Undoped	700	n.a.	0.59	0.93
	750	n.a.	0.51	0.49
Co-calcination	700	0.22	0.58	1.02
	750	0.22	0.57	0.50
Impregnation	700	0.22	0.45	1.01
	750	0.22	0.37	0.64
Co-precipitation	700	0.26	1.37	1.19
	750	0.26	1.22	0.51
Co-precipitation (pre-dried)	700	0.26	0.40	0.86
	750	0.26	0.36	0.68

Table II. Rietveld refinement results. Ni_{Li} describes Ni^{2+} occupancy on the Li-site and R_{Bragg} and χ^2 indicate the goodness of fit.

LNO sample	Calcination temperature ϑ/ °C	Crystallite size/nm	Unit-cell volume/Å^3	Ni_{Li}/%	R_{Bragg}	χ^2
Undoped	700	242	101.793	2.5	3.06	63.2
	750	512	101.829	3.2	2.64	95.3
Co-calcination	700	194	101.821	2.6	2.28	95.7
	750	454	101.841	3.4	2.38	93.1
Impregnation	700	183	101.711	2.2	2.41	83.1
	750	498	101.742	2.7	2.95	141.0
Co-precipitation	700	211	101.940	3.1	2.40	115.0
	750	352	101.958	3.0	2.31	121.0
Co-precipitation (pre-dried)	700	293	101.667	2.9	2.82	98.4
	750	672	101.723	2.8	3.09	124.0

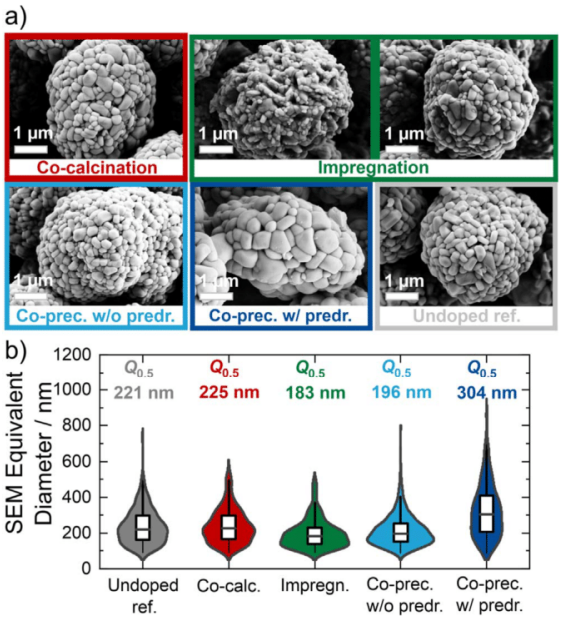

Figure 1. Dependence of (a) particle morphology and (b) size on process route for LNO calcined at 700 °C.

Dopant distribution after calcination.—The distribution of dopant both within and between secondary particles in dependence of the chosen process route is elucidated via STEM-EDS and LA-ICP-MS, as shown in Figs. 2a–2d and 3a–3d for all samples calcined at 700 °C. While EDS provides high-resolution images of the Zr^{4+} distribution within secondary particles, statistical evaluation and interparticle comparisons are difficult. On the other hand, LA-ICP-MS delivers the interparticle-dependent relative distribution and allows for statistical evaluation due to a high number of sampled secondary particles.[81,82] Particle or area-resolved ICP techniques have previously found applications in the battery context, for example in the study of NCM classification[83] and subsequent SOC heterogeneity,[84] transition-metal deposition on anodes[85] and local solid-electrolyte composition.[86]

Using EDS, it was found that all process routes result in an enrichment of zirconium at grain boundaries, as it was presumed in the previous section and is in accordance with literature reports.[31,51,53,61,62] The concentration within the primary particles is too close to the detection limit to be discussed quantitatively, but all primary particles appear to contain a rather similar concentration of Zr^{4+}. Only in LNO stemming from pre-dried, co-precipitated pCAM, a separation of small Zr-rich grains was observed in a few particles, see Fig. 2d. Similar observations, albeit with slightly less apparent grain-boundary enrichment, were made for the samples calcined at 750 °C (see Fig. S8).

Via LA-ICP-MS, the relative composition of individual secondary particles can be determined, here shown in a comparison of Zr and Ni counts. The absolute count number of Ni is directly proportional to the particle mass (i.e. to the cube of particle size), so that a high linearity between absolute Zr count and absolute Ni count indicates a uniform interparticulate Zr^{4+} distribution.[81,87,88] While all process routes lead to a rather uniform distribution of Zr^{4+} between secondary particles, co-precipitation without pre-drying gave an especially narrow dopant distribution. Outliers are visible in Fig. 3d and support the observation of separated, Zr-rich grains as discussed for Fig. 2d. At a calcination temperature of 750 °C, the distribution of Zr^{4+} between secondary particles became much broader for all process routes, i.e. more inhomogeneous, as shown in Fig. S9.

Electrochemical properties.—Having established the particle and dopant properties, all materials were tested electrochemically. Figure 4a shows the discharge capacity of coin half-cells (referred to as CHC) over 56 cycles for the LNO samples calcined at 700 °C. Even in the first two cycles at a rate of C/20, a difference of up to 10 mAh g^{-1} depending on the chosen process route is evident, with LNO obtained from impregnated pCAM delivering the highest (250 mAh g^{-1}) and LNO from pre-dried, co-precipitated pCAM delivering the lowest specific capacity (240 mAh g^{-1}). After a rate test and 50 cycles at C/3, this difference increased to 25 mAh g^{-1}, with LNO obtained from impregnated pCAM again delivering the highest (180 mAh g^{-1}) and LNO from pre-dried, co-precipitated pCAM delivering the lowest specific capacity (155 mAh g^{-1}). Undoped LNO, co-calcined LNO and LNO from non-pre-dried, co-precipitated pCAM all showed very similar performance, with 166 mAh g^{-1} remaining after cycling.

The initial difference in specific capacity, a consequence of the first-cycle irreversibility, was previously shown to be determined by primary particle size,[6,7,89] wherein smaller particles result in a larger interface area between CAM and electrolyte. This interface area was monitored in situ by the capacitance method of Oswald et al.,[67–69] with the resulting specific capacitance shown in Fig. 4b. Before cycling, all materials show similar capacitance values, in good agreement with the finding that the specific capacitance of pristine CAM is largely determined by the secondary particle size (specific surface area).[6] The only exception is a slightly higher specific capacitance of LNO obtained from non-pre-dried, co-precipitated pCAM. Since this material contains a higher amount of surface impurities, the difference may be explained by the exposure of fresh surface after their partial decomposition/dissolution into the electrolyte, similar to the effect of washing discussed in the literature.[6] In the following 4–5 cycles, an increase to an individual level is observed for all materials, with the capacitance then remaining close to this maximum level in the following cycles. The increase is due to particle fracture upon cycling, enabling the inner pore network of the

Journal of The Electrochemical Society, 2023 **170** 060530

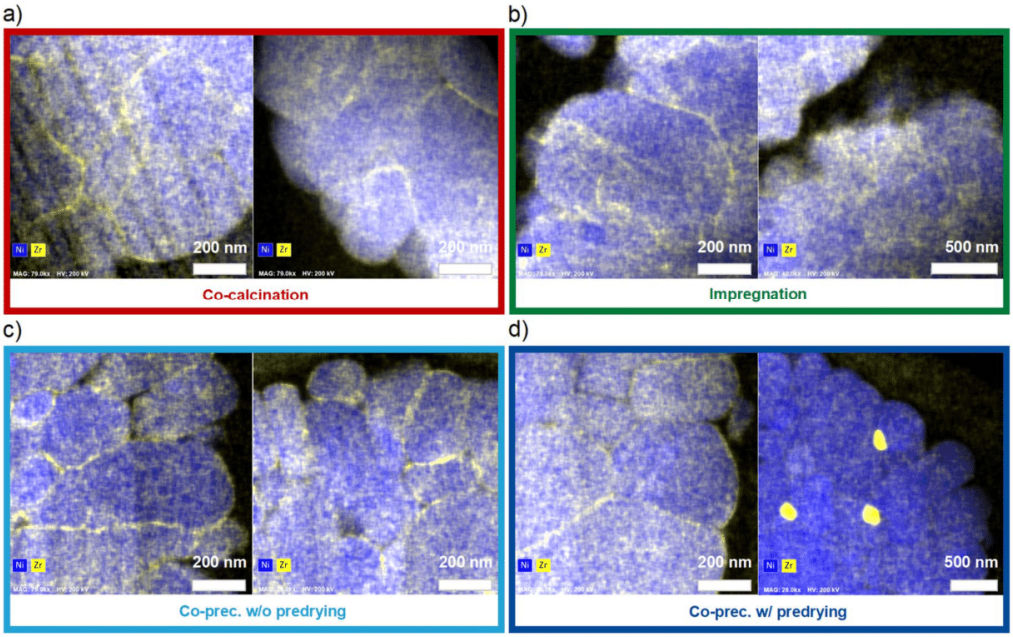

Figure 2. STEM-EDS investigation of Zr^{4+} distribution in secondary particles of LNO calcined at 700 °C. Ni is mapped in blue, Zr in yellow.

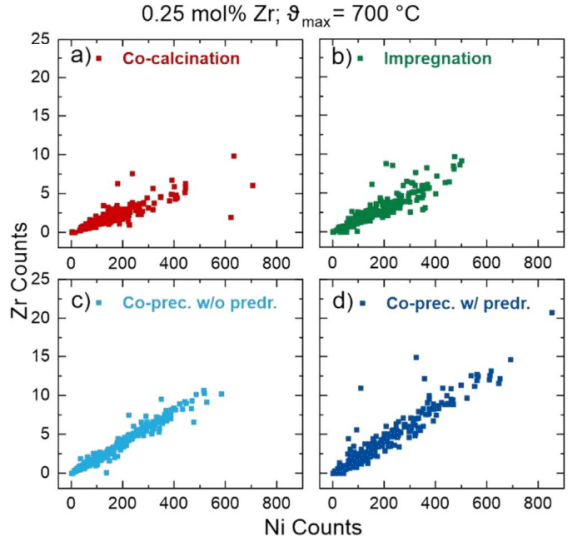

Figure 3. LA-ICP-MS investigation of Zr^{4+} distribution between secondary particles for LNO samples calcined at 700 °C.

secondary particles to be penetrated by electrolyte. The maximum value for each material is determined by the primary particle size, with smaller particles as those obtained from impregnated or non-pre-dried, co-precipitated pCAM resulting in higher capacitance because of their larger specific surface area. It is this surface area and specific capacitance that has been shown to determine both the first-cycle capacity loss and long-term cycling performance due to reduced kinetic hindrance of lithium intercalation at the end of discharge.[6]

For LNO from either impregnated or non-pre-dried, co-precipitated pCAM, the two materials with the smallest primary particle size and therefore largest capacitance, the same maximum value (0.69 F g^{-1}) is obtained. However, both a distinct difference in the increase of capacitance and a difference in cycling performance are found, suggesting these observations to be correlated. For LNO from non-pre-dried, co-precipitated pCAM, a rapid increase in capacitance, especially after just one cycle, is observed and the maximum value reached after five cycles. It can be assumed that the rapid capacitance increase is again due to the presence of surface impurities, which upon decomposition/dissolution during the first charge reveal previously covered surface and blocked pores. However, this also leads to further side reactions such as electrolyte degradation, which likely contributes to the lower cycling performance in comparison to the sample prepared by impregnation. At the same time, for LNO from impregnated pCAM a slower, continuous increase until the 12th cycle is observed. A possible explanation is a slower crack-formation process due to the previously discussed Zr-rich grain boundaries acting as a protective coating, while the beneficial kinetics resulting from the smaller primary particles still leads to greater specific capacities. The data for LNO calcined at 750 °C, where larger particle size reduced the electrochemical performance and specific capacitance, are shown in Fig. S10.

In various studies, it has been shown that a higher capacity retention of doped material correlates with a smaller particle or grain size relative to undoped material achieved by modification with high valence dopants.[20,49,50,59] In these cases, the smaller particle size resulted from dopant-induced grain growth suppression. In this work, a similar performance dependency on particle size is observed and especially clear in the comparison of impregnated and co-calcined LNO, while the surface impurities and their presence, respectively removal, may additionally affect the performance of co-precipitated LNO. Nevertheless, the observation of different primary particle sizes in nominally equally doped CAM depending on the process route, in combination with no difference in particle size and performance between co-calcined and undoped LNO, means that the route of dopant introduction, and not the sole addition of dopant, is at the root of performance improvement.

For the samples calcined at 700 °C, further characterization was performed. Figure 5a shows the discharge capacity of pouch full

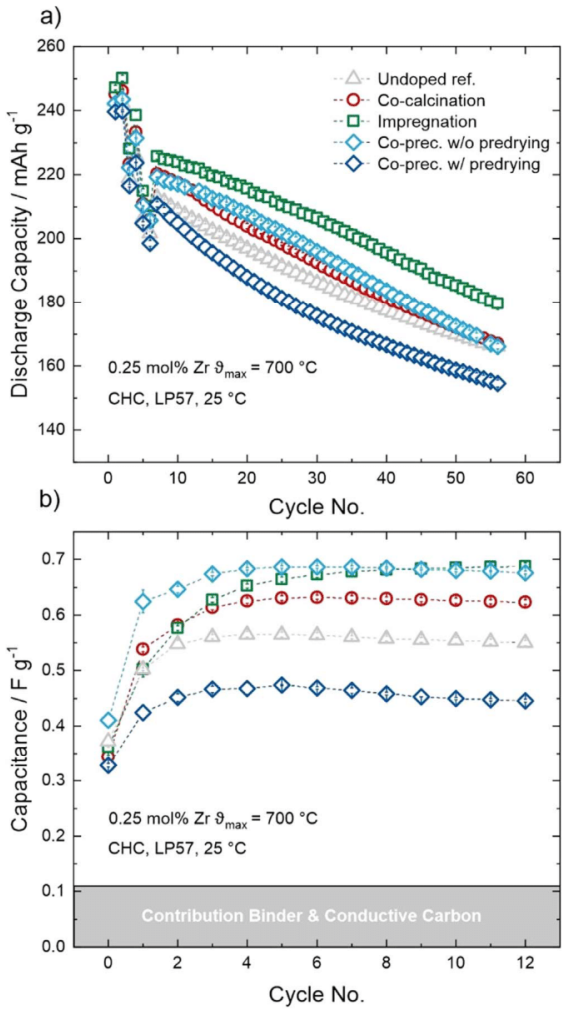

Figure 4. Electrochemical testing of Zr-doped LNO CAMs (calcined at 700 °C) in coin half-cells. (a) Specific discharge capacity in the two initial cycles at C/20, during a rate test (one cycle each at C/3, C/10, 1 C and 2 C) and upon C/3 cycling. (b) Specific capacitance evolution during C/10 cycling.

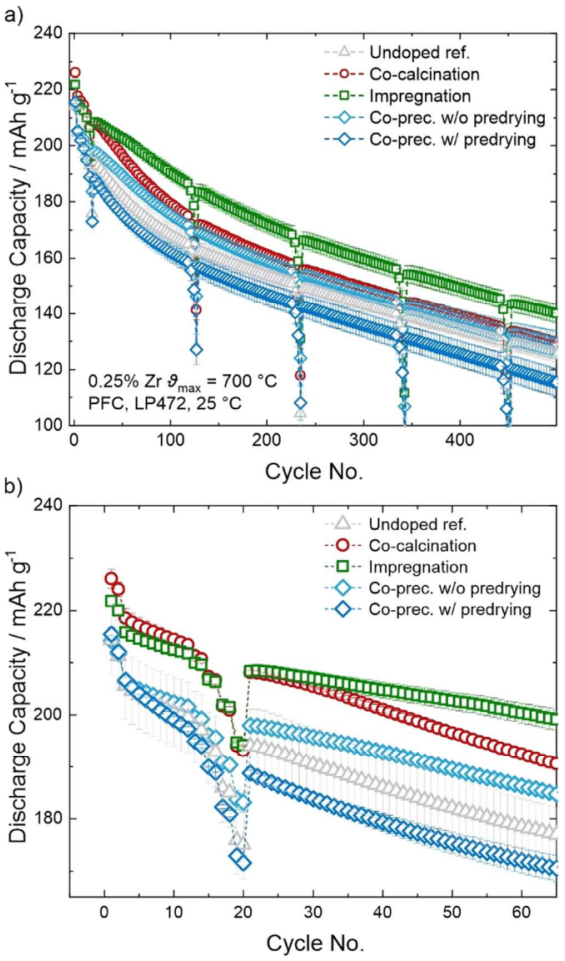

Figure 5. Electrochemical testing of Zr-doped LNO CAMs (calcined at 700 °C) in pouch full cells. Specific discharge capacity at C/3 with intermittent rate tests (C/3 charge and two cycles each at 0.5 C, 1 C, 2 C and 3 C discharge). (a) Long-term cycling performance and (b) first 50 cycles.

cells (referred to as PFC) during long-term cycling for each material. The overall performance is in the same order as for coin half-cells, except for the co-calcined LNO, where a slightly better cyclability is observed early in the testing, with 226 mAh g^{-1} at C/20 in the initial cycle and 208 mAh g^{-1} at C/3 after the rate test. The best performance is found for LNO obtained by pCAM impregnation (222 mAh g^{-1} in the initial cycle). The difference in capacity (capacity fade rate) between the materials remains rather constant from 150 cycles onward, as can be expected for uncoated CAM suffering mostly from continuous rocksalt-type phase formation and loss of Li inventory. While LNO obtained from pCAM impregnation, with a specific capacity of 180 mAh g^{-1} after 150 cycles and 140 mAh g^{-1} after 500 cycles, performs best in the later cycles, LNO from pre-dried, co-precipitated pCAM delivers specific capacities of only 215, 154 and 115 mAh g^{-1} in the 1st, 150th and 500th cycle, respectively. Figure 5b highlights the first 50 cycles, showing that, with the exception of slightly better performance of co-calcined LNO, the difference in cyclability between the materials is already established in the initial cycles (mostly due to the primary particle size), in agreement with both the coin cell data and capacitance trends discussed previously (see Fig. 4).

Lastly, for all CAMs calcined at 700 °C, the CO_2 evolution in the formation cycle was determined via DEMS. While the largest share of gas evolution during formation is due to solid electrolyte interphase (SEI) formation under release of ethylene at the anode, CO_2 generation is commonly observed at the cathode side.[72,90] In general, possible causes of CO_2 evolution are chemical oxidation of electrolyte by oxygen released from the CAM lattice during rocksalt-type layer formation at SOC > 80%,[91,92] electrochemical oxidation of carbonate electrolyte at potentials larger than ~4.6 V vs Li^+/Li[93] and decomposition of surface carbonate impurities.[94] In the initial cycle, and without overcharging, surface carbonate impurities often dominate the gas evolution, as the potential is too low for electrochemical oxidation and significant lattice oxygen release.[95] However, it is important to consider that a fair comparison of total gas evolution is thus only possible at similar SOC, i.e. specific charge capacity.[72,96,97] Therefore, Fig. 6 depicts both the total first-cycle CO_2 evolution and the charge capacity achieved with the DEMS cells. An exemplary gas evolution profile is shown for LNO from impregnated pCAM in Fig. S11. Note that delayed gas

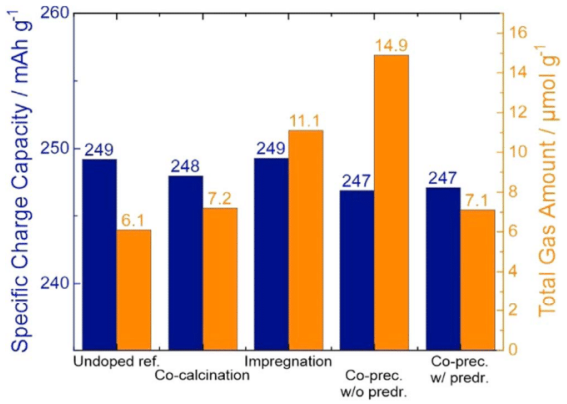

Figure 6. Comparison of total first-cycle gas evolution as determined by DEMS at similar specific charge capacity for LNO samples calcined at 700 °C.

evolution during discharge in the initial cycle is common for layered Ni-rich oxides.[98–100] Second-cycle gas evolution could not be quantified for all materials because of the low overall gassing of clean and dry-processed CAM at a regular cut-off potential of 4.3 vs Li^+/Li. Similarly, no molecular O_2 is detected, as it immediately reacts with the electrolyte upon release forming CO_2. The obtained gas amounts at this potential are in good agreement with previous reports.[69,92,95,99,101]

The observed larger total gas evolution for LNO obtained from non-pre-dried, co-precipitated pCAM is mostly a consequence of the higher amount of surface carbonates, as also reflected in the acid titration results shown in Table I. However, it should be noted that not all surface carbonates are decomposed to CO_2 in the initial cycle.[95,97] Given that an increased CO_2 amount is also observed for the LNO obtained from impregnated pCAM, the other material with smaller primary particles, a contribution of lower primary particle size, i.e. higher specific surface area, has to be considered too, since a larger surface for carbonate impurities and rocksalt-type layer formation is exposed to electrolyte, which has been demonstrated by correlation of capacitance measurements with gas evolution data.[69,101] These results demonstrate that even "advanced" characterization methods are affected by the doping process route and resulting primary particle size differences, as a mere comparison between doped and undoped material would lead to different results depending on the chosen route.

Conclusions

In this work, the relations between dopant, process route, primary particle size and electrochemical performance of LNO were investigated on the example of 0.25 mol% Zr^{4+} doping. A comparison of undoped LNO and doped LNO either from co-calcination, co-precipitation or impregnation revealed that, while all materials showed similar unit-cell parameters and off-stoichiometry, the primary particle size was greatly affected by the process route, yet not by the mere presence of dopant. The dopant distribution in precursors as well as within and between secondary LNO particles was examined. Zirconium enrichment was found at the grain boundaries, suggesting a crystal growth inhibition mechanism for the dopant, the extent of which is depending on the initial dopant localization during calcination, and explaining the role of the doping process route. As the primary particle size determines the electrochemical performance, the different process routes consequently also manifest in cyclability, which was demonstrated not only in coin half-cells but also by long-term cycling of pouch full cells. Finally, other properties such as specific capacitance and gas evolution during cycling were also shown to be affected by the doping process route. Impregnation resulted in the smallest primary particles and therefore best electrochemical performance. The obtained results highlight that when studying dopants in small, industrially relevant concentrations, the process route determines the outcome of the study and needs to be chosen carefully. The significance of the process route as a function of the dopant concentration remains to be studied, as higher concentrations may lead to more significant segregation/phase separation and lattice parameter changes.

Acknowledgments

Francois Fauth and the BL04-MSPD beamline team at the ALBA synchrotron are acknowledged for their support to the PXRD measurements. Marie Duffiet and Damian Goonetilleke from KIT are acknowledged for performing the PXRD measurements. Felix Riewald from BASF SE is acknowledged for insightful discussions. This work was partially supported by BASF SE. This project has received funding from the European Union's Horizon 2020 research and innovation programme under grant agreement no. 957189. The project is part of BATTERY 2030+, the large-scale European research initiative for inventing the sustainable batteries of the future.

Data Availability Statement

The data that support the findings of this study are available from the corresponding author upon reasonable request.

ORCID

Philipp Kurzhals https://orcid.org/0000-0002-7013-080X
Torsten Brezesinski https://orcid.org/0000-0002-4336-263X
Jürgen Janek https://orcid.org/0000-0002-9221-4756

References

1. A. Manthiram, *Nat. Commun.*, **11**, 1550 (2020).
2. U.-H. Kim et al., *Energy Environ. Sci.*, **11**, 1271 (2018).
3. C. S. Yoon, D.-W. Jun, S.-T. Myung, and Y.-K. Sun, *ACS Energy Lett.*, **2**, 1150 (2017).
4. M. Bianchini, M. Roca-Ayats, P. Hartmann, T. Brezesinski, and J. Janek, *Angew. Chem. Int. Ed.*, **58**, 10434 (2019).
5. P. Kurzhals, F. Riewald, M. Bianchini, H. Sommer, H. A. Gasteiger, and J. Janek, *J. Electrochem. Soc.*, **168**, 110518 (2021).
6. F. Riewald, P. Kurzhals, M. Bianchini, H. Sommer, J. Janek, and H. A. Gasteiger, *J. Electrochem. Soc.*, **169**, 020529 (2022).
7. Z. Xu, Z. Wang, X. Tan, H. Guo, W. Peng, X. Li, J. Wang, and G. Yan, *J. Electrochem. Soc.*, **169**, 090520 (2022).
8. H.-J. Noh, S. Youn, C. S. Yoon, and Y.-K. Sun, *J. Power Sources*, **233**, 121 (2013).
9. N. S. Luu, K.-Y. Park, and M. C. Hersam, *Acc. Mater. Res.*, **3**, 511 (2022).
10. H.-H. Sun and A. Manthiram, *Chem. Mater.*, **29**, 8486 (2017).
11. P. Mukherjee, P. Lu, N. Faenza, N. Pereira, G. Amatucci, G. Ceder, and F. Cosandey, *ACS Appl. Mater. Interfaces*, **13**, 17478 (2021).
12. J. Xu, E. Hu, D. Nordlund, A. Mehta, S. N. Ehrlich, X.-Q. Yang, and W. Tong, *ACS Appl. Mater. Interfaces*, **8**, 31677 (2016).
13. Z. Cui, X. Li, X. Bai, X. Ren, and X. Ou, *Energy Storage Mater.*, **57**, 14 (2023).
14. C. P. Grey and D. S. Hall, *Nat. Commun.*, **11**, 6279 (2020).
15. Z. Ahaliabadeh, X. Kong, E. Fedorovskaya, and T. Kallio, *J. Power Sources*, **540**, 231633 (2022).
16. J. Yan, H. Huang, J. Tong, W. Li, X. Liu, H. Zhang, H. Huang, and W. Zhou, *Interdiscip. Mater.*, **1**, 330 (2022).
17. K.-J. Park, H.-G. Jung, L.-Y. Kuo, P. Kaghazchi, C. S. Yoon, and Y.-K. Sun, *Adv. Energy Mater.*, **8**, 1801202 (2018).
18. H.-H. Ryu, S.-B. Lee, and Y.-K. Sun, *J. Solid State Electrochem.*, **26**, 2097 (2022).
19. Y. Levartovsky, X. Wu, C. Erk, S. Maiti, J. Grinblat, M. Talianker, and D. Aurbach, *Battery Supercaps*, **4**, 221 (2021).
20. H. H. Sun, U.-H. Kim, J.-H. Park, S.-W. Park, D.-H. Seo, A. Heller, C. B. Mullins, C. S. Yoon, and Y.-K. Sun, *Nat. Commun.*, **12**, 6552 (2021).
21. Y. Levartovsky, S. Kunnikuruvan, A. Chakraborty, S. Maiti, J. Grinblat, M. Talianker, D. T. Major, and D. Aurbach, *J. Electrochem. Soc.*, **168**, 060552 (2021).
22. X. Jia, M. Yan, Z. Zhou, X. Chen, C. Yao, D. Li, D. Chen, and Y. Chen, *Electrochim. Acta*, **254**, 50 (2017).
23. S. Liu, Z. Dang, D. Liu, C. Zhang, T. Huang, and A. Yu, *J. Power Sources*, **396**, 288 (2018).
24. Y. Ming et al., *ACS Appl. Mater. Interfaces*, **12**, 8146 (2020).
25. X. Tan, W. Peng, M. Wang, G. Luo, Z. Wang, G. Yan, H. Guo, Q. Li, and J. Wang, *Prog. Nat. Sci. Mater. Int.*, **33**, 108 (2023).

26. C. S. Yoon, M.-J. Choi, D.-W. Jun, Q. Zhang, P. Kaghazchi, K.-H. Kim, and Y.-K. Sun, *Chem. Mater.*, **30**, 1808 (2018).
27. L. Wang, G. Liu, X. Ding, C. Zhan, and X. Wang, *ACS Appl. Mater. Interfaces*, **11**, 33901 (2019).
28. Z. Huang, Z. Wang, X. Zheng, H. Guo, X. Li, Q. Jing, and Z. Yang, *Electrochim. Acta*, **182**, 795 (2015).
29. B. Zhang, L. Li, and J. Zheng, *J. Alloys Compd.*, **520**, 190 (2012).
30. A. L. Lipson et al., *ACS Appl. Mater. Interfaces*, **12**, 18512 (2020).
31. C. S. Yoon, U.-H. Kim, G.-T. Park, S. J. Kim, K.-H. Kim, J. Kim, and Y.-K. Sun, *ACS Energy Lett.*, **3**, 1634 (2018).
32. Y. Lu, M. Pang, S. Shi, Q. Ye, Z. Tian, and T. Wang, *Sci. Rep.*, **8**, 2981 (2018).
33. J. Cheng, L. Mu, C. Wang, Z. Yang, H. L. Xin, F. Lin, and K. A. Persson, *J. Mater. Chem. A*, **8**, 23293 (2020).
34. L. Mu et al., *Chem. Mater.*, **31**, 9769 (2019).
35. H. Li, P. Zhou, F. Liu, H. Li, F. Cheng, and J. Chen, *Chem. Sci.*, **10**, 1374 (2019).
36. L. Mu, W. H. Kan, C. Kuai, Z. Yang, L. Li, C.-J. Sun, S. Sainio, M. Avdeev, D. Nordlund, and F. Lin, *ACS Appl. Mater. Interfaces*, **12**, 12874 (2020).
37. A. Gomez-Martin, F. Reissig, L. Frankenstein, M. Heidbüchel, M. Winter, T. Placke, and R. Schmuch, *Adv. Energy Mater.*, **12**, 2103045 (2022).
38. M. Yi, W. Li, and A. Manthiram, *Chem. Mater.*, **34**, 629 (2022).
39. G. Li, X. Rao, W. Yao, M. Zeng, S. Zhong, and H. Cheng, *Ionics*, **28**, 1055 (2022).
40. R. Du, Y. Bi, W. Yang, Z. Peng, M. Liu, Y. Liu, B. Wu, B. Yang, F. Ding, and D. Wang, *Ceram. Int.*, **41**, 7133 (2015).
41. T. Chen, X. Li, H. Wang, X. Yan, L. Wang, B. Deng, W. Ge, and M. Qu, *J. Power Sources*, **374**, 1 (2018).
42. D. Kitsche, S. Schweidler, A. Mazilkin, H. Geßwein, F. Fauth, E. Suard, P. Hartmann, T. Brezesinski, J. Janek, and M. Bianchini, *Mater. Adv.*, **1**, 639 (2020).
43. B. Han, S. Xu, S. Zhao, G. Lin, Y. Feng, L. Chen, D. G. Ivey, P. Wang, and W. Wei, *ACS Appl. Mater. Interfaces*, **10**, 39599 (2018).
44. G.-H. Kang, K.-W. Lee, K. Kwon, and J. Song, *Metals*, **7**, 395 (2017).
45. F. Wu, N. Liu, L. Chen, N. Li, Y. Lu, D. Cao, M. Xu, Z. Wang, and Y. Su, *ACS Appl. Mater. Interfaces*, **13**, 24925 (2021).
46. C.-H. Jung et al., *J. Mater. Chem. A*, **9**, 17415 (2021).
47. Q. Li, Z. Li, S. Wu, Z. Wang, X. Liu, W. Li, N. Li, J. Wang, and W. Zhuang, *ACS Appl. Energy Mater.*, **3**, 11741 (2020).
48. Y. Shen, X. Yao, S. Wang, D. Zhang, D. Yin, L. Wang, and Y. Cheng, *ACS Appl. Mater. Interfaces*, **13**, 58871 (2021).
49. M. Dalkilic, A. Schmidt, T. D. Schladt, P. Axmann, M. Wohlfahrt-Mehrens, and M. Lindén, *J. Electrochem. Soc.*, **169**, 120501 (2022).
50. M. Dalkilic, A. Schmidt, T. D. Schladt, P. Axmann, M. Wohlfahrt-Mehrens, and M. Lindén, *J. Electrochem. Soc.*, **169**, 090504 (2022).
51. Y. Huang, J. Chen, J. Ni, H. Zhou, and X. Zhang, *J. Power Sources*, **188**, 538 (2009).
52. D. Goonetilleke, A. Mazilkin, D. Weber, Y. Ma, F. Fauth, J. Janek, T. Brezesinski, and M. Bianchini, *J. Mater. Chem. A*, **10**, 7841 (2022).
53. F. Schipper et al., *J. Mater. Chem. A*, **4**, 16073 (2016).
54. F. A. Susai et al., *Materials*, **14**, 2070 (2021).
55. I. H. Kwon, H. R. Park, and Y. Y. Song, *Russ. J. Electrochem.*, **49**, 221 (2013).
56. F. Schipper et al., *Adv. Energy Mater.*, **8**, 1701682 (2018).
57. T. R. Penki et al., *J. Solid State Electrochem.*, **25**, 1513 (2021).
58. D. Weber, J. Lin, A. Pokle, K. Volz, J. Janek, T. Brezesinski, and M. Bianchini, *J. Electrochem. Soc.*, **169**, 030540 (2022).
59. G.-T. Park et al., *Energy Environ. Sci.*, **14**, 6616 (2021).
60. S. Tubtimkuna, N. Phattharasupakun, P. Bunyanidhi, and M. Sawangphruk, *Adv. Mater. Technol.*, **7**, 2200436 (2022).
61. F. Reissig, M. A. Lange, L. Haneke, T. Placke, W. G. Zeier, M. Winter, R. Schmuch, and A. Gomez-Martin, *Chem. Sus. Chem.*, **15**, e202102220 (2022).
62. X. Li, K. Zhang, M. Wang, Y. Liu, M. Qu, W. Zhao, and J. Zheng, *Sustain. Energy Fuels*, **2**, 413 (2018).
63. S. Sivaprakash and S. B. Majumder, *J. Alloys Compd.*, **479**, 561 (2009).
64. Y. Kim, *Phys. Chem. Chem. Phys.*, **21**, 12505 (2019).
65. Q. Chen, C. Du, D. Qu, X. Zhang, and Z. Tang, *RSC Adv.*, **5**, 75248 (2015).
66. C.-S. Kim, K. M. Jeong, K. Kim, and C.-W. Yi, *Electrochim. Acta*, **155**, 431 (2015).
67. S. Oswald, F. Riewald, and H. A. Gasteiger, *J. Electrochem. Soc.*, **169**, 040552 (2022).
68. S. Oswald, D. Pritzl, M. Wetjen, and H. A. Gasteiger, *J. Electrochem. Soc.*, **167**, 100511 (2020).
69. S. Oswald, D. Pritzl, M. Wetjen, and H. A. Gasteiger, *J. Electrochem. Soc.*, **168**, 120501 (2021).
70. B. B. Berkes, A. Jozwiuk, H. Sommer, T. Brezesinski, and J. Janek, *Electrochem. Commun.*, **60**, 64 (2015).
71. B. B. Berkes, A. Jozwiuk, M. Vracar, H. Sommer, T. Brezesinski, and J. Janek, *Anal. Chem.*, **87**, 5878 (2015).
72. S. L. Dreyer, A. Kondrakov, J. Janek, and T. Brezesinski, *J. Mater. Res.*, **37**, 3146 (2022).
73. M. Bianchini, F. Fauth, P. Hartmann, T. Brezesinski, and J. Janek, *J. Mater. Chem. A*, **8**, 1808 (2020).
74. P. Kurzhals, F. Riewald, M. Bianchini, S. Ahmed, A. M. Kern, F. Walther, H. Sommer, K. Volz, and J. Janek, *J. Electrochem. Soc.*, **169**, 050526 (2022).
75. R. Wang, Z. Li, Z. Yang, M. Zhang, D. Zhang, and Y. Yan, *Ceram. Int.*, **47**, 1268 (2021).
76. J.-Z. Kong, H.-F. Zhai, C. Ren, G.-A. Tai, X.-Y. Yang, F. Zhou, H. Li, J.-X. Li, and Z. Tang, *J. Solid State Electrochem.*, **18**, 181 (2014).
77. J. Kim, H. Lee, H. Cha, M. Yoon, M. Park, and J. Cho, *Adv. Energy Mater.*, **8**, 1702028 (2018).
78. Y. Kim, H. Park, J. H. Warner, and A. Manthiram, *ACS Energy Lett.*, **6**, 941 (2021).
79. H. Li, S. Dey, and R. H. R. Castro, *Acta Mater.*, **150**, 394 (2018).
80. F. Liu and R. Kirchheim, *J. Cryst. Growth*, **264**, 385 (2004).
81. S. B. Seiffert, F. Riewald, R. B. Berk, and U. Karst, *Manuscript in Preparation*.
82. P. J. Sylvester and S. E. Jackson, *Elements*, **12**, 307 (2016).
83. T.-N. Kröger, S. Wiemers-Meyer, P. Harte, M. Winter, and S. Nowak, *Anal. Chem.*, **93**, 7532 (2021).
84. T.-N. Kröger, P. Harte, S. Klein, T. Beuse, M. Börner, M. Winter, S. Nowak, and S. Wiemers-Meyer, *J. Power Sources*, **527**, 231204 (2022).
85. T. Schwieters, M. Evertz, A. Fengler, M. Börner, T. Dagger, Y. Stenzel, P. Harte, M. Winter, and S. Nowak, *J. Power Sources*, **380**, 194 (2018).
86. S. Smetaczek, A. Wachter-Welzl, R. Wagner, D. Rettenwander, G. Amthauer, L. Andrejs, S. Taibl, A. Limbeck, and J. Fleig, *J. Mater. Chem. A*, **7**, 6818 (2019).
87. K. S. Ho, K. O. Lui, K. H. Lee, and W. T. Chan, *Spectrochim. Acta, Part B*, **89**, 30 (2013).
88. D. Mozhayeva and C. Engelhard, *J. Anal. At. Spectrom.*, **35**, 1740 (2020).
89. A. Liu, N. Phattharasupakun, M. M. E. Cormier, E. Zsoldos, N. Zhang, E. Lyle, P. Arab, M. Sawangphruk, and J. R. Dahn, *J. Electrochem. Soc.*, **168**, 070503 (2021).
90. B. Rowden and N. Garcia-Araez, *Energy Reports*, **6**, 10 (2020).
91. J. Wandt, A. T. S. Freiberg, A. Ogrodnik, and H. A. Gasteiger, *Mater. Today*, **21**, 825 (2018).
92. D. Streich, C. Erk, A. Guéguen, P. Müller, F.-F. Chesneau, and E. J. Berg, *J. Phys. Chem. C*, **121**, 13481 (2017).
93. R. Jung, M. Metzger, F. Maglia, C. Stinner, and H. A. Gasteiger, *J. Phys. Chem. Lett.*, **8**, 4820 (2017).
94. S. E. Renfrew and B. D. McCloskey, *J. Am. Chem. Soc.*, **139**, 17853 (2017).
95. T. Hatsukade, A. Schiele, P. Hartmann, T. Brezesinski, and J. Janek, *ACS Appl. Mater. Interfaces*, **10**, 38892 (2018).
96. S. L. Dreyer, K. R. Kretschmer, Đ. Tripković, A. Mazilkin, R. Chukwu, R. Azmi, P. Hartmann, M. Bianchini, T. Brezesinski, and J. Janek, *Adv. Mater. Interfaces*, **9**, 2101100 (2022).
97. F. Strauss, J. H. Teo, A. Schiele, T. Bartsch, T. Hatsukade, P. Hartmann, J. Janek, and T. Brezesinski, *ACS Appl. Mater. Interfaces*, **12**, 20462 (2020).
98. C. Misiewicz, R. Lundström, I. Ahmed, M. J. Lacey, W. R. Brant, and E. J. Berg, *J. Power Sources*, **554**, 232318 (2023).
99. L. de Biasi, A. Schiele, M. Roca-Ayats, G. Garcia, T. Brezesinski, P. Hartmann, and J. Janek, *ChemSusChem*, **12**, 2240 (2019).
100. R. Lundström and E. J. Berg, *J. Power Sources*, **485**, 229347 (2021).
101. S. Oswald, M. Bock, and H. A. Gasteiger, *J. Electrochem. Soc.*, **169**, 050501 (2022).

4.3. The effect of configurational entropy on acoustic emission of P2-type layered oxide cathodes for sodium-ion batteries

In previous AE studies at BELLA, the technique was used for *operando* characterization to detect and understand the degradation of active materials, mostly due to crack formation and the associated exposure of new surfaces, ranging from LNO[251] to Si[348] and high-entropy rock-salt anode materials.[252] In a further work on the high-entropy oxyfluoride CAM $Li_x(Co_{0.2}Cu_{0.2}Mg_{0.2}Ni_{0.2}Zn_{0.2})OF_x$, AE results in dependence of upper cut-off voltage were compared.[253]

Yet, so far neither a SIB material investigation nor a comparison, and thus evaluation of materials with a defined difference, had been performed via AE. The aim of this study was therefore to compare the AE of three P2-type SIB CAMs, $Na_{0.67}(Mn_{0.55}Ni_{0.21}Co_{0.24})O_2$, $Na_{0.67}(Mn_{0.45}Ni_{0.18}Co_{0.24}Ti_{0.1}Mg_{0.03})O_2$ and $Na_{0.67}(Mn_{0.45}Ni_{0.18}Co_{0.18}Ti_{0.1}Mg_{0.03}Al_{0.04}Fe_{0.02})O_2$, with increasing configurational entropy but otherwise similar properties, to derive a structure-property relationship, i.e. to identify how acoustic properties are affected by entropy variation, and how these can be used in evaluation of the materials. A detailed characterization, including the gas evolution of these materials, was carried out beforehand.[171]

Clear, step-like acoustic profiles with intensive emission recorded only during the P2-O2 phase transition were obtained for all materials, as cracking due to the volume variation associated with the phase change is a main degradation mechanism in P2-type CAM. A detailed analysis by AE hit classification based on peak frequency showed a significant difference between the materials, as with increasing entropy a larger share of high-frequency hits (>300 kHz) and lower share of medium-frequency hits (200-300 kHz) were observed. By *post-mortem* cross-sectional electron microscopy imaging and Rietveld refinement of the *c* lattice parameter change during cycling, a more solid-solution like desodiation and less pronounced phase transition, resulting in the formation of less intragranular cracks, were observed with increasing configurational entropy. In all cases, intergranular fracture, i.e. deagglomeration of particle aggregates, was observed. These findings establish that via AE a distinction of less degradative intergranular and more degradative intragranular fractures is possible by the respectively assigned high- and medium-frequency ranges of hits. It should be noted that the aforementioned capacitance method of Oswald *et al.*[335-337] to quantify surface area increase could not be applied, as it requires a full sodiation of the CAM to achieve

blocking conditions, and under these conditions, both Mn disproportionation and continues reduction of FEC occurred.[171]

This study bridges two fields of contemporary research activity, on the one hand the use of AE in battery health monitoring, which commonly focusses on signal processing and analysis while assuming a black box model for the cell and its components,[249,250] and the study of SIB CAM degradation on the other hand. In the latter, various works discuss the facet-dependent mechanism of crack formation,[349] the role of CAM composition,[328,350,351] including high-entropy materials,[331,352-354] as well as the contribution of cracking to the overall aging of CAM,[164,351] Yet, these all rely on laborious *post-mortem* electron microscopy to investigate cracks, while AE allows to study cracking in *operando* conditions.

The study was initiated and designed by Dr. Qingsong Wang and the author of this thesis. The AE measurement setup was initially designed and built by Dr. Simon Schweidler. Dr. Junbo Wang and Dr. Qingsong Wang prepared the materials and performed *operando* X-ray measurements and refinement. Electrode preparation, cell assembly, AE testing and data analysis as well as *post-mortem* electrode preparation and electron microscopy investigation were carried out by the author. Ruizhuo Zhang performed the cross-sectional electron microscopy analysis. The figures and the original manuscript were prepared by the author. Dr. Aleksandr Kondrakov, Dr. Qingsong Wang, Dr. Torsten Brezesinski and Prof. Dr. Jürgen Janek supervised the work. The manuscript was edited by all authors.

IOP Publishing J. Phys. Energy 5 (2023) 035002 https://doi.org/10.1088/2515-7655/acd41a

Journal of Physics: Energy

OPEN ACCESS

RECEIVED
27 January 2023

REVISED
3 May 2023

ACCEPTED FOR PUBLICATION
10 May 2023

PUBLISHED
19 May 2023

PAPER

The effect of configurational entropy on acoustic emission of P2-type layered oxide cathodes for sodium-ion batteries

Sören L Dreyer[1], Ruizhuo Zhang[1], Junbo Wang[1], Aleksandr Kondrakov[2], Qingsong Wang[1,3,*], Torsten Brezesinski[1,*] and Jürgen Janek[1,4]

[1] Institute of Nanotechnology, Karlsruhe Institute of Technology (KIT), Hermann-von-Helmholtz-Platz 1, 76344 Eggenstein-Leopoldshafen, Germany
[2] BASF SE, Carl-Bosch-Str. 38, 67056 Ludwigshafen, Germany
[3] Bavarian Center for Battery Technology (BayBatt), Department of Chemistry, University of Bayreuth, Universitätsstr. 30, 95447 Bayreuth, Germany
[4] Institute of Physical Chemistry & Center for Materials Research (ZfM/LaMa), Justus-Liebig-University Giessen, Heinrich-Buff-Ring 17, 35392 Giessen, Germany
* Authors to whom any correspondence should be addressed.

E-mail: qingsong.wang@uni-bayreuth.de and torsten.brezesinski@kit.edu

Keywords: acoustic emission, P2-type layered cathode, high-entropy oxide, sodium-ion battery, chemo-mechanical degradation

Supplementary material for this article is available online

Abstract

Sodium-ion batteries (SIBs) see intensive research and commercialization efforts, aiming to establish them as an alternative to lithium-ion batteries. Among the reported cathode material families for SIBs, Na-deficient P2-type layered oxides are promising candidates, benefiting from fast sodium diffusion and therefore high charge/discharge rates. However, upon sodium extraction at high potentials, a transition from the P2 to O2 phase occurs, with the corresponding change in cell volume resulting in particle fracture and capacity degradation. A possible solution to this is to increase configurational entropy by introducing more elements into the transition-metal layer (so-called high-entropy concept), leading to some kind of structural stabilization. In this work, the acoustic emission (AE) of a series of P2-type layered oxide cathodes with increasing configurational entropy [$Na_{0.67}(Mn_{0.55}Ni_{0.21}Co_{0.24})O_2$, $Na_{0.67}(Mn_{0.45}Ni_{0.18}Co_{0.24}Ti_{0.1}Mg_{0.03})O_2$ and $Na_{0.67}(Mn_{0.45}Ni_{0.18}Co_{0.18}Ti_{0.1}Mg_{0.03}Al_{0.04}Fe_{0.02})O_2$] is recorded during SIB operation and correlated to the materials properties, namely change in *c* lattice parameter and cracking behavior. A structure-property relationship between entropy, manifested in the extent of phase transition, and detected AE is derived, supported by the classification of signals by peak frequency. This classification in combination with microscopy imaging allows to distinguish between inter- and intragranular fracture. Relatively more intergranular and less intragranular crack formation is observed with increasing configurational entropy.

1. Introduction

Low cost and high abundancy of sodium, relative to lithium, are key driving forces in the research and development of sodium-ion batteries (SIBs) as a complementary and sustainable energy-storage alternative to lithium-ion batteries (LIBs) [1]. This development is aided and accelerated by the similarity of the two technologies, allowing for fast transfer of concepts and solutions [2]. An example are the cathode active material (CAM) families where for both SIBs and LIBs polyanionic structures [e.g. $LiFePO_4$ and $NaFePO_4$ or $Na_3V_2(PO_4)_2F_3$] and layered oxides are most common, depending on the required energy density and cost sensitivity [1–3].

Layered oxides for SIBs are mostly of either O3 or P2 type, which differ in the coordination and amount of Na^+ per formula unit, with P2 generally being Na-deficient and Mn-rich, but with a more open framework structure allowing fast ion diffusion through direct prismatic paths [3–5]. However, upon sodium extraction, P2-type structures ($P6_3/mmc$ space group) undergo a transition towards the O2 phase ($P6_3mc$ space group),

similar to the H2–H3 phase transition in layered Ni-rich oxide cathodes for LIBs, such as $LiNiO_2$ [6–9]. The continuous phase transition and associated anisotropic cell volume changes lead to the formation of cracks in CAM particles and therefore material and performance degradation [8, 9]. For this reason, effectively mitigating or suppressing the phase transition and instead obtaining a solid-solution-like single-phase de/sodiation behavior is a widely researched pathway towards more stable P2-type CAMs. Stability improvements can, for example, be achieved by optimized synthesis conditions [10] or particle coatings. [11, 12] The most common strategy to suppress phase transitions and associated volume changes is doping, either by single elements, such as Mg [13], Fe [14] and Ru [15], or by multielement substitution [16, 17].

The introduction of a large number of elements into a single-phase structure is often referred to as the high-entropy (HE) concept, yielding high configurational entropy, in an attempt to achieve entropy-mediated (structural) stabilization and improved material properties by the so-called cocktail effect [18–20]. Initially proven with metal alloys, the HE approach has been applied recently to organic-inorganic hybrid and (oxide) ceramic battery cathodes and anodes [21–24]. For SIBs, this includes Prussian blue analogues [25, 26] and O3- and P2-type oxides, such as $Na(Ni_{0.12}Cu_{0.12}Mg_{0.12}Fe_{0.15}Co_{0.15}Mn_{0.1}Ti_{0.1}Sn_{0.1}Sb_{0.04})O_2$ and $Na_{0.62}(Mn_{0.67}Ni_{0.23}Cu_{0.05}Mg_{0.07}Ti_{0.01})O_2$ [17, 27–29]. Recently, we have reported a series of P2-type layered oxide CAMs with gradually increasing entropy for SIB applications, namely $Na_{0.67}(Mn_{0.55}Ni_{0.21}Co_{0.24})O_2$, $Na_{0.67}(Mn_{0.45}Ni_{0.18}Co_{0.24}Ti_{0.1}Mg_{0.03})O_2$ and $Na_{0.67}(Mn_{0.45}Ni_{0.18}Co_{0.18}Ti_{0.1}Mg_{0.03}Al_{0.04}Fe_{0.02})O_2$, which will be referred to as 3-$NTMO_2$, 5-$NTMO_2$ and 7-$NTMO_2$, respectively, in the following. They possess configurational entropies of 0.99*R*, 1.34*R* and 1.52*R*, where *R* is the universal gas constant [30]. For these materials, we observed increased reversibility with increasing entropy, as the degradative P2–O2 phase transition was reduced, with the 7-$NTMO_2$ material displaying solid-solution behavior upon sodium extraction. The mitigation of both manganese dissolution and gas evolution was also demonstrated.

The investigation of processes leading to performance degradation is either performed *ex situ*/*post-mortem*, i.e. on disassembled cell parts after the end of operation, or *in situ*/*operando*, i.e. in real-time during cell cycling. A variety of *in situ* characterization techniques has been reported for batteries based mostly on interaction combinations of photons and electrons with the respective materials [31]. Exceptions to this broad generalization are, for example, neutron diffraction and imaging [32], techniques used for gas analysis, such as differential electrochemical mass spectrometry (DEMS) [33], and acoustic techniques. The latter can be separated into active monitoring, wherein an (ultrasonic) acoustic signal is generated externally and its propagation in the battery cell is studied [34–36], and passive monitoring, where acoustic signals emitted from the object under investigation are recorded, the so-called acoustic emission (AE) technique [37]. Acoustic waves can appear in various types and forms, but ultimately all originating from plastic deformation and cracking (i.e. local structural rearrangement), leading to a reduction in strain energy [37–39].

AE as a real-time, non-destructive and non-invasive technique has seen wide application in structural health monitoring, such as detecting fatigue and crack formation in construction materials [38]. For battery cells, AE has been used to monitor the state of health and predict the remaining cycle life [40–42]. However, AE monitoring in batteries is not limited to the cell as a whole, but can be applied to characterize individual electrodes. Various electrode materials have been studied by AE, including CAMs [e.g. $LiCoO_2$ [43], $LiMnO_2$ [44], $LiNiO_2$ [39] and HE $Li_x(Co_{0.2}Cu_{0.2}Mg_{0.2}Ni_{0.2}Zn_{0.2})OF_x$ [45]] and anode active materials [e.g. graphite [46], silicon [47–49], $NiSb_2$ [50] and HE $(Co_{0.2}Cu_{0.2}Mg_{0.2}Ni_{0.2}Zn_{0.2})O$ [51]]. For these materials, analysis of AE signals, with a single acoustic event usually referred to as a hit, allows gaining insights into solid electrolyte interphase (SEI) formation on the one hand and crack formation and propagation both on the particle and electrode level on the other hand. These processes can be distinguished by signal classification due to acoustic wave characteristics, such as peak frequency, rise time, duration or amplitude [39, 43–47, 51].

In the present work, we study and compare the aforementioned 3-$NTMO_2$, 5-$NTMO_2$ and 7-$NTMO_2$ SIB CAMs by AE, observing the effect of increasing configurational entropy as a change in phase-transition behavior (two-phase reaction versus solid solution), which results in different acoustic signatures of the associated crack formation. In so doing, inter- and intragranular particle fracture can be distinguished from one another.

2. Materials and methods

The materials were synthesized via solid-state reaction as described previously [30]. Electrodes were prepared by dispersing CAM (70 wt.%), carbon black (20 wt.%; Super C65, Imerys Graphite & Carbon) and polyvinylidene difluoride binder (10 wt.%; Solef 5130, Solvay) in *N*-methyl-2-pyrrolidone (Merck) and casting the resulting slurry on an Al current collector foil. For this study, electrodes with an active material loading of 8 mg cm^{-2} were produced. Disks of 13 mm diameter were punched out and dried overnight.

CR2032 coin cells (Hohsen) were then assembled inside an Ar-filled glovebox. Na metal and GF/D glass fiber filter paper (Whatman) were used as anode and separator, respectively. 95 μl of a 1.0 mol l^{-1} solution of $NaClO_4$ in ethylene carbonate, dimethyl carbonate and propylene carbonate (1:1:1 by volume) containing 5 vol.% fluoroethylene carbonate (FEC) was used as electrolyte.

For *operando* AE measurements, cells were cycled at 25 °C and at a rate of 0.1C, assuming 1C to be 200 mA g^{-1}, between 1.5 and 4.6 V vs. Na^+/Na using a BAT-SMALL potentiostat (Astrol Electronic AG). AE signals were recorded by a differential wideband sensor (125–1000 kHz; Mistras Group, Inc.) attached to the bottom of the coin cell using vacuum grease to improve contact. The setup further included an in-line preamplifier and a data acquisition system (USB AE Node; Mistras Group, Inc.). The preamp gain, analog filter and sampling rate were set to 40 dB, 20–1000 kHz and 5 MSPS, respectively. The sensor coupling was verified by the pencil-lead break test [52]. For each material, at least two samples were tested to ensure reproducibility. The AE setup and analysis procedure are described in more detail in the literature [39, 44–48, 51, 53]. Recordings were first processed by the AEwin software (Mistras Group, Inc.), filtering out background noise by eliminating all hits with less than two counts, peak frequencies lower than 100 kHz or amplitudes less than 27 dB, and then analyzed together with the respective electrochemical measurement data.

For *post-mortem* analysis, cells were cycled at 25 °C and 0.1C rate for up to 50 cycles using a Series 4000 battery test system (MACCOR), then crimped open and the cathode was washed with dimethyl carbonate to be recovered.

Scanning electron microscopy (SEM) was carried out on a LEO 1530 microscope (Zeiss) at 10 kV. For the preparation of cross-sectional images, an IB-19510CP cross-section polisher (JEOL) with Ar-gas source was used to polish the cathode in the pristine and cycled states. The respective SEM images were recorded under the same conditions as mentioned above.

Operando X-ray diffraction (XRD) measurements were carried out on a STOE Stadi P diffractometer (Ga K_β radiation, $\lambda = 1.20793$ Å). Further details can be found in the previous work [30]. Rietveld refinement and LeBail fitting were performed with the FullProf software package. Rietveld refinements of diffraction patterns collected from the pristine powders and the *operando* cells before electrochemical testing were first conducted to determine the zero shift. The zero shift was then kept constant for the LeBail fitting of the following patterns obtained during the charge/discharge process. Additionally, a larger hexagonal unit cell described by the space group $P6_3$ instead of $P6_3/mmc$ was considered for data refinement [54, 55].

3. Results and discussion

As previously reported, two potential ranges were explored in testing the cycling performance of the materials, one of them allowing for further reduction and possible disproportionation and dissolution of Mn [30]. For AE measurements, the wider range of 1.5–4.6 V vs. Na^+/Na was chosen, as it yields greater cell capacities and allows the Mn dissolution to be investigated. Figure 1(a) shows the specific charge/discharge capacities of 3-$NTMO_2$, 5-$NTMO_2$ and 7-$NTMO_2$ in coin half-cells cycled at 0.1C rate in the AE setup. The observed reduced charge capacity in the first cycle (q_{ch} = 142–143 mAh g^{-1}) is due to the intrinsic sodium deficiency of as-synthesized P2-type structures. The capacities are in line with those reported earlier when considering the different C-rates and also regarding the initial increase seen for 5-$NTMO_2$ and 7-$NTMO_2$ over the first few cycles [30]. The voltage profiles for the first five cycles are shown together with the cumulative number of AE hits and normalized hit rate for each material in figures 1(b)–(d).

The vast majority of hits are detected during charge, and with the exception of the first cycle, in the potential range from 4.2 to 4.6 V vs. Na^+/Na. In the initial cycle, hits are also detected below 4.2 V, starting from the beginning of charge. This is commonly attributed to the formation of the (cathode) SEI [39, 43, 45, 47, 56], as also observed for $LiCoO_2$ [43] and $LiNiO_2$ [39]. In anode active materials, the corresponding early SEI formation is also detectable via AE [46, 49, 51]. In agreement with previous results, the largest share of acoustic activity is observed in the potential range where particle cracking due to phase transitions and/or intense volume changes occurs, with the number of new hits per cycle slowly decreasing [39, 43–45, 57, 58]. Virtually no hits are detected at low potentials near the end of discharge, suggesting that the Mn reduction/disproportionation and CO_2 evolution due to FEC reduction, both of which are evident under these conditions [30], are not acoustically active. While the AE of gassing and subsequent bursting of gas bubbles is sometimes described in the literature [43, 46], it is further characterized by low peak frequencies and long rise times [56, 58–61] so that the attribution can be challenged if these conditions are not met by a given hit [39, 44, 47, 49]. In the setup used herein, gas evolution (detected via DEMS) was not [39, 51], or presumably only at extreme rates [45], observed by AE.

In general, the acoustic profiles appear simpler and clearer, due to high concentration of hits into a narrow voltage range, than those of CAMs for LIBs previously studied using the same setup [39, 45]. A likely

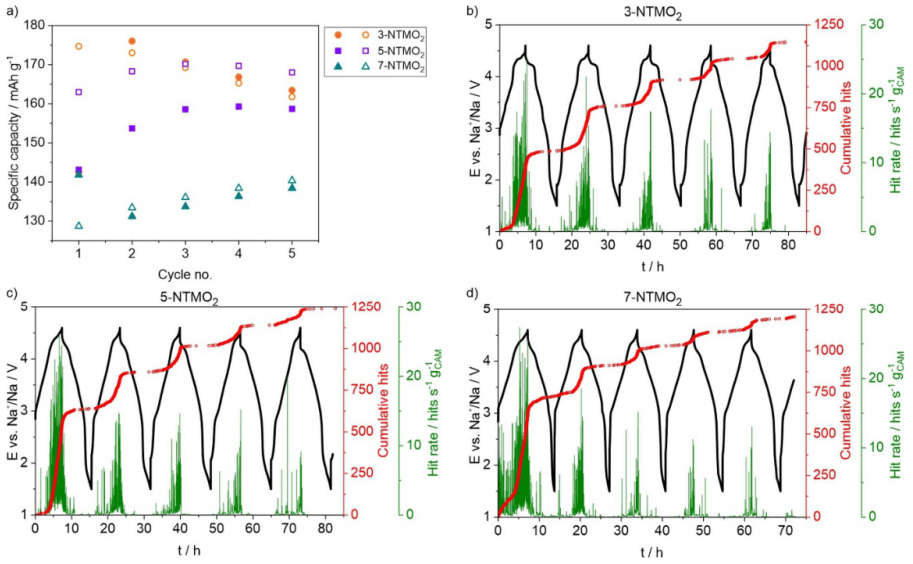

Figure 1. (a) Specific charge (solid symbols) and discharge capacities (hollow symbols) of 3-, 5- and 7-$NTMO_2$ and (b)–(d) corresponding acoustic profiles.

contribution to this is the morphology, with the materials studied herein consisting of micron-sized, monolithic (yet agglomerated) particles, while the LIB CAMs either consisted of primary particles agglomerated to micron-sized secondary particles [39] or nanoparticles [45]. Thus, a lower specific surface area and reduced contribution from surface side reactions can be expected. The particle size distribution of all three materials is shown in figure S1, with D_{50} between 9.4 μm (for 7-$NTMO_2$) and 12.4 μm (for 5-$NTMO_2$).

The apparent straightforwardness of the acoustic profiles not only allows, for the first time, characterizing different materials, but also comparing them. However, when comparing the different materials to one another, it should be considered that the similar number of hits detected after five cycles, as indicated in figures 1(b)–(d), is merely coincidental, as with the experimental setup used, the degree of acoustic transmission varies with the quality of contact between cell and sensor (screw pressure, amount of grease etc.), as well as with the individual coin cell (electrode alignment, crimping etc.). It is therefore hardly possible to directly compare absolute numbers. Instead, relative hits, i.e. normalized to the respective total number of hits, should be used. In figures 1(b)–(d), absolute numbers are shown for simplicity. Figure S2 represents the acoustic profiles of a second set of cells with normalized hits, thus also demonstrating the repeatability of the obtained results.

Because the AE is concentrated in the phase-transition region, figure S3 shows dq/dV plots for each material in this potential range during the first and second charge cycles. It is worth noting that the specific capacity stemming from desodiation above 4.0 V vs. Na^+/Na is similar between the materials, as shown in table S1, since differences in total capacity result mostly from a different degree of low-potential Mn^{3+} redox [30]. For the 3-$NTMO_2$ sample, a sharp main peak is observed around 4.35 V, corresponding to the voltage plateau in figure 1(b) and transition to the O2 phase, as previously found by *operando* XRD [30]. A shoulder at 4.2–4.3 V is believed to be related to lattice oxygen loss. It coincides with strong gas evolution in DEMS and is not seen during discharge, indicating an irreversible process [30]. The acoustic activity is concentrated within this phase-transition region, resulting in an S-shaped curve with little hits above 4.45 V in both cycles. The maximum gas evolution occurs around 4.3 V in the initial cycle, but above 4.45 V in the second one. Yet, the acoustic profile shapes are similar and do not show considerable activity above 4.45 V, and it can be concluded that high-potential gas evolution, including that associated with irreversible oxygen redox [33], is also not detected via AE in the given setup. For 5-$NTMO_2$ and especially the 7-$NTMO_2$ sample, on the other hand, a broader dq/dV peak without distinct lower shoulder is observed (figure S3), indicating a more solid-solution-like desodiation process, as also found via *operando* XRD [30]. At the same time, the hit curve changes from S-shape to a rather linear shape, including continuous hit detection at potentials above 4.45 V.

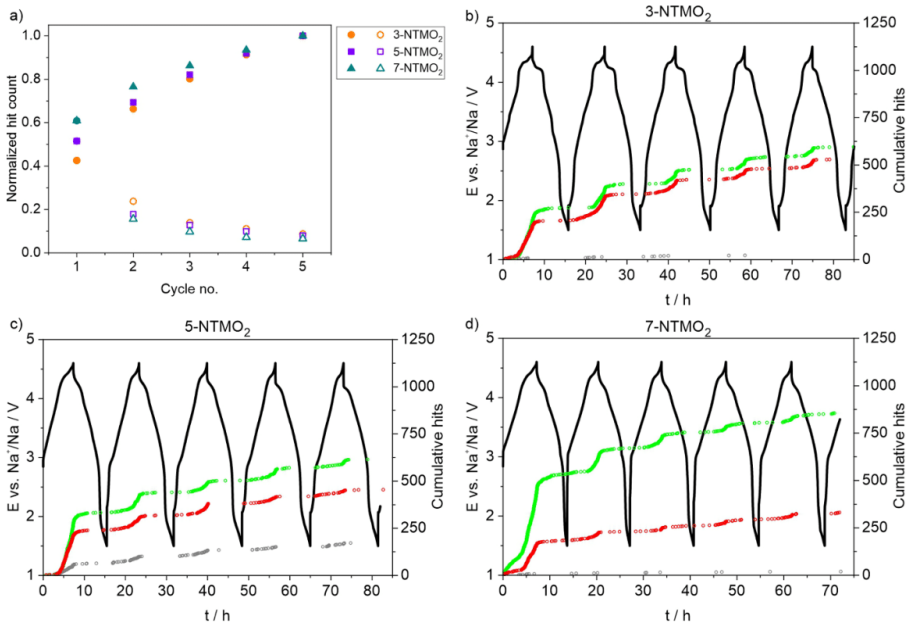

Figure 2. (a) Normalized hit count (solid symbols) and hits per cycle (hollow symbols) for 3-, 5- and 7-$NTMO_2$ and (b)–(d) corresponding acoustic profiles after classification by peak frequency into AE1 (gray), AE2 (red) and AE3 (green).

When considering the cumulative hits in the initial cycle according to figures 1(b)–(d) and S3 under the restriction of similar absolute numbers as discussed previously, it can be concluded that with increasing configurational entropy a larger amount of hits is detected, with less hits in the following cycles (i.e. flatter steps in the acoustic profiles in the later cycles).

Figure 2(a) shows the cumulative hits and hits per cycle for each material normalized to the total number after five cycles, confirming the trend towards concentration of AE into the first charge from 3-$NTMO_2$ to 7-$NTMO_2$. The hits are characterized further by additional parameters that can be used to classify AE events. While principal component analysis allows for the consideration of each parameter's contribution [47, 62], it is often found that the peak frequency is the most distinctive and allows to correlate AE hits with likely processes of their origin [43, 44, 47, 56–61]. For each material, hits are thus classified into three groups (AE1, AE2 and AE3) according to the peak frequency (<200, 200–300 and >300 kHz). In recent years, it has been found that low peak frequencies are often associated with gas bubble evolution or interfacial reactions, such as SEI formation, while higher frequencies can be attributed to mechanical stress-release processes, such as crack formation [43, 56, 58–62]. In some instances, AE classification by peak frequency is used to distinguish mechanical processes on different length scales, i.e. from microcrack formation over intragranular crack propagation/growth to intergranular (electrode) fracture, including deagglomeration of secondary particles [45, 47, 51].

Figures 2(b)–(d) show the acoustic profiles after classification by peak frequency and figure S4 presents histograms of frequency distribution. For the second set of cells (as shown in figure S2), figure S5 displays the normalized hit count. While 3-$NTMO_2$ and 7-$NTMO_2$ only show a negligible amount of AE1 activity, a few such hits were detected for 5-$NTMO_2$. Although low peak frequencies, as for AE1, are sometimes associated with gas evolution [43, 56, 58–61], all materials tested herein showed gassing of similar degree in the initial cycle [30], and other gas evolving processes have been ruled out above. Other processes in the AE1 range include electrode surface restructuring and SEI formation. A possible explanation therefore is an increased amount of surface impurities resulting in higher reactivity and AE from decomposition reactions. This assumption is supported by the slightly higher CO_2 evolution for 5-$NTMO_2$, which may indicate a larger concentration of residual carbonates on the surface [30, 33]. However, the main difference between the materials is found in the distribution of hits between AE2 and AE3. While 3-$NTMO_2$ shows only slightly more AE3 than AE2 hits, there is an increase in the share and total number of AE3 hits with increasing configurational entropy. Conversely, the share and total number of AE2 hits decreases. Considering prior AE

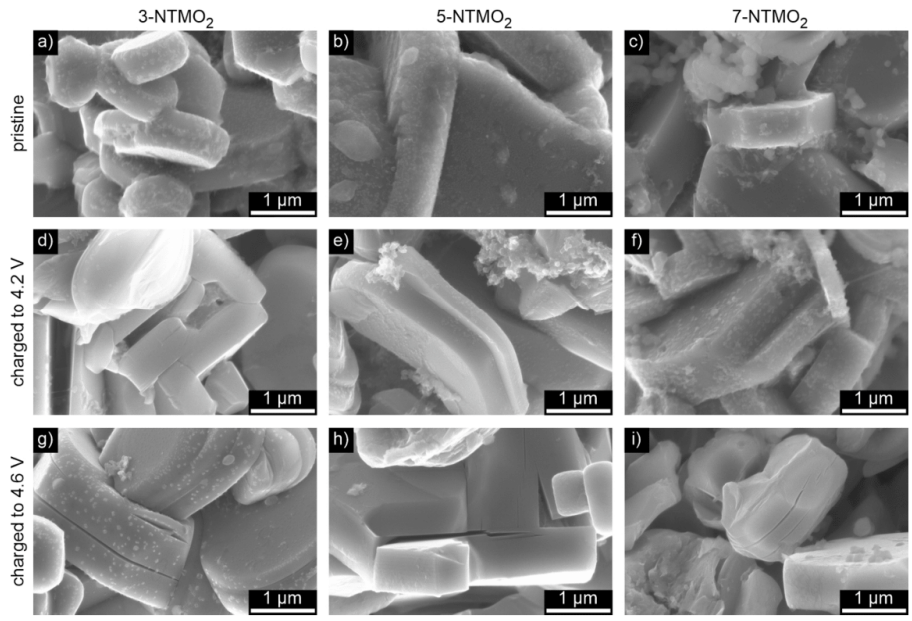

Figure 3. Top-view SEM images of pristine and charged (initial cycle) 3-, 5- and 7-$NTMO_2$ cathodes.

classification findings that show a relation between peak frequency and crack type or length scale/dimension [45, 47, 51], a likely hypothesis is that AE2 and AE3 represent the formation of one crack type each. As both a lower share of AE2 hits and lower degree of phase transition (or corresponding volume change) are observed with increasing configurational entropy in the materials, AE2 hits appear to be associated with the formation of intragranular cracks. Under this hypothesis, AE3 hits are then attributed to the formation of intergranular cracks, as was proposed in a previous study [45].

To correlate the observed differences in AE characterization and classification with material properties and especially to confirm the hypothesis regarding intragranular crack evolution and deagglomeration (intergranular cracking), *post-mortem* investigation of cycled electrodes was carried out. Figures 3(a)–(i) show top-view SEM images of the different CAMs in the pristine state and after charging to 4.2 V vs. Na^+/Na ($q_{ch} \approx 80$ mAh g^{-1}), i.e. prior to the onset of any phase transitions and appearance of most acoustic activity, and to 4.6 V, the cutoff potential with maximum change in lattice parameters according to *operando* XRD. In the pristine cathodes, the CAM particles are crack free and agglomerated or even sintered together. After charging to 4.2 V, small contact lines between the particles become visible and few initial intragranular cracks appear. At 4.6 V, more of these parallel-oriented crack lines can be observed and agglomerated particles have partially deagglomerated, as is evident from the presence of intergranular cracks. A voltage-plateau-dependent fracture behavior, with cracks oriented in parallel to the (002) plane, was previously reported for $Na_{2/3}Ni_{1/3}Mn_{2/3}O_2$, wherein Mg doping reduced the cracking tendency [9, 13]. Comparable behavior, including fracture along the (003) plane and the distinction of intra- and intergranular cracking, is also found in layered oxide LIB CAMs [63–65].

Cracks are usually formed because of anisotropic changes in unit cell volume. In this case, the particles first slightly expand during desodiation before the lattice collapses and shrinks at high states of charge [30, 66]. To quantitatively compare the root cause of particle fracture, *operando* XRD patterns were refined. The changes in lattice parameter *c* in the initial cycle are displayed in figure 4. In general, upon charging below 4.2 V, the extraction of Na^+ ions leads to increased repulsion of the oxygen layers (reduced shielding by the Na^+ ions), thus an increase in *c* is observed. During further desodiation, phase transition from P2 to O2 is prompted by the TMO_2 (or MO_2, to be more precise) slabs gliding in the *a-b* plane, because the empty prismatic sites are thermodynamically unstable [67]. Through metal substitution (HE approach), the P2-O2 transition is suppressed effectively and transferred to P2 to OP4 evolution in the case of 7-$NTMO_2$ (figure 4). The intergrown OP4 phase describes the alternate piling up (with possible stacking fault) of octahedral and trigonal prismatic layers (Na^+ ions are accommodated at the octahedral and prismatic sites) along the *c* axis. Overall, the P2–OP4 phase transition is more reversible [67]. The 5-$NTMO_2$ sample with medium

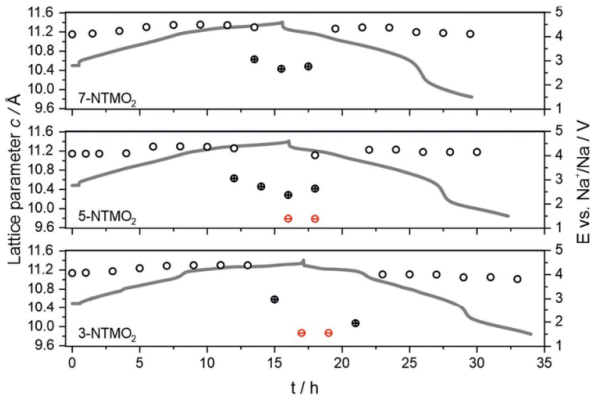

Figure 4. Changes in *c* lattice parameters during the initial cycle and corresponding phases (OP4 = black plus sign, O2 = red minus sign) at high potentials. The corresponding voltage profiles are shown in light gray. The error bars are included in the symbols.

configurational entropy shows existence of both the O2 and OP4 phases at high states of charge (figure 4). In the case of 3-$NTMO_2$, a complete transition (collapse in *c* axis) to O2 is observed at high potentials (figure 4). Hence, more severe lattice parameter/unit cell volume changes in 3-$NTMO_2$ lead to more particle fracture, supporting the assignment of AE2 hits to intergranular cracking.

Figure S6 shows additional top-view SEM images of particles at the end of discharge after both one and five cycles, demonstrating that cracks do not disappear after resodiation and return to the initial unit cell volume, while the occurrence of intragranular cracks and associated phenomena, such as delamination, exfoliation and electrochemical creep [17, 68–70], increases with the number of cycles. Top-view imaging relies on particles on the electrode surface after assembly and the study of deagglomeration is complicated by loss of such particles from the surface. For this reason, ion milling was carried out and the resulting cross sections were studied via SEM. For both 3- and 7-$NTMO_2$, figures 5(a)–(h) and S7 show images collected from the cathodes before and after cycling (1, 5 and 50 cycles). In cycled electrodes, not only the formation of intragranular crack planes, visible as parallel lines, can be observed, but also the expansive delamination and exfoliation of cracked (single-crystalline) particles in absence of other, directly adjacent particles, as also reported in the literature [11, 12, 17, 69, 70]. However, when such particles are present, signs of deagglomeration and formation of intergranular voids are increasingly apparent. It should be noted though that such voids are also present to some degree in the pristine electrodes. Intragranular fracture seems to result from compression and subsequent bending of particles and was also observed for $Na_{2/3}Ni_{1/3}Mn_{2/3}O_2$ [9]. For some monolithic particles that appear crack free, a likely explanation is that they are oriented in a way that the cracking planes are parallel to the cross-section plane. A large number of smaller cracks at the particle surface can be observed, with crack tips expanding into the bulk (especially in figures 5(g) and S7(g)), in good agreement with literature reports on P2 SIB CAMs [13, 71], where the crack nucleation and growth from the surface is explained by the P2–O2 transition during cycling [9]. For the 3-$NTMO_2$ material after 50 cycles, at high magnification (figure S8), additional surface corrosion is visible, which is probably related to the disproportionation and subsequent dissolution of Mn [30].

When comparing the samples, a difference in the number of intragranular cracks can be observed. After one cycle, for all materials, deagglomeration has set in, and next to these intergranular voids also some intragranular cracks are visible. At higher cycle numbers, 3-$NTMO_2$ shows both substantially more cracked particles and more intragranular cracks per particle, while intergranular fracture dominates the 7-$NTMO_2$ cathode cross sections. These findings qualitatively confirm the hypothesis that AE2 hits, more prevalent in 3-$NTMO_2$, are correlated with intragranular cracking, while AE3 hits, more prevalent in 7-$NTMO_2$, are correlated with intergranular fracture. With both qualitative and quantitative confirmation of the assignment hypothesis, this work presents a non-invasive, non-destructive method of monitoring formation of both intra- and intergranular cracks by the use of AE.

Further attempts to quantify crack formation via the expected increase in surface area (by Kr-BET and two-electrode electrochemical impedance spectroscopy measurements) did unfortunately not lead to concise results. The conductive carbon black used in the electrodes contributes a far greater specific surface area than the CAMs. Besides, the dissolution of Mn from the materials and subsequent deposition under continuous

IOP Publishing J. Phys. Energy 5 (2023) 035002 S L Dreyer et al

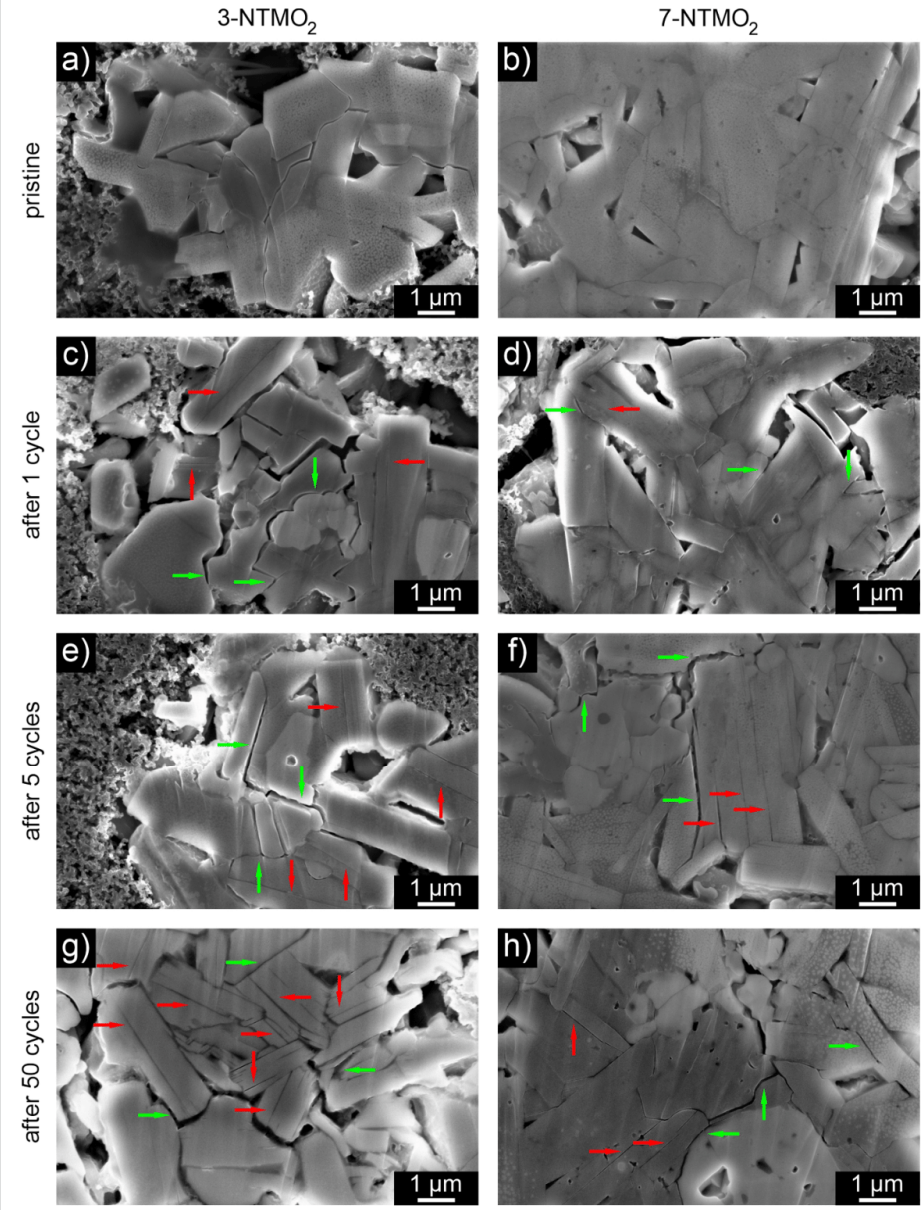

Figure 5. Cross-sectional SEM images of pristine and cycled (fifth and 50th cycle) 3- and 7-$NTMO_2$ cathodes. Arrows exemplify intergranular (green) and intragranular (red) cracks.

SEI formation at the anode [72, 73] leads to a strong rise in impedance, as shown in figure S9, albeit highlighting the effect of increased configurational entropy in suppressing Mn leaching (impedance growth). The role of cathode composition and manufacturing process on AE is outside the scope of this work and will be subject of future investigations.

4. Conclusions

For the first time, AE as a non-destructive characterization technique was applied to SIBs. Three structurally related P2-type CAMs, varying in their configurational entropy and, resulting from that, in the degree of phase transition (two-phase reaction versus solid solution) at potentials above 4.2 V vs. Na^+/Na, were not

only characterized, but also compared to one another. It was found that while acoustic activity in all materials is mainly related to crack formation and propagation, with increasing configurational entropy, it is more concentrated into the initial cycle and at higher peak frequencies. By correlation of electrochemical behavior and AE with *post-mortem* SEM imaging, a lower degree of intragranular fracture and particle delamination was observed with increasing solid-solution-like desodiation. A larger share of acoustic activity, specifically at high peak frequencies, thus stems from particle deagglomeration (intergranular fracture). These results are corroborated quantitatively by *operando* XRD.

It is demonstrated that AE cannot only be used to characterize, but also to compare and evaluate battery materials. Especially, P2-type SIB CAMs show a clear profile with almost only cracking contributing to acoustic activity (and again no effect of gas evolution on the AE). As a non-invasive technique, AE may find further use in battery health monitoring due to the ease of measurement. However, as of now, the complexity of the obtained information requires additional characterization to be interpreted and utilized fully.

Data availability statement

The data that support the findings of this study are available upon reasonable request from the authors.

Acknowledgments

The authors thank Simon Schweidler (Karlsruhe Institute of Technology) for introduction to and assistance with the AE technique and Philipp Quarz (Karlsruhe Institute of Technology) for particle size distribution measurements. Rafael Meinusch and Kilian Vettori (Justus-Liebig-University Giessen) are acknowledged for help with BET measurements and impedance spectroscopy, respectively.

Conflict of interest

The authors declare no conflict of interest.

ORCID iDs

Sören L Dreyer https://orcid.org/0000-0001-8867-4787
Ruizhuo Zhang https://orcid.org/0000-0003-0292-5026
Aleksandr Kondrakov https://orcid.org/0000-0003-1465-2854
Qingsong Wang https://orcid.org/0000-0001-5879-8009
Torsten Brezesinski https://orcid.org/0000-0002-4336-263X
Jürgen Janek https://orcid.org/0000-0002-9221-4756

References

[1] Tarascon J-M 2020 *Joule* **4** 1616–20
[2] Chayambuka K, Mulder G, Danilov D L and Notten P H L 2018 *Adv. Energy Mater.* **8** 1800079
[3] Tapia-Ruiz N *et al* 2021 *J. Phys. Energy* **3** 031503
[4] Chen T, Ouyang B, Fan X, Zhou W, Liu W and Liu K 2022 *Carbon Energy* **4** 170–99
[5] Liu Y, Wang D, Li H, Li P, Sun Y, Liu Y, Liu Y, Zhong B, Wu Z and Guo X 2022 *J. Mater. Chem.* A **10** 3869–88
[6] Lee D H, Xu J and Meng Y S 2013 *Phys. Chem. Chem. Phys.* **15** 3304–12
[7] Sun H-H and Manthiram A 2017 *Chem. Mater.* **29** 8486–93
[8] Yoon C S, Jun D-W, Myung S-T and Sun Y-K 2017 *ACS Energy Lett.* **2** 1150–5
[9] Wang K, Yan P and Sui M 2018 *Nano Energy* **54** 148–55
[10] Kulka A, Marino C, Walczak K, Borca C, Bolli C, Novák P and Villevieille C 2020 *J. Mater. Chem.* A **8** 6022–33
[11] Alvarado J, Ma C, Wang S, Nguyen K, Kodur M and Meng Y S 2017 *ACS Appl. Mater. Interfaces* **9** 26518–30
[12] Liu Y, Fang X, Zhang A, Shen C, Liu Q, Enaya H A and Zhou C 2016 *Nano Energy* **27** 27–34
[13] Wang K, Wan H, Yan P, Chen X, Fu J, Liu Z, Deng H, Gao F and Sui M 2019 *Adv. Mater.* **31** 1904816
[14] Yang Q, Wang P-F, Guo J-Z, Chen Z-M, Pang W-L, Huang K-C, Guo Y-G, Wu X-L and Zhang J-P 2018 *ACS Appl. Mater. Interfaces* **10** 34272–82
[15] Jiang K, Zhang X, Li H, Zhang X, He P, Guo S and Zhou H 2019 *ACS Appl. Mater. Interfaces* **11** 14848–53
[16] Cheng Z *et al* 2022 *Adv. Energy Mater.* **12** 2103461
[17] Fu F *et al* 2022 *Nat. Commun.* **13** 2826
[18] Zhang R-Z and Reece M J 2019 *J. Mater. Chem.* A **7** 22148–62
[19] Miracle D B and Senkov O N 2017 *Acta Mater.* **122** 448–511
[20] Wang Q, Velasco L, Breitung B and Presser V 2021 *Adv. Energy Mater.* **11** 2102355
[21] Sturman J W, Baranova E A and Abu-Lebdeh Y 2022 *Front. Energy Res.* **10** 862551
[22] Amiri A and Shahbazian-Yassar R 2021 *J. Mater. Chem.* A **9** 782–823
[23] Ma Y, Ma Y, Wang Q, Schweidler S, Botros M, Fu T, Hahn H, Brezesinski T and Breitung B 2021 *Energy Environ. Sci.* **14** 2883–905
[24] Chen Y, Fu H, Huang Y, Huang L, Zheng X, Dai Y, Huang Y and Luo W 2021 *ACS Mater. Lett.* **3** 160–70

[25] Ma Y et al 2021 Adv. Mater. 33 2101342
[26] Ma Y et al 2022 Adv. Funct. Mater. 32 2202372
[27] Zhao C, Ding F, Lu Y, Chen L and Hu Y-S 2020 Angew. Chem., Int. Ed. 59 264–9
[28] Yan S, Luo S, Yang L, Feng J, Li P, Wang Q, Zhang Y and Liu X 2022 J. Adv. Ceram. 11 158–71
[29] Lin C-C et al 2022 Energy Storage Mater. 51 159–71
[30] Wang J et al 2022 Mater. Futures 1 035104
[31] Shadike Z, Zhao E, Zhou Y-N, Yu X, Yang Y, Hu E, Bak S, Gu L and Yang X-Q 2018 Adv. Energy Mater. 8 1702588
[32] Zhao E, Zhang Z-G, Li X, He L, Yu X, Li H and Wang F 2020 Chin. Phys. 29 018201
[33] Dreyer S L, Kondrakov A, Janek J and Brezesinski T 2022 J. Mater. Res. 37 3146–68
[34] Bommier C, Chang W, Li J, Biswas S, Davies G, Nanda J and Steingart D 2020 J. Electrochem. Soc. 167 020517
[35] Zhang Y S, Pallipurath Radhakrishnan A N, Robinson J B, Owen R E, Tranter T G, Kendrick E, Shearing P R and Brett D J L 2021 ACS Appl. Mater. Interfaces 13 36605–20
[36] Appleberry M C et al 2022 J. Power Sources 535 231423
[37] Majasan J O, Robinson J B, Owen R E, Maier M, Radhakrishnan A N P, Pham M, Tranter T G, Zhang Y, Shearing P R and Brett D J L 2021 J. Phys. Energy 3 032011
[38] Enoki M, Inaba H, Mizutani Y, Nakano M and Ohtsu M 2016 Practical Acoustic Emission Testing (Tokyo: Springer) (https://doi.org/10.1007/978-4-431-55072-3)
[39] Schweidler S, Bianchini M, Hartmann P, Brezesinski T and Janek J 2020 Batteries Supercaps 3 1021–7
[40] Beganovic N and Söffker D 2019 J. Energy Resour. Technol. 141 041901
[41] Wang K, Chen Q, Yue Y, Tang R, Wang G, Tang L and He Y 2023 Nondestruct. Test. Eval. 38 480–99
[42] Zhang K, Yin J and He Y 2021 Sensors 21 712
[43] Choe C-Y, Jung W-S and Byeon J-W 2015 Mater. Trans. 56 269–73
[44] Kircheva N, Genies S, Chabrol C and Thivel P-X 2013 Electrochim. Acta 88 488–94
[45] Schweidler S, Dreyer S L, Breitung B and Brezesinski T 2022 Coatings 12 402
[46] Kircheva N, Genies S, Brun-Buisson D and Thivel P-X 2011 J. Electrochem. Soc. 159 A18–A25
[47] Tranchot A, Etiemble A, Thivel P-X, Idrissi H and Roué L 2015 J. Power Sources 279 259–66
[48] Tranchot A, Idrissi H, Thivel P-X and Roué L 2016 J. Power Sources 330 253–60
[49] Schiele A, Breitung B, Mazilkin A, Schweidler S, Janek J, Gumbel S, Fleischmann S, Burakowska-Meise E, Sommer H and Brezesinski T 2018 ACS Omega 3 16706–13
[50] Villevieille C, Boinet M and Monconduit L 2010 Electrochem. Commun. 12 1336–9
[51] Schweidler S, Dreyer S L, Breitung B and Brezesinski T 2021 Sci. Rep. 11 23381
[52] Hsu N N 1977 Acoustic emissions simulator US Patent 4,018,084 (available at: https://image-ppubs.uspto.gov/dirsearch-public/print/downloadPdf/4018084)
[53] Etiemble A, Idrissi H and Roué L 2012 J. Acoust. Emiss. 30 54–64 (available at: www.ndt.net/search/docs.php3?id=15395)
[54] Tapia-Ruiz N, Dose W M, Sharma N, Chen H, Heath J, Somerville J W, Maitra U, Islam M S and Bruce P G 2018 Energy Environ. Sci. 11 1470–9
[55] Paulsen J M, Donaberger R A and Dahn J R 2000 Chem. Mater. 12 2257–67
[56] Matsuo T, Uchida M and Cho H 2011 J. Solid Mech. Mater. Eng. 5 678–89
[57] Rhodes K, Dudney N, Lara-Curzio E and Daniel C 2010 J. Electrochem. Soc. 157 A1354–A1360
[58] Didier-Laurent S, Idrissi H and Roué L 2008 J. Power Sources 179 412–6
[59] Ramadan S and Idrissi H 2008 Desalination 219 358–66
[60] Etiemble A, Idrissi H and Roué L 2011 J. Power Sources 196 5168–73
[61] Etiemble A, Idrissi H, Meille S and Roué L 2012 J. Power Sources 205 500–5
[62] Simescu F and Idrissi H 2009 Meas. Sci. Technol. 20 055702
[63] Yan P, Zheng J, Gu M, Xiao J, Zhang J-G and Wang C-M 2017 Nat. Commun. 8 14101
[64] Yan P, Zheng J, Chen T, Luo L, Jiang Y, Wang K, Sui M, Zhang J-G, Zhang S and Wang C 2018 Nat. Commun. 9 2437
[65] Zhang H, Omenya F, Yan P, Luo L, Whittingham M S, Wang C and Zhou G 2017 ACS Energy Lett. 2 2607–15
[66] Somerville J W et al 2019 Energy Environ. Sci. 12 2223–32
[67] Yabuuchi N, Kajiyama M, Iwatate J, Nishikawa H, Hitomi S, Okuyama R, Usui R, Yamada Y and Komaba S 2012 Nat. Mater. 11 512–7
[68] Radin M D, Alvarado J, Meng Y S and Van der Ven A 2017 Nano Lett. 17 7789–95
[69] Hasa I, Passerini S and Hassoun J 2017 J. Mater. Chem. A 5 4467–77
[70] Sengupta A, Kumar A, Barik G, Ahuja A, Ghosh J, Lohani H, Kumari P, Bhandakkar T K and Mitra S 2023 Small 19 2206248
[71] Wang K, Yan P, Wang Z, Fu J, Zhang Z, Ke X and Sui M 2020 J. Mater. Chem. A 8 16690–7
[72] Lee Y K 2021 J. Power Sources 484 229270
[73] Shin H, Park J, Sastry A M and Lu W 2015 J. Power Sources 284 416–27

4.4. Elucidating Gas Evolution of Prussian White Cathodes for Sodium-ion Battery Application: The Effect of Electrolyte and Moisture

In an initial DEMS measurement of a high-entropy PBA undertaken at BELLA, the evolution of $(CN)_2$ near the end of charge was observed and assumed to be related to the release of O_2 from layered oxides, adhering to the motif of host structure anion oxidation.[189] In later comparisons of both Mn- and Fe-based PW SIB CAMs of varying configurational entropy, it was further observed that during phase transitions in the CAM also at lower potential additional H_2 and $(CN)_2$ were evolved, with a reduced evolution of $(CN)_2$ in high-entropy materials.[192,193] This suggested that also the exposure of additional surface to electrolyte may, in the form of surface impurities or reactions between electrolyte and CAM, contribute to the formation of $(CN)_2$. Geisler recently independently confirmed the $(CN)_2$ evolution from PW CAM.[266]

The removal of water is often discussed as a main obstacle in the development and commercialization of PBA/PW-based SIBs.[158,160] Furthermore, Li *et al.* challenged the perception of PBA/PW as safe CAMs by demonstrating that charged PBA releases HCN and $(CN)_2$ during thermal runaway already between 200 and 300 °C, undergoing further exothermic reactions with the electrolyte.[191] Taken together, with the apparent evolution of HCN and $(CN)_2$ even during regular cycling, PBA/PW safety issues appear at best as not well understood, and at worst, as a hard stop for further development.[355] The initial observations at BELLA were, however, made on high-entropy materials containing multiple metals prepared at a laboratory scale with little control over electrode inhomogeneity, surface impurities, vacancy and water content. To rule out artifacts and to identify the root cause and mechanism of $(CN)_2$ evolution and also possible HCN evolution, this study was carried out on commercial, purely Fe-based PW CAM in electrodes of high loading and production quality.

As no calibration gas mixture [$(CN)_2$ and possibly also HCN in He] was commercially available, a comparison of mass spectrometer detector currents was required. This is commonly carried out in DEMS studies when no calibration gas is available, e.g. for SO_2 from sulfide solid electrolyte oxidation[356,357] or for POF_3 from $LiPF_6$ decomposition,[358] or when the cell design does not allow for external calibration.[359] A calibration by stoichiometric decomposition of a known amount of reagent, as described for e.g. the DEMS fluoride probe trimethylsilyl fluoride,[360] or POF_3/PF_5,[120] was also not practical, as non-aqueous quantitative procedures require thermal decomposition of toxic

and explosive heavy-metal cyanides, such as $Ag(CN)_2$ and $Hg(CN)_2$.[361] However, the SEM gain of a mass spectrometer changes over time, which has to be accounted for in a study extending over multiple months and measurements, in contrast to a small number of comparative measurements carried out in quick succession. Therefore, this work also discusses, for the first time in battery gassing studies, SEM degradation,[362] a gradual adjustment of SEM voltage over time and the normalization of raw signals, not only by CAM mass but also by relative calibration factors obtained for H_2 and CO_2.

This study confirmed that the CAM drying process is of utmost importance, as significant H_2 evolution was observed when using undried PW electrodes, as obtained from an aqueous slurry formulation.[185] The evolution of CO_2 and $(CN)_2$ was found to depend mostly on the conductive salt used in the electrolyte in a series of comparisons of electrolytes containing either $NaPF_6$ or $NaClO_4$. In short, use of $NaPF_6$ leads to the formation of HF by hydrolysis, i.e. acidic conditions, while in the case of $NaClO_4$ hydroxide anions, i.e. basic conditions, formed from water reduction at the anode. Under basic conditions, CO_2 evolution from EC hydrolysis was subsequently observed. In the case of overcharge, electrochemical electrolyte oxidation further contributed to the H_2 and CO_2 evolution. While mass spectrometric evidence of HCN formation is discussed, $(CN)_2$ is formed in far greater amounts and thus poses the main safety risk. With $NaPF_6$, the $(CN)_2$ evolution was far lower than with $NaClO_4$, and the oxidative properties of the latter were identified as cause of increased $(CN)_2$ evolution, further also detecting ClO_2 as a reaction product via DEMS. Oxidation of Fe^{3+} to Fe^{4+} in a short-lived hexacyanoferrate(IV) intermediate, followed by reductive elimination of cyanide ligands, was proposed as a reaction mechanism in light of the available literature. Especially, this mechanism can explain both that overcharge in $NaPF_6$-based electrolyte also leads to $(CN)_2$ evolution (slower, but possible electrochemical formation of the Fe^{4+} intermediate) and, due to the reductive elimination, specifically $(CN)_2$ is formed instead of polycyanogen or various $(CN)_x$ oligomers that are otherwise found as products of electrochemical cyanide oxidation.[363,364] Quantitatively, the $(CN)_2$ evolution in any case must be rather low, as no significant difference in specific capacities and capacity fading is observed between cells containing $NaPF_6$ and $NaClO_4$. Likely, charge transfer from $NaClO_4$ is restricted to the surface of the PW material, and subsequent CEI formation limits the exposure of material to the bulk electrolyte.

While $(CN)_2$ evolution was confirmed to take place also in optimized, commercial PW materials and well-produced electrodes, and not to be a laboratory-scale material handling artifact, it was found to be due to $NaClO_4$, which itself is only used in laboratory environments, partly due to its oxidative nature. As was also presented in the review in chapter 4.1., this work combines previous observations that oxidation by ClO_4^--containing electrolyte causes gas evolution[365] and that the outcome of a SIB material study depends on the conductive salt.[366]

A study on the role of PW water content and drying conditions by Ge *et al*. was published three days prior to this work, including a DEMS investigation.[334] The auhors also observe the effect of water removal on suppressing H_2 and CO_2 evolution as well as a relase of water mostly at high SOC and associated with CO_2 evolution from EC hydrolysis, in line with this work and our previous studies.[189,192] Even though Ge *et al.* used a $NaClO_4$-based electrolyte, they did not detect $(CN)_2$ evolution, likely due to a lower sodium content, not using overcharge conditions and a combination of both a far smaller coin cell, lower electrode loading and a mass spectrometer of lower sensitivity. Neither mass spectrometry limitations nor SEM settings are discussed by the authors, their interpretation of m/z = 26 and m/z = 28 as C_2H_4 and C_2H_6 from SEI formation in the beginning of the first cycle may further be challenged, as without the use of a cold trap, the signals may merely result from fragements of excess electrolyte solvent, as was found in this study.

The study was initiated and designed by Prof. Dr. Ivana Hasa and the author of this thesis. The DEMS setup was initially designed and built by Dr. Balázs B. Berkes. Dr. Faduma M. Maddar prepared both dried and undried electrodes. DEMS experiments, data evaluation, figure preparation and writing were carried out by the author. Dr. Aleksandr Kondrakov, Prof. Dr. Ivana Hasa, Prof. Dr. Jürgen Janek and Dr. Torsten Brezesinski supervised the work. The manuscript was edited by all authors.

Batteries & Supercaps

Research Article
doi.org/10.1002/batt.202300595

Chemistry Europe
European Chemical Societies Publishing

www.batteries-supercaps.org

Elucidating Gas Evolution of Prussian White Cathodes for Sodium-ion Battery Application: The Effect of Electrolyte and Moisture

Sören L. Dreyer,[a] Faduma M. Maddar,[b] Aleksandr Kondrakov,[a, c] Jürgen Janek,[a, d] Ivana Hasa,*[b] and Torsten Brezesinski*[a]

As global energy storage demand increases, sodium-ion batteries are often considered as an alternative to lithium-ion batteries. Hexacyanoferrate cathodes, commonly referred to as Prussian blue analogues (PBAs), are of particular interest due their low-cost synthesis and promising electrochemical response. However, because they consist of ~50 wt% cyanide anions, a possible release of highly toxic cyanide gases poses a significant safety risk. Previously, we observed the evolution of $(CN)_2$ during cycling via differential electrochemical mass spectrometry (DEMS), but were unable to determine a root cause or mechanism. In this work, we present a systematical investigation of the gas evolution of Prussian white (PW) with different water content via DEMS. While H_2 is the main gas detected, especially in hydrated PW and during overcharge (4.6 V vs. Na^+/Na), the evolution of CO_2 and $(CN)_2$ depends on the electrolyte conductive salt. The use of oxidative $NaClO_4$ instead of $NaPF_6$ is the leading cause for the formation of $(CN)_2$. Mass spectrometric evidence of trace amounts of HCN is also found, but to a much lower extent than $(CN)_2$, which is the dominant safety risk when using $NaClO_4$-containing electrolyte, which despite being a good model salt, is not a viable option for commercial applications.

1. Introduction

Electrochemical energy-storage systems, such as rechargeable batteries, are at the heart of the energy transition, contributing to decarbonization of transport and grid energy storage.[1,2] Lithium-ion batteries (LIBs) have been intensively developed and commercialized to fulfil both application requirements, however the rising prices of the raw materials used for their production and supply constraints triggered an accelerated development of alternative battery chemistries.[3,4] Sodium-ion batteries (SIBs), which can be manufactured using the same process equipment as LIBs, are therefore developed as a complementary technology, especially for use cases where cost factors play a more important role than energy density.[5–8] Several cathode active material (CAM) families have been proposed for SIBs, including layered oxides, polyanionic compounds, and Prussian blue analogues (PBAs).[9–11] The latter ones are considered particularly promising due to their low-cost synthesis methods, eliminating the need for high temperature treatments, their tunable redox behavior achieved through the use of sustainable and abundant metals, such as iron and manganese, and their satisfactory capacity and power capability conferred by their open framework structure with large interstitial sites enabling 3D diffusion pathways while minimizing volume changes upon cycling.[9,12,13] Furthermore, they can be operated both in aqueous electrolytes, with a limited cell voltage, and in organic electrolytes similar to those for LIBs, thereby realizing higher cell voltages.[14–18] Strong research and commercialization efforts for these materials are therefore underway, including manufacturers, such as CATL, Natron Energy, and Altris.[19,20]

PBAs for SIBs present the general formula of $Na_xM_a[M_b(CN)_6]_{1-y}\square_y{\cdot}zH_2O$, where M_a and M_b are transition metals, x ($0<x<2$), sometimes instead written as $2-x$, denotes the sodium content of the as-synthesized material, y ($0<y<1$) represent the content of $M_b(CN)_6$ vacancies symbolized as $\square$, and z the number of lattice water molecules per PBA unit.[14,15,18] The Na- and Fe-rich structures are often referred to as Prussian white (PW), indicating all iron to be fully reduced (Fe^{2+}/Fe^{2+}). Vacancies, sodium content, and water play a crucial role in the chemistry of these materials. Three main types of water molecules are present in the structure of PBAs, including chemically bonded coordinated water, interstitial water, and adsorbed water, which all affect their Na^+ storage behavior and cause side reactions with the electrolyte, leading to capacity

[a] S. L. Dreyer, Dr. A. Kondrakov, Prof. J. Janek, Dr. T. Brezesinski
Battery and Electrochemistry Laboratory (BELLA), Institute of Nanotechnology, Karlsruhe Institute of Technology (KIT), Hermann-von-Helmholtz-Platz 1, 76344 Eggenstein-Leopoldshafen, Germany
E-mail: torsten.brezesinski@kit.edu

[b] Dr. F. M. Maddar, Dr. I. Hasa
WMG, The University of Warwick, Coventry CV4 7AL, United Kingdom
E-mail: ivana.hasa@warwick.ac.uk

[c] Dr. A. Kondrakov
BASF SE, Carl-Bosch-Str. 38, 67056 Ludwigshafen, Germany

[d] Prof. J. Janek
Institute of Physical Chemistry & Center for Materials Research (ZfM/LaMa), Justus-Liebig-University Giessen, Heinrich-Buff-Ring 17, 35392 Giessen, Germany

Supporting information for this article is available on the WWW under https://doi.org/10.1002/batt.202300595

Batteries & Supercaps | Research Article
doi.org/10.1002/batt.202300595
Chemistry Europe
European Chemical Societies Publishing

fading.[10,21–24] Therefore, for best CAM performance, a high Na content, but low fraction of vacancies and water, is desirable.[6] In recent years, many studies have been reported on optimized composition,[25–27] synthesis procedures,[28–34] drying procedures,[23,24,26,33,35] and chelating agents[36–40] to obtain PBA/PW materials with such properties. At the same time, various characterization methods and *in-situ* experiments have been employed to study the composition and behavior of PBA/PW materials during electrochemical cycling, mostly focusing on the evolution of crystal phases in dependence of state of charge (SOC) and water content.[41,42] Some of us have shown that an optimal dehydration process for the composite electrodes obtained by a more sustainable aqueous processing is even more critical when compared to the sole CAM powders.[43]

Various electrolyte solvent and salt combinations in PBA/PW-based cells have been reported and reviewed in the literature, with $NaPF_6$[21–23,26,35,40,43–47] and $NaClO_4$[24,25,27,29–34,36–39,48–56] being the most widely used conductive salts. Common solvents are organic carbonates, such as ethylene carbonate (EC), propylene carbonate (PC), dimethyl carbonate (DMC), diethyl carbonate (DEC), and combinations thereof, often also including the additive fluoroethylene carbonate (FEC).[57–59] For a PBA CAM, Piernas-Muñoz *et al.* reported a comparison of various solvent and salt combinations and electrode binders, finding 1 M $NaPF_6$ in EC:PC:FEC 49:49:2 to show the best performance in terms of specific capacity and capacity retention, and in this electrolyte, polyvinylidene difluoride (PVDF), closely followed by carboxymethyl cellulose (CMC), to be the best-performing binder.[60] However, the performance of $NaClO_4$-electrolytes was only slightly different, and the choice of electrolyte, salt, and additives also affects the anode material, electrolyte handling, and considerations related to safety and cost.[61–63]

Glycol ethers, such as diglyme, are another family of possible solvents, which generally lead to the formation of a more stable solid electrolyte interphase (SEI) both in half- and in full-cell configuration when compared to carbonates. In addition, when combined with PW cathodes, their lower anodic stability is not limiting, as PW operates within the electrochemical stability window of glymes.[64] In general, the formation and composition of both SEI and cathode electrolyte interphase (CEI) strongly depend on the chosen salt and solvent combinations.[57,58,65,66]

During battery operation, reactions of and between electrode materials and electrolyte, such as the SEI formation or the release of lattice oxygen from charged layered oxides, with subsequent oxidation of electrolyte, result in gas evolution, which can be studied *in-situ* via differential electrochemical mass spectrometry (DEMS).[67–70] While the gas evolution of LIBs has been studied in great detail, investigations of SIB gassing are still relatively sparse.[67,69,71,72] In previous works on high-entropy PBA and PW CAMs for SIBs, some of us have performed DEMS measurements, in which not only the commonly evolved gases H_2 and CO_2, but also cyanogen [$(CN)_2$] (assumed to be the product of oxidative dimerization of CAM anions, similar to the release of O_2 from layered oxides) were observed.[48–50,67] This finding, although at a lower level, was recently confirmed by Geisler.[72] At the same time, Li *et al.* observed the release of both hydrogen cyanide (HCN) and $(CN)_2$ during thermal runaway of PBA-based cells, and $(CN)_2$ release during the thermal decomposition of PBA/PW has previously been reported.[46,73]

While $(CN)_2$ finds some application as a fumigant and in organic synthesis, it forms HCN upon hydrolysis and also *in vivo*, resulting in an acute toxicity only slightly lower than that of HCN itself.[74–76] The observation of these gases challenges the perception of PBA/PW as being non-toxic and raises safety concerns regarding SIBs using such CAMs. This is especially relevant when considering overcharge events, both intentional and unintentional, and application in confined and poorly ventilated spaces, as commonly found in stationary energy-storage systems located in basements, server rooms, etc.[10,41,46,77]

In this work, we elucidate the role of carbonate solvents, conductive salts, and water content on the gas evolution of aqueous processed PW cathodes, investigated via DEMS during cycling and overcharge. By using a $Na_{1.80(5)}Fe[Fe(CN)_6]\cdot 1.84(3)H_2O$ PW CAM with Fe as the only transition metal and studying it in optimized electrodes of high areal loading,[43] any observation can be understood as genuinely deriving from the material properties and not as immediate artifacts, e.g. from the presence of other metals in the previously studied high-entropy materials[48–50] or from the use of small-scale material and electrode preparation and handling (more prone to the introduction of impurities). Overall, it is found that H_2 is the main gas detected, with CO_2 and $(CN)_2$ evolution strongly depending on the electrolyte conductive salt and its oxidative nature. The use of $NaClO_4$ is the leading cause for the formation of $(CN)_2$, especially during overcharge, which however is not a commercially viable electrolyte salt.

2. Results and Discussion

2.1. Initial Gassing Measurements and Considerations

In this study, DEMS measurements were performed on PW/Na-metal cells cycled at 0.1 C rate (14 mA g^{-1}) in the potential window of 2.0–4.0 V vs. Na^+/Na for two cycles, reflecting regular cycling conditions, and then between 2.0 and 4.6 V in a third cycle, reflecting an overcharge scenario (see more details in Experimental section). It should be noted that due to the two-electrode cell setup, the reported potentials may be affected by SEI formation on the Na-metal anode.[72] Detailed conditions for each measurement presented can be found in Table S1 (Supporting Information), with a summary of the respective specific charge/discharge capacities obtained and gas amounts detected given in Table S2 (Supporting Information).

The initial set of experiments consisted on the comparison of the gassing behavior of PW/Na-metal cells employing two commonly used electrolyte solutions in SIB research, i.e. 1 M $NaClO_4$ in EC:PC:DMC = 1:1:1 (v/v/v) with 5 v% FEC and 1 M $NaPF_6$ in EC:DEC = 3:7 (v/v). While the first one, used in previous DEMS studies on PBAs/PW,[48–50] constitutes a more

Batteries & Supercaps | Research Article
doi.org/10.1002/batt.202300595
Chemistry Europe
European Chemical Societies Publishing

academic approach involving the use of $NaClO_4$ salt, the second one resembles a more industrially relevant electrolyte employing $NaPF_6$. However, these two electrolytes serve as model electrolytes to investigate different gas evolution mechanisms induced by chemically different salts and solvents when cycling dehydrated PW electrodes. Figure 1a and b displays the gas evolution obtained over two initial cycles and an overcharge event during the third cycle. While almost the same capacities and voltage profiles are obtained (see values in Table S2 and Figure S1a, Supporting Information), the gassing behavior differs significantly.

During regular cycling, H_2 evolution is observed for the cell containing $NaClO_4$-electrolyte only at the onset of the first charge process, while it is observed during the whole first charge with a maximum peak at the end of the de-sodiation at 4.0 V, and to a lower extent also at the end of the second charge for the cell containing $NaPF_6$-electrolyte.

In both cases, the formation of H_2 is most likely associated to reduction of residual electrolyte moisture at the anode side. In addition, coordinated water in the PW, which cannot be removed during dehydration, leads to potential further water release in the form of $Na(OH_2)^+$ into the electrolyte during de-sodiation, and particularly so at the end of charge, where the coordination becomes weaker.[33,78] Loosely bound lattice water is likely released fully in the initial cycle, explaining the early H_2 evolution onset, specifically in the first cycle. The larger amount of H_2 detected for the cell containing $NaPF_6$-electrolyte can be explained considering the additional hydrolysis of $NaPF_6$, yielding acidic conditions due to HF formation, which is then further reduced to H_2 at the anode.[79–82] In the cell containing $NaClO_4$-electrolyte, on the other hand, no acid formation is occurring, and the reduction of water at the sodium metal leaves OH^- anions behind. These, in turn, lead to basic electrolyte conditions and hydrolysis of EC and other organic carbonates, which results in CO_2 evolution and explains the stronger evolution of CO_2 in the cell containing $NaClO_4$-electrolyte during regular cycling within the stability window of the solvent molecules.[83,84] The decomposition of surface carbonate impurities,[67,85,86] which have recently been shown to be present also on PW materials,[21] may also contribute to CO_2 evolution and explain the weak signal observed for the cell containing $NaPF_6$-electrolyte. In the absence of lattice oxygen, no chemical oxidation of electrolyte by reactive species released from the lattice may occur. However, the electrochemical oxidation of EC has been shown to occur at potentials above ~4.6 V vs. Li^+/Li, i.e. ~4.3 V vs. Na^+/Na, providing an explanation for the strong

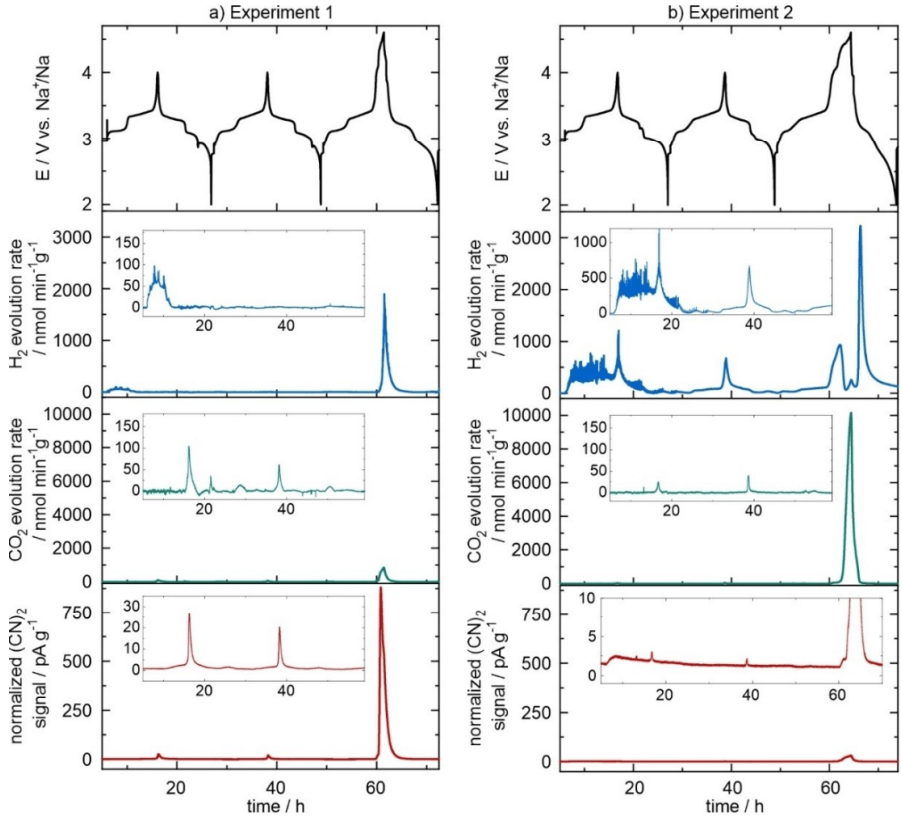

Figure 1. Gas evolution detected in Na half-cells using a dehydrated PW cathode in two different electrolytes: (a) 1 M $NaClO_4$ in EC:PC:DMC = 1:1:1 (v/v/v) with 5 v% FEC and (b) 1 M $NaPF_6$ in EC:DEC = 3:7 (v/v).

Batteries & Supercaps | Research Article
doi.org/10.1002/batt.202300595
Chemistry Europe
European Chemical Societies Publishing

CO_2 evolution during overcharge.[79,87] The drastic difference in CO_2 evolution rates during overcharge is due to the presence of the more oxidation-sensitive DEC[88] in the $NaPF_6$-electrolyte, as will be shown in section 2.3. It should also be noted that the overall time at high potentials is higher for the cell containing $NaPF_6$-electrolyte (3.6 h charge above 4.0 V vs. 1.4 h for the cell containing $NaClO_4$-electrolyte), as can be seen from the direct comparison of voltage profiles in Figure S1a (Supporting Information). Concurrent H_2 evolution during overcharge is caused not only by remaining coordinated water, but also by the electrochemical oxidation of electrolyte, as protic oxidation products are reduced at the anode.[89] The observed suppression of H_2 evolution for the DEC-containing electrolyte during peak CO_2 evolution is likely due to displacement of the former by the latter in carrier gas. The effect is particularly noticeable in the ionization within the mass spectrometer, where a decrease even in carrier gas signal is detected due to high CO_2 concentration. As will be shown in section 2.3., this displacement only occurs in the presence of strongly CO_2-evolving DEC.

Lastly, the evolution of cyanogen, i.e. $(CN)_2$, is also reported for both measurements. Shown is $m/z = 52$, but the fragments and heavier isotope species at $m/z = 26$, 27, and 53 are detected too (see section 2.6.). Since unfortunately no calibration gas is available for this compound in He, a conversion of the measured signal to an absolute gas amount is not directly possible. For a single measurement, detector currents may be reported,[48,90,91] but a semi-quantitative normalization by both CAM mass and spectrometer calibration sensitivity has to be applied to allow comparisons between different measurements.[92] In the mass spectrometer, each species' ion current is amplified using a secondary electron multiplier (SEM) instead of a Faraday cup detector. With a signal gain of around 3 decades, this allows for trace detection and distinction from background noise in the first place. However, especially in newly installed SEMs, such as the one used for this study, aging and degradation lead to a decrease in ion current and SEM gain over time, which can be roughly adjusted for by spectrometer bake-out and applying a higher voltage.[93–95] Since both H_2 and CO_2 signals are also amplified by the SEM, their calibration sensitivity, i.e. the slope of their calibration curves, is known, and a relative comparison can be made between the slopes of each gas for various measurements. The $(CN)_2$ signal is then normalized between measurements by this relative factor, as detailed in Figure S2a and b, Table S3 (Supporting Information), and the literature.[50] In this study, factors between 0.71 and 1.37 have been applied to yield the reported normalized $(CN)_2$ signals. As shown in Figure 1a and b and Figure S1b (Supporting Information), in all cycles, a difference far greater is observed between the $(CN)_2$ evolution in the two electrolytes, with a factor of 26 and 28 between peak currents during regular cycling and overcharge, respectively. In both cases, $(CN)_2$ evolution is observed at high SOC and potential near the end of charge, yet the evolution is far stronger for the cell containing $NaClO_4$-electrolyte, and during regular cycling hardly visible against the background for the cell containing $NaPF_6$-electrolyte.

To confirm the observed gas evolution trends, repeat measurements were conducted, as shown in Figure S3 (Supporting Information). $NaClO_4$-containing electrolyte (Figure S3a, Supporting Information) was prepared freshly in an attempt to both ensure repeatability over electrolyte batches and reduce the H_2 evolution at the onset of cycling. As a result, the H_2 evolution is suppressed and the CO_2 evolution during regular cycling is reduced, further confirming the effect of residual moisture in the electrolyte as the main source for water. Again, $(CN)_2$ evolution was observed, especially during overcharge for the $NaClO_4$-electrolyte. A deviation of the peak normalized $(CN)_2$ signal by a factor of ~2 (881 pA g^{-1} vs. 414 pA g^{-1}) demonstrates that, while there are limitations of the presented semi-quantitative normalization, the uncertainties obtained are an order of magnitude smaller than the difference between the two electrolytes. We note that this repeat measurement was carried out five months after the first measurement and, to adjust for the aforementioned SEM degradation, with 1380 V instead of 1200 V applied to the SEM. Figure S3b (Supporting Information) shows that for a repeat measurement (in this case, shortly after the initial measurement) on a cell containing the $NaPF_6$-electrolyte, similar gas evolution profiles were obtained, with the only variations observed in the total amount of gas generated during overcharge, which depends strongly on the exact duration of the overcharge and electrode specific surface area.

As oxidation of cyanide anions is required to form $(CN)_2$, the presence of the ClO_4^- anion with its oxidative properties appears to be an explanation for the formation of cyanogen. Metzger *et al.* previously reported CO_2 evolution stemming from the oxidation of conductive carbon by $LiClO_4$ at potentials higher than 5 V vs. Li^+/Li.[87] However, $(CN)_2$ signal is also observed during overcharge for the cell containing $NaPF_6$-electrolyte, and because different cell sets were used, $NaClO_4$ contamination can be ruled out. Therefore, either a competing or a more complex mechanism must occur, such as one involving a previous release of CN^- and/or HCN or involving iron. Possible considerations include the roles of SOC and potential as oxidation causes, as well as the roles of water content, electrolyte solvents, acidity/basicity, and various experimental settings in the gas evolution. These will be disentangled in the following in order to understand the gassing behavior of PW CAM better and narrow down the root cause of $(CN)_2$ evolution during overcharge above 4.0 V.

The analysis will focus on H_2, CO_2, and $(CN)_2$. Two other species commonly discussed in gas evolution studies are CO ($m/z = 28$) and C_2H_4 ($m/z = 26$ and 28), with the former formed together with CO_2 during electrolyte decomposition and the latter generated during SEI formation from EC.[67–70] Indeed, as shown in Figure S4a (Supporting Information), a strong $m/z = 28$ signal is observed during overcharge. However, CO is also formed as a fragment of CO_2 or DEC in the mass spectrometer, which has to be corrected for. Additionally, a correction for C_2H_4 is needed, which is also present in the calibration gas and can normally be analyzed at $m/z = 26$ as $C_2H_2^+$, yet not in the case of PW, as $m/z = 26$ is dominated by the CN^+ fragment or $(CN)_2^{2+}$ ions. A precise quantitative determination of CO would

Batteries & Supercaps | Research Article
doi.org/10.1002/batt.202300595
Chemistry Europe
European Chemical Societies Publishing

only be possible via differential electrochemical infrared spectroscopy (DEIRS).[90] Since the evolution of CO typically occurs concurrently with that of CO_2 and from the same underlying electrolyte oxidation mechanisms, it is therefore not reported individually. This is also shown in Figure S4a (Supporting Information), where after correction for the CO fragment of CO_2 no remaining signal (but also no negative signal) is observed during regular cycling, because hydrolysis of EC and decomposition of Na_2CO_3 do not generate CO.[83,84] Nevertheless, during overcharge a signal of genuine CO from electrolyte oxidation remains after correction.

POF_3 ($m/z = 85$ and 104) is detected as the product of $NaPF_6$ hydrolysis and decomposition, also yielding highly reactive PF_5, which however was found to further decompose to POF_3 in the steel tubing leading to the mass analyzer.[80–82] As shown in Figure S4b (Supporting Information), POF_3 can indeed be detected from the cell containing $NaPF_6$-electrolyte. However, its traces are too dilute in the constant carrier gas stream of the open headspace DEMS setup used in this work, and therefore no precise measurement outside of overcharge conditions is possible.[67]

2.2. Effect of Water Content

By using undried electrodes as described previously,[43] the effect of interstitial and adsorbed water on gas evolution is studied, as shown in Figure 2a for a cell containing $NaClO_4$-electrolyte and in Figure 2b for a cell containing $NaPF_6$-electrolyte. In both cases, gas evolution peaks appear broader, with a distinctive different voltage profile associated to the electrochemical activity of the monoclinic PW phase exhibiting lower capacities within the standard 2.0–4.0 V potential range. As expected, a strong H_2 evolution is now observed even during regular cycling for the cell containing $NaClO_4$-electrolyte. The release of water into the electrolyte upon charge results in increased EC hydrolysis, thus also increasing the CO_2 evolution. The $(CN)_2$ evolution, on the other hand, is reduced when compared to that of the dehydrated electrode, so that a dependence of $(CN)_2$ evolution on SOC and sodium content in the structure can be assumed. The same findings apply also during overcharge. It is worth mentioning that the hydrated monoclinic PW phase enables extraction of one sodium per formula unit at about 3 V *vs.* Na^+/Na and that the water content of the structure shifts the potential for the low-spin iron to almost 4 V vs. Na^+/Na. Rudola *et al.* reported that accessing this

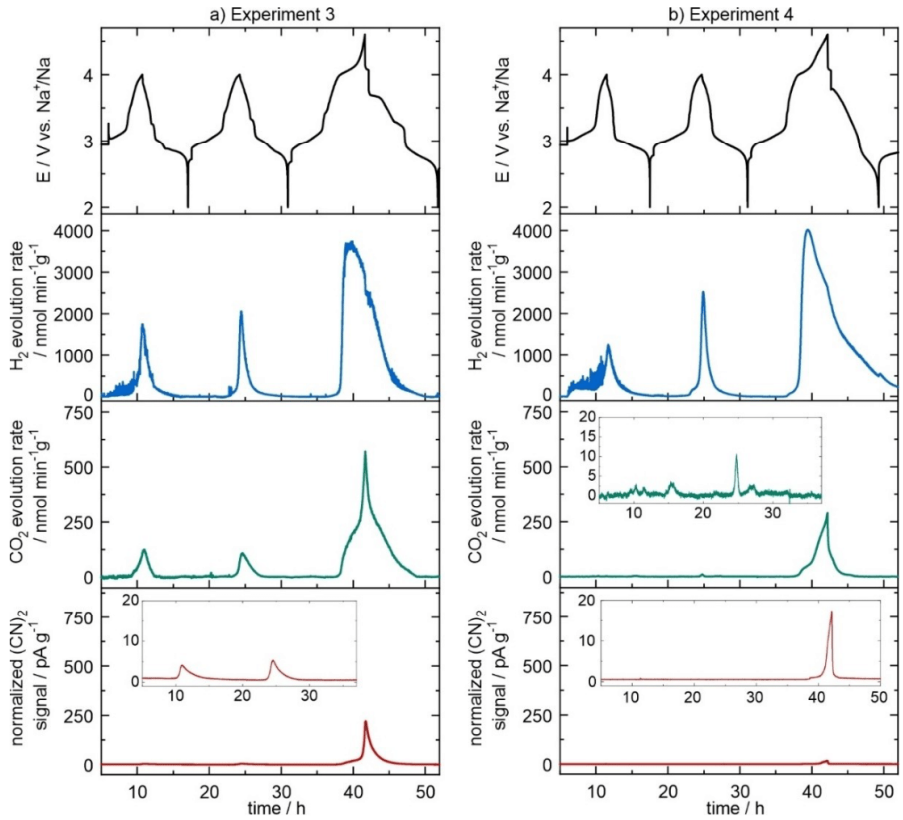

Figure 2. Gas evolution in Na half-cells with an undried PW cathode using two different electrolytes: (a) 1 M $NaClO_4$ in EC:PC:DMC = 1:1:1 (v/v/v) with 5 v% FEC and (b) 1 M $NaPF_6$ in EC:DEC = 3:7 (v/v).

Batteries & Supercaps | Research Article
doi.org/10.1002/batt.202300595
Chemistry Europe
European Chemical Societies Publishing

plateau rapidly degrades the cell performance, as further structural water is released.[96] However, for the cell containing $NaPF_6$-electrolyte, the first-cycle H_2 evolution appears similar as with the dehydrated electrode, with a rather constant H_2 evolution starting immediately upon passing current through the cell and only becoming more intensive near the end of charge. In the second cycle, the H_2 evolution is then similar between both electrolytes, demonstrating the dominating role of PW water content. Because the electrolyte is acidic due to PF_6^- hydrolysis, no CO_2 evolution from EC hydrolysis is observed, as this would require basic conditions. Under regular cycling conditions, only a weak $(CN)_2$ signal is detected. Interestingly, a different overcharge behavior is evident for this electrolyte with an undried electrode, with now H_2 evolution from water release (similar to the other electrolyte) dominating the gas evolution instead of CO_2 from DEC oxidation. Likely, the presence of water or more acidic conditions affects the DEC oxidation and explains the lower CO_2 evolution. The $(CN)_2$ evolution is again suppressed, both compared to the combinations of either $NaPF_6$-electrolyte and dehydrated electrode or $NaClO_4$-electrolyte and undried electrode. Regarding mechanistic considerations, the reduced evolution at the same potential when compared with dehydrated electrodes rules out an electrochemical oxidation as the rate limiting step, while the reduced evolution at lower SOC might indicate a contribution of chemical oxidation.

At this point, two effects of increased water content shall be discussed. At high potentials and water contents (undried electrodes), and especially during overcharge, one might assume water oxidation to occur via electrocatalysis by the desodiated PW framework,[97] yet no O_2 evolution was detected, as shown in Figure S5a and b (Supporting Information). The high H_2 evolution amounts, i.e. curve integrals as listed in Table S2 (Supporting Information), can be converted into water loss from the CAM, as exemplified in Table S4 and Figure S6 (Supporting Information), yielding a water release between 1.15 and 1.37 wt% during regular cycling and 4.93 to 6.44 wt% during overcharge. This is in good agreement with the ~10 wt% total water content of undried PW or water uptake of dry material often observed via thermogravimetric analysis, highlighting the importance of PW dehydration to mitigate the risk of cell swelling and rupture due to H_2 accumulation.[21,22,24,43,51] As is shown in Table S5 (Supporting Information), an average weight loss of 10.43 wt% relative to the CAM mass was observed when drying the electrodes used in this study (i.e. difference in water content between undried and dried electrodes).

2.3. Effect of Electrolyte Solvent

The effect of electrolyte solvents on gas evolution was also investigated. To this end, 1 M $NaPF_6$ in EC:PC:DMC = 1:1:1 (v/v/v) with 5 v% FEC was prepared and data were obtained for both dehydrated and undried PW electrodes. These data can then be evaluated in comparison with the results obtained by using 1 M $NaPF_6$ in EC:DEC = 3:7 (v/v) (Figure 1b and 2b), but this time avoiding the strong CO_2 evolution of DEC. The solubility of $NaClO_4$ in EC:DEC = 3:7 (v/v) was found to be unsatisfactory at room temperature, while at higher temperatures degradation was observed in the form of turbidity and dark precipitate, thus the $NaClO_4$ version of this electrolyte was not investigated.

As shown in Figure 3a, the combination of a dehydrated PW electrode and the new electrolyte resulted in no significant H_2 evolution during regular cycling, indicating a lower water content when compared with Figure 1b. Possible reasons include a lower moisture level in the freshly prepared electrolyte than that shipped before use or a reduced release of interstitial and adsorbed water into the electrolyte containing different solvents. By contrast, slightly stronger CO_2 evolution and $(CN)_2$ evolution were observed. During overcharge, it becomes apparent that the change of electrolyte solvents, i.e. the replacement of DEC, strongly affects the gassing behavior, as Figure 3a no longer shows the strong CO_2 evolution and displacement of H_2 evolution found in Figure 1b for EC:DEC. Instead, the evolution of these gases is now similar in profile and quantity to that of Figure 1a, where the same solvent mixture, but a different conductive salt, was used, suggesting that under overcharge conditions, the electrochemical oxidation of solvent molecules is the main contribution to the evolution of these gases. On the other hand, the $(CN)_2$ evolution remained low, similar to that in Figure 1b, highlighting that it is not the choice of solvent, but of conductive salt, that affects the $(CN)_2$ release.

Figure 3b shows the gassing resulting from a combination of an undried PW electrode and the newly prepared electrolyte. The H_2 evolution is drastically increased when compared with the dehydrated electrode in Figure 3a and similar to that observed for undried electrodes in Figure 2. The CO_2 evolution during regular cycling is increased when compared with that in Figure 2b and 3a (slightly), indicating that the solvent mixture may be more prone to hydrolysis of the organic carbonates. A very weak $(CN)_2$ release is observed during regular cycling, but interestingly the evolution is the strongest out of all $NaPF_6$-containing measurements reported in this study. A possible explanation other than cross-contamination for this observation is discussed in section 2.7.

We note that an analysis using diglyme as electrolyte solvent, as reported by Geisler,[72] was attempted but proven unsuccessful, since it was quickly purged out by the carrier gas stream, leaving a cell too dry to cycle behind. Because the same effect is observed with organic carbonate solvents when using polypropylene instead of glass fiber separators, a possible explanation is the weaker retention of an electrolyte reservoir, akin to poor wetting.

2.4. Effect of Conductive Salt

Having narrowed down the reason for strong $(CN)_2$ evolution from PW to the use of $NaClO_4$ as conductive salt, two hypotheses regarding its role may be made, i.e. either the oxidative nature of $NaClO_4$ results in an increased oxidation of CN^- to $(CN)_2$ or the electrolyte acidity/basicity (the former from

Batteries & Supercaps | Research Article
doi.org/10.1002/batt.202300595
Chemistry Europe
European Chemical Societies Publishing

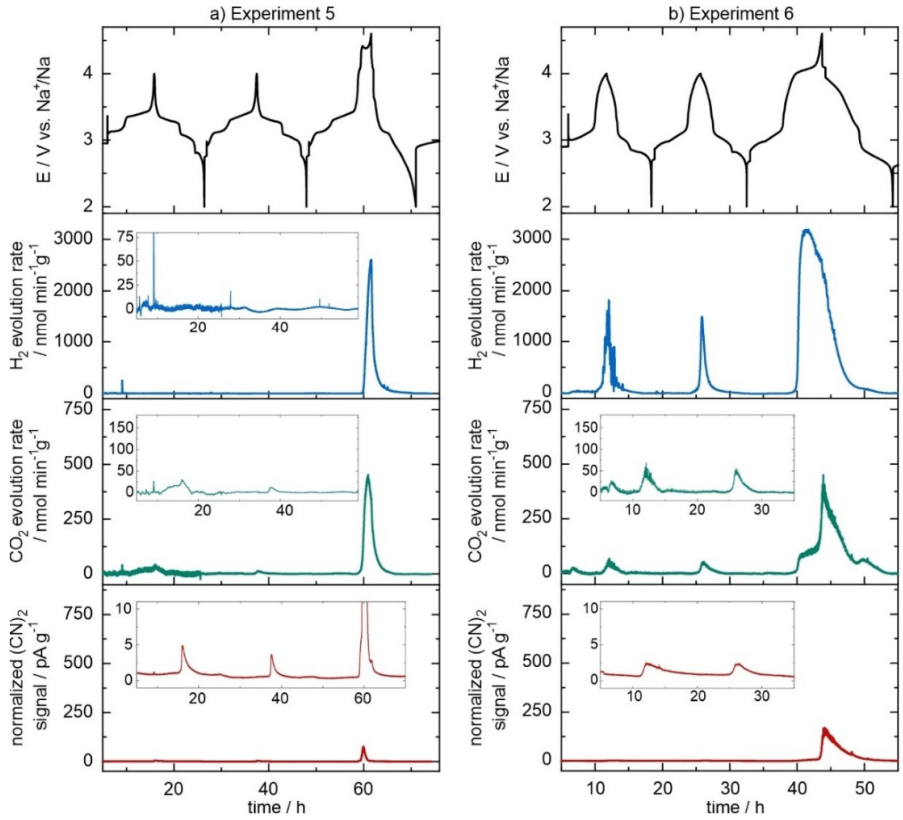

Figure 3. Gas evolution in Na half-cells with (a) a dehydrated and (b) undried PW cathode using 1 M $NaPF_6$ in EC:PC:DMC = 1:1:1 (v/v/v) with 5 v% FEC as electrolyte.

$NaPF_6$ and the latter from $NaClO_4$, as discussed previously) influences the $(CN)_2$ evolution, with basic conditions favoring it. To differentiate the two hypotheses, two additional electrolytes were prepared, both based on the previously used EC:PC:DMC mixture containing 5 v% FEC. The first electrolyte contained 0.3 M $NaClO_4$, the other 0.3 M $NaClO_4$ and 0.7 M $NaPF_6$, with the respective DEMS results shown in Figure 4a and b, respectively.

The effect of conductive salt concentration on the achieved capacity (Table S2, Supporting Information) is negligible because of the low cycling rate. If the oxidative effect of $NaClO_4$ is causing $(CN)_2$ formation, both electrolytes should result in evolution of a similar magnitude to that shown in Figure 1a for the 1 M $NaClO_4$ electrolyte, however with the reduced concentration of $NaClO_4$ possibly leading to a partial decrease in $(CN)_2$ evolution. It is worth noting that the evolution should not be limited by the available $NaClO_4$. Indeed, in a typical experiment, around 0.25 mmol of CAM is used, but either 0.35 mmol or 0.75 mmol of $NaClO_4$ is contained in the electrolyte, and the CAM does not exhibit substantial degradation according to the voltage profile and capacity. In the case of electrolyte acidity/basicity, a strong difference between the two electrolytes should be observed, as the first has a basicity similar to the initial $NaClO_4$ electrolyte (Figure 1a), while the second should be acidic similar to the initial $NaPF_6$-electrolyte (Figure 1b).

Because the same solvents are used and the water content of electrolyte and PW electrodes is low, the evolution of H_2 and CO_2 reported for both measurements in Figure 4 is similar during charge and overcharge. The release of $(CN)_2$ is observed in both electrolytes, with a pronounced amount detected during overcharge, and with an evolution profile similar to that obtained with a higher concentration of $NaClO_4$, as in Figure 1a. Therefore, the oxidative properties of $NaClO_4$ are confirmed to cause $(CN)_2$ evolution. A difference in peak evolution rates between Figure 1a and 4a is likely due to the dilution of the electrolyte, while the small difference between Figure 4a and 4b may be attributed to a further displacement of ClO_4^- anions in the CEI and electric double layer by PF_6^- anions. This finding also explains the difference in $(CN)_2$ signal intensity observed between previous works in our group (using $NaClO_4$)[48–50] and Geisler's work (using $NaPF_6$).[72] Interestingly, a similar, seemingly contradictory finding at the anode side of SIBs has been also explained by the use of different conductive salts by Goktas *et al.*[65]

Batteries & Supercaps | Research Article
doi.org/10.1002/batt.202300595
Chemistry Europe
European Chemical Societies Publishing

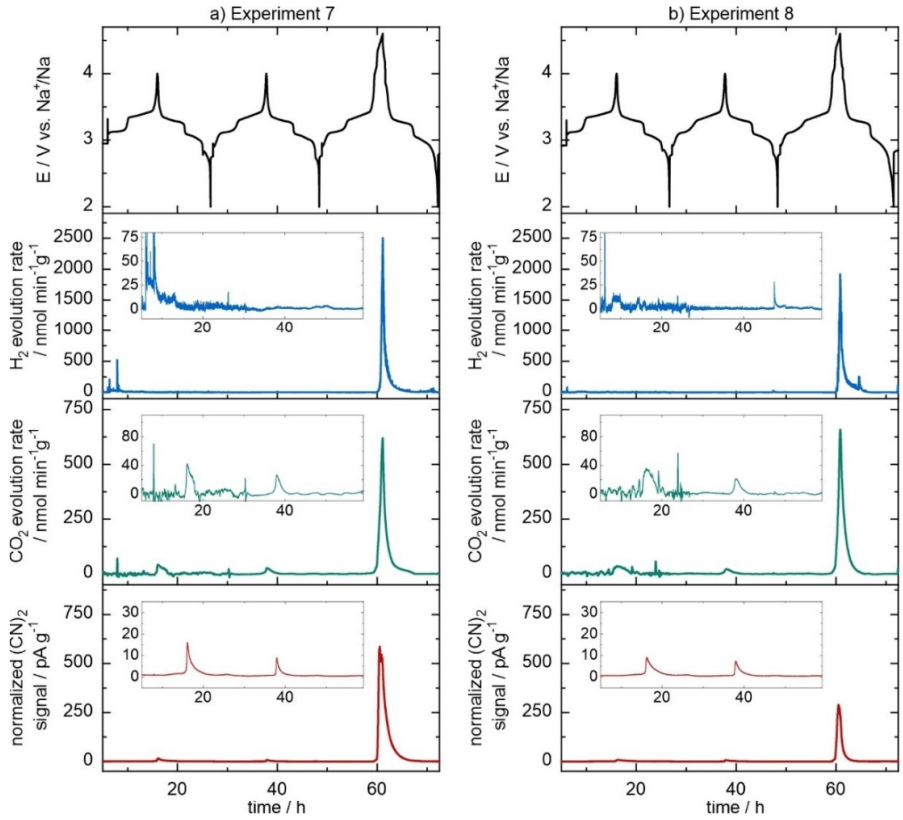

Figure 4. Gas evolution in Na half-cells with a dehydrated PW cathode using EC:PC:DMC = 1:1:1 (v/v/v) with 5 v% FEC as electrolyte solvent and (a) 0.3 M $NaClO_4$ or (b) 0.3 M $NaClO_4$ and 0.7 M $NaPF_6$ as conductive salt.

The detection of $(CN)_2$ evolution in PW-containing cells has significant relevance to the commercial application of PBA/PW cathodes. It is equally relevant to highlight that the cause of $(CN)_2$ evolution is the oxidative nature of the $NaClO_4$ salt, which, while representing a valid model electrolyte salt for laboratory-scale research, cannot be considered a viable option in commercial applications due to its strong oxidation properties and explosive nature in the dry state.[87,98,99] In fact, various novel electrolyte formulations, including alternative conductive salts, such as sodium bis(oxalate)borate, are developed to mitigate safety concerns (to reduce flammability and HF generation, for example) and are already applied to PW CAMs.[47,58,98,100–102]

2.5. Effect of Other Measurement Conditions

Further experiments to evaluate the role of DEMS measurement conditions and trace gas evolution have been carried out and are discussed below. Figure 5a shows the result of a measurement performed at 45 °C instead of 25 °C. Due to increased electrolyte evaporation, a more volatile baseline for H_2 and CO_2 is obtained, with the evolution of these gases being increased both during regular cycling and overcharge. This finding is expected, as electrolyte degradation by hydrolysis and oxidation is increased at elevated temperatures.[83,87] However, the $(CN)_2$ evolution was found to be increased compared to cycling at 25 °C, while it slightly decreased from the 1st to the 2nd charge during regular cycling and then increased during overcharge, but to a much lower extent when compared to the test conducted at 25 °C.

At the same time, the voltage profile of the electrode cycled at 45 °C also strongly deviates after the overcharge, showing a much lower discharge capacity characterized by high irreversibility. Reduced performance of PBA/PW CAMs at elevated temperatures has been reported previously and attributed to degradation and formation of a resistive CEI.[32,45,103] It can be assumed that the formation of such a resistive CEI is not only more severe under overcharge conditions, but that it also prevents further oxidation of the cyanide ions to $(CN)_2$ by restricting charge transfer between ClO_4^- and CAM.

Figure 5b shows the gas evolution from a DEMS measurement conducted with only 350 µL of electrolyte instead of 750 µL. While such a measurement in our setup is more likely to fail due to cell dry-out by carrier gas, it is more realistic in terms

Batteries & Supercaps
Research Article
doi.org/10.1002/batt.202300595
Chemistry Europe
European Chemical Societies Publishing

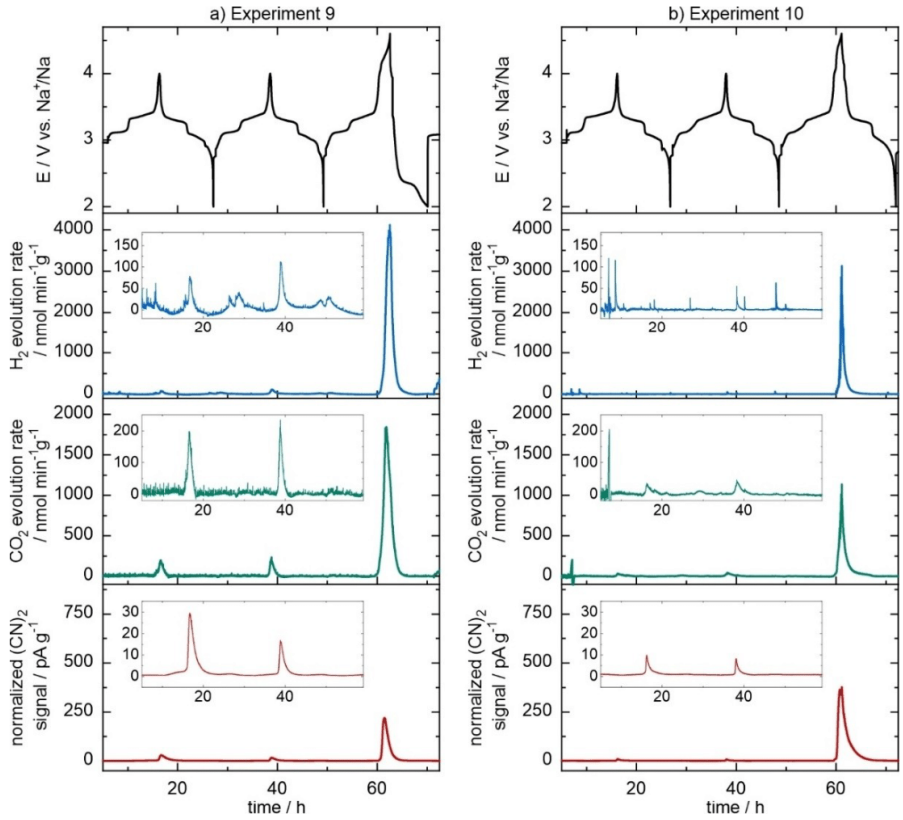

Figure 5. Gas evolution in Na half-cells with a dehydrated PW cathode using 1 M $NaClO_4$ in EC:PC:DMC = 1:1:1 (v/v/v) with 5 v% FEC after (a) increasing temperature from 25 to 45 °C and (b) reducing electrolyte volume from 750 to 350 µL.

of electrolyte to active mass ratio[104] (~5:1 vs. ~12:1, assuming ~1.3 g/mL electrolyte density) and can be more precise due to lower dissolution of gases in the bulk electrolyte, leading to tailing of the evolution curves.[67,105] In this case, no effect on peak tailing is observed and the amounts of H_2 and CO_2 evolved do not differ significantly. Interestingly, the $(CN)_2$ evolution is reduced, yet still significant, especially during overcharge, with a slight peak broadening appearing. A probable explanation is the different absolute amount of $NaClO_4$ in the cell, although a quantitative consumption of $NaClO_4$ is unlikely. Instead, as excess electrolyte is purged out of the cell, the salt concentration is increased in the remaining electrolyte, i.e. that in the glass fiber separator's reservoir, which is less affected by the carrier gas stream. With more initial electrolyte, this effect is more pronounced and leads to a higher effective concentration of $NaClO_4$, similar to the findings of salt concentration variation shown in Figure 4a.

Having established that the lower electrolyte volume does not affect the observed gas evolution beyond the previously discussed differences, lastly, a measurement with this reduced electrolyte volume is carried out without cooling the cold trap of the DEMS setup.[90,91] Since it comes at the price of increased SEM degradation and background noise, as well as reduced target molecule ionization due to electrolyte molecules in the spectrometer, a lower electrolyte volume is necessary to still gather relevant data. This measurement allows to rule out a significant effect of $(CN)_2$ condensation into the cold trap and will also be of interest in the following section on HCN evolution. The resulting gas evolution is shown in Figure S7 (Supporting Information), and as can be seen, none of the gas evolution trends show a significant difference to the measurement with cold trap (Figure 5b). The variation of the peak $(CN)_2$ evolution rate during overcharge appears to be in agreement with the limitations of relative quantification and the observed differences between the experiments combining $NaClO_4$-electrolyte and dehydrated PW electrodes.

2.6. Evolution of Hydrogen Cyanide

Because HCN formation is a side reaction of some PW synthesis routes[22,35,41] and has been previously observed during thermal runaway of PBA cells,[46] and $(CN)_2$ is known to hydrolyze under formation of HCN, in the following, we consider whether HCN is

Batteries & Supercaps | Research Article
doi.org/10.1002/batt.202300595
Chemistry Europe
European Chemical Societies Publishing

also present during the DEMS measurements. For this, the mass spectrometer's ability to discriminate between molecules of the same gas, but of other isotope composition, referred to as isotopologues, is utilized, which is a powerful enhancement of DEMS study capabilities.[67]

The detection of HCN in the presence of $(CN)_2$ is complicated by fragmentation. At standard conditions (25 °C, 70 eV ionization energy), HCN is detected mostly at $m/z=27$ (HCN^+, 100% relative intensity) and $m/z=26$ (CN^+, ~16% relative intensity), as well as in the form of molecules containing a heavier isotope at $m/z=28$ (~2% relative intensity).[106] $(CN)_2$, on the other hand, is not only detected at $m/z=52$ (100% relative intensity), but also at $m/z=26$ (CN^+ fragment and $(CN)_2^{2+}$, ~5% relative intensity) and, due to isotopologues containing either ^{13}C or ^{15}N, at $m/z=53$ (~3% relative intensity), as well as very weakly in combination of heavy isotope content and fragmentation at $m/z=27$.[107] In a standard mass spectrometry application, short of gas chromatography, the simultaneous determination of species with overlapping signals, such as HCN and $(CN)_2$, requires solving a set of linear equations obtained with a calibration matrix that contains the fragmentation intensity patterns of all gases of interest.[72,108] In a battery DEMS application, a further difficulty arises from fluctuating background signals, e.g. various $C_2H_x^+$ species from ethylene and DEC fragments ($m/z=26$, 27, and 28). As background signals are present and no calibration gases and matrix are available, two considerations are presented instead, which allow discussing the relative presence of HCN. In these considerations, three assumptions are made: (1) Molecules other than HCN and $(CN)_2$ contribute only to the baseline, but not to the signal peaks observed for $m/z=26$, 27, 52, and 53. This is supported by DEMS data of a previous study utilizing the same electrolyte and cutoff potential, but layered oxide CAMs.[109] The respective signal profiles are shown in Figure S8a-c (Supporting Information). (2) The formation rates of $(CN)_2$ isotopologues are similar, i.e. the kinetic isotope effect is weak. (3) There is no significant isotope effect between isotopologues with regards to probabilities of ionization and fragmentation.

Firstly, in all measurements carried out with $NaClO_4$-electrolyte (all DEC-free), $m/z=27$ peaks can be detected against the background noise, i.e. when the signal noise from excess electrolyte has decreased sufficiently. As evident from Figure 6a-d and S9a-c (Supporting Information), the peak raw signal of $m/z=27$ is detected between 2.9 and 9.8 min earlier than that of $(CN)_2$ at $m/z=26$ and 52 in some measurements. However, each mass channel is scanned every 13.5 s for the experiments in this study, resulting in a 13 to 43 scan cycle difference between peak signal rates. In Figure 6d, instead of an earlier peak signal, a stronger peak shoulder is observed for $m/z=27$. However, as shown in Figure S9a (Supporting Information), the effect is reversed in the case of simultaneous presence of $NaClO_4$ and $NaPF_6$.

If fragmentation were the sole source of signal beyond background in all three of these channels, peak signal rates would occur figuratively simultaneously, as they have a common source in the $(CN)_2$ molecule, which is only ionized and fragmented in the mass spectrometer. The time between ionization at the ion source and detection at the SEM is extremely short compared to the duration of the experiment and even the length of one scan cycle. The fact that the $m/z=27$ signal peak occurs much earlier suggests that, additionally to the $^{13}C^{14}N^+$ or $^{12}C^{15}N^+$ fragment of $(CN)_2$, another gas (in this case, HCN) contributes to the overall signal, which is either formed slightly earlier or transported to the spectrometer faster.

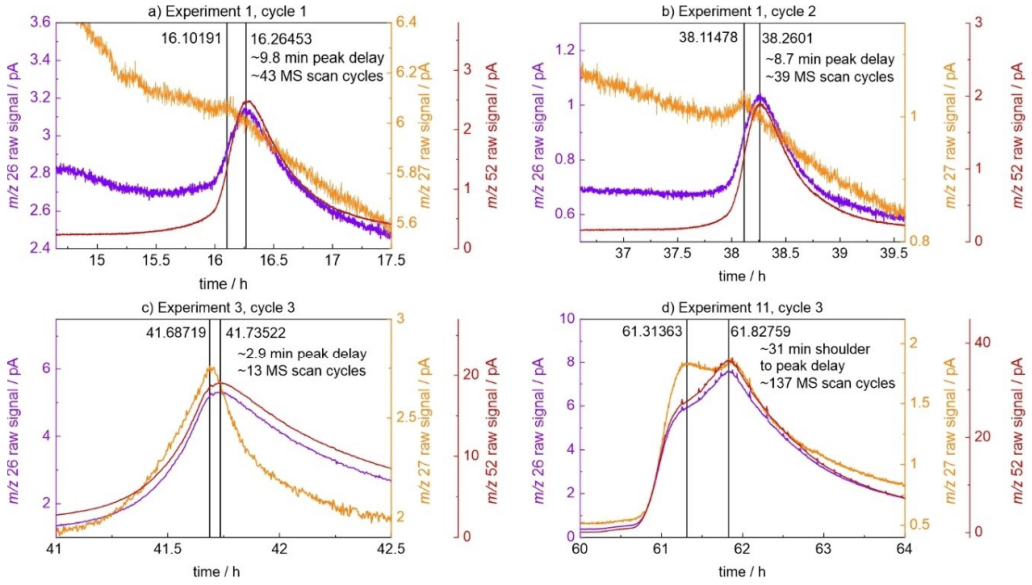

Figure 6. Delay in signal peaks between m/z = 26 and m/z = 27 and 52 indicating the presence of trace amounts of HCN.

Batteries & Supercaps | Research Article
doi.org/10.1002/batt.202300595
Chemistry Europe
European Chemical Societies Publishing

Assuming laminar flow of carrier gas, a slightly earlier peak formation rate of HCN in the cell may be assumed. However, from the low signal-to-noise ratio in $m/z=27$, a low concentration of HCN can be inferred. Another limitation that should be considered is the reactivity of $(CN)_2$, both in the presence of traces of moisture and H_2. The earlier peak formation rate is not necessarily found in the cell, but can occur in the DEMS tubing by hydrolysis or reduction of $(CN)_2$, similar to the detection of PF_5 as POF_3, as reported by Solchenbach *et al.*[81] A similar HCN formation reaction, albeit not affecting peak evolution rate time differences, is reduction of $(CN)_2$ in the presence of H_2 at the hot filament of the mass spectrometer, a reaction known to occur under these conditions between Cl_2 and H_2.[110] Secondly, one may consider isotope abundance and relative intensity ratios. At this point, it should be noted that while both for National Institute of Standards and Technology (NIST) reference data[106,107] and for the DEMS measurements an ionization energy of 70 eV was applied, yet a slight deviation of relative intensities can be observed due to different temperatures during ionization.[81,87]

Under the previously made assumptions, in the case of pure $(CN)_2$, the peak intensity ratio (1) between $m/z=26$ and 52, on the one hand, and $m/z=53$ and 52, on the other hand, should be close to the NIST reference values of 4.7 and 3.1%, respectively,[107] and (2) between $m/z=27$ and 26 should be around half that between $m/z=53$ ("heavy $(CN)_2$") and 52. Since only one of the two fragments of "heavy $(CN)_2$" carries a heavy isotope, single ionization followed by fragmentation leads to only one of the two fragments carrying the charge. Additionally, the $m/z=26$ signal may also be increased from traces of $(CN)_2^{2+}$. However, if an increasing concentration of HCN is present, both the $m/z=26$ and 27 signals are increased, with the latter increasing almost 6 times more, as in pure HCN the ratio between $m/z=26$ and 27 is ~17%.[106] A deviation of the ratios discussed above can therefore indicate the presence of HCN.

As shown in Figure 7a-c and Figure S10a-c and Table S6 (Supporting Information), the intensity of all four raw signal peaks is determined and compared for a series of measurements. The ratio between $m/z=53$ and 52 was found to be between 2.5 and 2.9%, close to the NIST reference value of 3.1%.[107] However, the ratio between $m/z=26$ and 52 was found to be between 20.3 and 24.2% in the measurements, far above the NIST reference value of 4.7%. A stronger relative signal of $m/z=27$ is then also found for the ratio between $m/z=27$ and 26, between 12.2 and 20%. While a linear equation system could be solved for the shares of HCN and $(CN)_2$ that generate these relative intensities, the result would be the share of ionized molecules. The latter differs significantly from the actual share of molecules due to different electron ionization cross sections between HCN and $(CN)_2$, so that again a calibration gas containing known quantities of both gases would be needed for a precise determination, even of ratios.[72,108,111] If, for a rough estimation, the ionization probability of both gases is assumed to be equal and all $m/z=27$ signal is attributed to HCN, the ratio between $m/z=27$ and 52 would indicate additional HCN evolution in the range of 2.9 to 4.8% of the $(CN)_2$ evolution. No major differences in the observed ratios between the measurements (see Table S6, Supporting Information) further demonstrate that neither water content nor electrolyte volume or cold-trap settings significantly affect the perceived ratio between HCN and $(CN)_2$.

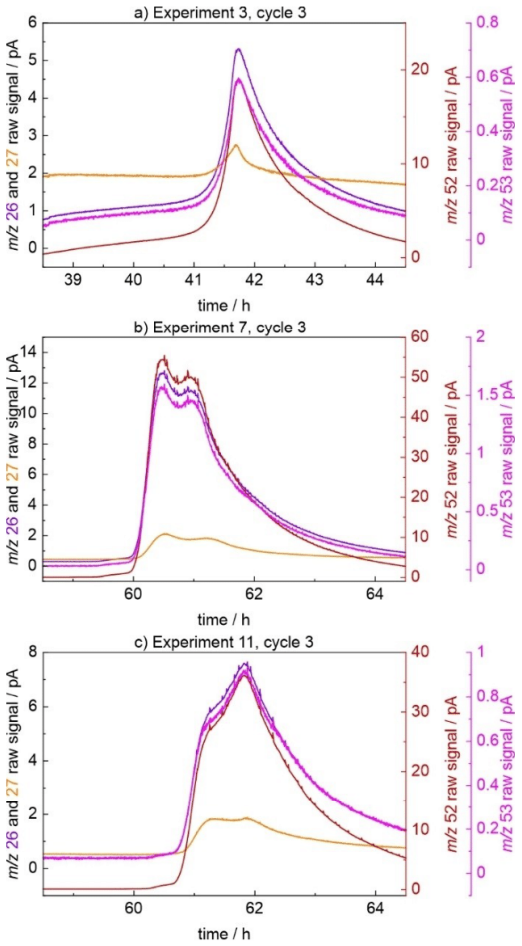

Figure 7. Ratios of m/z = 26, 27, 52, and 53 raw signal intensities indicating the formation of trace amounts of HCN, as m/z = 27 signal is stronger than expected for a mere isotopologue fragment.

2.7. Mechanistic Considerations and Discussion

In light of the results presented so far and the available literature, a consideration of likely gas amount and formation mechanism of $(CN)_2$ shall be discussed. In the initially reported observation of $(CN)_2$ evolution, a comparison was made to the release of lattice oxygen from layered oxide CAMs, another anion oxidation process.[48] Having found $NaClO_4$ to play a significant role in the $(CN)_2$ formation, this now has to be reconsidered, also taking into account a difference in reversi-

Batteries & Supercaps | Research Article
doi.org/10.1002/batt.202300595
Chemistry Europe
European Chemical Societies Publishing

bility. Between O^{2-} ions and oxygen gas, peroxides and hyperoxide anions exist, allowing for an often at least partially reversible, capacity providing anion redox.[112,113] While a respective $(CN)_2^-$ anion has been discussed in the literature, this discussion is limited to theoretical calculations of anions in the atmosphere of Saturn's moon Titan.[114,115] The presence of this species in PW CAM therefore appears unlikely, so that cyanide oxidation is irreversible. Still, some similarities between the loss of O_2 from layered oxides and $(CN)_2$ from PW may exist. In layered oxides, an oxygen-depleted surface forms, commonly referred to as rocksalt-type phase. This layer impedes ion diffusion (the transition metals in it become redox inactive) and with its thickness increasing during cycle life, helps explain some of the capacity fading seen in layered oxide CAMs.[116] In the case of rocksalt-type layer, a measurement of the evolved gases can be used to calculate the fraction of CAM converted to oxygen-depleted material and, taking the specific surface area of the CAM particles into account, layer thickness, with a conversion of ~2% being reported for strong overcharge conditions.[117,118]

A similar, cyanide-depleted surface may form on the PW particles, as contact to $NaClO_4$ and gas diffusion into the electrolyte are only possible at the particle surface. While its detection via transmission electron microscopy (TEM) proves troublesome due to the susceptibility of hexacyanoferrates to beam damage, Yan *et al.* reported X-ray photoelectron spectroscopy (XPS) and Fourier-transform infrared spectroscopy (FTIR) findings of a cycled PBA cathode that indicate the formation of an altered surface layer or CEI when using $NaPF_6$-electrolyte.[45] Interestingly, Sottmann *et al.* observed the formation of $NaMnCl_3$ via X-ray diffraction (XRD) of a cycled manganese hexacyanoferrate cathode, with a reduction of $NaClO_4$ as the only possible source of Cl^- anions.[56] A reaction of no more than 1 to 2% of PBA/PW CAM seems probable. Firstly, as also reported by Sottmann *et al.*[56] and Piernas-Muñoz *et al.*,[60] a change of conductive salt to $NaPF_6$ does not lead to a substantial increase in capacity retention, ruling out a noticeably stronger decomposition of the CAM by $NaClO_4$. Furthermore, long-term cycling of PBA/PW CAM is still possible in $NaClO_4$-electrolyte, suggesting that the degradation reaction is limited in its extent. Thus, a likely reason is the limitation of the reaction to the available particle surface.

However, the calculation of how much $(CN)_2$ is evolved requires the number of reacting cyanide ions per formula unit of degrading hexacyanoferrate to be known. A full conversion (3 molecules of $(CN)_2$ per $Fe[Fe(CN)_6]$ unit) would yield iron oxides, hydroxides or chlorides, in agreement with the observation of $NaMnCl_3$ formation by Sottmann *et al.*,[56] yet through a series of intermediate species of unknown reactivity. Alternatively, only one or two cyanide ligands per hexacyanoferrate unit may be oxidized, further reducing the estimated amount of $(CN)_2$ evolution by a factor of 1/6 or 1/3. Cheah *et al.* reported $(CN)_2$ evolution due to an irreversible electrochemical oxidation of hexacyanoferrate at 0.586 V vs. Fc^+/Fc in acetonitrile.[119] Interestingly, this potential corresponds to ~3.93 V vs. Na^+/Na [$E^0(Fc^+/Fc) = 0.63$ V vs. SHE,[120] $E^0(Na^+/Na) = 2.714$ V vs. SHE], close to the onset of $(CN)_2$ evolution observed in this work. Cheah *et al.* proposed an ECE-type reaction, involving both electron transfer and chemical reaction steps, in which the electrochemical formation of an Fe^{4+} intermediate is followed by $(CN)_2$ release in a reductive elimination reaction of two cyanide ligands, and the resulting Fe^{2+} complex is subsequently electrochemically oxidized to Fe^{3+}. The solvent then coordinates the iron in place of the missing cyanide ligands, which Cheah *et al.* demonstrated via *in-situ* FTIR and X-ray absorption spectroscopy (XAS) in combination with density-functional theory (DFT) calculations.[119] For the PBA/PW CAM discussed here, a coordination is similarly possible by electrolyte solvent, water or hydroxide anions. The findings of Cheah *et al.* are significant for the interpretation of results in this study in multiple ways. Most importantly, they explain why a lower $(CN)_2$ evolution is observed also in cells containing $NaPF_6$-electrolyte, since Fe^{4+} may be formed both electrochemically (to a lesser extent, but in all electrolytes) and via oxidation by $NaClO_4$ (to a greater extent). Consequently, this means that electron transfer occurs between Fe^{3+} and ClO_4^- or a ClO_x species formed by decomposition of the latter and does not immediately involve the cyanide anions. This, in turn, helps to explain the otherwise contrary findings of Pan *et al.*, who reported on gas-free oxidation of NaCN/carbon electrodes in $NaClO_4$-electrolyte for sodium-ion capacitors, finding polycyanogen (also called paracyanogen) instead of $(CN)_2$ gas, as supported by pressure measurements (and DEMS, but without explicitly monitoring $m/z = 52$).[121] Polycyanogen formation was then demonstrated by elemental analysis, as well as by ultraviolet (UV)- and IR-spectroscopy, and assumed to occur due to anionic polymerization in the presence of cyanide anions.[121,122] Guo *et al.* studied the electrochemical oxidation of cyanide in acetonitrile by electrospray-mass spectrometry (ES-MS) and similarly reported nucleophilic addition of cyanide to cyanogen, observing various $(CN)_n$ oligomers, but no $(CN)_2$.[123]

An attempt was made by us to conduct DEMS measurements on NaCN/carbon composite electrodes similar to those of Pan *et al.*,[121] with the further intent, similar to the Li_2CO_3 decomposition study of Freiberg *et al.*,[85] to also quantify the consumed NaCN and thereby $(CN)_2$ amounts. However, this proved unsuccessful, as with the only available PVDF binder, slurry gelation was observed upon the presence of NaCN. Since PVDF slurry gelation occurs by dehydrofluorination,[124] the formed HF likely reacts with NaCN to form HCN. This not only invalidates quantification, but also poses a significant safety risk, and no further attempts were made to prepare NaCN electrodes.

In this study, polycyanogen formation could be neither proved nor disproved. Still, taking the literature findings detailed above into consideration, some characteristics of $(CN)_2$ formation and evolution can be discussed. The $(CN)_2$ formation via reductive elimination in an Fe^{4+} complex explains why the oxidation of cyanide, in at least some cases, ends already at $(CN)_2$ and does not carry on to cyanate ions. Furthermore, the relative absence of free cyanide anions inhibits the anionic polymerization to polycyanogen by nucleophilic addition. The anions present in the electrolyte are far less nucleophilic, with the notable exception of hydroxide anions. The reduced $(CN)_2$

Batteries & Supercaps | Research Article
doi.org/10.1002/batt.202300595
Chemistry Europe
European Chemical Societies Publishing

evolution observed in the case of overcharge of undried electrodes and $NaClO_4$ (Figure 2a) may then also be partially attributed to the addition of hydroxide to formed $(CN)_2$, yielding 1-cyanoformamide instead.[125] At the same time, the presence of water under acidic conditions (Figure 3b) may not lead to $(CN)_2$ polymerization, and may also induce formation of reactive oxygen species upon electrochemical water oxidation, in both cases explaining the higher $(CN)_2$ evolution observed in this measurement.

For the reductive elimination reaction, a preceding dissolution of one cyanide ligand to form a more reactive, five-coordinate intermediate cannot be ruled out and may explain the observed $m/z = 27$ signals and their earlier peak evolution rate.[126] While Fe^{4+} is unusual and its presence in a hexacyanoferrate complex, as proposed by Cheah *et al.*,[119] is likely too short-lived to be detected, it has been previously reported both as an electrochemically formed intermediate prone to reductive elimination in organometallic chemistry[127] and in battery materials, often showing spontaneous reduction at high SOC as part of a reductive coupling mechanism, leading to oxidized anions.[128–132]

Lastly, the fate of the ClO_4^- anion shall be considered. Eggert *et al.* studied the gas evolution of $LiClO_4$ in PC on Pt electrodes and proposed a single electron-transfer reaction, yielding a $ClO_4^{\bullet}$ radical, which decomposes to ClO_2 and oxygen. The oxygen then contributes to electrolyte oxidation, leaving both ClO_2 ($m/z = 67$, $m/z = 69$ due to ^{35}Cl and ^{37}Cl) and CO_2 as detected gases.[133] Cattaneo *et al.* also reported ClO_2 evolution of this electrolyte on acetylene black electrodes above 4.5 V vs. Li^+/Li.[134] On the other hand, Metzger *et al.* did not observe any ClO_2 signals in their study of conductive carbon oxidation by $LiClO_4$ and additionally ruled out the formation of LiCl via XPS, thus assuming $LiClO_x$ species as the reaction product.[87] However, Sottmann *et al.* reported the formation of $NaMnCl_3$, which does contain the Cl^- anion.[56] As is shown in Figure S11a-e (Supporting Information), in this work, under overcharge conditions and especially at increased temperature, signals at $m/z = 67$, 69, and 51 ($^{35}ClO^+$, $m/z = 53$ occupied by $(CN)_2$ isotopologue) are observed, mirroring the correct isotope ratio of ^{35}Cl and ^{37}Cl. No clear signal could be made out for $m/z = 35$ and 37. However, due to the strong level of background noise and possible other contributions, the finding can only be considered with caution. Furthermore, the formation of a $ClO_4^{\bullet}$ radical itself is not proven, and it is an oxidation (not the reduction) required to facilitate the Fe^{3+} to Fe^{4+} electron removal. For this, either the reverse reaction, or more likely oxidation by a formed decomposition species (ClO_x), itself an oxidative radical, is required. This is supported by the lack of ClO_2 signals in previous measurements with the same electrolyte on layered oxide CAMs (Figure S8, Supporting Information), indicating that ClO_2 is only formed together with PW degradation and not itself causing the degradation.

Taken together, a plausible reductive elimination mechanism for the formation of $(CN)_2$ and the observed formation of ClO_2 from $NaClO_4$ suggests that a reactive ClO_x species facilitates the formation of a Fe^{4+} intermediate.

3. Conclusions

In this work, we have shown (quantitatively) that the outgassing of PW materials is dominated by the evolution of H_2, especially in hydrated CAM and especially during overcharge (4.6 V). CO_2 evolution during regular cycling occurs from the hydrolysis of organic carbonates by hydroxide anions and therefore depends not only on the water content of the CAM, but also on the conductive salt, as $NaPF_6$ hydrolysis leads to acidic conditions (less hydrolysis), while $NaClO_4$ leads to basic conditions (more hydrolysis). Only under overcharge conditions at higher potentials, electrochemical oxidation of electrolyte with CO_2 release occurs. In addition, the evolution of $(CN)_2$ was investigated in detail in this study, indicating that significant $(CN)_2$ release stems from the use of oxidative $NaClO_4$, while $(CN)_2$ release from electrolyte with $NaPF_6$ is much lower. With further experiments, other influence factors and the evolution of HCN were discussed, finding that HCN is likely present in traces, but due to the higher concentration of $(CN)_2$, the latter dominates in terms of safety risks. A hypothesis regarding the formation mechanism and quantity of $(CN)_2$ is presented, centering on the formation of a reactive, cyanide-coordinated Fe^{4+} intermediate that undergoes reductive elimination.

4. Outlook

$(CN)_2$ evolution during cycling of PW-based SIBs has severe implications regarding not only safety and handling of the materials and cells, but also their commercial application. However, we would like to emphasize that it is the commercially irrelevant $NaClO_4$ salt – often used in lab-scale studies – that mainly causes the $(CN)_2$ evolution. Furthermore, as also shown in this study, H_2 evolved due to PW water content is the predominant gas and comes with its own safety risks. The implied further development needs for PW-based SIBs are therefore, on the one hand, safer electrolytes and conductive salts and, on the other hand, careful and controlled dehydration procedures while maintaining high sodium content, especially when using aqueous processed electrodes.

Lastly, some important experimental considerations represent the limitations of the DEMS setup employed here. Reported potentials are determined against Na metal acting both as counter and reference electrode, which may have been affected by the formation of a resistive SEI. While it was shown that the use of a cold trap did not lead to substantial amounts of HCN or $(CN)_2$ being condensed, the evolved $(CN)_2$ was continually extracted, whereas in a regular cell, it would remain in the headspace and also partially be dissolved into the electrolyte. Under these conditions, polymerization to polycyanogen or follow-up reactions, such as with the H_2 or electrolyte solvent, may occur, forming HCN or organic nitrile species, and change the outcome of gas evolution studies performed on a closed headspace, such as crimped-capillary online electrochemical mass spectrometry (OEMS) or GC-MS headspace sampling.[66,104,135] On a similar note, if $(CN)_2$ evolution occurs in aqueous electrolyte,[16] often $NaClO_4$ based, it would be

Batteries & Supercaps | Research Article
doi.org/10.1002/batt.202300595
Chemistry Europe
European Chemical Societies Publishing

followed up by hydrolysis, yielding cyanate and cyanide ions, of which the latter may be oxidized again, leaving cyanate ions as the main degradation product instead of $(CN)_2$. Therefore, additional experiments are still required to evaluate the significance of $(CN)_2$ evolution for the application of PBAs/PWs as battery materials. This includes experiments in full cells and with a reference electrode,[72,136] experiments where a correct electrolyte-to-active material ratio limits the amount of conductive salt and electrolyte available for degradation reactions, i.e. measurements in larger cell formats,[137,138] and a reliable and precise quantification and separation of both HCN and $(CN)_2$, which may be achieved by novel DEMS cell designs, such as on-chip electrochemistry-mass spectrometry (EC-MS).[139]

To better understand follow-up reactions, we envision that labeling the PW CAM with ^{13}CN may allow for the detection of gaseous products via DEMS/OEMS and electrolyte side products via ^{13}C nuclear magnetic resonance (NMR) spectroscopy. Overall, the findings highlight the importance of gas evolution measurements for an exhaustive characterization of battery materials, and the effect of coating, doping, additives, synthesis, and processing procedures on suppression of $(CN)_2$ evolution may become a new field of consideration in PBA/PW research.

Experimental Section

Electrodes based on PW CAM with a nominal composition of $Na_{1.80(5)}Fe[Fe(CN)_6]\cdot 1.84(3)H_2O$ were prepared as described previously.[43] In short, an aqueous slurry was produced from PW, carboxymethyl cellulose (CMC) and styrene-butadiene rubber (SBR) binder, and conductive carbon additive in a weight ratio of 93.5 : 3.5 : 3.0. After degassing, the slurry was coated onto a 15 μm aluminium foil (Avotec Steel). Electrodes were calendared to a targeted density of ~1.5 g cm^{-3}, with an average mass loading of 13 (±1) mg cm^{-2}. Electrode disks of 30 mm diameter were punched out and dried under a dynamic vacuum for 24 h at 170 °C using a Glass Oven b-585 (BUCHI UK Ltd) to allow for dehydration of the Na-rich hydrated PW system. Undried electrodes were also used in this work to investigate the effect of interstitial and adsorbed water on gas evolution upon cycling.[43]

For DEMS measurements, a customized cell was assembled using a Na-metal (BASF SE) counter electrode, a GF/D separator (Whatman), and the 30 mm PW cathode as working electrode, with an additional 4 mm diameter hole punched out in the center to allow for gas flow. 750 μL of electrolyte was spread out on the separator dropwise. Different electrolyte systems were used in the work, including 1 M $NaPF_6$ in a mixture of ethylene carbonate (EC) and diethyl carbonate (DEC) in a ratio of 3 : 7 (v/v) (Fluorochem Ltd.) and 0.3 or 1 M $NaClO_4$ (Sigma-Aldrich), 1 M $NaPF_6$ or 0.3 M $NaClO_4$ and 0.7 M $NaPF_6$ in a mixture of EC, propylene carbonate (PC, Merck KGaA), and dimethyl carbonate (DMC, BASF SE) in a ratio of 1 : 1 : 1 (v/v/v) containing an additional 5 v% of fluoroethylene carbonate (FEC, BASF SE). Cells were cycled galvanostatically at 14 mA g^{-1} (1 C = 140 mA g^{-1}) for two cycles within a standard potential range between 2.0 and 4.0 V vs. Na^+/Na, and then charged up to 4.6 V before being discharged to 2.0 V in the third cycle. A constant stream of He carrier gas (2.5 mL min^{-1}, purity 6.0) was passed through the cell during cycling, and the extracted gas mixture then passed through a cold trap (−8 °C) before being analyzed by a mass spectrometer (GSD320, Pfeiffer Vacuum GmbH). A more detailed description of the DEMS setup and measurement principle can be found in the literature.[67,90,91] A baseline correction is applied to the $m/z = 2$, 26, and 44 signals to subtract the background signal stemming from electrolyte solvent molecules, residual air, and cell leakage. Calibration curves for H_2 ($m/z = 2$) and CO_2 ($m/z = 44$) were obtained by subsequently passing a calibration gas with known concentrations of these species in He through the cell in various dilutions. This is demonstrated for the first four measurements in Figure S2 (Supporting Information). The secondary electron multiplier (SEM) voltage was adjusted before each measurement in a range of 1200–1380 V to obtain a He ($m/z = 4$) raw signal close to 10^{-7} A. To compensate for differences in SEM gain and electrode loading, the $(CN)_2$ raw signal ($m/z = 52$) was normalized to CAM weight and relative H_2/CO_2 calibration curve slopes, as discussed in the main text. To this end, the quotients between each slope and the average slope of the first four measurements were calculated for both H_2 and CO_2, then averaged and the $m/z = 52$ raw signal divided by this value.[50] Table S3 (Supporting Information) contains the H_2 and CO_2 calibration slopes and resulting adjustment factors for all measurements.

Acknowledgements

The authors thank Yanjiao Ma (KIT, now Nanjing Normal University) for providing the high-entropy PW materials that initially started this research project as well as $NaClO_4$-electrolyte and Na metal. Leonhard Karger (KIT) is acknowledged for insightful mechanistic considerations. This study was partially supported by BASF SE. J. J. acknowledges funding and discussion within the POLiS Cluster of Excellence (ID 390874152, DFG – German Research Foundation). I. H. and F. M. M. acknowledge funding received from the European Union's Horizon 2020 research and innovation programme under grant agreement no. 883753 (SIMBA – Sodium-Ion and Sodium Metal Batteries for Efficient and Sustainable Next-Generation Energy Storage). I. H. acknowledges also funding received by the Royal Society through Research Grant RGS\R1\231519 "Gas Evolution Monitoring in Na-Ion Batteries (GEMINI)". Open Access funding enabled and organized by Projekt DEAL.

Conflict of Interests

The authors declare no conflict of interests.

Data Availability Statement

The data that support the findings of this study are available from the corresponding author upon reasonable request.

Keywords: Prussian white cathode · sodium-ion battery · gas evolution · cyanogen · hydrogen cyanide

[1] Z. Zhu, T. Jiang, M. Ali, Y. Meng, Y. Jin, Y. Cui, W. Chen, *Chem. Rev.* **2022**, *122*, 16610–16751.
[2] A. Masias, J. Marcicki, W. A. Paxton, *ACS Energy Lett.* **2021**, *6*, 621–630.
[3] D. Karabelli, S. Kiemel, S. Singh, J. Koller, S. Ehrenberger, R. Miehe, M. Weeber, K. P. Birke, *Front. Energy Res.* **2020**, *8*, 594857.

Batteries & Supercaps | Research Article
doi.org/10.1002/batt.202300595
Chemistry Europe
European Chemical Societies Publishing

[4] C. Xu, Q. Dai, L. Gaines, M. Hu, A. Tukker, B. Steubing, *Commun. Mater.* **2020**, *1*, 99.
[5] J. M. Tarascon, *Joule* **2020**, *4*, 1616–1620.
[6] T. Yu, G. Li, Y. Dian, Y. Wu, T. Zhang, X. Zhao, M. Luo, Y. Liu, *J. Alloys Compd.* **2023**, *958*, 170486.
[7] L. Zhao, T. Zhang, W. Li, T. Li, L. Zhang, X. Zhang, Z. Wang, *Engineering* **2023**, *24*, 172–183.
[8] Y. Tian, G. Zeng, A. Rutt, T. Shi, H. Kim, J. Wang, J. Koettgen, Y. Sun, B. Ouyang, T. Chen, Z. Lun, Z. Rong, K. Persson, G. Ceder, *Chem. Rev.* **2021**, *121*, 1623–1669.
[9] Q. Liu, Z. Hu, M. Chen, C. Zou, H. Jin, S. Wang, S. L. Chou, Y. Liu, S. X. Dou, *Adv. Funct. Mater.* **2020**, *30*, 1909530.
[10] H. S. Hirsh, Y. Li, D. H. S. Tan, M. Zhang, E. Zhao, Y. S. Meng, *Adv. Energy Mater.* **2020**, *10*, 2001274.
[11] I. Hasa, S. Mariyappan, D. Saurel, P. Adelhelm, A. Y. Koposov, C. Masquelier, L. Croguennec, M. Casas-Cabanas, *J. Power Sources* **2021**, *482*, 228872.
[12] M. Baumann, M. Häringer, M. Schmidt, L. Schneider, J. F. Peters, W. Bauer, J. R. Binder, M. Weil, *Adv. Energy Mater.* **2022**, *12*, 2202636.
[13] A. N. Singh, M. Islam, A. Meena, M. Faizan, D. Han, C. Bathula, A. Hajibabaei, R. Anand, K.-W. Nam, *Adv. Funct. Mater.* **2023**, *33*, 2304617.
[14] J. Qian, C. Wu, Y. Cao, Z. Ma, Y. Huang, X. Ai, H. Yang, *Adv. Energy Mater.* **2018**, *8*, 1702619.
[15] J. Peng, W. Zhang, Q. Liu, J. Wang, S. Chou, H. Liu, S. Dou, *Adv. Mater.* **2022**, *34*, 2108384.
[16] M. Jiang, Z. Hou, L. Ren, Y. Zhang, J. G. Wang, *Energy Storage Mater.* **2022**, *50*, 618–640.
[17] K. Hurlbutt, S. Wheeler, I. Capone, M. Pasta, *Joule* **2018**, *2*, 1950–1960.
[18] H. Jiaqi, R. Du, H. Zhang, Y. Liu, C. Jian, Y. Liu, L. Li, J. Peng, Y. Qiao, S. Chou, *Chem. Commun.* **2023**, *2*, 9320–9335.
[19] I. Hasa, N. Tapia-Ruiz, M. Galceran, *Front. Energy Res.* **2022**, *10*, 1076764.
[20] I. Hasa, J. Barker, G. Elia, S. Passerini, *Sodium Systems | Low Temperature: Overview, in: Reference Module in Chemistry, Molecular Sciences and Chemical Engineering*, **2023**, Elsevier: Amsterdam (DOI: 10.1016/B978-0-323-96022-9.00061-X).
[21] L. Hartmann, J. Deshmukh, L. Zhang, S. Buechele, M. Metzger, *J. Electrochem. Soc.* **2023**, *170*, 030540.
[22] D. O. Ojwang, M. Svensson, C. Njel, R. Mogensen, A. S. Menon, T. Ericsson, L. Häggström, J. Maibach, W. R. Brant, *ACS Appl. Mater. Interfaces* **2021**, *13*, 10054–10063.
[23] D. O. Ojwang, L. Häggström, T. Ericsson, R. Mogensen, W. R. Brant, *Dalton Trans.* **2022**, *51*, 14712–14720.
[24] W. Wang, Y. Gang, J. Peng, Z. Hu, Z. Yan, W. Lai, Y. Zhu, D. Appadoo, M. Ye, Y. Cao, Q.-F. Gu, H.-K. Liu, S.-X. Dou, S.-L. Chou, *Adv. Funct. Mater.* **2022**, *32*, 2111727.
[25] Y. Ma, Y. Hu, Y. Pramudya, T. Diemant, Q. Wang, D. Goonetilleke, Y. Tang, B. Zhou, H. Hahn, W. Wenzel, M. Fichtner, Y. Ma, B. Breitung, T. Brezesinski, *Adv. Funct. Mater.* **2022**, *32*, 2202372.
[26] Y. Xi, Y. Lu, *ACS Appl. Mater. Interfaces* **2022**, *14*, 39022–39030.
[27] Y. Huang, X. Zhang, L. Ji, L. Wang, B. Bin Xu, M. W. Shahzad, Y. Tang, Y. Zhu, M. Yan, G. Sun, Y. Jiang, *Energy Storage Mater.* **2023**, *58*, 1–8.
[28] Y. You, X. L. Wu, Y. X. Yin, Y. G. Guo, *Energy Environ. Sci.* **2014**, *7*, 1643–1647.
[29] J. Peng, Y. Gao, H. Zhang, Z. Liu, W. Zhang, L. Li, Y. Qiao, W. Yang, J. Wang, S. Dou, S. Chou, *Angew. Chem. Int. Ed.* **2022**, *61*, e202205867.
[30] J. Peng, W. Zhang, Z. Hu, L. Zhao, C. Wu, G. Peleckis, Q. Gu, J. Z. Wang, H. K. Liu, S. X. Dou, S. Chou, *Nano Lett.* **2022**, *22*, 1302–1310.
[31] J. Peng, M. Ou, H. Yi, X. Sun, Y. Zhang, B. Zhang, Y. Ding, F. Wang, S. Gu, C. A. López, W. Zhang, Y. Liu, J. Fang, P. Wei, Y. Li, L. Miao, J. Jiang, C. Fang, Q. Li, M. T. Fernández-Díaz, J. A. Alonso, S. Chou, J. Han, *Energy Environ. Sci.* **2021**, *14*, 3130–3140.
[32] X. Huang, C. Yang, Y. You, *ACS Appl. Energ. Mater.* **2022**, *5*, 8123–8131.
[33] Y. Yang, E. Liu, X. Yan, C. Ma, W. Wen, X.-Z. Liao, Z.-F. Ma, *J. Electrochem. Soc.* **2016**, *163*, A2117–A2123.
[34] S. Wang, M. Qin, M. Huang, X. Huang, Q. Li, Y. You, *ACS Appl. Energ. Mater.* **2022**, *5*, 6927–6935.
[35] W. R. Brant, R. Mogensen, S. Colbin, D. O. Ojwang, S. Schmid, L. Häggström, T. Ericsson, A. Jaworski, A. J. Pell, R. Younesi, *Chem. Mater.* **2019**, *31*, 7203–7211.
[36] L. Shen, Y. Jiang, Y. Jiang, J. Ma, K. Yang, H. Ma, Q. Liu, N. Zhu, *ACS Appl. Mater. Interfaces* **2022**, *14*, 24332–24340.
[37] J. Peng, J. Huang, Y. Gao, Y. Qiao, H. Dong, Y. Liu, L. Li, J. Wang, S. Dou, S. Chou, *Small* **2023**, 2300435.
[38] Y. Liu, S. Fan, Y. Gao, Y. Liu, H. Zhang, J. Chen, X. Chen, J. Huang, X. Liu, L. Li, Y. Qiao, S. Chou, *Small* **2023**, 2302687.
[39] P. Wang, Y. Li, D. Zhu, F. Gong, S. Fang, Y. Zhang, S. Sun, *Dalton Trans.* **2022**, *51*, 9622–9626.
[40] M. Li, M. Gaboardi, A. Mullaliu, M. Maisuradze, X. Xue, G. Aquilanti, J. R. Plaisier, S. Passerini, M. Giorgetti, *ChemSusChem* **2023**, *16*, e202300201.
[41] X. H. Liu, J. Peng, W. H. Lai, Y. Gao, H. Zhang, L. Li, Y. Qiao, S. L. Chou, *Adv. Funct. Mater.* **2022**, *32*, 2108616.
[42] X. M. Lin, X. T. Yang, H. N. Chen, Y. L. Deng, W. H. Chen, J. C. Dong, Y. M. Wei, J. F. Li, *J. Energy Chem.* **2023**, *76*, 146–164.
[43] F. Maddar, D. Walker, T. W. Chamberlain, J. Compton, A. S. Menon, M. Copley, I. Hasa, *J. Mater. Chem. A* **2023**, *11*, 15778–15791.
[44] S. Gourang Patnaik, I. Escher, G. A. Ferrero, P. Adelhelm, *Batteries & Supercaps* **2022**, *5*, e202200043.
[45] X. Yan, Y. Yang, E. Liu, L. Sun, H. Wang, X. Z. Liao, Y. He, Z. F. Ma, *Electrochim. Acta* **2017**, *225*, 235–242.
[46] Z. Li, M. Dadsetan, J. Gao, S. Zhang, L. Cai, A. Naseri, M. E. Jimenez-Castaneda, T. Filley, J. T. Miller, M. J. Thomson, V. G. Pol, *Adv. Energy Mater.* **2021**, *11*, 2101764.
[47] R. Mogensen, S. Colbin, R. Younesi, *Batteries & Supercaps* **2021**, *4*, 791–814.
[48] Y. Ma, Y. Ma, S. L. Dreyer, Q. Wang, K. Wang, D. Goonetilleke, A. Omar, D. Mikhailova, H. Hahn, B. Breitung, T. Brezesinski, *Adv. Mater.* **2021**, *33*, 2101342.
[49] Y. He, S. L. Dreyer, Y.-Y. Ting, Y. Ma, Y. Hu, D. Goonetilleke, Y. Tang, T. Diemant, B. Zhou, P. M. Kowalski, M. Fichtner, H. Hahn, J. Aghassi-Hagmann, T. Brezesinski, B. Breitung, Y. Ma, *Angew. Chem. Int. Ed.* **2023**, e202315371 (DOI: 10.1002/anie.202315371).
[50] Y. He, S. L. Dreyer, T. Akcay, T. Diemant, R. Mönig, Y. Ma, Y. Tang, H. Wang, H. Liu, J. Lin, S. Schweidler, M. Fichtner, H. Hahn, J. Aghassi-Hagmann, T. Brezesinski, B. Breitung, Y. Ma, *manuscript in preparation*, **2024**.
[51] J. Hu, H. Tao, M. Chen, Z. Zhang, S. Cao, Y. Shen, K. Jiang, M. Zhou, *ACS Appl. Mater. Interfaces* **2022**, *14*, 12234–12242.
[52] Y. Xi, Y. Lu, *J. Power Sources* **2021**, *513*, 230554.
[53] M. Ye, S. You, J. Xiong, Y. Yang, Y. Zhang, C. C. Li, *Mater. Today Energy* **2022**, *23*, 100898.
[54] Y. Liu, Y. Qiao, W. Zhang, Z. Li, X. Ji, L. Miao, L. Yuan, X. Hu, Y. Huang, *Nano Energy* **2015**, *12*, 386–393.
[55] Y. Lu, L. Wang, J. Cheng, J. B. Goodenough, *Chem. Commun.* **2012**, *48*, 6544–6546.
[56] J. Sottmann, F. L. M. Bernal, K. V. Yusenko, M. Herrmann, H. Emerich, D. S. Wragg, S. Margadonna, *Electrochim. Acta* **2016**, *200*, 305–313.
[57] T. L. Kulova, A. M. Skundin, *Energies* **2022**, *15*, 8615.
[58] G. G. Eshetu, G. A. Elia, M. Armand, M. Forsyth, S. Komaba, T. Rojo, S. Passerini, *Adv. Energy Mater.* **2020**, *10*, 2000093.
[59] Y. Lee, J. Lee, H. Kim, K. Kang, N. S. Choi, *J. Power Sources* **2016**, *320*, 49–58.
[60] M. Piernas-Muñoz, E. Castillo-Martínez, J. L. Gómez-Cámer, T. Rojo, *Electrochim. Acta* **2016**, *200*, 123–130.
[61] G. G. Eshetu, M. Martinez-Ibañez, E. Sánchez-Diez, I. Gracia, C. Li, L. M. Rodriguez-Martinez, T. Rojo, H. Zhang, M. Armand, *Chem. Asian J.* **2018**, *13*, 2770–2780.
[62] A. Ponrouch, E. Marchante, M. Courty, J. M. Tarascon, M. R. Palacín, *Energy Environ. Sci.* **2012**, *5*, 8572–8583.
[63] A. Hofmann, Z. Wang, S. P. Bautista, M. Weil, F. Müller, R. Löwe, L. Schneider, I. U. Mohsin, T. Hanemann, *Electrochim. Acta* **2022**, *403*, 139670.
[64] K. Westman, R. Dugas, P. Jankowski, W. Wieczorek, G. Gachot, M. Morcrette, E. Irisarri, A. Ponrouch, M. R. Palacín, J. M. Tarascon, P. Johansson, *ACS Appl. Energ. Mater.* **2018**, *1*, 2671–2680.
[65] M. Goktas, C. Bolli, J. Buchheim, E. J. Berg, P. Novák, F. Bonilla, T. Rojo, S. Komaba, K. Kubota, P. Adelhelm, *ACS Appl. Mater. Interfaces* **2019**, *11*, 32844–32855.
[66] M. Á. Muñoz-Márquez, M. Zarrabeitia, S. Passerini, T. Rojo, *Adv. Mater. Interfaces* **2022**, *9*, 2101773.
[67] S. L. Dreyer, A. Kondrakov, J. Janek, T. Brezesinski, *J. Mater. Res.* **2022**, *37*, 3146–3168.
[68] P. Liu, L. Yang, B. Xiao, H. Wang, L. Li, S. Ye, Y. Li, X. Ren, X. Ouyang, J. Hu, F. Pan, Q. Zhang, J. Liu, *Adv. Funct. Mater.* **2022**, *32*, 2208586.
[69] S. Kim, H.-S. Kim, B. Kim, Y.-J. Kim, J.-W. Jung, W.-H. Ryu, *Adv. Energy Mater.* **2023**, *13*, 2301983.
[70] B. Salomez, S. Grugeon, M. Armand, P. Tran-Van, S. Laruelle, *J. Electrochem. Soc.* **2023**, *170*, 050537.

Batteries & Supercaps | Research Article doi.org/10.1002/batt.202300595 | Chemistry Europe European Chemical Societies Publishing

[71] L. Zhang, C. Tsolakidou, S. Mariyappan, J. M. Tarascon, S. Trabesinger, *Energy Storage Mater.* **2021**, *42*, 12–21.
[72] J. Geisler, *Online gas analysis of electrochemical reactions*, Dissertation, Humboldt-Universität Berlin, **2023**, DOI: 10.18452/26417.
[73] D. O. Ojwang, L. Häggström, T. Ericsson, J. Angström, W. R. Brant, *Dalton Trans.* **2020**, *49*, 3570–3579.
[74] M. Prieschl, J. Sedelmeier, K. Püntener, S. Hildbrand, J. D. Williams, C. O. Kappe, *J. Org. Chem.* **2023**, 9594–9598.
[75] J. M. Mcnerney, H. H. Schrenk, *Am. Ind. Hyg. Assoc. J.* **1960**, *21*, 121–124.
[76] Oxalsäuredinitril [MAK Value Documentation in German Language, 2003], 2012, Wiley-VCH, DOI: 10.1002/3527600418.mb46019d0036.
[77] H. Kim, *ACS Mater. Au* **2023**, *3*, 571–575.
[78] S. G. Patnaik, P. Adelhelm, *Prussian Blue Electrodes for Sodium-Ion Batteries, in: Sodium-Ion Batteries: Materials, Characterization, and Technology*, Eds: M.-M. Titirici, P. Adelhelm, Y.-S. Hu, 1st edition, **2023**, Wiley-VCH: Weinheim.
[79] R. Bernhard, M. Metzger, H. A. Gasteiger, *J. Electrochem. Soc.* **2015**, *162*, A1984–A1989.
[80] A. Guéguen, D. Streich, M. He, M. Mendez, F. F. Chesneau, P. Novák, E. J. Berg, *J. Electrochem. Soc.* **2016**, *163*, A1095–A1100.
[81] S. Solchenbach, M. Metzger, M. Egawa, H. Beyer, H. A. Gasteiger, *J. Electrochem. Soc.* **2018**, *165*, A3022–A3028.
[82] C. Bolli, A. Guéguen, M. A. Mendez, E. J. Berg, *Chem. Mater.* **2019**, *31*, 1258–1267.
[83] M. Metzger, B. Strehle, S. Solchenbach, H. A. Gasteiger, *J. Electrochem. Soc.* **2016**, *163*, A1219–A1225.
[84] R. Lundström, N. Gogoi, X. Hou, E. J. Berg, *J. Electrochem. Soc.* **2023**, *170*, 040516.
[85] A. T. S. Freiberg, J. Sicklinger, S. Solchenbach, H. A. Gasteiger, *Electrochim. Acta* **2020**, *346*, 136271.
[86] S. E. Renfrew, B. D. McCloskey, *J. Am. Chem. Soc.* **2017**, *139*, 17853–17860.
[87] M. Metzger, P. Walke, S. Solchenbach, G. Salitra, D. Aurbach, H. A. Gasteiger, *J. Electrochem. Soc.* **2020**, *167*, 160522.
[88] J. M. Tarascon, D. Guyomard, *Solid State Ionics* **1994**, *69*, 293–305.
[89] M. Metzger, B. Strehle, S. Solchenbach, H. A. Gasteiger, *J. Electrochem. Soc.* **2016**, *163*, A798–A809.
[90] B. B. Berkes, A. Jozwiuk, H. Sommer, T. Brezesinski, J. Janek, *Electrochem. Commun.* **2015**, *60*, 64–69.
[91] B. B. Berkes, A. Jozwiuk, M. Vračar, H. Sommer, T. Brezesinski, J. Janek, *Anal. Chem.* **2015**, *87*, 5878–5883.
[92] A. J. Demello, *ACS Sens.* **2022**, *7*, 1235–1236.
[93] M. Dong, W. Sun, C. Wu, T. Feng, L. Zhao, H. Zhang, L. Chen, X. Pei, Z. Ren, Y. Cheng, *Vacuum* **2021**, *191*, 110357.
[94] J. H. Batey, *Vacuum* **2014**, *101*, 410–415.
[95] W. R. Blanchard, P. J. McCarthy, H. F. Dylla, P. H. LaMarche, J. E. Simpkins, *J. Vac. Sci. Technol. A: Vacuum, Surfaces, and Films* **1986**, *4*, 1715–1719.
[96] A. Rudola, K. Du, P. Balaya, *J. Electrochem. Soc.* **2017**, *164*, A1098–A1109.
[97] R. L. Germscheidt, D. Da Silva Francischini, M. B. Silva, M. A. Zezzi Arruda, A. L. Barboza Formiga, T. C. Rizuti Da Rocha, J. A. Bonacin, *ACS Appl. Energ. Mater.* **2022**, *5*, 9447–9454.
[98] G. Hernández, R. Mogensen, R. Younesi, J. Mindemark, *Batteries & Supercaps* **2022**, *5*, e202100373.
[99] A. Bhide, J. Hofmann, A. Katharina Dürr, J. Janek, P. Adelhelm, *Phys. Chem. Chem. Phys.* **2014**, *16*, 1987–1998.
[100] R. Mogensen, S. Colbin, A. S. Menon, E. Björklund, R. Younesi, *ACS Appl. Energ. Mater.* **2020**, *3*, 4974–4982.
[101] R. Mogensen, A. Buckel, S. Colbin, R. Younesi, *Chem. Mater.* **2021**, *33*, 1130–1139.
[102] J. Welch, R. Mogensen, W. van Ekeren, H. Eriksson, A. J. Naylor, R. Younesi, *J. Electrochem. Soc.* **2022**, *169*, 120523.
[103] R. Sun, Y. You, *ACS Appl. Mater. Interfaces* **2023**, *15*, 44599–44606.
[104] M. Metzger, H. A. Gasteiger, *Energy Environ. Mater.* **2022**, *5*, 688–692.
[105] L. Karger, S. Korneychuk, W. van den Bergh, S. L. Dreyer, R. Zhang, A. Kondrakov, J. Janek, T. Brezesinski, *Chem. Mater.* **2023**, DOI: 10.1021/acs.chemmater.3c02727.
[106] W. E. Wallace, NIST Mass Spectrometry Data Center, https://webbook.nist.gov/cgi/inchi?ID=C74908, retrieved 04.10.2023.
[107] W. E. Wallace, NIST Mass Spectrometry Data Center, https://webbook.nist.gov/cgi/inchi?ID=C460195, retrieved 04.10.2023.
[108] R. Lundström, E. J. Berg, *J. Power Sources* **2021**, *485*, 229347.
[109] J. Wang, S. L. Dreyer, K. Wang, Z. Ding, T. Diemant, G. Karkera, Y. Ma, A. Sarkar, B. Zhou, M. V. Gorbunov, A. Omar, D. Mikhailova, V. Presser, M. Fichtner, H. Hahn, T. Brezesinski, B. Breitung, Q. Wang, *Mater. Futures* **2022**, *1*, 035104.
[110] C. A. Rego, R. S. Tsang, P. W. May, M. N. R. Ashfold, K. N. Rosser, *J. Appl. Phys.* **1996**, *79*, 7264–7273.
[111] D. Heathcote, C. Vallance, *J. Phys. B: At. Mol. Opt. Phys.* **2018**, *51*, 195203.
[112] H. Ren, Y. Li, Q. Ni, Y. Bai, H. Zhao, C. Wu, *Adv. Mater.* **2022**, *34*, 2106171.
[113] A. R. Genreith-Schriever, H. Banerjee, A. S. Menon, E. N. Bassey, L. F. J. Piper, C. P. Grey, A. J. Morris, *Joule* **2023**, *7*, 1623–1640.
[114] M. Nsangou, M. L. Senent, M. Hochlaf, *Chem. Phys.* **2009**, *355*, 164–168.
[115] F. Sebastianelli, F. Carelli, F. A. Gianturco, *Chem. Phys.* **2012**, *398*, 199–205.
[116] P. Mukherjee, N. V. Faenza, N. Pereira, J. Ciston, L. F. J. Piper, G. G. Amatucci, F. Cosandey, *Chem. Mater.* **2018**, *30*, 8431–8445.
[117] S. Oswald, D. Pritzl, M. Wetjen, H. A. Gasteiger, *J. Electrochem. Soc.* **2021**, *168*, 120501.
[118] R. Jung, M. Metzger, F. Maglia, C. Stinner, H. A. Gasteiger, *J. Electrochem. Soc.* **2017**, *164*, A1361–A1377.
[119] M. H. Cheah, P. Chernev, *Sci. Rep.* **2021**, *11*, 23058.
[120] V. V. Pavlishchuk, A. W. Addison, *Inorg. Chim. Acta* **2000**, *298*, 97–102.
[121] X. Pan, A. Chojnacka, F. Béguin, *J. Energy Chem.* **2022**, *72*, 33–40.
[122] V. Skarda, D. Ivkovich, M. M. Labes, *J. Polym. Sci. Polym. Chem. Ed.* **1985**, *23*, 107–117.
[123] T. Guo, A. Illies, V. Cammarata, M. Arndt, W. Sonzogni, *J. Electroanal. Chem.* **2007**, *610*, 102–105.
[124] S. Roberts, L. Chen, B. Kishore, C. E. J. Dancer, M. J. H. Simmons, E. Kendrick, *J. Colloid Interface Sci.* **2022**, *627*, 427–437.
[125] Y. L. Wang, H. D. Lee, M. W. Beach, D. W. Margerum, *Inorg. Chem.* **1987**, *26*, 2444–2449.
[126] D. M. Crumpton-Bregel, K. I. Goldberg, *J. Am. Chem. Soc.* **2003**, *125*, 9442–9456.
[127] W. Lau, J. C. Huffman, J. K. Kochi, *Organometallics* **1982**, *1*, 155–169.
[128] D. Dixon, S. Mangold, M. Knapp, H. Ehrenberg, A. Bhaskar, *Adv. Energy Mater.* **2021**, *11*, 2100479.
[129] E. Lee, D. E. Brown, E. E. Alp, Y. Ren, J. Lu, J. J. Woo, C. S. Johnson, *Chem. Mater.* **2015**, *27*, 6755–6764.
[130] E. McCalla, M. T. Sougrati, G. Rousse, E. J. Berg, A. Abakumov, N. Recham, K. Ramesha, M. Sathiya, R. Dominko, G. Van Tendeloo, P. Novák, J.-M. Tarascon, *J. Am. Chem. Soc.* **2015**, *137*, 4804–4814.
[131] S. Xu, Y. Wang, L. Ben, Y. Lyu, N. Song, Z. Yang, Y. Li, L. Mu, H. T. Yang, L. Gu, Y.-S. Hu, H. Li, Z.-H. Cheng, L. Chen, X. Huang, *Adv. Energy Mater.* **2015**, *5*, 1501156.
[132] A. S. Christiansen, R. E. Johnsen, P. Norby, C. Frandsen, S. Mørup, S. H. Jensen, K. K. Hansen, P. Holtappels, *J. Electrochem. Soc.* **2015**, *162*, A531–A537.
[133] G. Eggert, J. Heitbaum, *Electrochim. Acta* **1986**, *31*, 1443–1448.
[134] E. Cattaneo, J. Ruch, *J. Power Sources* **1993**, *44*, 341–347.
[135] J.-P. Schmiegel, M. Leißing, F. Weddeling, F. Horsthemke, J. Reiter, Q. Fan, S. Nowak, M. Winter, T. Placke, *J. Electrochem. Soc.* **2020**, *167*, 060516.
[136] J. Geisler, L. Pfeiffer, G. A. Ferrero, P. Axmann, P. Adelhelm, *ChemRxiv.* (Analytical Chemistry) **2023**, DOI: 10.26434/chemrxiv-2023-md389.
[137] C. Misiewicz, R. Lundström, I. Ahmed, M. J. Lacey, W. R. Brant, E. J. Berg, *J. Power Sources* **2023**, *554*, 232318.
[138] U. Mattinen, M. Klett, G. Lindbergh, R. Wreland Lindström, *J. Power Sources* **2020**, *477*, 228968.
[139] D. B. Thornton, B. J. V. Davies, S. B. Scott, A. Aguadero, M. P. Ryan, I. E. L. Stephens, *Angew. Chem. Int. Ed.* **2023**, e202315357 (DOI: 10.1002/anie.202315357).

Manuscript received: December 14, 2023
Revised manuscript received: January 12, 2024
Accepted manuscript online: January 15, 2024
Version of record online: ■■, ■■

5. Conclusions and Outlook

The works forming this dissertation focused on the surface of CAMs from various perspectives, from surface creation during synthesis over exposure of new surfaces to electrolyte after particle fracture to decomposition at its surface due to electrolyte contact. While each of these perspectives alone allows conclusions on properties of CAM surfaces, as will be discussed below, a key finding in this dissertation is that each perspective is not isolated. Instead, surface-related properties are the result of a complex interplay between synthesis conditions, properties of the underlying bulk phase and the environment the respective surface is exposed to, as will also be highlighted for each of the works. *In situ* gas evolution studies served as a further connecting element between all materials studied in this dissertation. A review of such *in situ* gas evolution studies is presented in chapter 4.1., finding that they offer unique insights into reactions of various novel materials and in new cell concepts, and will likely see increased attention in the development of alternatives to LIBs with NCM cathodes. Especially, the gas evolution of SIBs was identified as a relevant future field and is also a key component of this thesis.

In chapter 4.2., it was shown that the process route by which Zr^{4+} is introduced as a dopant into LNO affects both the formation of impurities on the primary particle surface and the grain growth, and thus the specific surface area and electrochemical properties of the LNO primary particles. This was explained by a grain growth inhibition due to enrichment at the grain boundaries, wherein the process route determined the initial distribution of Zr^{4+}. Therefore, impregnation of pCAM with the dopant leads to the smallest particles and best-performing CAM, as Zr^{4+} is already present at the grain boundaries from the beginning of the calcination on. At the same time, the low Zr^{4+} concentration of 0.25 mol% did not affect bulk properties, such as unit-cell parameters and off-stoichiometry, which are commonly understood as dopant-dependent. The findings highlight both the sensitivity of the CAM surface towards small variations in composition and the importance of surface reactivity on electrochemical performance. Yet, the variation of the synthesis process also had an effect on the rate of particle fracture and electrolyte exposure, as measured via the increase in specific capacitance, and on the gas evolution of each material, as determined via DEMS, which is due to different specific surface areas with different degrees of Li_2CO_3 impurity contamination.

The cracking behavior of the P2-type SIB CAMs discussed in chapter 4.3. was found to vary in dependence of the bulk composition, as a higher configurational entropy resulted in less anisotropic volume change, especially due to the increased suppression of the P2-O2 phase transition in favor of a solid-solution desodiation, as determined via *in situ* XRD. Classification of AE hits by their peak frequency then allowed, in combination with *post-mortem* electron microscopy, to distinguish between inter- and intragranular particle fracture, the latter of which is a main degradation mechanism in P2-type SIB CAMs. As different fracturing behavior was found for the materials, it was thus shown that not only characterization, but also comparison and evaluation of CAM is possible via AE. Yet, it is the synthesis and processing of the materials that determines the initial degree of agglomeration, and thus the amount of CAM surface initially not exposed to electrolyte. Furthermore, other techniques to analyze surface area increase were, in this work, hindered by the exposure to electrolyte and reactions with it: At the end of discharge, continuous formation and disproportionation of Mn^{3+} with subsequent dissolution of Mn^{2+} from the surface were observed. At the same time, the decomposition of the electrolyte additive FEC at the surface, as observed via DEMS, leads to the formation of a CEI film. Taken together, these reactions did not allow for the blocking conditions required for the capacitance measurement and overshadowed an increase in specific surface area in the electrochemical impedance spectra.

In chapter 4.4., it was shown that while the gas evolution of PW SIB CAM is dominated by the evolution of H_2, as a result of water content, and CO_2 by ethylene carbonate hydrolysis or electrochemical electrolyte oxidation during overcharge, the exposure of the CAM surface to $NaClO_4$ in the electrolyte leads to evolution of $(CN)_2$, as well as traces of HCN. The evolution of these gasses even from optimized, commercial CAM is a main safety concern, which is mitigated by the required presence of $NaClO_4$ for their formation, as this conductive salt is commonly used only on a laboratory scale. In a series of experiments, a mechanism involving $NaClO_4$ as an oxidant was proposed, and other influence factors were ruled out. The suggested mechanism, supported by a literature survey, proceeds via an oxidation of the hexacyanoferrate from Fe^{3+} to a short-lived Fe^{4+} intermediate, from which $(CN)_2$ is released by reductive elimination, while ClO_2 is formed by the concurrent reduction of $NaClO_4$. As a charge transfer from salt to Fe can only occur at the CAM surface, the extent of the reaction is limited, and a CEI composed of chlorides, hydroxides and polycyanogen is likely formed over time.

Yet, the surface area available for the degradation reaction is mostly determined by the synthesis conditions, especially when chelating agents are used that again slow the growth of particles and also reduce their agglomeration and the amount of vacancies in the material. With water coordinating in place of these vacancies, the later H_2 evolution is also affected by the synthesis conditions. Lastly, if crack formation and deagglomeration exposes new PW surface to the electrolyte, further evolution of $(CN)_2$ is possible in later cycles, too.

In each of the experimental works constituting this dissertation, analytical methods that are not widespread in battery research were employed. It was shown that LA-ICP-MS can be utilized instead of STEM-EDS to study dopant distribution between secondary particles, especially as it can cover a greater number of particles and is less time consuming. Therefore, the technique may see further development and application, especially in the context of industrial CAM manufacturing.

The two-electrode capacitance method of Oswald *et al.*[335-337] and AE both allow gaining insights into particle fracture without requiring a third electrode and may thus be applied also to commercial cells during real-world application. However, both come with individual shortcomings, as the determination of capacitance in a two-electrode setup requires a deep discharge to achieve blocking conditions, while AE requires an external sensor and a more complex data interpretation, as quantification is not straightforward. Combining capacitance and AE measurements may alleviate this issue and allow AE to be used also in sensing applications. The use of fiber optic sensors, which are less sensitive to assembly pressure than piezo sensors, may allow application of AE not only on, but also inside SSBs.

Recent developments in the field of instrumentation for *in situ* gas evolution studies have been discussed in chapter 4.1., and especially measurements under more realistic conditions, i.e. in commercial large-format cells, with correct electrolyte to active material ratio etc., may widen the scope of application from materials' characterization and development into optimization and monitoring of e.g. electrolyte additives, formation protocols and abuse testing. For PBA/PW gas evolution, specifically, this approach would overcome the limitations presented in chapter 4.4., as it would allow to also monitor follow-up reactions of $(CN)_2$, such as formation of HCN in the presence of H_2 and consumption by reactions with electrolyte or by polymerization into a polycyanogen-containing CEI. Detailed investigations on suppression of PBA/PW degradation

via $(CN)_2$ evolution on the one hand and the electrolyte-dependent CEI composition and formation in PW materials on the other hand, are a consequential follow-up to the study presented in chapter 4.4. Yet, the identification of CEI components in the presence of the bulk material is likely to remain challenging. Lastly, BELLA's capability to perform DEMS measurements on SSBs may be utilized on sodium-SSBs containing PBA/PW CAM, or even solid electrolytes, as recently proposed.[367] This may allow to rule out electrolyte contributions selectively and thus to further study the role of composition, esp. vacancies, water content and metal combinations, on the gassing of PBA and PW materials.

Bibliography

[1] A. Volta, *Phil. Trans.* **1800**, *90*, 403–431.

[2] H. Davy, *Phil. Trans.* **1807**, *97*, 1–56.

[3] H. Davy, *Phil. Trans.* **1808**, *98*, 1–44.

[4] H. Davy, *Phil. Trans.* **1808**, *98*, 333–370.

[5] H. Davy, *Phil. Trans.* **1809**, *99*, 39–104.

[6] H. Davy, *Phil. Trans.* **1811**, *101*, 1–35.

[7] M. Faraday, *Phil. Trans.* **1834**, *124*, 77–122.

[8] J. M. Thomas, *Chem. Commun.* **2017**, *53*, 9179–9184.

[9] J. F. Daniell, *Phil. Trans.* **1836**, *126*, 107–129.

[10] P. P. Lopes, V. R. Stamenkovic, *Science* **2020**, *369*, 923–924.

[11] Y. Liang, C.-Z. Zhao, H. Yuan, Y. Chen, W. Zhang, J.-Q. Huang, D. Yu, Y. Liu, M. M.-M. Titirici, Y.-L. Chueh, H. Yu, Q. Zhang, *InfoMat* **2019**, *1*, 6–32.

[12] M. Winter, B. Barnett, K. Xu, *Chem. Rev.* **2018**, *118*, 11433–11456.

[13] T. S. Rappaport, *IEEE Communications Magazine*, **1991**, *29*, 52–71.

[14] K. Xu, *Energy Environ. Mater.* **2019**, *2*, 229–233.

[15] A. König, L. Nicoletti, D. Schröder, S. Wolff, A. Waclaw, M. Lienkamp, *World Electr. Veh. J.* **2021**, *12*, 21.

[16] The Faraday Institution, *Forecasted demand for electric vehicle batteries worldwide from 2020 to 2050*, **2020**, accessed on 21.11.2023 via https://www.statista.com/statistics/1129463/forecasted-electric-vehicle-battery-demand-worldwide/

[17] BloombergNEF, *Projected battery costs as a share of large battery electric vehicle costs from 2016 to 2030*, **2017**, accessed on 21.11.2023 via https://www.statista.com/statistics/797638/battery-share-of-large-electric-vehicle-cost/

[18] McKinsey, *Battery 2030: Resilient, sustainable, and circular*, **2023**, accessed on 21.11.2023 via https://www.mckinsey.com/industries/automotive-and-assembly/our-insights/battery-2030-resilient-sustainable-and-circular#/

[19] J. Abrell, S. Rausch, C. Streitberger, *Energy Econ.* **2019**, *84*, 104463.

[20] E. Martinot, *Annu. Rev. Environ. Resour.* **2016**, *41*, 223–251.

[21] H. Löbberding, S. Wessel, C. Offermanns, M. Kehrer, J. Rother, H. Heimes, A. Kampker, *World Electr. Veh. J.* **2020**, *11*, 77.

[22] R. Schröder, M. Aydemir, G. Seliger, *Procedia Manuf.* **2017**, *8*, 104–111.

[23] G. Zubi, R. Dufo-López, M. Carvalho, G. Pasaoglu, *Renew. Sustain. Energy Rev.* **2018**, *89*, 292–308.

[24] A. Opitz, P. Badami, L. Shen, K. Vignarooban, A. M. Kannan, *Renew. Sustain. Energy Rev.* **2017**, *68*, 685–692.

[25] B. Dunn, H. Kamath, J.-M. Tarascon, *Science* **2011**, *334*, 928–935.

[26] A. Masias, J. Marcicki, W. A. Paxton, *ACS Energy Lett.* **2021**, *6*, 621–630.

[27] M. S. Ziegler, J. Song, J. E. Trancik, *Energy Environ. Sci.* **2021**, *14*, 6074–6098.

[28] M. S. Ziegler, J. E. Trancik, *Energy Environ. Sci.* **2021**, *14*, 1635–1651.

[29] A. D. Pathak, S. Saha, V. K. Bharti, M. M. Gaikwad, C. S. Sharma, *J. Energy Storage* **2023**, *61*, 106792.

[30] D. C. Bock, A. C. Marschilok, K. J. Takeuchi, E. S. Takeuchi, *Electrochim. Acta* **2012**, *84*, 155–164.

[31] O. Gröger, H. A. Gasteiger, J.-P. Suchsland, *J. Electrochem. Soc.* **2015**, *162*, A2605–A2622.

[32] L. F. Arenas, C. Ponce de León, F. C. Walsh, *Curr. Opin. Electrochem.* **2019**, *16*, 117–126.

[33] A. Manthiram, S. H. Chung, C. Zu, *Adv. Mater.* **2015**, *27*, 1980–2006.

[34] G. Nikiforidis, M. C. M. Van de Sanden, M. N. Tsampas, *RSC Adv.* **2019**, *9*, 5649–5673.

[35] T. Li, M. Huang, X. Bai, Y. X. Wang, *Prog. Nat. Sci. Mater. Int.* **2023**, *33*, 151–171.

[36] N. Tapia-Ruiz, A. R. Armstrong, H. Alptekin, M. A. Amores, H. Au, J. Barker, R. Boston, W. R. Brant, J. M. Brittain, Y. Chen, M. Chhowalla, Y. Choi, S. I. R. Costa, M. C. Ribadeneyra, S. A. M. Dickson, E. I. Eweka, J. D. Forero-Saboya, C. P. Grey, Z. Li, S. F. L. Mertens, R. Mogensen, L. Monconduit, D. M. C. Ould, R. G. Palgrave, P. Poizot, A. Ponrouch, S. Renault, E. M. Reynolds, A. Rudola, R. Sayers, D. O. Scanlon, S. Sen, V. R. Seymour, B. Silv, G. S. Stone, C. I. Thomas, M. Titirici, J. Tong, T. J. Wood, D. S. Wright, R. Younesi, *J. Phys. Energy* **2021**, *3*, 031503–031592.

[37] X. Min, J. Xiao, M. Fang, W. Wang, Y. Zhao, Y. Liu, A. M. Abdelkader, K. Xi, R. V. Kumar, Z. Huang, *Energy Environ. Sci.* **2021**, *14*, 2186–2243.

[38] H. Huo, J. Janek, *Natl. Sci. Rev.* **2023**, *10*, nwad098.

[39] J.-M. Tarascon, *Joule* **2020**, *4*, 1616–1620.

[40] F. Duffner, N. Kronemeyer, J. Tübke, J. Leker, M. Winter, R. Schmuch, *Nat. Energy* **2021**, *6*, 123–134.

[41] M. S. Whittingham, *Science* **1976**, *192*, 1126–1127.

[42] K. Mizushima, P. C. Jones, P. J. Wiseman, J. B. Goodenough, *Mater. Res. Bull.* **1980**, *15*, 783–789.

[43] K. Brandt, *Solid State Ionics* **1994**, *69*, 173–183.

[44] M. Armand, P. Touzain, *Mater. Sci. Eng.* **1977**, *31*, 319–329.

[45] J. O. Besenhard, *Carbon* **1976**, *14*, 111–115.

[46] A. Yoshino, *Angew. Chem. Int. Ed.* **2012**, *51*, 5798–5800.

[47] K. Xu, *J. Electrochem. Soc.* **2009**, *156*, A751.

[48] R. Fong, U. von Sacken, J. R. Dahn, *J. Electrochem. Soc.* **1990**, *137*, 2009–2013.

[49] B. Scrosati, *J. Electrochem. Soc.* **1992**, *139*, 2776–2781.

[50] K. Xu, *Chem. Rev.* **2004**, *104*, 4303–4418.

[51] N. Nitta, G. Yushin, *Part. Part. Syst. Charact.* **2014**, *31*, 317–336.

[52] H. Zhang, Y. Yang, D. Ren, L. Wang, X. He, *Energy Storage Mater.* **2021**, *36*, 147–170.

[53] J. Asenbauer, T. Eisenmann, M. Kuenzel, A. Kazzazi, Z. Chen, D. Bresser, *Sustain. Energy Fuels* **2020**, *4*, 5387–5416.

[54] S. Schweidler, L. De Biasi, A. Schiele, P. Hartmann, T. Brezesinski, J. Janek, *J. Phys. Chem. C* **2018**, *122*, 8829–8835.

[55] S. J. An, J. Li, C. Daniel, D. Mohanty, S. Nagpure, D. L. Wood, *Carbon* **2016**, *105*, 52–76.

[56] L. Sun, Y. Liu, R. Shao, J. Wu, R. Jiang, Z. Jin, *Energy Storage Mater.* **2022**, *46*, 482–502.

[57] J. Kasnatscheew, T. Placke, B. Streipert, S. Rothermel, R. Wagner, P. Meister, I. C. Laskovic, M. Winter, *J. Electrochem. Soc.* **2017**, *164*, A2479–A2486.

[58] D. Hu, L. Chen, J. Tian, Y. Su, N. Li, G. Chen, Y. Hu, Y. Dou, S. Chen, F. Wu, *Chinese J. Chem.* **2021**, *39*, 165–173.

[59] Y. Zhang, T. T. Zuo, J. Popovic, K. Lim, Y. X. Yin, J. Maier, Y. G. Guo, *Mater. Today* **2020**, *33*, 56–74.

[60] C. Daniel, D. Mohanty, J. Li, D. L. Wood, *AIP Conf. Proc.* **2014**, *1597*, 26–43.

[61] J. Liu, J. Wang, Y. Ni, K. Zhang, F. Cheng, J. Chen, *Mater. Today* **2021**, *43*, 132–165.

[62] J. Xiang, Y. Wei, Y. Zhong, Y. Yang, H. Cheng, L. Yuan, H. Xu, Y. Huang, *Adv. Mater.* **2022**, *34*, 2200912.

[63] N. Mohamed, N. K. Allam, *RSC Adv.* **2020**, *10*, 21662–21685.

[64] A. Mauger, C. M. Julien, *Batteries* **2018**, *4*, 39.

[65] L. Yang, W. Deng, W. Xu, Y. Tian, A. Wang, B. Wang, G. Zou, H. Hou, W. Deng, X. Ji, *J. Mater. Chem. A* **2021**, *9*, 14214–14232.

[66] G. Liang, V. K. Peterson, K. W. See, Z. Guo, W. K. Pang, *J. Mater. Chem. A* **2020**, *8*, 15373–15398.

[67] M. Bianchini, M. Roca-Ayats, P. Hartmann, T. Brezesinski, J. Janek, *Angew. Chem. Int. Ed.* **2019**, *58*, 10434–10458.

[68] S.-T. Myung, F. Maglia, K.-J. Park, C. S. Yoon, P. Lamp, S. Kim, Y. Sun, *ACS Energy Lett.* **2017**, *2*, 196–223.

[69] H. Noh, S. Youn, C. S. Yoon, Y. Sun, *J. Power Sources* **2013**, *233*, 121–130.

[70] L. De Biasi, A. O. Kondrakov, H. Geßwein, T. Brezesinski, P. Hartmann, J. Janek, *J. Phys. Chem. C* **2017**, *121*, 26163–26171.

[71] H. Li, M. Cormier, N. Zhang, J. Inglis, J. Li, J. R. Dahn, *J. Electrochem. Soc.* **2019**, *166*, A429–A439.

[72] Z. Cui, Z. Guo, A. Manthiram, *Adv. Energy Mater.* **2023**, *13*, 2203853.

[73] J. Rana, J. K. Papp, Z. Lebens-Higgins, M. Zuba, L. A. Kaufman, A. Goel, R. Schmuch, M. Winter, M. S. Whittingham, W. Yang, B. D. McCloskey, L. F. J. Piper, *ACS Energy Lett.* **2020**, *5*, 634–641.

[74] M. Bianchini, A. Schiele, S. Schweidler, S. Sicolo, F. Fauth, E. Suard, S. Indris, A. Mazilkin, P. Nagel, S. Schuppler, M. Merz, P. Hartmann, T. Brezesinski, J. Janek, *Chem. Mater.* **2020**, *32*, 9211–9227.

[75] S. Kang, D. Choi, H. Lee, B. Choi, Y. Kang, *Adv. Mater.* **2023**, *35*, 2211965.

[76] T. Cui, X. Li, Y. Fu, *Adv. Funct. Mater.* **2023**, 33, 2303191.

[77] T. Teufl, B. Strehle, P. Müller, H. A. Gasteiger, M. A. Mendez, *J. Electrochem. Soc.* **2018**, *165*, A2718–A2731.

[78] J. Lee, A. Urban, X. Li, D. Su, G. Hautier, G. Ceder, *Science* **2014**, *343*, 519–522.

[79] R. J. Clément, Z. Lun, G. Ceder, *Energy Environ. Sci.* **2020**, *13*, 345–373.

[80] W. Liu, P. Oh, X. Liu, M. Lee, W. Cho, S. Chae, Y. Kim, J. Cho, *Angew. Chem. Int. Ed.* **2015**, *54*, 4440–4457.

[81] R. D. Shannon, *Acta Crystallogr. Sect. A* **1976**, *32*, 751–767.

[82] L. Karger, D. Weber, D. Goonetilleke, A. Mazilkin, H. Li, R. Zhang, Y. Ma, S. Indris, A. Kondrakov, J. Janek, T. Brezesinski, *Chem. Mater.* **2023**, *35*, 648–657.

[83] H. Dong, G. M. Koenig, *CrystEngComm* **2020**, *22*, 1514–1530.

[84] P. Kurzhals, F. Riewald, M. Bianchini, H. Sommer, H. A. Gasteiger, J. Janek, *J. Electrochem. Soc.* **2021**, *168*, 110518.

[85] E. McCalla, G. H. Carey, J. R. Dahn, *Solid State Ionics* **2012**, *219*, 11–19.

[86] F. Riewald, P. Kurzhals, M. Bianchini, H. Sommer, J. Janek, H. A. Gasteiger, *J. Electrochem. Soc.* **2022**, *169*, 020529.

[87] N. V. Faenza, L. Bruce, Z. W. Lebens-Higgins, I. Plitz, N. Pereira, L. F. J. Piper, G. G. Amatucci, *J. Electrochem. Soc.* **2017**, *164*, A3727–A3741.

[88] D. Weber, Đ. Tripković, K. Kretschmer, M. Bianchini, T. Brezesinski, *Eur. J. Inorg. Chem.* **2020**, *2020*, 3117–3130.

[89] W. Zhang, C. Yuan, J. Zhu, T. Jin, C. Shen, K. Xie, *Adv. Energy Mater.* **2023**, *13*, 2202993.

[90] K. Matsumoto, R. Kuzuo, K. Takeya, A. Yamanaka, *J. Power Sources* **1999**, *81–82*, 558–561.

[91] I. Hamam, N. Zhang, A. Liu, M. B. Johnson, J. R. Dahn, *J. Electrochem. Soc.* **2020**, *167*, 130521.

[92] I. A. Shkrob, J. A. Gilbert, P. J. Phillips, R. Klie, R. T. Haasch, J. Bareño, D. P. Abraham, *J. Electrochem. Soc.* **2017**, *164*, A1489–A1498.

[93] C. V. Ramana, A. Mauger, F. Gendron, C. M. Julien, K. Zaghib, *J. Power Sources* **2009**, *187*, 555–564.

[94] X. Zhang, M. Van Hulzen, D. P. Singh, A. Brownrigg, J. P. Wright, N. H. Van Dijk, M. Wagemaker, *Nat. Commun.* **2015**, *6*, 8333.

[95] Y. Orikasa, T. Maeda, Y. Koyama, H. Murayama, K. Fukuda, H. Tanida, H. Arai, E. Matsubara, Y. Uchimoto, Z. Ogumi, *Chem. Mater.* **2013**, *25*, 1032–1039.

[96] C. Xu, P. J. Reeves, Q. Jacquet, C. P. Grey, *Adv. Energy Mater.* **2021**, *11*, 2003404.

[97] J. P. Peres, F. Weill, C. Delmas, *Solid State Ionics* **1999**, *116*, 19–27.

[98] L. de Biasi, A. Schiele, M. Roca-Ayats, G. Garcia, T. Brezesinski, P. Hartmann, J. Janek, *ChemSusChem* **2019**, *12*, 2240–2250.

[99] A. O. Kondrakov, A. Schmidt, J. Xu, H. Geßwein, R. Mönig, P. Hartmann, H. Sommer, T. Brezesinski, J. Janek, *J. Phys. Chem. C* **2017**, *121*, 3286–3294.

[100] H. H. Sun, A. Manthiram, *Chem. Mater.* **2017**, *29*, 8486–8493.

[101] C. S. Yoon, D. W. Jun, S. T. Myung, Y. K. Sun, *ACS Energy Lett.* **2017**, *2*, 1150–1155.

[102] P. Yan, J. Zheng, M. Gu, J. Xiao, J. G. Zhang, C. M. Wang, *Nat. Commun.* **2017**, *8*, 14101.

[103] H. Zhang, F. Omenya, P. Yan, L. Luo, M. S. Whittingham, C. Wang, G. Zhou, *ACS Energy Lett.* **2017**, *2*, 2607–2615.

[104] P. Mukherjee, P. Lu, N. Faenza, N. Pereira, G. Amatucci, G. Ceder, F. Cosandey, *ACS Appl. Mater. Interfaces* **2021**, *13*, 17478–17486.

[105] S. Jung, H. Gwon, J. Hong, K. Park, D. Seo, H. Kim, J. Hyun, W. Yang, K. Kang, *Adv. Energy Mater.* **2014**, *4*, 1300787.

[106] S. Oswald, H. A. Gasteiger, *J. Electrochem. Soc.* **2023**, *170*, 030506.

[107] M. Bianchini, F. Fauth, P. Hartmann, T. Brezesinski, J. Janek, *J. Mater. Chem. A* **2020**, *8*, 1808–1820.

[108] P. Kurzhals, F. Riewald, M. Bianchini, S. Ahmed, A. M. Kern, F. Walther, H. Sommer, K. Volz, J. Janek, *J. Electrochem. Soc.* **2022**, *169*, 050526.

[109] S. Schweidler, L. De Biasi, G. Garcia, A. Mazilkin, P. Hartmann, T. Brezesinski, J. Janek, *ACS Appl. Energy Mater.* **2019**, *2*, 7375–7384.

[110] J. Wandt, A. T. S. Freiberg, A. Ogrodnik, H. A. Gasteiger, *Mater. Today* **2018**, *21*, 825–833.

[111] R. Jung, M. Metzger, F. Maglia, C. Stinner, H. A. Gasteiger, *J. Phys. Chem. Lett.* **2017**, *8*, 4820–4825.

[112] A. Schürmann, B. Luerßen, D. Mollenhauer, J. Janek, D. Schröder, *Chem. Rev.* **2021**, *121*, 12445–12464.

[113] A. R. Genreith-Schriever, H. Banerjee, A. S. Menon, E. N. Bassey, L. F. J. Piper, C. P. Grey, A. J. Morris, *Joule* **2023**, *7*, 1623–1640.

[114] R. Jung, M. Metzger, F. Maglia, C. Stinner, H. A. Gasteiger, *J. Electrochem. Soc.* **2017**, *164*, A1361–A1377.

[115] D. Streich, C. Erk, A. Guéguen, P. Müller, F. F. Chesneau, E. J. Berg, *J. Phys. Chem. C* **2017**, *121*, 13481–13486.

[116] C. Xu, K. Märker, J. Lee, A. Mahadevegowda, P. J. Reeves, S. J. Day, M. F. Groh, S. P. Emge, C. Ducati, B. L. Mehdi, C. C. Tang, C. P. Grey, *Nat. Mater.* **2021**, *20*, 84–92.

[117] S. Ahmed, A. Pokle, S. Schweidler, A. Beyer, M. Bianchini, F. Walther, A. Mazilkin, P. Hartmann, T. Brezesinski, J. Janek, et al., *ACS Nano* **2019**, *13*, 10694–10704.

[118] Y. Wu, D. Ren, X. Liu, G. Xu, X. Feng, Y. Zheng, Y. Li, M. Yang, Y. Peng, X. Han, L. Wang, Z. Chen, Y. Ren, L. Lu, X. He, J. Chen, K. Amine, M. Ouyang, *Adv. Energy Mater.* **2021**, *11*, 2102299.

[119] A. Tornheim, S. Sharifi-Asl, J. C. Garcia, J. Bareño, H. Iddir, R. Shahbazian-Yassar, Z. Zhang, *Nano Energy* **2019**, *55*, 216–225.

[120] S. Solchenbach, M. Metzger, M. Egawa, H. Beyer, H. A. Gasteiger, *J. Electrochem. Soc.* **2018**, *165*, A3022–A3028.

[121] S. L. Dreyer, K. R. Kretschmer, Đ. Tripković, A. Mazilkin, R. Chukwu, R. Azmi, P. Hartmann, M. Bianchini, T. Brezesinski, J. Janek, *Adv. Mater. Interfaces* **2022**, *9*, 2101100.

[122] J. Lüchtefeld, H. Hemmelmann, S. Wachs, K. J. Mayrhofer, M. T. Elm, B. B. Berkes, *J. Phys. Chem. C* **2022**, *126*, 17204–17211.

[123] J. Vetter, P. Novák, M. R. Wagner, C. Veit, K. C. Möller, J. O. Besenhard, M. Winter, M. Wohlfahrt-Mehrens, C. Vogler, A. Hammouche, *J. Power Sources* **2005**, *147*, 269–281.

[124] C. Fang, T. N. Tran, Y. Zhao, G. Liu, *Electrochim. Acta* **2021**, *399*, 139362.

[125] T. Lombardo, F. Walther, C. Kern, Y. Moryson, T. Weintraut, A. Henss, M. Rohnke, *J. Vac. Sci. Technol. A* **2023**, *41*, 053207.

[126] J. C. Hestenes, L. E. Marbella, *ACS Energy Lett.* **2023**, *8*, 4572–4596.

[127] C. P. Grey, D. S. Hall, *Nat. Commun.* **2020**, *11*, 6279.

[128] J. Yan, H. Huang, J. Tong, W. Li, X. Liu, H. Zhang, H. Huang, W. Zhou, *Interdiscip. Mater.* **2022**, *1*, 330–353.

[129] Z. Ahaliabadeh, X. Kong, E. Fedorovskaya, T. Kallio, *J. Power Sources* **2022**, *540*, 231633.

[130] P. Hou, H. Zhang, Z. Zi, L. Zhang, X. Xu, *J. Mater. Chem. A* **2017**, *5*, 4254–4279.

[131] Z. Meng, X. Ma, L. Azhari, J. Hou, Y. Wang, *Commun. Mater.* **2023**, *4*, 90.

[132] X. Xu, H. Huo, J. Jian, L. Wang, H. Zhu, S. Xu, X. He, G. Yin, C. Du, X. Sun, *Adv. Energy Mater.* **2019**, *9*, 1803963.

[133] T. Thien Nguyen, U. H. Kim, C. S. Yoon, Y. K. Sun, *Chem. Eng. J.* **2021**, *405*, 126887.

[134] S. Lu, L. Tang, H. Wei, Y. Huang, C. Yan, Z. He, Y. Li, J. Mao, K. Dai, J. Zheng, *Electrochem. Energy Rev.* **2022**, *5*, 15.

[135] J. Hu, H. Wang, B. Xiao, P. Liu, T. Huang, Y. Li, X. Ren, Q. Zhang, J. Liu, X. Ouyang, X. Sun, *Natl. Sci. Rev.* **2023**, *10*, nwad252.

[136] M. Kim, L. Zou, S. B. Son, I. D. Bloom, C. Wang, G. Chen, *J. Mater. Chem. A* **2022**, *10*, 12890–12899.

[137] J. Zhu, G. Chen, *J. Mater. Chem. A* **2019**, *7*, 5463–5474.

[138] D. Karabelli, S. Kiemel, S. Singh, J. Koller, S. Ehrenberger, R. Miehe, M. Weeber, K. P. Birke, *Front. Energy Res.* **2020**, *8*, 594857.

[139] X. Sun, M. Ouyang, H. Hao, *Joule* **2022**, *6*, 1738–1742.

[140] L. Mauler, X. Lou, F. Duffner, J. Leker, *Energy Adv.* **2022**, *1*, 136–145.

[141] B. M. Spears, W. J. Brownlie, D. Cordell, L. Hermann, J. M. Mogollón, *Commun. Mater.* **2022**, *3*, 14.

[142] C. Xu, Q. Dai, L. Gaines, M. Hu, A. Tukker, B. Steubing, *Commun. Mater.* **2022**, *3*, 15.

[143] C. Xu, Q. Dai, L. Gaines, M. Hu, A. Tukker, B. Steubing, *Commun. Mater.* **2020**, *1*, 99.

[144] J. Neumann, M. Petranikova, M. Meeus, J. D. Gamarra, R. Younesi, M. Winter, S. Nowak, *Adv. Energy Mater.* **2022**, *12*, 2102917.

[145] G. Harper, R. Sommerville, E. Kendrick, L. Driscoll, P. Slater, R. Stolkin, A. Walton, P. Christensen, O. Heidrich, S. Lambert, A. Abbott, K. Ryder, L. Gaines, P. Anderson, *Nature* **2019**, *575*, 75–86.

[146] C. Vaalma, D. Buchholz, M. Weil, S. Passerini, *Nat. Rev. Mater.* **2018**, *3*, 18013.

[147] P. K. Nayak, L. Yang, W. Brehm, P. Adelhelm, *Angew. Chem. Int. Ed.* **2018**, *57*, 102–120.

[148] P. Vanýsek, *Electrochemical Series*, in: *CRC Handbook of Chemistry and Physics*, *ed.* W. M. Haynes, *92nd edition*, **2011**, CRC Press: Boca Raton, USA.

[149] S. P. Ong, V. L. Chevrier, G. Hautier, A. Jain, C. Moore, S. Kim, X. Ma, G. Ceder, *Energy Environ. Sci.* **2011**, *4*, 3680–3688.

[150] R. Guo, L. Lu, M. Ouyang, X. Feng, *Sci. Rep.* **2016**, *6*, 30248.

[151] P. Desai, J. Huang, D. Foix, J. M. Tarascon, S. Mariyappan, *J. Power Sources* **2022**, *551*, 232177.

[152] B. Jache, P. Adelhelm, *Angew. Chem. Int. Ed.* **2014**, *53*, 10169–10173.

[153] Y. Wan, Y. Liu, D. Chao, W. Li, D. Zhao, *Nano Mater. Sci.* **2023**, *5*, 189–201.

[154] X. Dou, I. Hasa, D. Saurel, C. Vaalma, L. Wu, D. Buchholz, D. Bresser, S. Komaba, S. Passerini, *Mater. Today* **2019**, *23*, 87–104.

[155] E. Irisarri, A. Ponrouch, M. R. Palacin, *J. Electrochem. Soc.* **2015**, *162*, A2476–A2482.

[156] A. Bauer, J. Song, S. Vail, W. Pan, J. Barker, Y. Lu, *Adv. Energy Mater.* **2018**, *8*, 1702869.

[157] L. Zhao, T. Zhang, W. Li, T. Li, L. Zhang, X. Zhang, Z. Wang, *Engineering* **2023**, *24*, 172–183.

[158] I. Hasa, S. Mariyappan, D. Saurel, P. Adelhelm, A. Y. Koposov, C. Masquelier, L. Croguennec, M. Casas-Cabanas, *J. Power Sources* **2021**, *482*, 228872.

[159] S. Xu, H. Dong, D. Yang, C. Wu, Y. Yao, X. Rui, S. Chou, Y. Yu, *ACS Cent. Sci.* **2023**, 9, 2012–2035.

[160] K. Sada, J. Darga, A. Manthiram, *Adv. Energy Mater.* **2023**, *13*, 2302321.

[161] P. Desai, J. Forero-Saboya, V. Meunier, G. Rousse, M. Deschamps, A. M. Abakumov, J.-M. Tarascon, S. Mariyappan, *Energy Storage Mater.* **2023**, *57*, 102–117.

[162] C. Delmas, D. Carlier, M. Guignard, *Adv. Energy Mater.* **2021**, *11*, 2001201.

[163] C. Zhao, Q. Wang, Z. Yao, J. Wang, B. Sánchez-Lengeling, F. Ding, X. Qi, Y. Lu, X. Bai, B. Li, H. Li, A. Aspuru-Guzik, X. Huang, C. Delmas, M. Wagemaker, L. Chen, Y.-S. Hu, *Science* **2020**, *370*, 708–712.

[164] L. F. Pfeiffer, Y. Li, M. Mundszinger, J. Geisler, C. Pfeifer, D. Mikhailova, A. Omar, V. Baran, J. Biskupek, U. Kaiser, P. Adelhelm, M. Wohlfahrt-Mehrens, S. Passerini, P. Axmann, *Chem. Mater.* **2023**, 35, 8065–8080.

[165] T. Risthaus, D. Zhou, X. Cao, X. He, B. Qiu, J. Wang, L. Zhang, Z. Liu, E. Paillard, G. Schumacher, M. Winter, J. Li, *J. Power Sources* **2018**, *395*, 16–24.

[166] C. Luo, A. Langrock, X. Fan, Y. Liang, C. Wang, *J. Mater. Chem. A* **2017**, *5*, 18214–18220.

[167] Q. Liu, Z. Hu, M. Chen, C. Zou, H. Jin, S. Wang, Q. Gu, S. Chou, *J. Mater. Chem. A* **2019**, *7*, 9215–9221.

[168] T. Zhang, J. Kong, C. Shen, S. Cui, Z. Lin, Y. Deng, M. Song, L. Jiao, H. Huang, T. Jin, K. Xie, *ACS Energy Lett.* **2023**, 4753–4761.

[169] Z. Song, K. Zou, X. Xiao, X. Deng, S. Li, H. Hou, X. Lou, G. Zou, X. Ji, *Chem. Eur. J.* **2021**, *27*, 16082–16092.

[170] S. L. Dreyer, R. Zhang, J. Wang, A. Kondrakov, Q. Wang, T. Brezesinski, J. Janek, *J. Phys. Energy* **2023**, *5*, 035002.

[171] J. Wang, S. L. Dreyer, K. Wang, Z. Ding, T. Diemant, G. Karkera, Y. Ma, A. Sarkar, B. Zhou, M. V. Gorbunov, A. Omar, D. Mikhailova, V. Presser, M. Fichtner, H. Hahn, T. Brezesinski, B. Breitung, Q. Wang, *Mater. Futures* **2022**, *1*, 035104.

[172] J. Jin, Y. Liu, X. Pang, Y. Wang, X. Xing, J. Chen, *Sci. China Chem.* **2021**, *64*, 385–402.

[173] M. Baumann, M. Häringer, M. Schmidt, L. Schneider, J. F. Peters, W. Bauer, J. R. Binder, M. Weil, *Adv. Energy Mater.* **2022**, *12*, 2202636.

[174] J. Peng, W. Zhang, Q. Liu, J. Wang, S. Chou, H. Liu, S. Dou, *Adv. Mater.* **2022**, *34*, 2108384.

[175] Q. Liu, Z. Hu, M. Chen, C. Zou, H. Jin, S. Wang, S. Chou, Y. Liu, S. Dou, *Adv. Funct. Mater.* **2020**, *30*, 1909530.

[176] Y. Tian, G. Zeng, A. Rutt, T. Shi, H. Kim, J. Wang, J. Koettgen, Y. Sun, B. Ouyang, T. Chen, Z. Lun, Z. Rong, K. Persson, G. Ceder, *Chem. Rev.* **2021**, *121*, 1623–1669.

[177] J. Qian, C. Wu, Y. Cao, Z. Ma, Y. Huang, X. Ai, H. Yang, *Adv. Energy Mater.* **2018**, *8*, 1702619.

[178] H. W. Lee, R. Y. Wang, M. Pasta, S. W. Lee, N. Liu, Y. Cui, *Nat. Commun.* **2014**, *5*, 5280.

[179] Y. You, X. L. Wu, Y. X. Yin, Y. G. Guo, *Energy Environ. Sci.* **2014**, *7*, 1643–1647.

[180] S. G. Patnaik, I. Escher, G. A. Ferrero, P. Adelhelm, *Batter. Supercaps* **2022**, *5*, e202200043.

[181] W. R. Brant, R. Mogensen, S. Colbin, D. O. Ojwang, S. Schmid, L. Häggström, T. Ericsson, A. Jaworski, A. J. Pell, R. Younesi, *Chem. Mater.* **2019**, *31*, 7203–7211.

[182] M. Jiang, Z. Hou, L. Ren, Y. Zhang, J. G. Wang, *Energy Storage Mater.* **2022**, *50*, 618–640.

[183] C. Q. X. Lim, Z. K. Tan, *ACS Appl. Energy Mater.* **2021**, *4*, 6214–6220.

[184] L. Andrussow, *Angew. Chem.* **1935**, *48*, 593–595.

[185] F. M. Maddar, D. Walker, T. W. Chamberlain, J. Compton, A. S. Menon, M. Copley, I. Hasa, *J. Mater. Chem. A* **2023**, *11*, 15778–15791.

[186] D. O. Ojwang, L. Häggström, T. Ericsson, R. Mogensen, W. R. Brant, *Dalt. Trans.* **2022**, *51*, 14712–14720.

[187] W. Wang, Y. Gang, J. Peng, Z. Hu, Z. Yan, W. Lai, Y. Zhu, D. Appadoo, M. Ye, Y. Cao, Q.-F. Gu, H.-K. Liu, S.-X. Dou, S.-L. Chou, *Adv. Funct. Mater.* **2022**, *32*, 2111727.

[188] D. O. Ojwang, M. Svensson, C. Njel, R. Mogensen, A. S. Menon, T. Ericsson, L. Häggström, J. Maibach, W. R. Brant, *ACS Appl. Mater. Interfaces* **2021**, *13*, 10054–10063.

[189] Y. Ma, Y. Ma, S. L. Dreyer, Q. Wang, K. Wang, D. Goonetilleke, A. Omar, D. Mikhailova, H. Hahn, B. Breitung, T. Brezesinski, *Adv. Mater.* **2021**, *33*, 2101342.

[190] Northvolt AB, *Northvolt develops state-of-the-art sodium-ion battery validated at 160 Wh/kg*, accessed on 18.12.2023 via https://northvolt.com/articles/northvolt-sodium-ion/.

[191] Z. Li, M. Dadsetan, J. Gao, S. Zhang, L. Cai, A. Naseri, M. E. Jimenez-Castaneda, T. Filley, J. T. Miller, M. J. Thomson, V. G. Pol, *Adv. Energy Mater.* **2021**, *11*, 2101764.

[192] Y. He, S. L. Dreyer, Y.-Y. Ting, Y. Ma, Y. Hu, D. Goonetilleke, Y. Tang, T. Diemant, B. Zhou, P. M. Kowalski, M. Fichtner, H. Hahn, J. Aghassi-Hagmann, T. Brezesinski, B. Breitung, Y. Ma, *Angew. Chem. Int. Ed.* **2024**, *63*, e202315371.

[193] Y. He, S. L. Dreyer, T. Akcay, T. Diemant, R. Mönig, Y. Ma, Y. Tang, H. Wang, H. Liu, J. Lin, S. Schweidler, M. Fichtner, H. Hahn, J. Aghassi-Hagmann, T. Brezesinski, B. Breitung, Y. Ma, *manuscript in preparation*, **2024**.

[194] Y. Ma, Y. Ma, Q. Wang, S. Schweidler, M. Botros, T. Fu, H. Hahn, T. Brezesinski, B. Breitung, *Energy Environ. Sci.* **2021**, *14*, 2883–2905.

[195] A. Amiri, R. Shahbazian-Yassar, *J. Mater. Chem. A* **2021**, *9*, 782–823.

[196] J. W. Sturman, E. A. Baranova, Y. Abu-Lebdeh, *Front. Energy Res.* **2022**, *10*, 862551.

[197] D. B. Miracle, O. N. Senkov, *Acta Mater.* **2017**, *122*, 448–511.

[198] Q. Wang, L. Velasco, B. Breitung, V. Presser, *Adv. Energy Mater.* **2021**, *11*, 2102355.

[199] J. H. Gross, *Mass Spectrometry*, 3rd edition, **2017**, Springer International Publishing: Cham, Switzerland.

[200] E. de Hoffmann, V. Stroobant, *Mass Spectrometry – Principles and Applications*, 3rd edition, **2007**, John Wiley & Sons, Ltd: Chichester, England.

[201] A. L. Yergey, A. K. Yergey, *J. Am. Soc. Mass Spectrom.* **1997**, *8*, 943–953.

[202] S. Bruckenstein, R. R. Gadde, *J. Am. Chem. Soc.* **1971**, *93*, 793–794.

[203] O. Wolter, J. Heitbaum, *Ber. Bunsenges. Physik. Chem.* **1984**, *88*, 2–6.

[204] H. Baltruschat, *J. Am. Soc. Mass Spectrom.* **2004**, *15*, 1693–1706.

[205] G. Eggert, J. Heitbaum, *Electrochim. Acta* **1986**, *31*, 1443–1448.

[206] R. Imhof, P. Novák, *J. Electrochem. Soc.* **1998**, *145*, 1081–1087.

[207] R. Imhof, P. Novák, *J. Electrochem. Soc.* **1999**, *146*, 1702–1706.

[208] B. D. McCloskey, D. S. Bethune, R. M. Shelby, G. Girishkumar, A. C. Luntz, *J. Phys. Chem. Lett.* **2011**, *2*, 1161–1166.

[209] N. Tsiouvaras, S. Meini, I. Buchberger, H. A. Gasteiger, *J. Electrochem. Soc.* **2013**, *160*, A471–A477.

[210] B. B. Berkes, A. Jozwiuk, M. Vračar, H. Sommer, T. Brezesinski, J. Janek, *Anal. Chem.* **2015**, *87*, 5878–5883.

[211] B. B. Berkes, A. Jozwiuk, H. Sommer, T. Brezesinski, J. Janek, *Electrochem. commun.* **2015**, *60*, 64–69.

[212] Pfeiffer Vacuum GmbH, *Quadrupole mass spectrometers*, accessed on 19.12.2023 via https://www.pfeiffer-vacuum.com/en/know-how/mass-spectrometers-and-residual-gas-analysis/quadrupole-mass-spectrometers-qms

[213] D. Goonetilleke, J. H. Stansby, N. Sharma, *Curr. Opin. Electrochem.* **2019**, *15*, 18–26.

[214] L. Brückner, J. Frank, T. Elwert, *Metals* **2020**, *10*, 1107.

[215] L. Gaines, Q. Dai, J. T. Vaughey, S. Gillard, *Recycling* **2021**, *6*, 31.

[216] L. H. J. Raijmakers, D. L. Danilov, R. A. Eichel, P. H. L. Notten, *Appl. Energy* **2019**, *240*, 918–945.

[217] M. Dotoli, R. Rocca, M. Giuliano, G. Nicol, F. Parussa, M. Baricco, A. M. Ferrari, C. Nervi, M. F. Sgroi, *Sensors* **2022**, *22*, 1763.

[218] Q. Yu, C. Wang, J. Li, R. Xiong, M. Pecht, *eTransportation* **2023**, *17*, 100254.

[219] X. C. A. Chacón, S. Laureti, M. Ricci, G. Cappuccino, *World Electr. Veh. J.* **2023**, *14*, 305.

[220] C. Gervillie-Mouravieff, W. Bao, D. A. Steingart, Y. S. Meng, *Non-destructive characterization techniques for battery performance and lifecycle assessment*, **2023**, DOI 10.48550/arXiv.2310.15396.

[221] J. Huang, S. T. Boles, J. M. Tarascon, *Nat. Sustain.* **2022**, *5*, 194–204.

[222] Y. D. Su, Y. Preger, H. Burroughs, C. Sun, P. R. Ohodnicki, *Sensors* **2021**, *21*, 1397.

[223] L. Albero Blanquer, F. Marchini, J. R. Seitz, N. Daher, F. Bétermier, J. Huang, C. Gervillié, J. M. Tarascon, *Nat. Commun.* **2022**, *13*, 1153.

[224] J. Huang, L. Albero Blanquer, J. Bonefacino, E. R. Logan, D. Alves Dalla Corte, C. Delacourt, B. M. Gallant, S. T. Boles, J. R. Dahn, H. Y. Tam, J.-M. Tarascon, *Nat. Energy* **2020**, *5*, 674–683.

[225] J. Huang, X. Han, F. Liu, C. Gervillié, L. Albero Blanquer, T. Guo, J. M. Tarascon, *Energy Environ. Sci.* **2021**, *14*, 6464–6475.

[226] C. Gervillié-Mouravieff, C. Boussard-Plédel, J. Huang, C. Leau, L. Albero Blanquer, M. Ben Yahia, M. L. Doublet, S. T. Boles, X. H. Zhang, J. L. Adam, J.-M. Tarascon, *Nat. Energy* **2022**, *7*, 1157–1169.

[227] J. O. Majasan, J. B. Robinson, R. E. Owen, M. Maier, A. N. P. Radhakrishnan, M. Pham, T. G. Tranter, Y. Zhang, P. R. Shearing, D. J. L. Brett, *J. Phys. Energy* **2021**, *3*, 032011.

[228] D. Williams, R. Copley, P. Bugryniec, R. Dwyer-Joyce, S. Brown, *J. Power Sources* **2024**, *590*, 233777.

[229] M. C. Appleberry, J. A. Kowalski, S. A. Africk, J. Mitchell, T. C. Ferree, V. Chang, V. Parekh, Z. Xu, Z. Ye, J. F. Whitacre, S. D. Murphy, *J. Power Sources* **2022**, *535*, 231423.

[230] J. B. Robinson, R. E. Owen, M. D. R. Kok, M. Maier, J. Majasan, M. Braglia, R. Stocker, T. Amietszajew, A. J. Roberts, R. Bhagat, D. Billsson, J. Z. Olson, J. Park, G. Hinds, A. A. Tidblad, D. J. L. Brett, P. R. Shearing, *J. Electrochem. Soc.* **2020**, *167*, 120530.

[231] D. Wasylowski, S. Neubauer, M. Faber, H. Ditler, M. Sonnet, A. Blömeke, P. Dechent, A. Gitis, D. U. Sauer, *J. Power Sources* **2023**, *580*, 233295.

[232] Liminal Insights, Inc., *Demystifying EchoStat®: Understanding Ultrasound Diagnostics in EV Batteries*, **2023**, accessed on 22.11.2023 via https://www.liminalinsights.com/blog/demystifying-echostat-understanding-ultrasound-diagnostics-in-ev-battery-cell-inspection/.

[233] Titan Advanced Energy Solutions, Inc., *IonSight™ – See Inside Every Cell in Your Production Line*, **2023**, accessed on 22.11.2023 via https://www.titanaes.com/battery-manufacturing.

[234] V. Barat, A. Marchenkov, V. Bardakov, M. Karpova, D. Zhgut, S. Elizarov, *Appl. Sci.* **2021**, *11*, 11892.

[235] M. Saeedifar, D. Zarouchas, *Compos. Part B Eng.* **2020**, *195*, 108039.

[236] Y. He, M. Li, Z. Meng, S. Chen, S. Huang, Y. Hu, X. Zou, *Mech. Syst. Signal Process.* **2021**, *148*, 107146.

[237] D. Lockner, *Int. J. Rock Mech. Min. Sci.* **1993**, *30*, 883–899.

[238] M. Enoki, H. Inaba, Y. Mizutani, M. Nakano, M. Ohtsu, *Practical Acoustic Emission Testing*, **2016**, Springer: Tokyo, Japan.

[239] V. Nasir, S. Ayanleye, S. Kazemirad, F. Sassani, S. Adamopoulos, *Constr. Build. Mater.* **2022**, *350*, 128877.

[240] Y. Indrayani, T. Yoshimura, Y. Yanase, Y. Fujii, Y. Imamura, *J. Wood Sci.* **2007**, *53*, 76–79.

[241] L. Calabrese, E. Proverbio, *Corros. Mater. Degrad.* **2021**, *2*, 1–33.

[242] Z. Nazarchuk, V. Skalskyi, O. Serhiyenko, *Acoustic Emission: Methodology and Application* in: *Foundations of Engineering Mechanics*, Eds.: V. I. Babitsky, J. Wittenburg, **2017**, Springer International: Cham, Switzerland.

[243] C. B. Scruby, *J. Phys. E.* **1987**, *20*, 946–953.

[244] M. G. R. Sause, *J. Acoust. Emiss.* **2011**, *29*, 184–196.

[245] M. Shateri, M. Ghaib, D. Svecova, D. Thomson, *Smart Mater. Struct.* **2017**, *26*, 065023.

[246] G. Ciaburro, G. Iannace, *Appl. Sci.* **2022**, *12*, 10476.

[247] A. A. Abd-El-Latif, P. Sichler, M. Kasper, T. Waldmann, M. Wohlfahrt-Mehrens, *Batter. Supercaps* **2021**, *4*, 1135–1144.

[248] M. Feinauer, A. A. Abd-El-Latif, P. Sichler, A. Aracil Regalado, M. Wohlfahrt-Mehrens, T. Waldmann, *J. Power Sources* **2023**, *570*, 233046.

[249] Z. Wang, X. Zhao, H. Zhang, D. Zhen, F. Gu, A. Ball, *J. Energy Storage* **2023**, *64*, 107192.

[250] K. Wang, Q. Chen, Y. Yue, R. Tang, G. Wang, L. Tang, Y. He, *Nondestruct. Test. Eval.* **2023**, *38*, 480–499.

[251] S. Schweidler, M. Bianchini, P. Hartmann, T. Brezesinski, J. Janek, *Batter. Supercaps* **2020**, *3*, 1021–1027.

[252] S. Schweidler, S. L. Dreyer, B. Breitung, T. Brezesinski, *Sci. Rep.* **2021**, *11*, 23381.

[253] S. Schweidler, S. L. Dreyer, B. Breitung, T. Brezesinski, *Coatings* **2022**, *12*, 402.

[254] B. Michalak, B. B. Berkes, H. Sommer, T. Brezesinski, J. Janek, *J. Phys. Chem. C* **2017**, *121*, 211–216.

[255] A. Schiele, B. Breitung, T. Hatsukade, B.B. Berkes, P. Hartmann, J. Janek, T. Brezesinski, *ACS Energy Lett.* **2017**, *2*, 2228–2233.

[256] A. Schiele, H. Sommer, T. Brezesinski, J. Janek, B. B. Berkes, *Differential Electrochemical Mass Spectrometry in Lithium Battery Research*, in: *Encyclopedia of Interfacial Chemistry*, *Surface Science and Electrochemistry*, Ed.: K. Wandelt, **2018**, Elsevier: Amsterdam, The Netherlands.

[257] B. Rowden, N. Garcia-Araez, *Energy Reports* **2020**, *6*, 10–18.

[258] Z. Cui, A. Manthiram, *Angew. Chem. Int. Ed.* **2023**, *62*, e202307243.

[259] P. Liu, L. Yang, B. Xiao, H. Wang, L. Li, S. Ye, Y. Li, X. Ren, X. Ouyang, J. Hu, F. Pan, Q. Zhang, J. Liu, *Adv. Funct. Mater.* **2022**, *32*, 2208586.

[260] R. Aalund, B. Endreddy, M. Pecht, *Front. Chem. Eng.* **2022**, *4*, 828375.

[261] Z. Zhao, L. Pang, Z. Yang, Y. Zhang, Z. Peng, L. Guo, *Differential Electrochemical Mass Spectrometry for Lithium-Ion Batteries*, in: *Microscopy and Microanalysis for Lithium-Ion Batteries*, Ed.: C. Shen, *1st edition*, **2023**, CRC Press: Boca Raton, USA.

[262] S. Kim, H. Kim, B. Kim, Y. Kim, J. Jung, W. Ryu, *Adv. Energy Mater.* **2023**, *13*, 2301983.

[263] B. Salomez, S. Grugeon, M. Armand, P. Tran-Van, S. Laruelle, *J. Electrochem. Soc.* **2023**, *170*, 050537.

[264] W. Chen, F. He, Y.-X. Chen, *Curr. Opin. Electrochem.* **2023**, *42*, 101393.

[265] R. Sim, J. Langdon, A. Manthiram, *Small Methods* **2023**, *7*, 2201438.

[266] J. Geisler, *Online gas analysis of electrochemical reactions*, Dissertation, Humboldt-Universität Berlin, **2023**, DOI 10.18452/26417.

[267] L. Pang, Z. Zhao, X. Y. Ma, W. Bin Cai, L. Guo, S. Dong, C. Liu, Z. Peng, *J. Chem. Phys.* **2023**, *158*, 174701.

[268] J. Geisler, L. Pfeiffer, G. A. Ferrero, P. Axmann, P. Adelhelm, *Gas evolution in sodium ion batteries – DEMS setup, data evaluation and application to a Mn-rich layered cathode material*, **2023**, DOI 10.26434/chemrxiv-2023-md389.

[269] C. Misiewicz, R. Lundström, I. Ahmed, M. J. Lacey, W. R. Brant, E. J. Berg, *J. Power Sources* **2023**, *554*, 232318.

[270] H. Zhang, J. Chen, B. Zhang, X. Wu, Z. Li, L. Chen, J. Wang, X. Yu, H. Luo, J. Xue, Y.-H. Hong, Y. Qiao, S.-G. Sun, *J. Energy Chem.* **2023**, *84*, 286–291.

[271] L. Bläubaum, *Elektrochemische und gasanalytische Untersuchungen an Lithium-Ionen-Batterien*, Dissertation, Karlsruher Institut für Technologie, **2023**, DOI 10.5445/IR/1000161140.

[272] R. Venâncio, R. Vicentini, M. Pinzón, D. A. Corrêa, A. N. de Miranda, A. C. Queiroz, F. T. Degasperi, L. J. A. Siqueira, L. M. Da Silva, H. Zanin, *Energy Storage Mater.* **2023**, *62*, 102943.

[273] B. L. D. Rinkel, J. P. Vivek, N. Garcia-Araez, C. P. Grey, *Energy Environ. Sci.* **2022**, *15*, 3416–3438.

[274] W. M. Dose, W. Li, I. Temprano, C. A. O'Keefe, B. L. Mehdi, M. F. L. De Volder, C. P. Grey, *ACS Energy Lett.* **2022**, *7*, 3524–3530.

[275] W. M. Dose, I. Temprano, J. P. Allen, E. Björklund, C. A. O'Keefe, W. Li, B. L. Mehdi, R. S. Weatherup, M. F. L. De Volder, C. P. Grey, *ACS Appl. Mater. Interfaces* **2022**, *14*, 13206–13222.

[276] D. B. Thornton, B. J. V. Davies, S. B. Scott, A. Aguadero, M. P. Ryan, I. E. L. Stephens, *Angew. Chem. Int. Ed.* **2023**, *62*, e202315357.

[277] J. Scharf, F. M. Matysik, *Monatsh. Chem.* **2023**, *154*, 1025–1033.

[278] E. W. C. Spotte-Smith, S. M. Blau, D. Barter, N. J. Leon, N. T. Hahn, N. S. Redkar, K. R. Zavadil, C. Liao, K. A. Persson, *J. Am. Chem. Soc.* **2023**, *145*, 12181–12192.

[279] J. Hemmerling, J. Schäfer, T. Jung, T. Kreher, M. Ströbel, C. Gassmann, J. Günther, A. Fill, K. P. Birke, *J. Energy Storage* **2023**, *59*, 106444.

[280] K. Tan, W. Li, Z. Lin, X. Han, X. Dai, S. Li, Z. Liu, H. Liu, L. Sun, J. Jiang, T. Liu, K. Wu, T. Guo, S. Wang, *J. Power Sources* **2023**, *580*, 233471.

[281] H. Radinger, *Surface Properties of Graphite for Efficient Electrocatalysis of Vanadium Redox Reactions*, Dissertation, Karlsruher Institut für Technologie, **2022**, DOI 10.5445/IR/1000150874.

[282] W. Wei, Z. Wang, L. Yao, H. Jiang, C. Li, *J. Mater. Chem. A* **2023**, *11*, 2979–2984.

[283] R. Sim, Z. Cui, A. Manthiram, *ACS Energy Lett.* **2023**, *8*, 5143–5148.

[284] Y. Song, Y. Cui, L. Geng, B. Li, L. Ge, L. Zhou, Z. Qiu, J. Nan, W. Wu, H. Xu, X. Li, Z. Yan, Q. Xue, Y. Tang, W. Xing, *Adv. Energy Mater.* **2023**, DOI 10.1002/aenm.202303207.

[285] L. Karger, S. Korneychuk, W. van den Bergh, S. L. Dreyer, R. Zhang, A. Kondrakov, J. Janek, T. Brezesinski, *Chem. Mater.* **2023**, DOI 10.1021/acs.chemmater.3c02727.

[286] S. Oswald, M. Bock, H. A. Gasteiger, *J. Electrochem. Soc.* **2023**, *170*, 090505.

[287] G. J. P. Fajardo, E. Fiamegkou, J. A. Gott, H. Wang, I. Temprano, I. D. Seymour, A. S. Menon, I. E. L. Stephens, M. Ans, T.-L. Lee, P. K. Thakur, W. M. Dose, M. F. L. De Volder, C. P. Grey, L. F. J. Piper, *ACS Energy Lett.* **2023**, *8*, 5025–5031.

[288] G. Li, R. Xu, B. Chu, J. Chen, L. Xue, L. You, X. Ren, Y. Wang, Y. Zhang, T. Huang, A. Yu, *J. Power Sources* **2024**, *589*, 233714.

[289] R. Lundström, N. Gogoi, X. Hou, E. J. Berg, *J. Electrochem. Soc.* **2023**, *170*, 040516.

[290] M. Martins, D. Haering, J. G. Connell, H. Wan, K. L. Svane, B. Genorio, P. Farinazzo Bergamo Dias Martins, P. P. Lopes, B. Gould, F. Maglia, R. Jung, V. Stamenkovic, I. E. Castelli, N. M. Markovic, J. Rossmeisl, D. Strmcnik, *ACS Catal.* **2023**, *13*, 9289–9301.

[291] F. Jeschull, L. Zhang, Ł. Kondracki, F. Scott, S. Trabesinger, *J. Phys. Energy* **2023**, *5*, 025003.

[292] N. Gogoi, E. Bowall, R. Lundström, N. Mozhzhukhina, G. Hernández, P. Broqvist, E. J. Berg, *Chem. Mater.* **2022**, *34*, 3831–3838.

[293] X. Min, C. Han, S. Zhang, J. Ma, N. Hu, J. Li, X. Du, B. Xie, H.-J. Lin, C.-Y. Kuo, C.-T. Chen, Z. Hu, L. Qiao, Z. Cui, G. Xu, G. Cui, *Angew. Chem. Int. Ed.* **2023**, *62*, e202302664.

[294] Z. Guo, Z. Cui, R. Sim, A. Manthiram, *Small* **2023**, *19*, 2305055.

[295] R. Sim, L. Su, A. Manthiram, *Adv. Energy Mater.* **2023**, *13*, 2300096.

[296] J. Langdon, R. Sim, A. Manthiram, *ACS Energy Lett.* **2022**, *7*, 2634–2640.

[297] C. Li, Y. Xiao, X. Zhang, H. Cheng, Y.-J. Cheng, Y. Xia, *ACS Appl. Mater. Interfaces* **2023**, *15*, 44921–44931.

[298] L. Zheng, G. Li, J. Zhang, *Chem. Eng. J.* **2023**, *475*, 146285.

[299] J. Cai, Z. Yang, X. Zhou, B. Wang, A. Suzana, J. Bai, C. Liao, Y. Liu, Y. Chen, S. Song, X. Zhang, L. Wang, X. He, X. Meng, N. Karami, B. A. S. Sulaiman, N. A. Chernova, S. Upreti, B. Prevel, F. Wang, Z. Chen, *J. Energy Chem.* **2023**, *85*, 126–136.

[300] M. Song, D. Lee, J. Kim, Y. Heo, C. Nam, D. Ko, J. Lim, *J. Power Sources* **2023**, *560*, 232699.

[301] D. Cao, C. Tan, Y. Chen, *Nat. Commun.* **2022**, *13*, 4908.

[302] H. Zhang, J. Chen, Y. Hong, X. Wu, X. Huang, P. Dai, H. Luo, B. Zhang, Y. Qiao, S. G. Sun, *Nano Lett.* **2022**, *22*, 9972–9981.

[303] T. Y. Huang, Z. Cai, M. J. Crafton, L. A. Kaufman, Z. M. Konz, H. K. Bergstrom, E. A. Kedzie, H. M. Hao, G. Ceder, B. D. McCloskey, *Adv. Energy Mater.* **2023**, *13*, 2300241.

[304] M. J. Crafton, T. Y. Huang, Y. Yue, R. Giovine, V. C. Wu, C. Dun, J. J. Urban, R. J. Clément, W. Tong, B. D. McCloskey, *ACS Appl. Mater. Interfaces* **2023**, *15*, 18747–18762.

[305] R. Schmitz, R. A. Müller, R. W. Schmitz, C. Schreiner, M. Kunze, A. Lex-Balducci, S. Passerini, M. Winter, *J. Power Sources* **2013**, *233*, 110–114.

[306] C. Fang, J. Li, M. Zhang, Y. Zhang, F. Yang, J. Z. Lee, M. H. Lee, J. Alvarado, M. A. Schroeder, Y. Yang, B. Lu, N. Williams, M. Ceja, L. Yang, M. Cai, J. Gu, K. Xu, X. Wang, Y. S. Meng, *Nature* **2019**, *572*, 511–515.

[307] E. J. McShane, A. M. Colclasure, D. E. Brown, Z. M. Konz, K. Smith, B. D. McCloskey, *ACS Energy Lett.* **2020**, *5*, 2045–2051.

[308] G. M. Hobold, B. M. Gallant, *ACS Energy Lett.* **2022**, *7*, 3458–3466.

[309] W. Deng, X. Yin, W. Bao, X. Zhou, Z. Hu, B. He, B. Qiu, Y. S. Meng, Z. Liu, *Nat. Energy* **2022**, *7*, 1031–1041.

[310] E. J. McShane, H. K. Bergstrom, P. J. Weddle, D. E. Brown, A. M. Colclasure, B. D. McCloskey, *ACS Energy Lett.* **2022**, *7*, 2734–2744.

[311] E. J. McShane, P. P. Paul, T. R. Tanim, C. Cao, H. G. Steinrück, V. Thampy, S. E. Trask, A. R. Dunlop, A. N. Jansen, E. J. Dufek, M. F. Toney, J. N. Weker, B. D. McCloskey, *J. Mater. Chem. A* **2022**, *367*, 23927–23939.

[312] M. Tao, Y. Xiang, D. Zhao, P. Shan, Y. Sun, Y. Yang, *Nano Lett.* **2022**, *22*, 6775–6781.

[313] M. Tao, Y. Xiang, D. Zhao, P. Shan, Y. Yang, *Commun. Mater.* **2022**, *3*, 50.

[314] A. V. Morozov, I. A. Moiseev, A. A. Savina, A. O. Boev, D. A. Aksyonov, L. Zhang, P. A. Morozova, V. A. Nikitina, E. M. Pazhetnov, E. J. Berg, S. S. Fedotov, J.-M. Tarascon, E. V. Antipov, A. M. Abakumov, *Chem. Mater.* **2022**, *34*, 6779–6791.

[315] Y. Li, Z. Shi, B. Qiu, J. Zhao, X. Li, Y. Zhang, T. Li, Q. Gu, J. Gao, Z. Liu, *Adv. Funct. Mater.* **2023**, *33*, 2302236.

[316] W. Liu, J. Xu, W. H. Kan, W. Yin, *Small* **2023**, *19*, 2302912.

[317] T. Y. Huang, M. J. Crafton, Y. Yue, W. Tong, B. D. McCloskey, *Energy Environ. Sci.* **2021**, *14*, 1553–1562.

[318] W. Yin, J. Alvarado, E. A. Kedzie, B. D. McCloskey, C. Dun, J. J. Urban, Z. Zhuo, W. Yang, M. M. Doeff, *J. Mater. Chem. A* **2023**, *11*, 23048.

[319] S. Zhou, Y. Sun, T. Gao, J. Liao, S. Zhao, G. Cao, *Angew. Chem. Int. Ed.* **2023**, *62*, e202311930.

[320] R. A. House, U. Maitra, M. A. Pérez-Osorio, J. G. Lozano, L. Jin, J. W. Somerville, L. C. Duda, A. Nag, A. Walters, K. J. Zhou, M. R. Roberts, P. G. Bruce, *Nature* **2020**, *577*, 502–508.

[321] R. A. House, J. J. Marie, M. A. Pérez-Osorio, G. J. Rees, E. Boivin, P. G. Bruce, *Nat. Energy* **2021**, *6*, 781–789.

[322] R. A. House, H. Y. Playford, R. I. Smith, J. Holter, I. Griffiths, K. J. Zhou, P. G. Bruce, *Energy Environ. Sci.* **2022**, *15*, 376–383.

[323] R. A. House, G. J. Rees, K. McColl, J. J. Marie, M. Garcia-Fernandez, A. Nag, K. J. Zhou, S. Cassidy, B. J. Morgan, M. Saiful Islam, P. G. Bruce, *Nat. Energy* **2023**, *8*, 351–360.

[324] Q. Li, D. Ning, D. Wong, K. An, Y. Tang, D. Zhou, G. Schuck, Z. Chen, N. Zhang, X. Liu, *Nat. Commun.* **2022**, *13*, 1123.

[325] K. Wu, P. Ran, S. Wang, L. He, W. Yin, B. Wang, F. Wang, J. Zhao, E. Zhao, *Nano Energy* **2023**, *113*, 108602.

[326] A. S. Menon, B. J. Johnston, S. G. Booth, L. Zhang, K. Kress, B. E. Murdock, G. Paez Fajardo, N. N. Anthonisamy, N. Tapia-Ruiz, S. Agrestini, M. Garcia-Fernandez, K. Zhou, P. K. Thakur, T. L. Lee, A. J. Nedoma, S. A. Cussen, L. F. J. Piper, *PRX Energy* **2023**, *2*, 013005.

[327] H. Lu, S. Chu, J. Tian, Q. Wang, C. Sheng, C. Cheng, R. Liu, A. M. D'Angelo, W. K. Pang, L. Zhang, H. Zhou, S. Guo, *Adv. Funct. Mater.* **2024**, *34*, 2305470.

[328] Z. Liu, J. Wu, J. Zeng, F. Li, C. Peng, D. Xue, M. Zhu, J. Liu, *Adv. Energy Mater.* **2023**, *13*, 2301471.

[329] G. Shao, W. Kong, Y. Yu, J. Zhang, W. Yang, J. Yang, Y. Li, X. Liu, *Inorg. Chem.* **2023**, *62*, 9314–9323.

[330] S. L. Dreyer, P. Kurzhals, S. B. Seiffert, P. Müller, A. Kondrakov, T. Brezesinski, J. Janek, *J. Electrochem. Soc.* **2023**, *170*, 060530.

[331] F. Ding, H. Wang, Q. Zhang, L. Zheng, H. Guo, P. Yu, N. Zhang, Q. Guo, F. Xie, R. Dang, X. Rong, Y. Lu, R. Xiao, L. Chen, Y.-S. Hu, *J. Am. Chem. Soc.* **2023**, *145*, 13592–13602.

[332] S. Lee, S. W. Doo, M. S. Jung, S. G. Lim, K. Kim, K. T. Lee, *J. Mater. Chem. A* **2021**, *9*, 14074–14084.

[333] A. Wiebe, T. Gieshoff, S. Möhle, E. Rodrigo, M. Zirbes, S. R. Waldvogel, *Angew. Chem. Int. Ed.* **2018**, *57*, 5594–5619.

[334] L. Ge, Y. Song, P. Niu, B. Li, L. Zhou, W. Feng, C. Ma, X. Li, D. Kong, Z. Yan, Q. Xue, Y. Cui, W. Xing, *ACS Nano* **2024**, 18,3542–3552.

[335] S. Oswald, D. Pritzl, M. Wetjen, H. A. Gasteiger, *J. Electrochem. Soc.* **2020**, *167*, 100511.

[336] S. Oswald, D. Pritzl, M. Wetjen, H. A. Gasteiger, *J. Electrochem. Soc.* **2021**, *168*, 120501.

[337] S. Oswald, F. Riewald, H. A. Gasteiger, *J. Electrochem. Soc.* **2022**, *169*, 040552.

[338] X. Wang, C. Zhu, L. Ren, S. Wang, M. Zuo, W. Xing, W. Fan, B. Zhang, Z. Zheng, C. Shu, W. Xiang, *Energy Technol.* **2023**, *11*, 2300133.

[339] N. Park, S. Kim, M. Kim, S. Han, D. Kim, M. Kim, Y. Sun, *Adv. Energy Mater.* **2023**, *13*, 2301530.

[340] H. Kim, Y. Kong, W. M. Seong, A. Manthiram, *ACS Appl. Mater. Interfaces* **2023**, *15*, 26585–26592.

[341] G. T. Park, D. R. Yoon, U. H. Kim, B. Namkoong, J. Lee, M. M. Wang, A. C. Lee, X. W. Gu, W. C. Chueh, C. S. Yoon, Y.-K. Sun, *Energy Environ. Sci.* **2021**, *14*, 6616–6626.

[342] H. H. Sun, U. H. Kim, J. H. Park, S. W. Park, D. H. Seo, A. Heller, C. B. Mullins, C. S. Yoon, Y. K. Sun, *Nat. Commun.* **2021**, *12*, 6552.

[343] Y. Kim, H. Kim, W. Shin, E. Jo, A. Manthiram, *Adv. Energy Mater.* **2023**, *13*, 2204054.

[344] X. M. Fan, Z. Zhang, G. Q. Mao, Y. J. Tong, K. B. Lin, H. Tong, W. F. Wei, Q. H. Tian, X. Y. Guo, *Rare Met.* **2023**, *42*, 2993–3003.

[345] Z. Luo, G. Hu, W. Wang, Z. Peng, Z. Fang, B. Zhao, H. Li, K. Du, Y. Cao, *J. Energy Storage* **2023**, *68*, 107777.

[346] L. Ni, H. Chen, S. Guo, A. Dai, J. Gao, L. Yu, Y. Mei, H. Wang, Z. Long, J. Wen, W. Deng, G. Zou, H. Hou, T. Liu, K. Amine, X. Ji, *Adv. Funct. Mater.* **2023**, *33*, 2307126.

[347] M.-Y. Qi, S.-D. Zhang, S. Guo, P.-X. Ji, J.-J. Mao, T.-T. Wu, S.-Q. Lu, X. Zhang, S.-G. Chen, D. Su, G.-H. Chen, A.-M. Cao, *Small Methods* **2023**, *7*, 2300280.

[348] A. Schiele, B. Breitung, A. Mazilkin, S. Schweidler, J. Janek, S. Gumbel, S. Fleischmann, E. Burakowska-Meise, H. Sommer, T. Brezesinski, *ACS Omega* **2018**, *3*, 16706–16713.

[349] K. Wang, Z. Zhang, Y. Ding, S. Cheng, B. Xiao, M. Sui, P. Yan, *Adv. Funct. Mater.* **2023**, *33*, 2302023.

[350] P. Thanwisai, P. Vanaphuti, Z. Yao, J. Hou, Z. Meng, X. Ma, H. Guo, G. Gao, Z. Yang, Y. Wang, *Small* **2023**, *19*, 2306465.

[351] B. Zhang, Y. Zhao, M. Li, Q. Wang, L. Cheng, L. Ming, X. Ou, X. Wang, *J. Energy Chem.* **2024**, *89*, 1–9.

[352] Y. Wang, Y. Wang, Y. Xing, C. Jiang, Y. Pang, H. Liu, F. Wu, H. Gao, *J. Mater. Chem. A* **2023**, 11, 19955–19964.

[353] H. Guo, C. Zhao, J. Gao, W. Yang, X. Hu, X. Ma, X. Jiao, J. Yang, K. Sun, D. Chen, *ACS Appl. Mater. Interfaces* **2023**, *15*, 34789–34796.

[354] S. Ma, P. Zou, H. L. Xin, *Mater. Today Energy* **2023**, *38*, 101446.

[355] H. Kim, *ACS Mater. Au* **2023**, *3*, 571–575.

[356] J. H. Teo, F. Strauss, Đ. Tripković, S. Schweidler, Y. Ma, M. Bianchini, J. Janek, T. Brezesinski, *Cell Reports Phys. Sci.* **2021**, *2*, 100465.

[357] J. H. Teo, F. Strauss, F. Walther, Y. Ma, S. Payandeh, T. Scherer, M. Bianchini, J. Janek, T. Brezesinski, *Mater. Futur.* **2022**, *1*, 015102.

[358] L. Zhang, C. Tsolakidou, S. Mariyappan, J. M. Tarascon, S. Trabesinger, *Energy Storage Mater.* **2021**, *42*, 12–21.

[359] Z. Jusys, M. Binder, J. Schnaidt, R. J. Behm, *Electrochim. Acta* **2019**, *314*, 188–201.

[360] C. Bolli, A. Guéguen, M. A. Mendez, E. J. Berg, *Chem. Mater.* **2019**, *31*, 1258–1267.

[361] T. K. Brotherton, J. W. Lynn, *Chem. Rev.* **1959**, *59*, 841–883.

[362] W. R. Blanchard, P. J. McCarthy, H. F. Dylla, P. H. LaMarche, J. E. Simpkins, *J. Vac. Sci. Technol. A Vacuum, Surfaces, Film.* **1986**, *4*, 1715–1719.

[363] X. Pan, A. Chojnacka, F. Béguin, *J. Energy Chem.* **2022**, *72*, 33–40.

[364] T. Guo, A. Illies, V. Cammarata, M. Arndt, W. Sonzogni, *J. Electroanal. Chem.* **2007**, *610*, 102–105.

[365] M. Metzger, P. Walke, S. Solchenbach, G. Salitra, D. Aurbach, H. A. Gasteiger, *J. Electrochem. Soc.* **2020**, *167*, 160522.

[366] M. Goktas, C. Bolli, J. Buchheim, E. J. Berg, P. Novák, F. Bonilla, T. Rojo, S. Komaba, K. Kubota, P. Adelhelm, *ACS Appl. Mater. Interfaces* **2019**, *11*, 32844–32855.

[367] T. Kim, S. H. Ahn, Y. Y. Song, B. Jin Park, C. Lee, A. Choi, M. H. Kim, D. H. Seo, S. K. Jung, H. W. Lee, *Angew. Chem. Int. Ed.* **2023**, *62*, e202309852.

Appendix

Supporting Information to Chapter 4.2.

Supporting Information

The Effect of Doping Process Route on $LiNiO_2$ Cathode Material Properties

Sören L. Dreyer, Philipp Kurzhals, Svenja B. Seiffert, Philipp Müller, Aleksandr Kondrakov, Torsten Brezesinski and Jürgen Janek*

S. L. Dreyer, Dr. T. Brezesinski, Prof. J. Janek
Battery and Electrochemistry Laboratory (BELLA), Institute of Nanotechnology, Karlsruhe Institute of Technology (KIT), Hermann-von-Helmholtz-Platz 1, 76344 Eggenstein-Leopoldshafen, Germany; E-mail: torsten.brezesinski@kit.edu

Dr. P. Kurzhals, Dr. S. B. Seiffert, Dr. P. Müller, Dr. A. Kondrakov
BASF SE, Carl-Bosch-Str. 38, 67056 Ludwigshafen, Germany

Prof. J. Janek
Institute of Physical Chemistry & Center for Materials Research (ZfM/LaMa), Justus-Liebig-University Giessen, Heinrich-Buff-Ring 17, 35392 Giessen, Germany

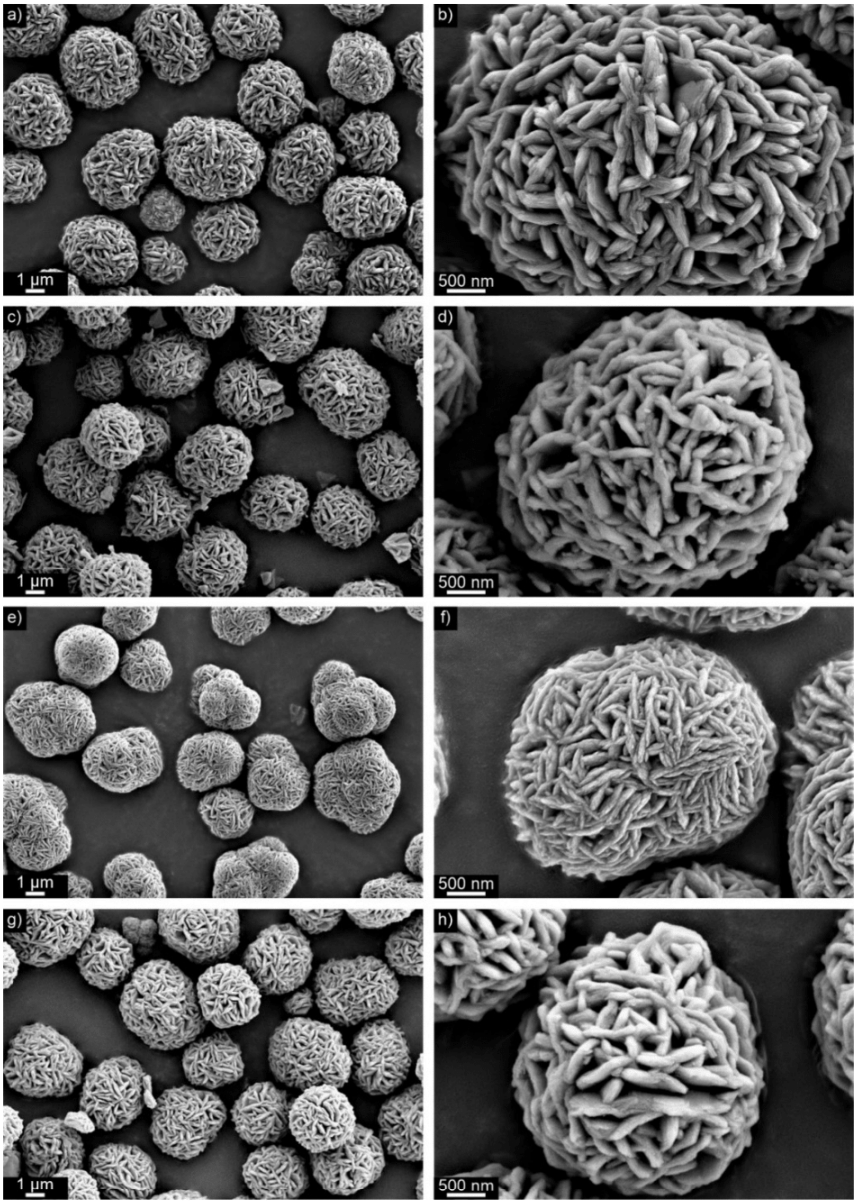

Figure S1. SEM images of the pCAMs used in this study. a,b) Pristine $Ni(OH)_2$; c,d) Zr-impregnated NiO; e, f) Zr-co-precipitated $Ni(OH)_2$ (before pre-drying); and g,h) Zr-co-precipitated NiO after pre-drying.

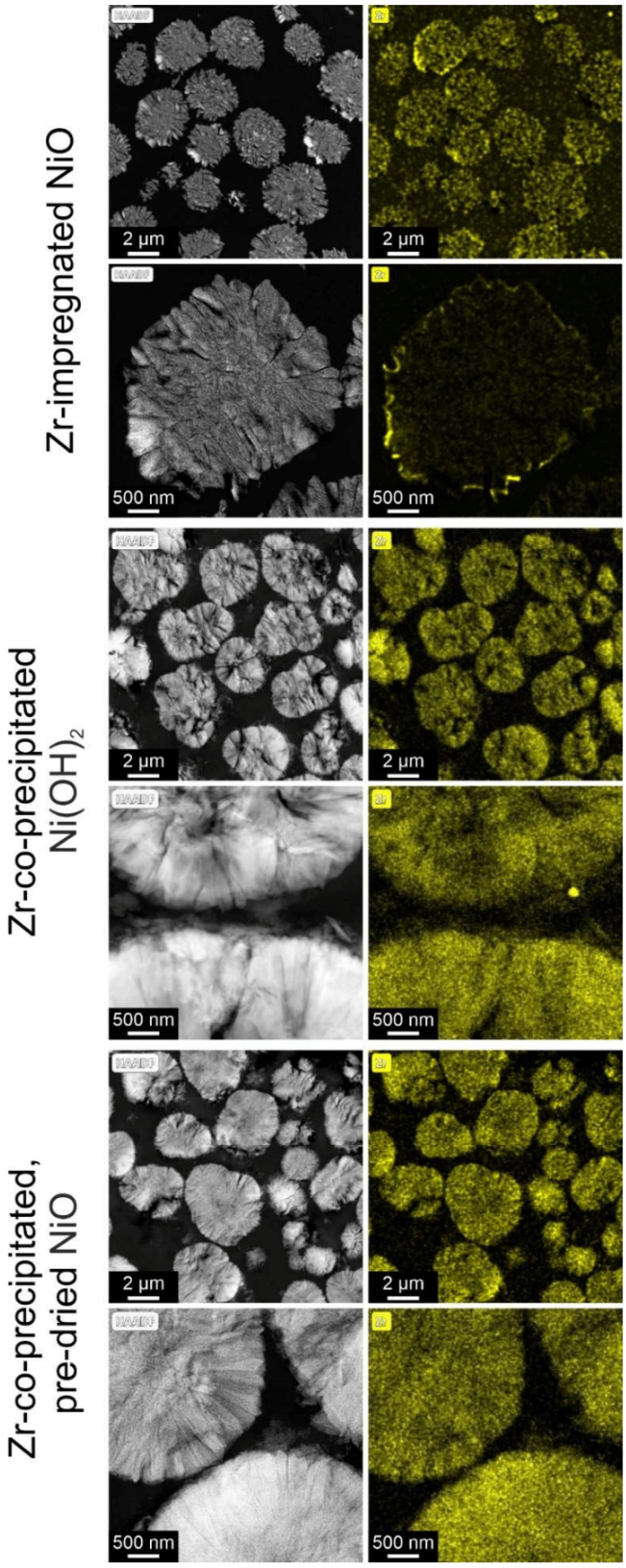

Figure S2. STEM-EDS investigation of Zr^{4+} distribution in Zr-containing precursors.

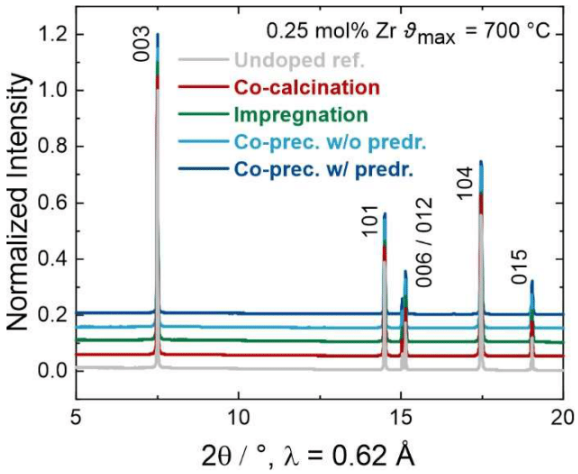

Figure S3. Synchrotron PXRD patterns for LNO samples calcined at 700 °C.

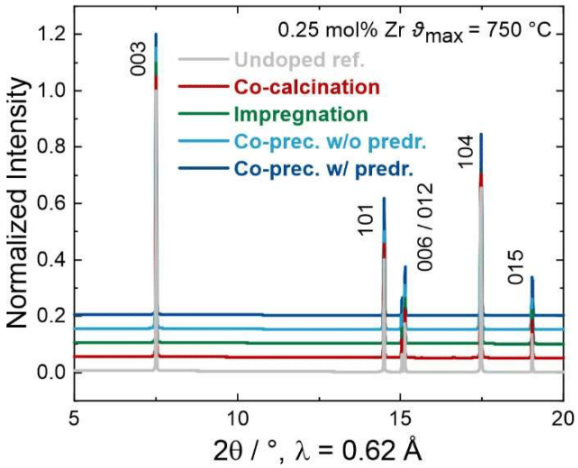

Figure S4. Synchrotron PXRD patterns for LNO samples calcined at 750 °C.

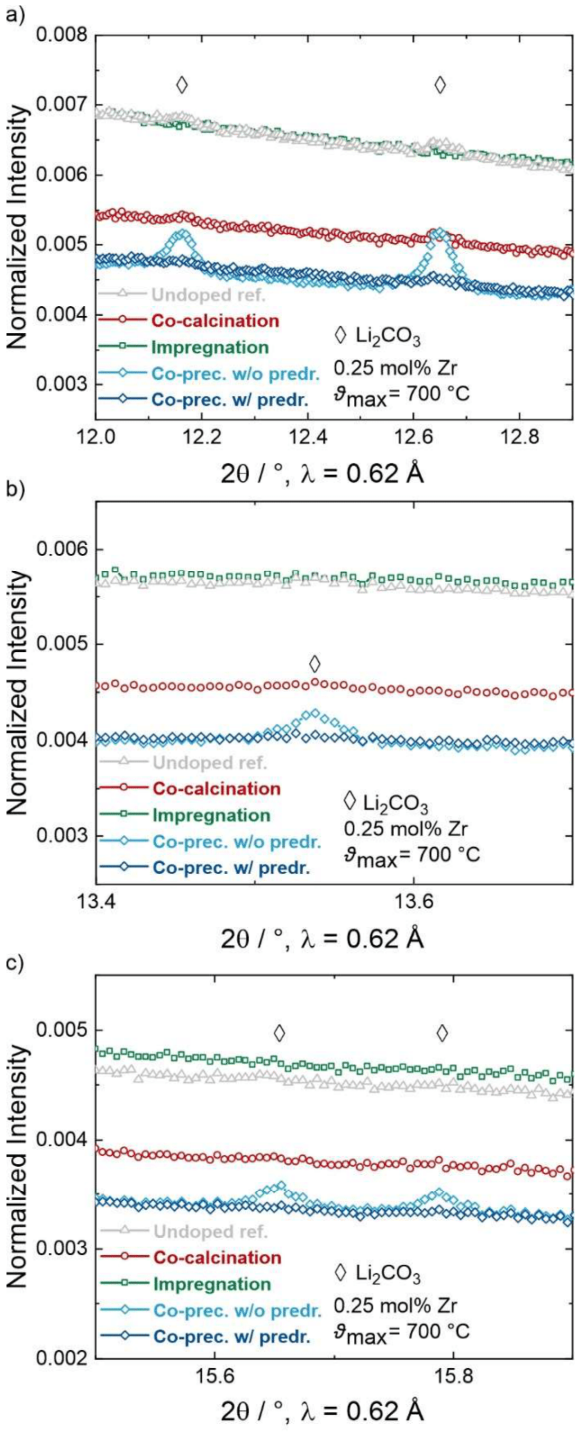

Figure S5. a-c) Li_2CO_3 impurity reflections in synchrotron PXRD patterns for LNO samples calcined at 700 °C.

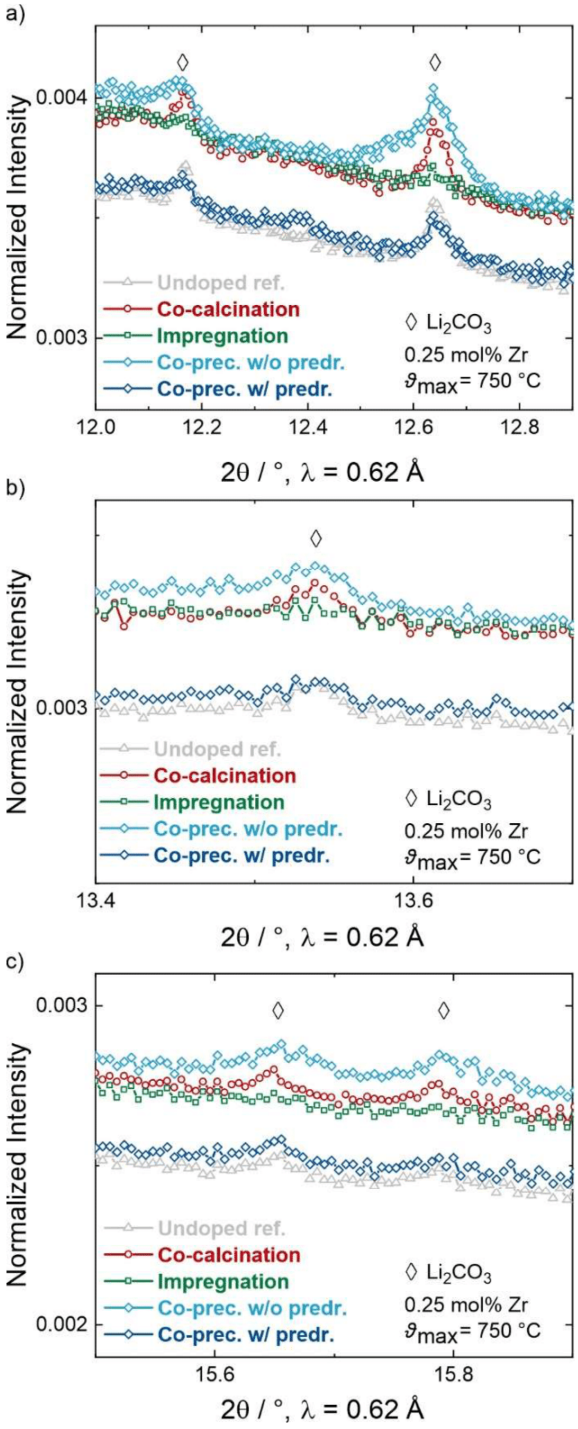

Figure S6. a-c) Li_2CO_3 impurity reflections in synchrotron PXRD patterns for LNO samples calcined at 750 °C.

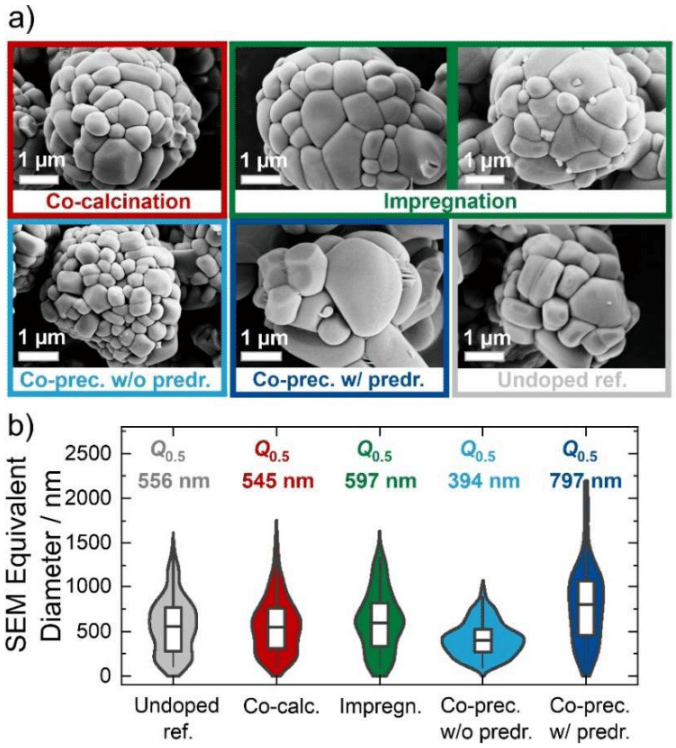

Figure S7. Dependence of a) particle morphology and b) size on process route for LNO calcined at 750 °C.

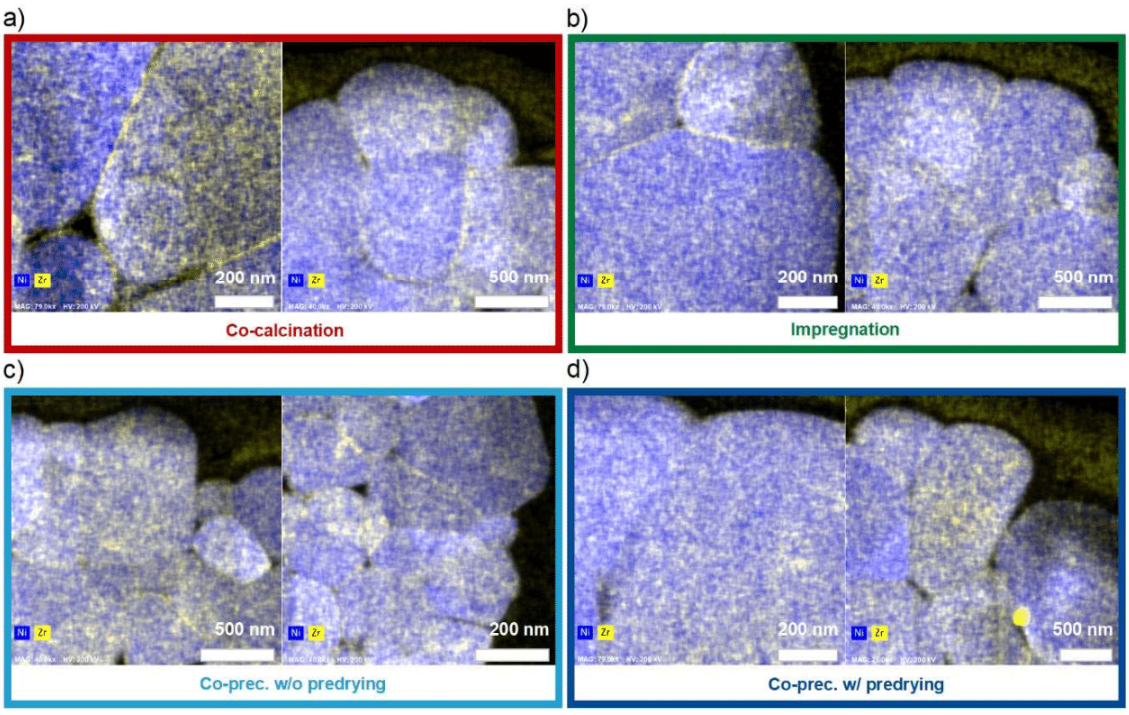

Figure S8. a-d) STEM-EDS investigation of Zr^{4+} distribution in secondary particles of LNO calcined at 750 °C. Ni is mapped in blue, Zr in yellow.

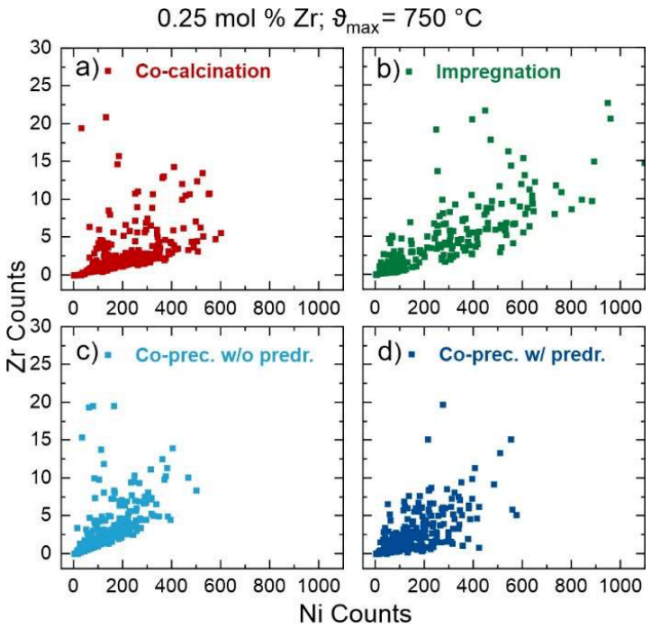

Figure S9. a-d) LA-ICP-MS investigation of Zr^{4+} distribution between secondary particles for all samples calcined at 750 °C.

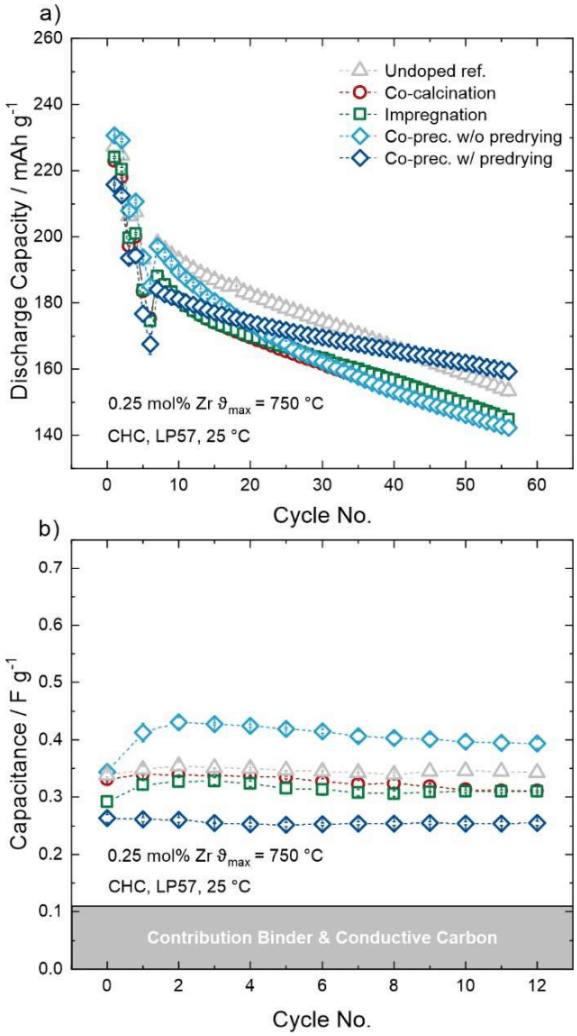

Figure S10. Electrochemical characterization of Zr-doped LNO (calcined at 750 °C) in coin half-cells in dependence of chosen process route. a) Specific discharge capacity in the two initial cycles at C/20, during a rate test (C/3, C/10, 1C and 2C) and upon C/3 cycling. b) Specific capacitance evolution during C/10 cycling.

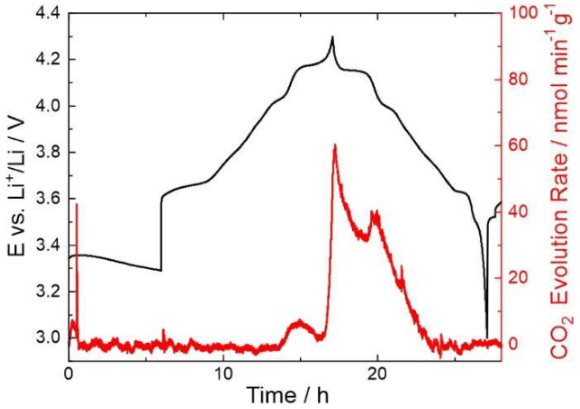

Figure S11. Exemplary DEMS profile of the initial cycle for LNO obtained from impregnated pCAM calcined at 700 °C.

Table S1. Carbon content of pristine, co-precipitated and co-precipitated and pre-dried pCAM as determined by elemental analysis.

pCAM	**Carbon / wt%**
Pristine $Ni(OH)_2$	0.05
Co-precipitated $Ni(OH)_2$	0.17
Co-precipitated, pre-dried NiO	0.03

Supporting Information to Chapter 4.3.

Supporting Information

The Effect of Configurational Entropy on Acoustic Emission of P2-Type Layered Oxide Cathodes for Sodium-Ion Batteries

Sören L. Dreyer[1], Ruizhuo Zhang[1], Junbo Wang[1], Aleksandr Kondrakov[2], Qingsong Wang[1,3,*], Torsten Brezesinski[1,*] and Jürgen Janek[1,4]

[1] Institute of Nanotechnology, Karlsruhe Institute of Technology (KIT), Hermann-von-Helmholtz-Platz 1, 76344 Eggenstein-Leopoldshafen, Germany

[2] BASF SE, Carl-Bosch-Str. 38, 67056 Ludwigshafen, Germany

[3] Bavarian Center for Battery Technology (BayBatt), Department of Chemistry, University of Bayreuth, Universitätsstr. 30, 95447 Bayreuth, Germany

[4] Institute of Physical Chemistry & Center for Materials Research (ZfM/LaMa), Justus-Liebig-University Giessen, Heinrich-Buff-Ring 17, 35392 Giessen, Germany

* Authors to whom any correspondence should be addressed.

E-mail: qingsong.wang@uni-bayreuth.de and torsten.brezesinski@kit.edu

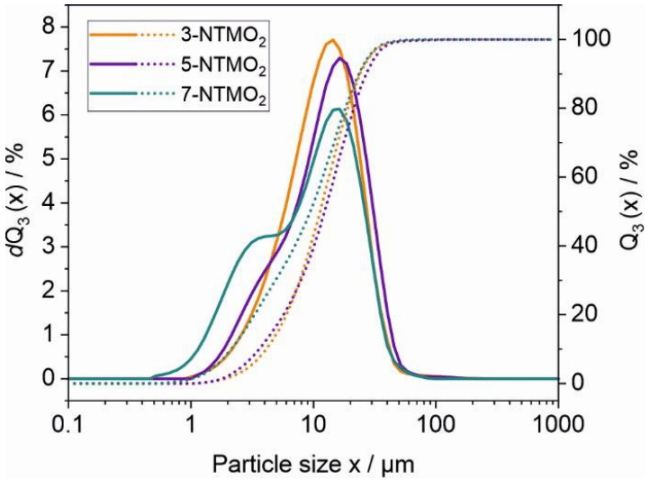

Figure S1. Differential (dQ_3, solid lines) and cumulative (Q_3, dotted lines) volume-based particle size distribution curves of all three materials determined by laser diffraction (Mastersizer 3000, Malvern Panalytical).

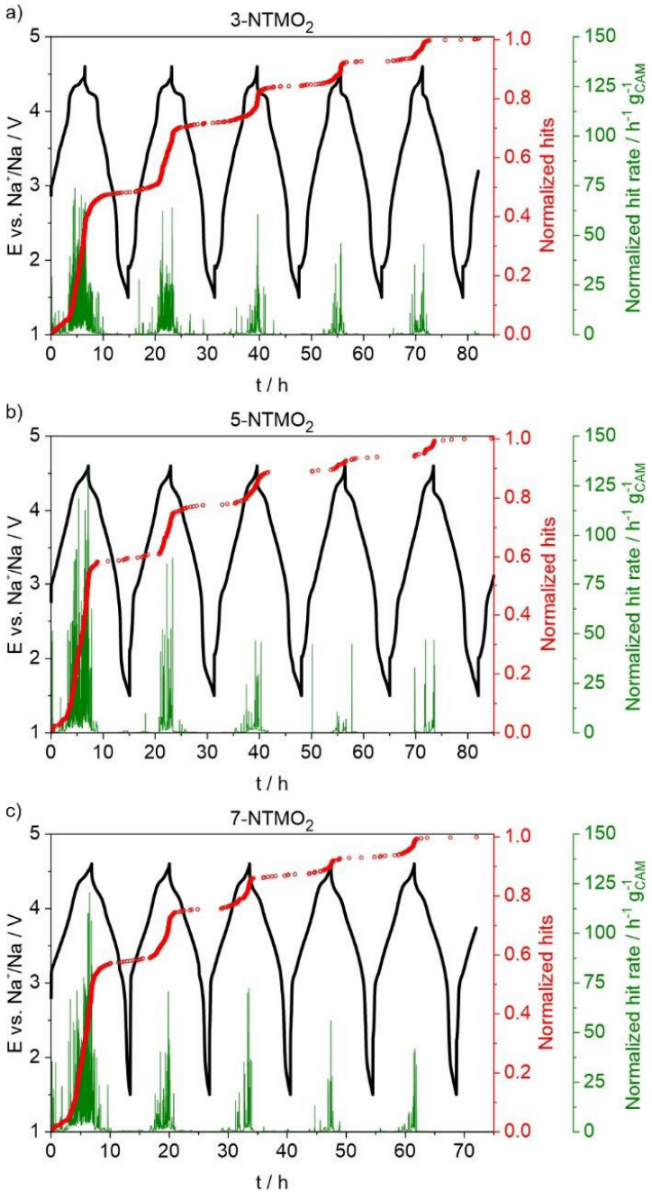

Figure S2. Normalized hits and hit rate for a) 3-$NTMO_2$, b) 5-$NTMO_2$ and c) 7-$NTMO_2$.

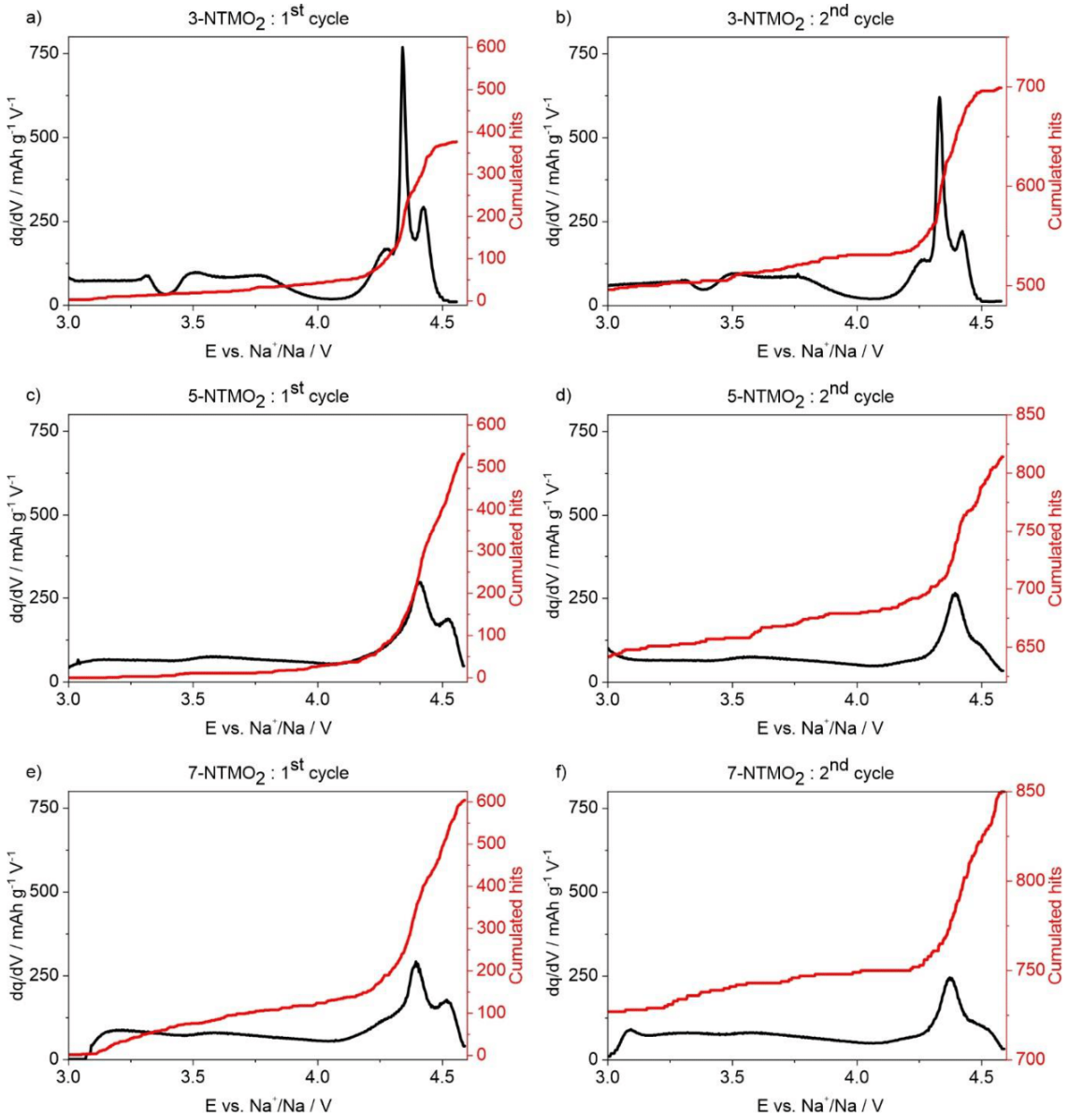

Figure S3. dq/dV plots of the first and second charge cycle and corresponding cumulative hits for a,b) 3-$NTMO_2$, c,d) 5-$NTMO_2$ and e,f) 7-$NTMO_2$.

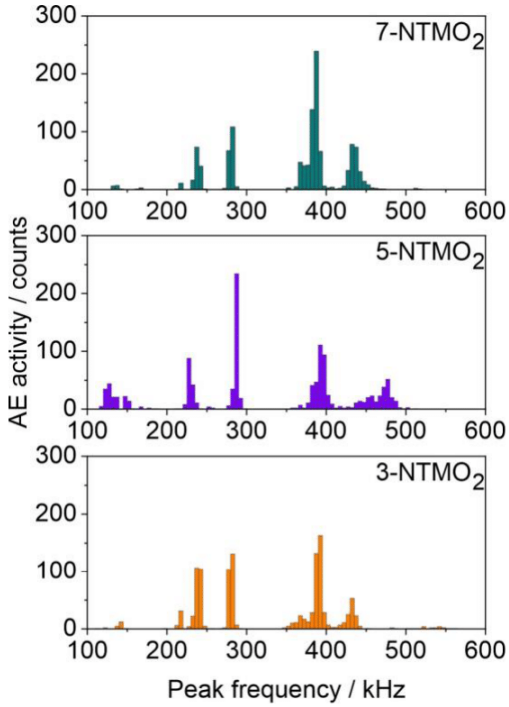

Figure S4. Histogram of peak frequency distribution for 3-$NTMO_2$ (bottom), 5-$NTMO_2$ (middle) and 7-$NTMO_2$ (top).

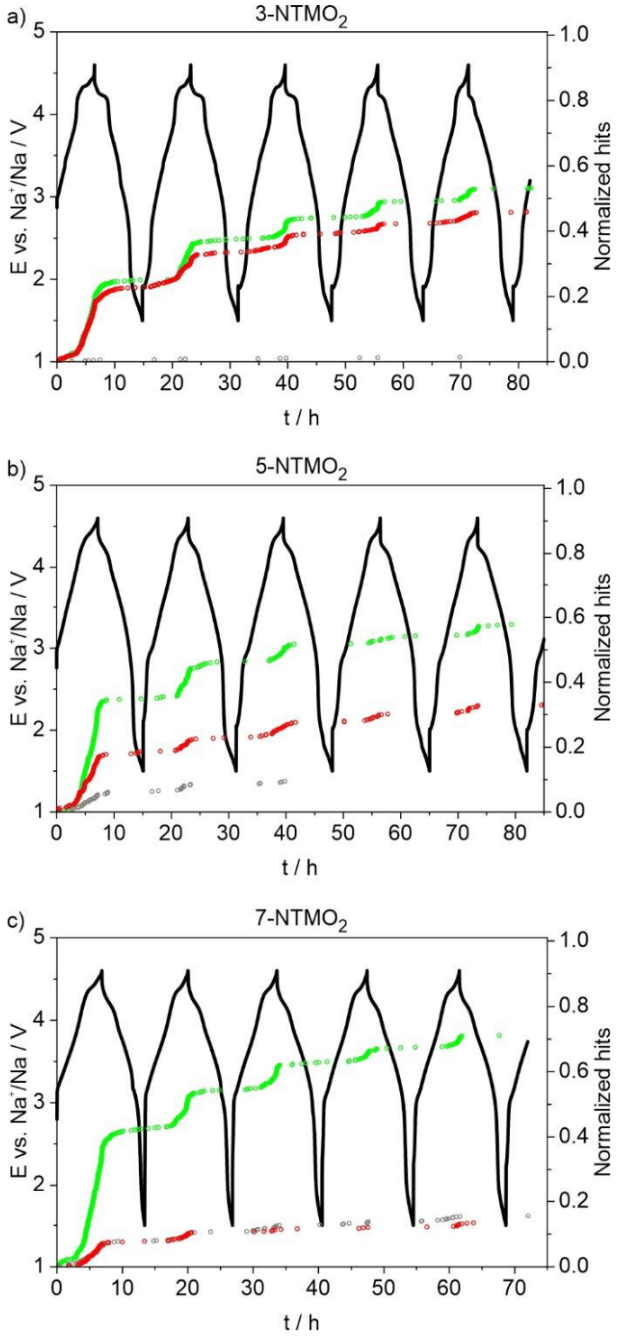

Figure S5. Second cell set acoustic profiles normalized to the total hit count after five cycles for a) 3-$NTMO_2$, b) 5-$NTMO_2$ and c) 7-$NTMO_2$ and classified by peak frequency into AE1 (gray), AE2 (red) and AE3 (green).

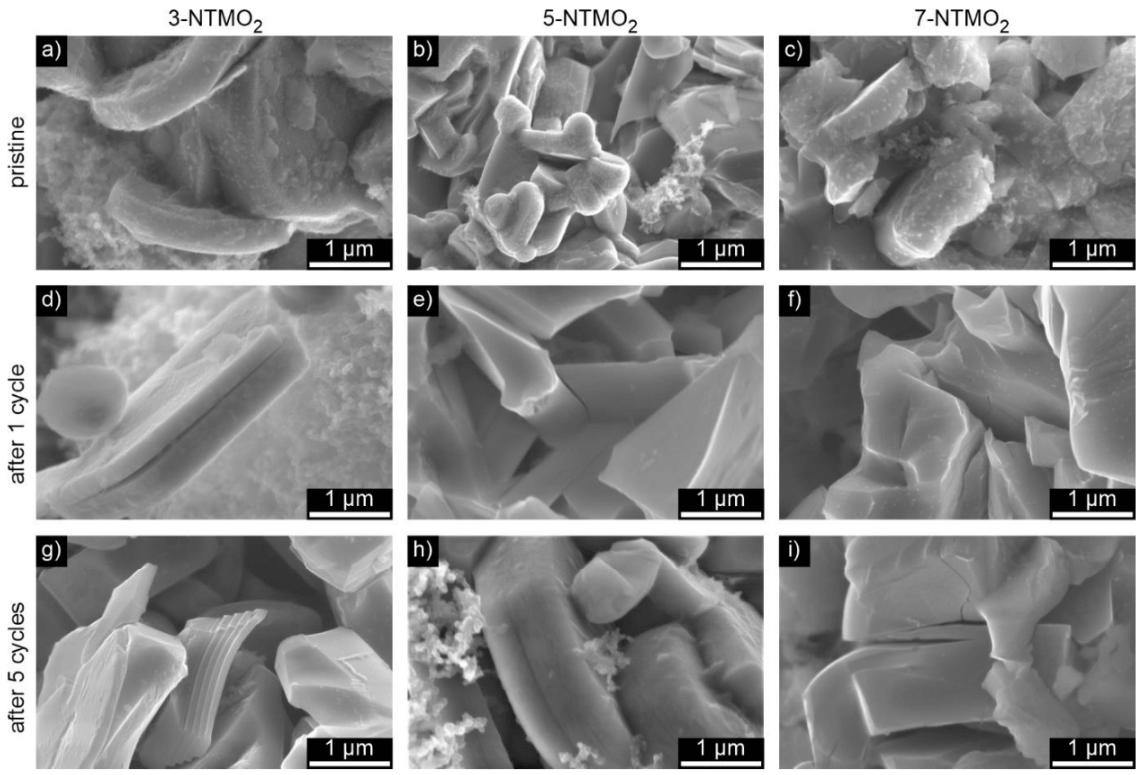

Figure S6. Top-view SEM images of cathodes in pristine state and after one and five cycles (each at the end of discharge).

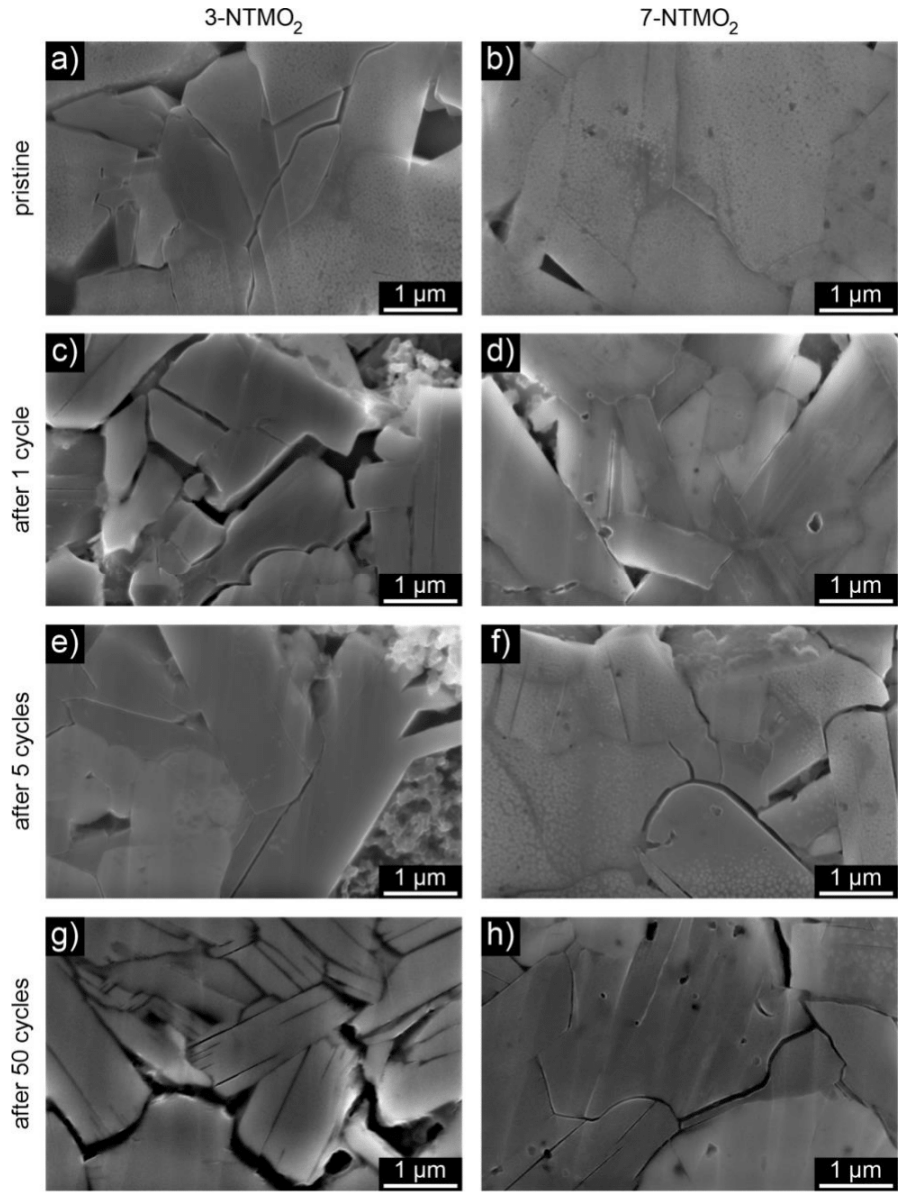

Figure S7. Higher-magnification cross-sectional SEM images of pristine and cycled cathodes.

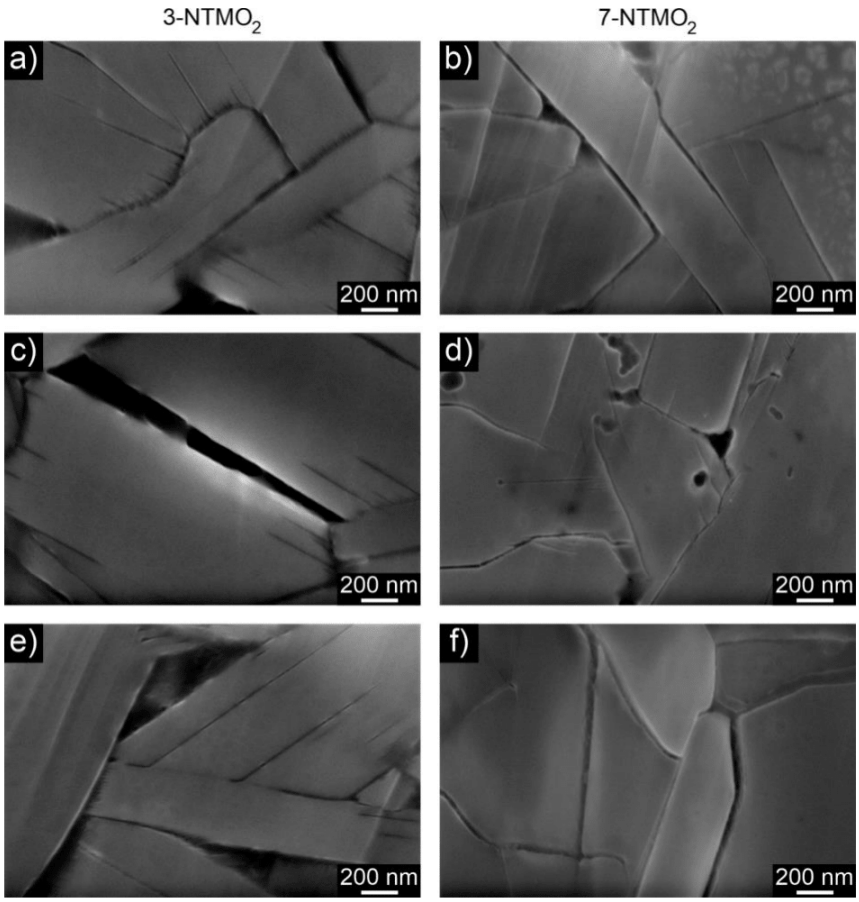

Figure S8. Corrosion and crack nucleation is found at higher magnification on the surface of 3-$NTMO_2$, but much less for 7-$NTMO_2$ after 50 cycles.

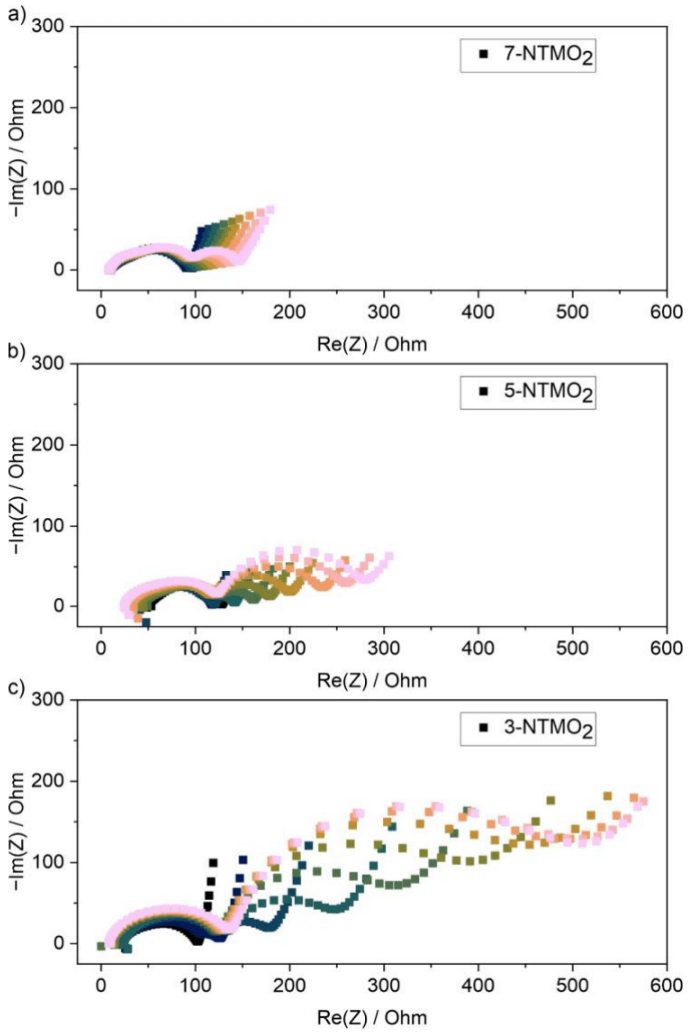

Figure S9. Increase in impedance and formation of a second semicircle, presumably due to SEI formation upon Mn dissolution, obfuscate increasing specific surface area. Measured during charge over 10 cycles [cycle no. 1 (black) to cycle no. 10 (pink)] at 4.0 V.

Table S1. Specific charge capacities delivered below and above 4.0 V vs. Na^+/Na.

Cycle	E / V vs. Na^+/Na	q_{ch} / mAh/g		
		3-$NTMO_2$	5-$NTMO_2$	7-$NTMO_2$
1	< 4.0	72.6	67.2	67.9
	≥ 4.0	69.9	75.9	73.9
2	< 4.0	115.4	96.0	74.1
	≥ 4.0	60.6	57.7	57.1
3	< 4.0	114.0	103.6	79.1
	≥ 4.0	56.7	55.0	54.6

Supporting Information to Chapter 4.4.

Supporting Information

Elucidating Gas Evolution of Prussian White Cathodes for Sodium-ion Battery Application: The Effect of Electrolyte and Moisture

Sören L. Dreyer, Faduma M. Maddar, Aleksandr Kondrakov, Jürgen Janek, Ivana Hasa and Torsten Brezesinski**

S. L. Dreyer, Dr. A. Kondrakov, Prof. J. Janek, Dr. T. Brezesinski
Battery and Electrochemistry Laboratory (BELLA), Institute of Nanotechnology, Karlsruhe Institute of Technology (KIT), Hermann-von-Helmholtz-Platz 1, 76344 Eggenstein-Leopoldshafen, Germany; E-mail: torsten.brezesinski@kit.edu

Dr. F. M. Maddar, Prof. I. Hasa
WMG, The University of Warwick, Coventry CV4 7AL, United Kingdom; E-Mail: ivana.hasa@warwick.ac.uk

Dr. A. Kondrakov
BASF SE, Carl-Bosch-Str. 38, 67056 Ludwigshafen, Germany

Prof. J. Janek
Institute of Physical Chemistry & Center for Materials Research (ZfM/LaMa), Justus-Liebig-University Giessen, Heinrich-Buff-Ring 17, 35392 Giessen, Germany

Table S1. Overview of measurement conditions and variations for each experiment.

Exp. no.	Shown in figure	Conductive salt	Solvents	Other conditions
1	1a	1 M $NaClO_4$	EC:PC:DMC = 1:1:1 (v/v/v) with 5 v% FEC	Dried electrode
2	1b	1 M $NaPF_6$	EC:DEC = 3:7 (v/v)	Dried electrode
3	2a	1 M $NaClO_4$	EC:PC:DMC = 1:1:1 (v/v/v) with 5 v% FEC	Undried electrode
4	2b	1 M $NaPF_6$	EC:DEC = 3:7 (v/v)	Undried electrode
5	3a	1 M $NaPF_6$	EC:PC:DMC = 1:1:1 (v/v/v) with 5 v% FEC	Dried electrode
6	3b	1 M $NaPF_6$	EC:PC:DMC = 1:1:1 (v/v/v) with 5 v% FEC	Undried electrode
7	4a	0.3 M $NaClO_4$	EC:PC:DMC = 1:1:1 (v/v/v) with 5 v% FEC	Dried electrode
8	4b	0.3 M $NaClO_4$ and 0.7 M $NaPF_6$	EC:PC:DMC = 1:1:1 (v/v/v) with 5 v% FEC	Dried electrode
9	5a	1 M $NaClO_4$	EC:PC:DMC = 1:1:1 (v/v/v) with 5 v% FEC	Dried electrode, 45 °C instead of 25 °C
10	5b	1 M $NaClO_4$	EC:PC:DMC = 1:1:1 (v/v/v) with 5 v% FEC	Dried electrode, 350 µL electrolyte only
11	S3a	1 M $NaClO_4$	EC:PC:DMC = 1:1:1 (v/v/v) with 5 v% FEC	Dried electrode
12	S3b	1 M $NaPF_6$	EC:DEC = 3:7 (v/v)	Dried electrode
13	S7	1 M $NaClO_4$	EC:PC:DMC = 1:1:1 (v/v/v) with 5 v% FEC	Dried electrode, no cold trap

Table S2. Specific capacities and total gas amounts [integrals of evolution rates; normalized in case of $(CN)_2$] for each experiment.

Measurement	1	2	3	4	5	6	7	8	9	10	11	12	13
1st-cycle charge (discharge) capacity / mAh g^{-1}	142 (149)	151 (143)	66 (88)	76 (83)	138 (146)	80 (92)	140 (148)	140 (147)	145 (150)	142 (148)	143 (150)	149 (142)	140 (147)
2nd-cycle charge (discharge) capacity / mAh g^{-1}	151 (148)	156 (141)	93 (93)	94 (88)	148 (146)	95 (95)	149 (148)	148 (147)	148 (143)	150 (147)	152 (149)	155 (140)	148 (146)
3rd-cycle charge (discharge) capacity / mAh g^{-1}	170 (144)	211 (123)	143 (134)	149 (93)	184 (125)	150 (140)	171 (148)	168 (143)	180 (99)	170 (145)	171 (147)	252 (114)	170 (144)
1st-cycle H_2 integral / µmol g^{-1}	15	270	172	199	<1	117	<1	<1	5	<1	<1	179	<1
2nd-cycle H_2 integral / µmol g^{-1}	<1	102	148	183	<1	80	<1	<1	9	<1	<1	93	<1
3rd-cycle H_2 integral / µmol g^{-1}	101	465	1050	1405	254	909	115	95	381	122	97	395	162
1st-cycle CO_2 integral / µmol g^{-1}	5.4	1.2	10.5	0.5	5.6	5.9	3.0	6.9	13.8	4.5	2.4	0.8	2.8
2nd-cycle CO_2 integral / µmol g^{-1}	3.6	1.5	10.7	0.5	0.9	4.5	2.4	2.3	11.4	3.9	1.5	0.5	1.9
3rd-cycle CO_2 integral / µmol g^{-1}	67.7	904	109	36.3	55.1	90.6	41.3	52.8	193	75.7	63.2	521	88.1
1st-cycle $(CN)_2$ integral / pAh g^{-1}	40.2	0.7	10.1	<0.1	8.2	9.8	30.2	24.5	60.5	17.0	15.7	<0.1	17.4
2nd-cycle $(CN)_2$ integral / pAh g^{-1}	28.1	0.4	11.4	<0.1	5.7	8.3	11.5	13.2	26.2	10.7	10.4	0.4	16.6

Measurement	1	2	3	4	5	6	7	8	9	10	11	12	13
3rd-cycle $(CN)_2$ integral / pAh g^{-1}	1022	64.0	351	19.4	67.3	480	1017	327	421	743	860	56.3	1002

Table S1. H_2 and CO_2 calibration slopes and derived m/z = 52 normalization quotient for each experiment.

Exp. no.	Calibration slope H_2 / fA ppm^{-1}	Relative H_2 slope to average	Calibration slope CO_2 / fA ppm^{-1}	Relative CO_2 slope to average	Normalization quotient
1	261	0.878	202	1.07	0.974
2	236	0.795	120	0.633	0.714
3	268	0.902	186	0.984	0.943
4	423	1.425	248	1.313	1.369
5	299	1.006	197	1.039	1.023
6	281	0.947	181	0.957	0.952
7	282	0.95	190	1.004	0.977
8	319	1.074	217	1.149	1.111
9	361	1.216	243	1.285	1.25
10	257	0.865	183	0.965	0.915
11	274	0.923	183	0.967	0.945
12	335	1.129	209	1.103	1.116
13	248	0.835	161	0.851	0.843

Table S4. Water content calculation from H_2 integral, assuming two water molecules to yield one hydrogen molecule ($2\ H_2O + 2\ e^- \rightarrow 2\ OH^- + H_2$). After conversion of water amount to water weight, a relative weight loss can be calculated.

Exp. no.	3	4
Total H_2 amount after 2 cycles / mmol g_{PW}^{-1}	0.32	0.38
Consumed H_2O amount / mmol g_{PW}^{-1}	0.64	0.76
Consumed H_2O weight after 2 cycles / g g_{PW}^{-1} (wt%)	1.15	1.37
Total H_2 amount after 3 cycles / mmol g_{PW}^{-1}	1.37	1.79
Consumed H_2O amount after 3 cycles / mmol g_{PW}^{-1}	2.74	3.58
Consumed H_2O weight after 3 cycles / g g_{PW}^{-1} (wt%)	4.93	6.44

Table S5. Weight loss observed upon drying of the electrodes used in this study.

Electrode for exp. no.	Undried weight (with Al foil) [mg]	Dry weight (with Al foil) [mg]	Weight loss [mg]	CAM mass [mg]	Weight loss relative to CAM mass [%]
1	143.8	133.9	9.9	98.0	10.10
2	130.0	121.6	8.4	86.5	9.71
5	145.1	134.6	10.5	98.7	10.64
7	145.1	134.7	10.4	98.8	10.53
8	129.3	120.2	9.1	85.2	10.68
9	130.3	121.3	9.0	86.3	10.43
10	129.2	120.3	8.9	85.3	10.43
11	143.9	133.5	10.4	97.7	10.65
12	128.4	119.5	8.9	84.6	10.52
13	129.0	120.0	9.0	85.0	10.58

Table S6. Background subtracted peak intensity ratios for m/z = 26, 27, 52, and 53 may indicate additional presence of HCN traces in selected measurements. In experiment 1, no m/z = 53 signal was recorded due to omission in the measurement program.

Exp. no.	m/z = 26 / pA	m/z = 27 / pA	m/z = 52 / pA	m/z = 53 / pA	27/26 ratio / %	26/52 ratio / %	27/52 ratio / %	53/52 ratio / %
1	19.1	3.0	81.8	-	15.7	23.3	3.7	-
3	4.1	0.8	17.3	0.5	19.5	23.7	4.6	2.9
7	12.3	1.7	55.4	1.5	13.8	22.2	3.1	2.7
10	7.0	1.4	28.9	0.8	20.0	24.2	4.8	2.8
11	7.3	1.3	36.0	0.9	17.8	20.3	3.6	2.5
13	9.0	1.1	37.6	1.1	12.2	23.9	2.9	2.9

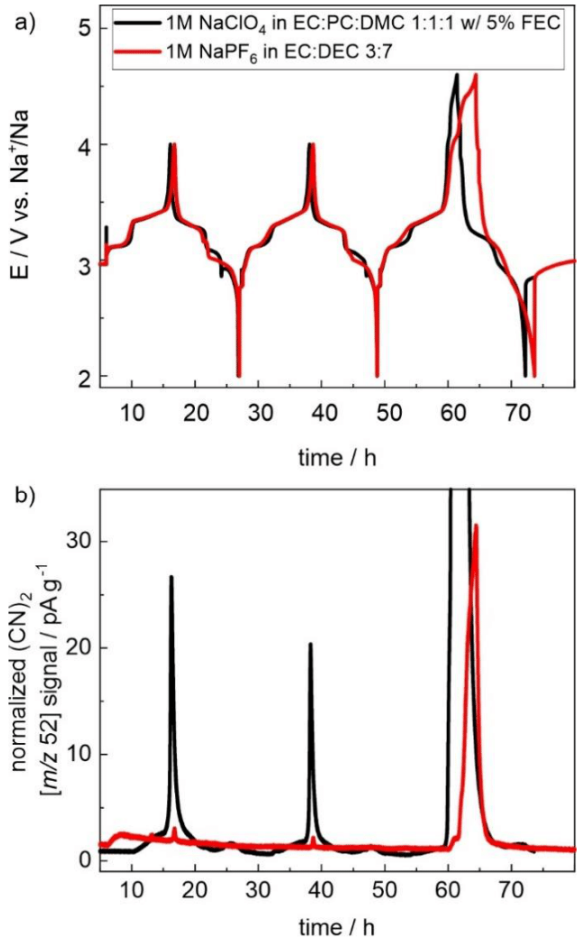

Figure S1. Overlay of voltage profiles (a) and gas evolution (b) as shown in **Figure 1**.

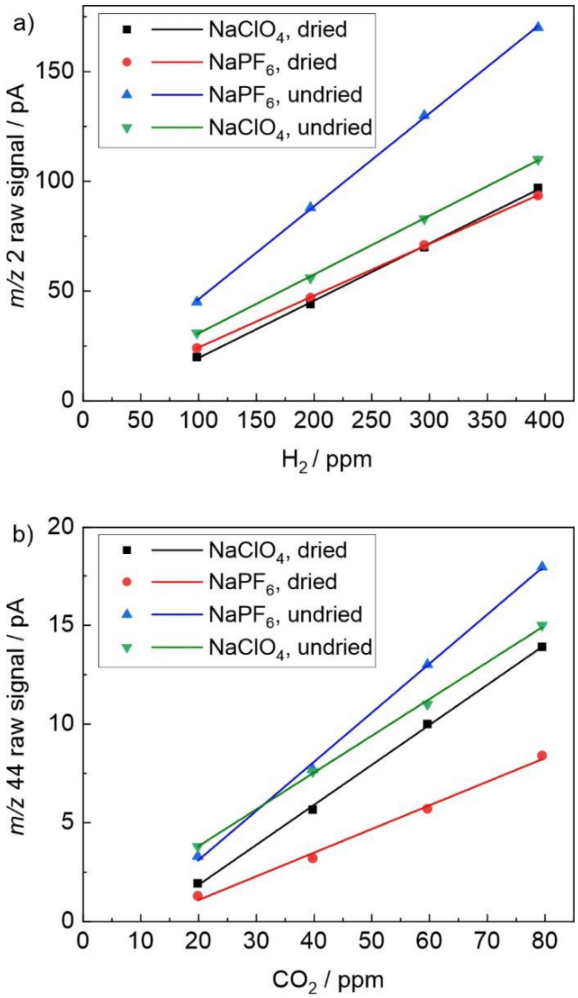

Figure S2. (a) H_2 and (b) CO_2 calibration slopes as determined in the four measurements obtained using 1 M $NaClO_4$ in EC:PC:DMC = 1:1:1 (v/v/v) + 5 v% FEC electrolyte in combination with dehydrated (black curves) and undried electrodes (green curves) and 1 M $NaPF_6$ in EC:DEC = 3:7 (v/v) in combination with dehydrated (red curves) and undried electrodes (blue curves).

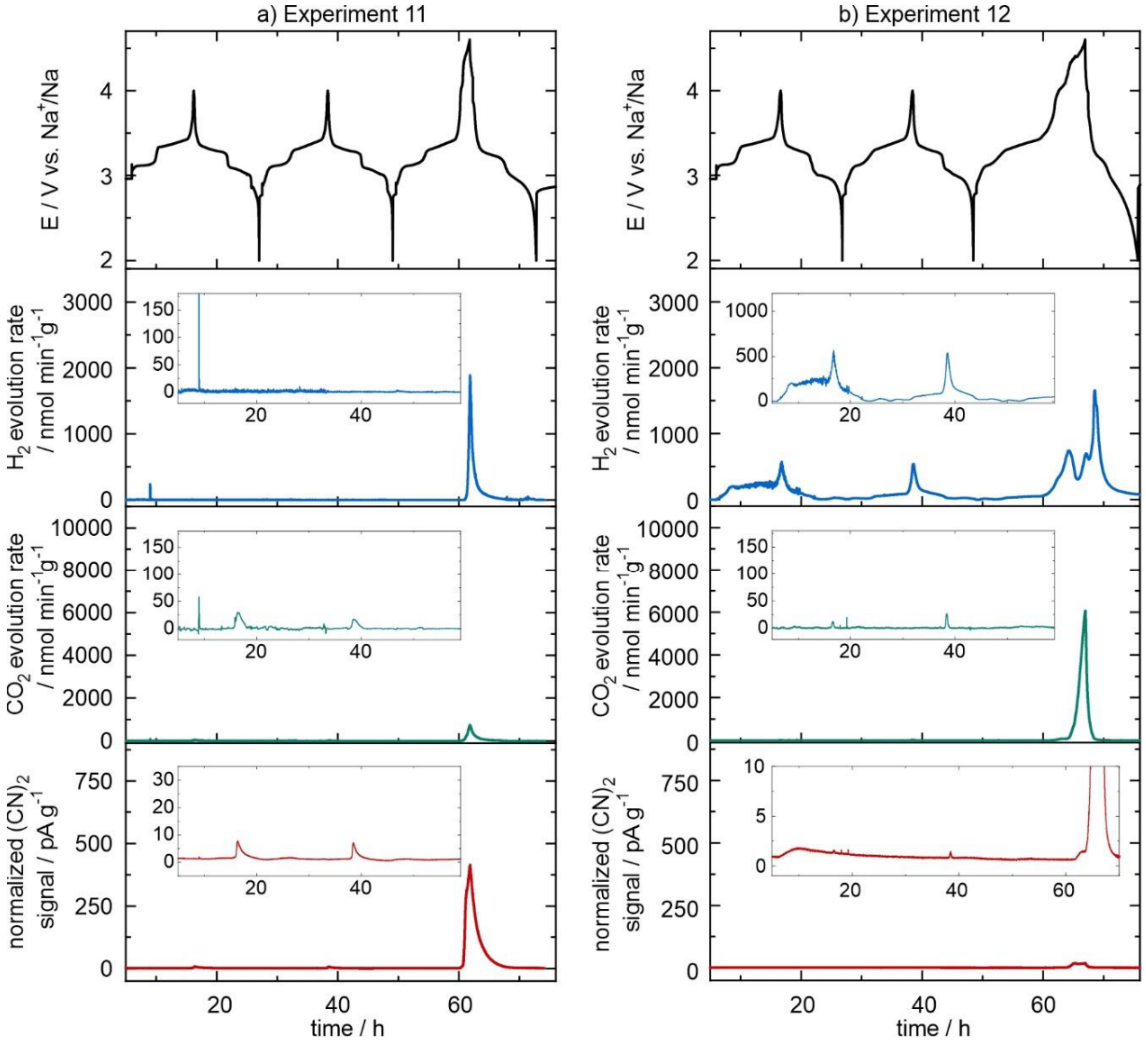

Figure S3. Repeated measurements under the same conditions as experiments 1 and 2 (shown in **Figure 1**) to confirm the observed gas evolution trends.

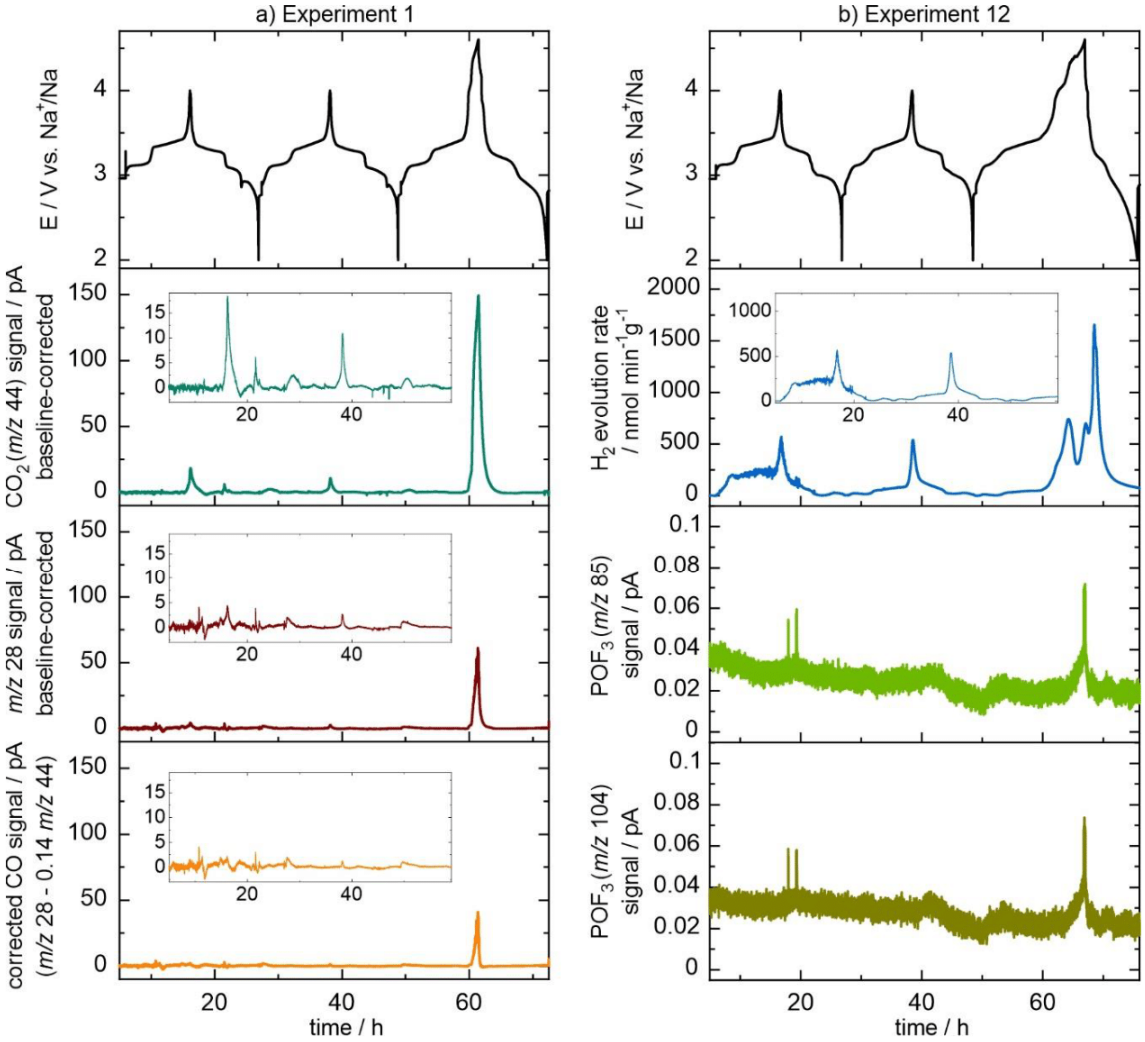

Figure S4. Other gasses detected via DEMS. (a) Correction of m/z = 28 raw signal by fraction of m/z = 44 (CO_2) signal to determine CO evolution in experiment 1. (b) Traces of POF_3 (m/z = 85 and 104) detected in cell containing $NaPF_6$-electrolyte (experiment 12).

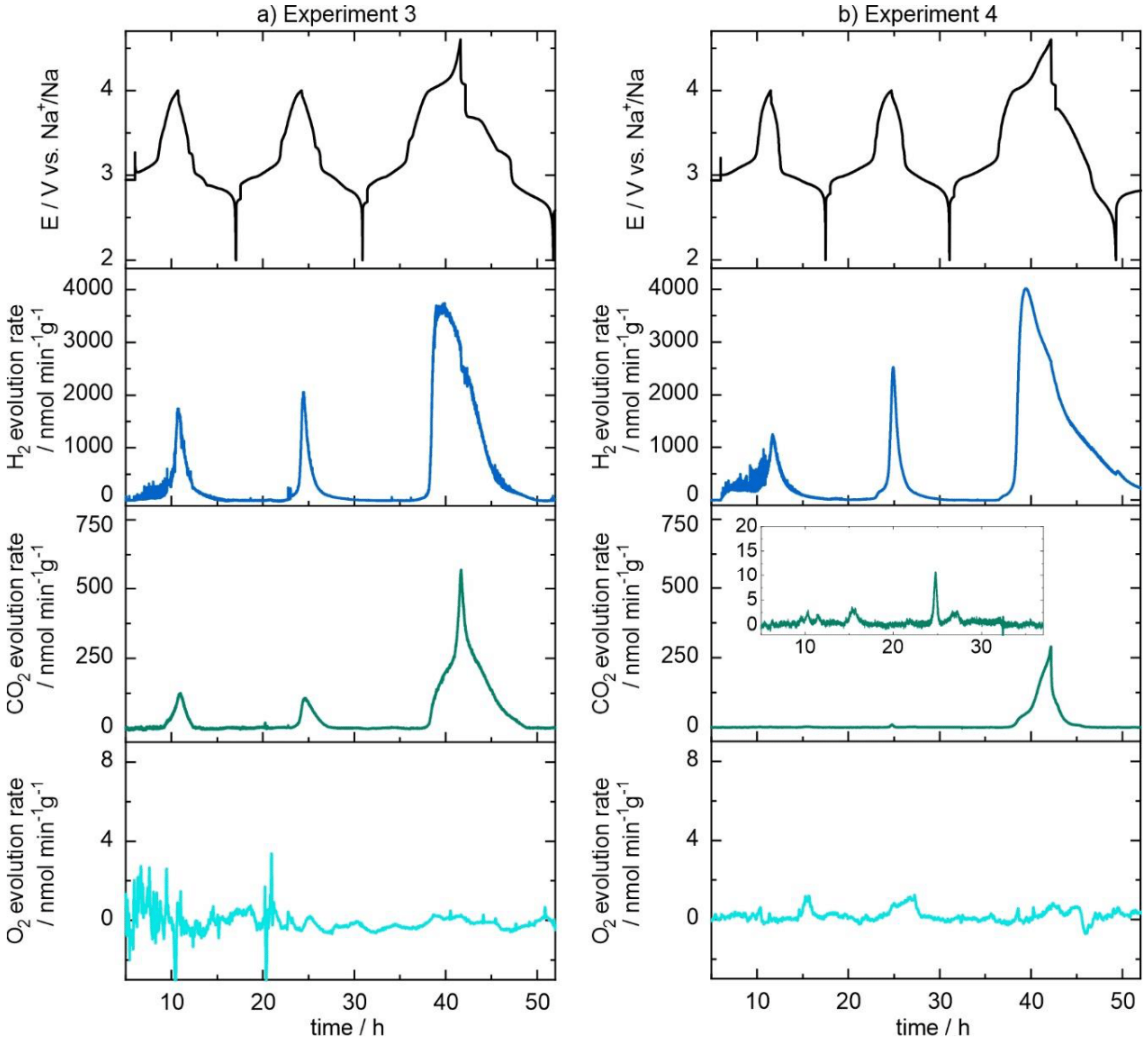

Figure S5. No detected O_2 evolution ($m/z = 32$) in half-cells containing an undried PW cathode in two different electrolytes. (a) 1 M $NaClO_4$ in EC:PC:DMC = 1:1:1 (v/v/v) with 5 v% FEC and (b) 1 M $NaPF_6$ in EC:DEC = 3:7 (v/v).

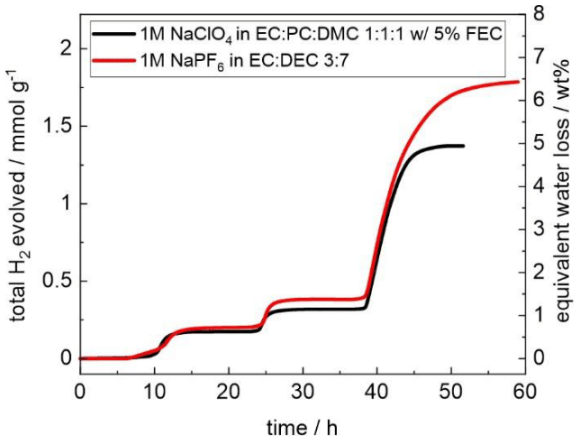

Figure S6. Cumulated water loss from undried electrodes as determined from H_2 evolution quantified via DEMS.

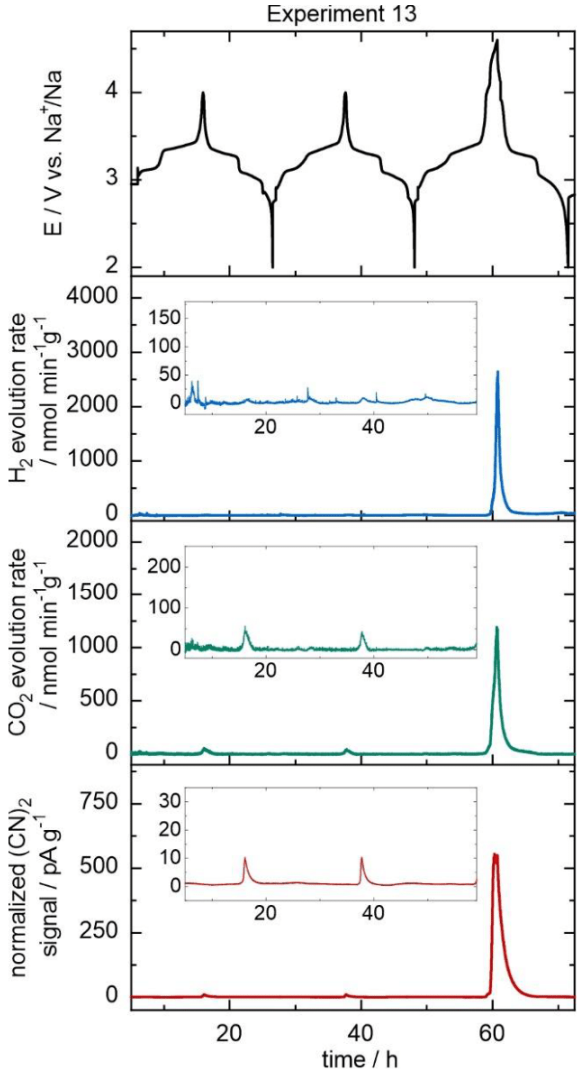

Figure S7. Measurement under the same conditions as experiment 10 (displayed in **Figure 5b**), but performed without cold trap.

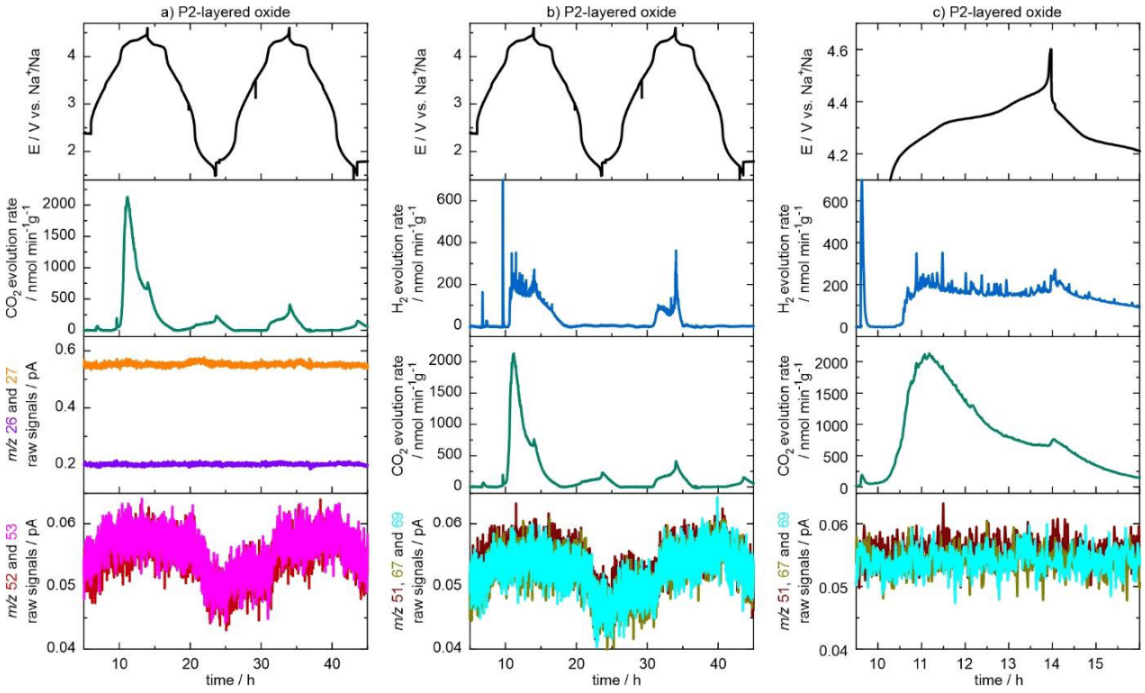

Figure S8. Gas evolution and raw signals for (a) m/z = 26, 27, 52, and 53 and (b, c) m/z = 51, 67, and 69 from layered $Na_{0.67}(Mn_{0.55}Ni_{0.21}Co_{0.24})O_2$ charged up to 4.6 V vs. Na^+/Na in 1 M $NaClO_4$ in EC:PC:DMC = 1:1:1 (v/v/v) with 5 v% FEC. Data from ref. [1].

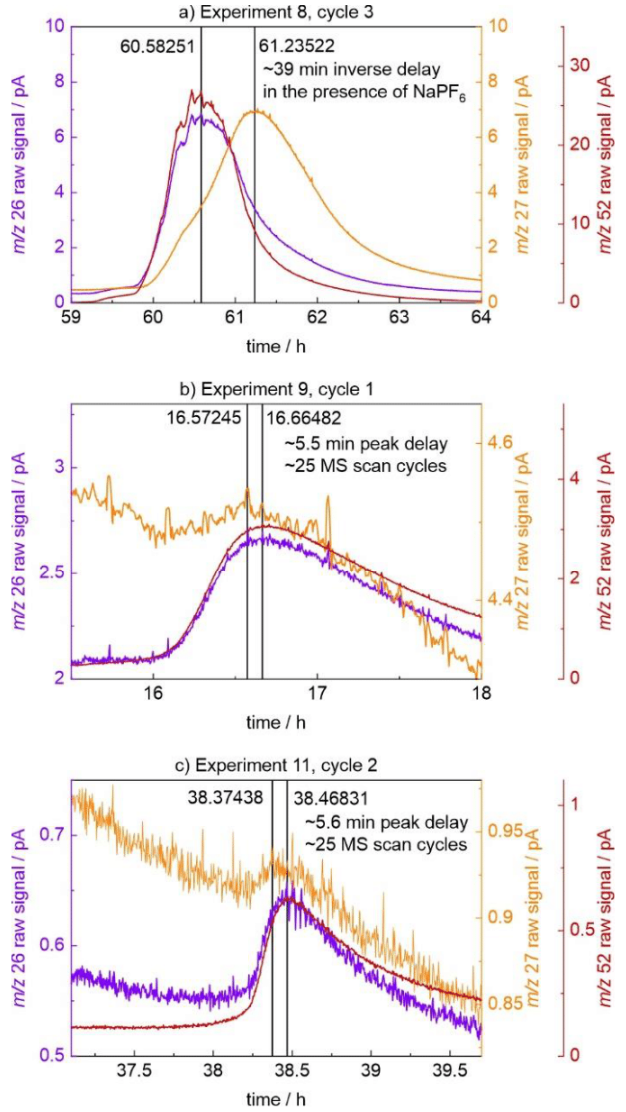

Figure S9. (a-c) Additional raw signal peak time differences between m/z = 26, 27, and 52.

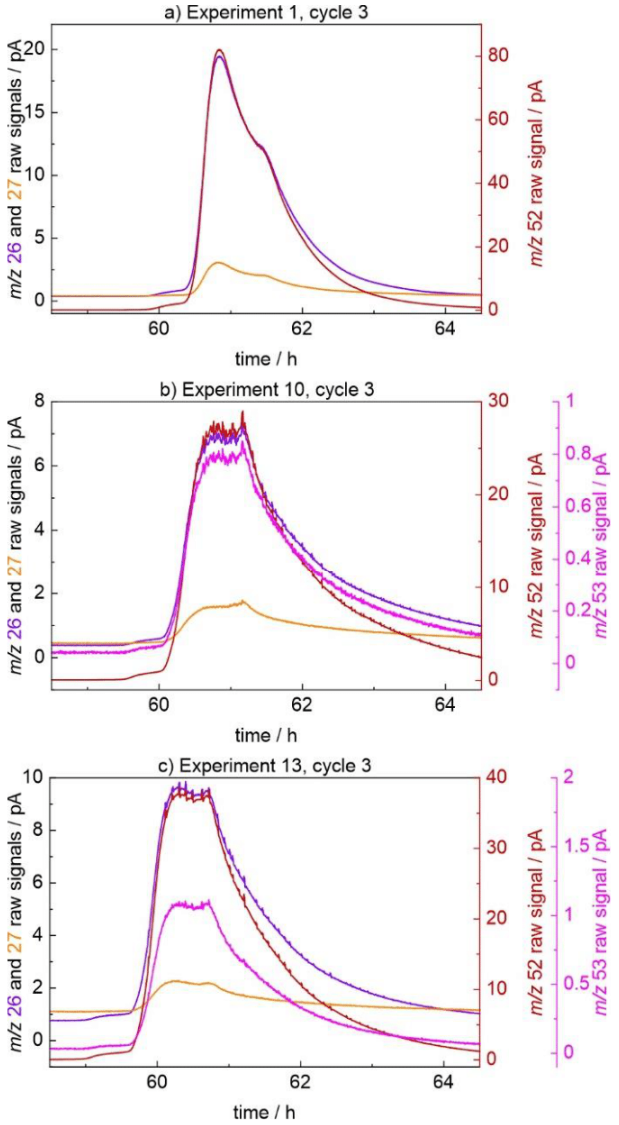

Figure S10. (a-c) Consideration of peak raw signal ratios between *m/z* = 26, 27, 52, and 53.

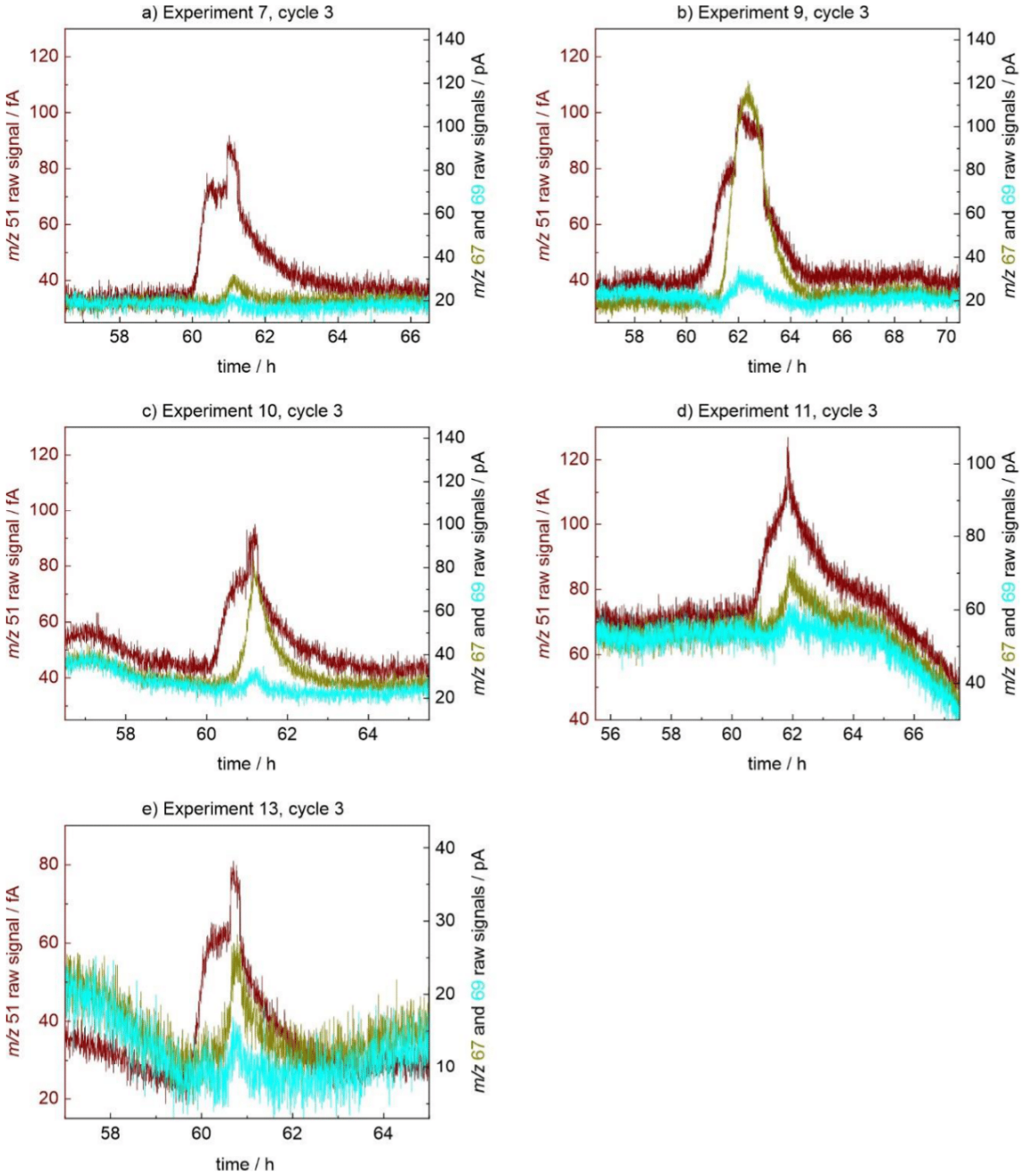

Figure S11. (a-e) m/z = 51, 67, and 69 peaks indicate formation of ClO_2, especially highlighted by signal strength conforming to ^{35}Cl and ^{37}Cl isotope ratio in m/z = 67 and 69.

[1] J. Wang, S. L. Dreyer, K. Wang, Z. Ding, T. Diemant, G. Karkera, Y. Ma, A. Sarkar, B. Zhou, M. V. Gorbunov, A. Omar, D. Mikhailova, V. Presser, M. Fichtner, H. Hahn, T. Brezesinski, B. Breitung, Q. Wang, *Mater. Futures* **2022**, *1*, 035104.

Equations

(1) $$\mathrm{LiTMO_2 \rightleftharpoons Li_{1-x}TMO_2 + x\,Li^+ + x\,e^-\ \ (TM = Ni, Co)}$$ 4

(2) $$\mathrm{C_6 + x\,Li^+ + x\,e^- \rightleftharpoons Li_xC_6}$$ 4

(3) $$\mathrm{LiTMO_2 + C_6 \rightleftharpoons Li_{1-x}TMO_2 + Li_xC_6}$$ 4

(4) $$\mathrm{TMCl_2 + Na_4[Fe(CN)_6] \longrightarrow Na_2TM[Fe(CN)_6]\downarrow + 2\,NaCl}$$ 18

(5) $$\mathrm{2\,Mn(NO_3)_2 + 6\,NaCN \longrightarrow Na_2Mn[Mn(CN)_6]\downarrow + 4\,NaNO_3}$$ 19

(6) $$\mathrm{2\,Na_4[Fe(CN)_6] + 6\,HCl \longrightarrow Na_2Fe[Fe(CN)_6]\downarrow + 6\,HCN + 6\,NaCl}$$ 19

(7) $$\Delta S_{conf} = -R\sum_{i=1}^{n}(x_i \ln x_i)$$ 22

Figures

List of Scientific Contributions

Publications

1. Y. Ma, Y. Ma, **S. L. Dreyer**, Q. Wang, K. Wang, D. Goonetilleke, A. Omar, D. Mikhailova, H. Hahn, B. Breitung, T. Brezesinski, High Entropy Metal–Organic Frameworks for Highly Reversible Sodium Storage, *Adv. Mater.* **2021**, *33*, 2101342.
2. S. Schweidler, **S. L. Dreyer**, B. Breitung, T. Brezesinski, *Operando* acoustic emission monitoring of degradation processes in lithium-ion batteries with a high-entropy oxide anode, *Sci. Rep.* **2021**, *11*, 23381.
3. **S. L. Dreyer**, K. R. Kretschmer, Đ. Tripković, A. Mazilkin, R. Chukwu, R. Azmi, P. Hartmann, M. Bianchini, T. Brezesinski, J. Janek, Multi-Element Surface Coating of Layered Ni-Rich Oxide Cathode Materials and Their Long-Term Cycling Performance in Lithium-Ion Batteries, *Adv. Mater. Interfaces* **2022**, *9*, 2101100.
4. S. Schweidler, **S. L. Dreyer**, B. Breitung, T. Brezesinski, Acoustic Emission Monitoring of High-Entropy Oxyfluoride Rock-Salt Cathodes during Battery Operation, *Coatings* **2022**, *12*, 402.
5. P. Minnmann, F. Strauss, A. Bielefeld, R. Ruess, P. Adelhelm, S. Burkhardt, **S. L. Dreyer**, E. Trevisanello, H. Ehrenberg, T. Brezesinski, F. H. Richter, J. Janek, Designing Cathodes and Cathode Active Materials for Solid-State Batteries, *Adv. Energy Mater.* **2022**, *12*, 2201425.
6. J. Wang, **S. L. Dreyer**, K. Wang, Z. Ding, T. Diemant, G. Karkera, Y. Ma, A. Sarkar, B. Zhou, M. V. Gorbunov, A. Omar, D. Mikhailova, V. Presser, M. Fichtner, H. Hahn, T. Brezesinski, B. Breitung, Q. Wang, P2-type layered high-entropy oxides as sodium-ion cathode materials, *Mater. Futures* **2022**, *1*, 035104.
7. **S. L. Dreyer**, A. Kondrakov, J. Janek, T. Brezesinski, In situ analysis of gas evolution in liquid-and solid-electrolyte-based batteries with current and next-generation cathode materials, *J. Mater. Res.* **2022**, *37*, 3146–3168.
8. **S. L. Dreyer**, R. Zhang, J. Wang, A. Kondrakov, Q. Wang, T. Brezesinski, J. Janek, The effect of configurational entropy on acoustic emission of P2-type layered oxide cathodes for sodium-ion batteries, *J. Phys. Energy* **2023**, *5*, 035002.

9. **S. L. Dreyer**, P. Kurzhals, S. B. Seiffert, P. Müller, A. Kondrakov, T. Brezesinski, J. Janek, The Effect of Doping Process Route on $LiNiO_2$ Cathode Material Properties, *J. Electrochem. Soc.* **2023**, *170*, 060530.
10. L. Karger, S. Korneychuk, W. van den Bergh, **S. L. Dreyer**, R. Zhang, A. Kondrakov, J. Janek, T. Brezesinski, Seesaw Effect of Substitutional Point Defects on the Electrochemical Performance of Single-Crystal $LiNiO_2$ Cathodes, *Chem. Mater.* **2023**, DOI 10.1021/acs.chemmater.3c02727.
11. Y. He, **S. L. Dreyer**, Y.-Y. Ting, Y. Ma, Y. Hu, D. Goonetilleke, Y. Tang, T. Diemant, B. Zhou, P. M. Kowalski, M. Fichtner, H. Hahn, J. Aghassi-Hagmann, T. Brezesinski, B. Breitung, Y. Ma, Entropy-Mediated Stable Structural Evolution of Prussian White Cathodes for Long-Life Na-Ion Batteries, *Angew. Chem. Int. Ed.* **2024**, *63*, e202315371.
12. **S. L. Dreyer**, F. M. Maddar, A. Kondrakov, J. Janek, I. Hasa, T. Brezesinski, Elucidating Gas Evolution in Prussian White Cathodes for Sodium-ion Battery Application: The Effect of Electrolyte and Moisture, *Batter. Supercaps* **2024**, 7, e202300595.

Manuscripts submitted and in preparation

1. B. Zhou, S. An, D. Kitsche, **S. L. Dreyer**, K. Wang, X. Huang, J. Thanner, M. Bianchini, T. Brezesinski, B. Breitung, H. Hahn, Q. Wang, Improved Performance of High-Entropy Disordered Rock-Salt Oxyfluoride Cathode by Atomic Layer Deposition Coating for Li-Ion Batteries, *manuscript submitted*, **2024**.
2. Y. He, **S. L. Dreyer**, T. Akcay, T. Diemant, R. Mönig, Y. Ma, Y. Tang, H. Wang, H. Liu, J. Lin, S. Schweidler, M. Fichtner, H. Hahn, J. Aghassi-Hagmann, T. Brezesinski, B. Breitung, Y. Ma, Unveiling the Influence of Configurational Entropy on the Crystal Structure of Multicomponent Hexacyanoferrate Cathodes for Sodium-Ion Batteries, *manuscript in preparation*, **2024**.
3. S. An, L. Karger, **S. L. Dreyer**, J. Lin, R. Zhang, A. Kondrakov, T. Brezesinski, J. Janek, Novel Ti-modified $NaNiO_2$ Cathodes for Sodium-Ion Batteries, *manuscript in preparation*, **2024**.

Oral and Poster Presentations

1. **S. L. Dreyer**, J. H. Teo, A. Kondrakov, T. Brezesinski, J. Janek, Differential Electrochemical Mass-Spectrometry (DEMS) for In Situ Gas Evolution Studies on Solid-State and Sodium-Ion Batteries, *IBA 2022*, Bled, Slovenia, October 2nd–7th, **2022**.
2. **S. L. Dreyer**, R. Zhang, J. Wang, A. Kondrakov, Q. Wang, T. Brezesinski, J. Janek, The Effect of Configurational Entropy on Acoustic Emission of P2-type Layered Oxide Cathodes for Sodium-Ion Batteries, *E-MRS 2023 Spring Meeting*, Strasbourg, France, May 29th–June 2nd, **2023**.
3. **S. L. Dreyer**, P. Kurzhals, S. B. Seiffert, P. Müller, A. Kondrakov, T. Brezesinski, J. Janek, The effect of doping process route on $LiNiO_2$ cathode active material properties, *BASF Collaboration Forum 2023*, Ludwigshafen, Germany, September 28th, **2023**.
4. **S. L. Dreyer**, P. Kurzhals, S. B. Seiffert, P. Müller, A. Kondrakov, T. Brezesinski, J. Janek, Effect of doping process route on $LiNiO_2$ cathode active material properties, *244th Meeting of the Electrochemical Society*, Gothenburg, Sweden, October 8th–12th, **2023**.

Acknowledgements

The last section of this thesis is dedicated to all those who have helped and supported me during this journey.

First of all, I would like to thank Prof. Dr. Jürgen Janek for supervising this work with everlasting curiosity, humor and respect. His confidence, interest and optimism regarding my research was a constant source of encouragement that I highly appreciate. I would like to also thank Prof. Dr. Philipp Adelhelm for taking the time to be the second reviewer of my thesis.

To Dr. Torsten Brezesinski I am eternally grateful for being not only a supervisor, but a role model scientist. His creativity, rigor and keen eye have helped me a lot in my research and especially in writing it down.

On the BASF side of BELLA, I would like to thank Dr. Pascal Hartmann for initially hiring me, Prof. Dr. Matteo Bianchini for giving me the chance to carry out the doping process route study at BASF and Dr. Andreas Fischer and Dr. Aleksandr Kondrakov both for conference tickets, industry insights, career advice and manuscript review. I especially thank Dr. Philipp Kurzhals for the great time at BASF and for introducing the Palatine specialty *Dampfnudel* to me. Dr. Frank Haunert has been an excellent mentor and I am deeply grateful for his advice and support.

I would like to thank all friends, colleagues and former colleagues at BELLA for their support, helpfulness and companionship. Especially, I would like to thank Dr. Katja Kretschmer and Dr. Đordije Tripković for introducing me to battery research, Dr. Marie Duffiet for patient explanations and assistance with Rietveld refinement and all of BELLA's canteen regulars for entertaining and interesting lunch breaks.

I am very grateful to the High-Entropy materials group at INT, namely Yueyue He, Dr. Junbo Wang, Dr. Simon Schweidler, Dr. Qingsong Wang, Prof. Dr. Yanjiao Ma and Dr. Ben Breitung for a steady supply of samples, sodium-ion battery components and research questions that resulted in many co-authorships and sparked the creation of two manuscripts contained in this thesis.

My predecessors Dr. Jun Hao Teo, Dr. Alexander Schiele and Dr. Balázs Berkes have established and improved the DEMS setup at BELLA. I would like to thank them for passing this well-maintained manuscript machine on to me and their assistance in getting acquainted to it. Also, none of the DEMS results would exist without the skillful

work and helpful demonstrations of Rolf Brandt, Pfeiffer Vacuum. The same is true for the AE setup and Dr. Simon Schweidler.

A productive research environment requires reliable infrastructure and complex, specialized equipment. I would like to thank Albert Schmitt, Torsten Stehli and the mechanical and electrical workshops at INT for providing this environment and, whenever needed, fast and professional help with equipment repairs.

I am grateful to the Gesellschaft Deutscher Chemiker and the Studienstiftung des Deutschen Volkes for generously providing scholarships during my studies, which also allowed me to expand my horizon and venture the world.

Lastly, I would like to thank my friends back home and, above all, my family for being steady pillars of support during my entire time at university, for their faith in me and for their ongoing interest in my work and life. Xiaoxuan Tang, my wife, embodies this like no one else. I am blessed to have you by my side at all times and look forward to our future together!